Finite-frequency tomography using regional P-waves, with application to the western Pacific upper mantle

Eoghan Joseph Totten

Hertford College
University of Oxford

A thesis submitted for the degree of
Doctor of Philosophy

Michaelmas 2021

Abstract

This thesis aims to present the data measurement process, waveform modelling, full waveform sensitivity measurements, and inversion workflow, required to produce a P-wave tomography of the upper mantle, including the mantle transition zone, down to 1000km depth.

Improved seismic velocity models are needed: many tomography models do not include regional travel-time datasets. This is because the first arrivals identified in travel-time datasbases are not enough on their own to seismically sample the mantle transition zone. Sharp velocity gradients at the top (410km) and bottom (660km) of the mantle transition zone induce triplications in body waves. This means that there is more than one possible path between source and receiver for a given waveform: these can range from a topside reflection off the 410km discontinuity, through to refraction at the base of the 660km discontinuity. It is therefore difficult to attribute the first arrival time in a body waveform to its true path in an automated manner, as needed for tomography. This is heightened by discrepancies between the assumed reference background model for data processing and inversion, with respect to the true background model: therefore, seismic travel-times must be measured relative to synthetic data based on full waveform modelling. A limited number of regional body wave velocity models based on the full seismic waveform exist, which can provide sufficient seismic illumination of the mantle transition zone, a known barrier for subducting oceanic lithosphere.

In this study I present JEABOX, a P-wave tomography of the western Pacific upper mantle, using the joint inversion of existing teleseismic P-wave travel times based on multifrequency cross-correlation, with regional P-wave measurements between 14-30 degrees epicentral distance. I calculate Born sensitivity kernels for these latter triplicated data using the MC Kernel software based on the spectral element solver, Axisem. I showcase the integration of these novel triplicated data and their sensitivity kernels into a tried-and-tested finite-frequency tomography workflow, to perform joint inversion of teleseismic data and Dahlen kernels with regional travel-times and MC Kernels, to produce a hybridised P-wave velocity model based on Axisem, the first tomography of its kind.

The resulting model corroborates several major seismic structures observed across western Pacific subduction zones in previous studies, including what appears to be slab stagnation beneath the Kuril and Japan trenches, and steep subduction under the Izu-Bonin trench. In the southern hemisphere, seismic signatures imply protracted subduction beneath the Sunda-Java trench under Borneo and surrounding area. Future work will tectonically interpret the JEABOX model in full.

Finite-frequency tomography using regional P-waves, with application to the western Pacific upper mantle



Eoghan Joseph Totten

Hertford College

University of Oxford

A thesis submitted for the degree of

Doctor of Philosophy

Michaelmas 2021

Acknowledgements

Personal

My thanks are due to my supervisors, Professor Karin Sigloch and Professor Tarje Nissen-Meyer, from whom I have gained an appreciation for the importance of creative ambition as a scientific researcher. I have at times taken for granted that the software that I have been so lucky to work with, though at times challenging, is truly world class.

I would like to extend particular thanks to Dr. Kasra Hosseini, for his significant technical support: your input has been foundational to my development as a scientist. Thanks to Dr. Maria Tsekhmistrenko for helping to get me on my feet with the tomography workflow. Thanks are also due to Simon Stähler for support with the MC Kernel software and to Tom Garth and Kuangdai Leng for technical conversations over the years. Thanks are due to Professor Mitch Mihalynuk, Andy Parsons and Nestor Cerpa and Gwynfor Morgan for conversations about geodynamics and plate tectonics. Thanks are due to Andy Parsons and Jonny Wu (University of Houston) discussions about Pacific plate subduction history.Thanks are due to Benjamin Schwarz, for both mentoring and helping me to explore triplications in a new way with his coherence methodology and for letting me use his BEAM software. A special thank you is due to Steve Usher, IT Systems Administrator of the Earth Sciences Department, whose assistance and patience with hardware support and software recovery has been vital.

Thanks are also due to the support teams at the Oxford ARC and ARCHER UK national supercomputers.

Thank you to my office mates and group colleagues over the years for some happy memories: Ben Fernando, Claudia Haindl, Kuangdai Leng, Alex Szenicer, Harriet Godwin, Professor Jessica Hawthorne, Marta Pienkowska-Cote, Maria Tsekhmistrenko, Paula Koelemeijer, Matthew Kemp, Lucia Perez-Diaz, Amber Madden-Nadeau and Afsaneh Mohammadzaheri. I would like to take the opportunity to especially thank Afsaneh, who provided important steers and feedback during

resolution testing, and for her patience.

I am grateful to Victoria Forth and Christa Muller of the NERC DTP for Environmental Research for their support over the years, in particular during the COVID-19 pandemic, as well as Professor Mike Kendall for his help as Director of Graduate Studies, and Robyn Mitchell at Mathematical, Physical and Life Sciences Division. Thank you to Fran Brearton, Stephen Sexton and everyone else at The Seamus Heaney Centre for Poetry who has given me the opportunity for a new adventure.

Thank you to my three musketeers, Guillermo Javier Marrero Samarin, Jake Greenfield and Pierre Dufrasne, all of whom have tolerated my eccentricities and shortcomings for nearly a decade. Thanks to Chris Thomas for being a committed friend over the years. Thanks to my former housemates Callum Williams and Conor Fallon McGuigan for some good times and conversations.

Athletics forms the backbone of my life. I am grateful for the camaraderie of my friends and fellow athletes in Oxford University Cross Country Club, from whose humility and remarkable feats I have learned many valuable lessons. Thanks are especially due to Luke Cotter, Miles Weatherseed, Jamie Parkinson, Alexander Betts, Rahil Sachak-Patwa, Oliver Paulin, Joseph Woods, Tom Lamont, Liam Smith, Dan Mulryan and Charlotte Dannatt. I have been lucky enough to receive support from the Oxford University Sport Blues Scheme, which helped me develop both as a marathon runner and a person. In particular I would like to thank Paul Ledger, for reminding me to stand tall, in addition to Kyle Bennett, Duncan Bennett, Lesley Bryant and sports psychologist Dr. Mark Bellamy, all of whom have mentored and supported me over the years. Thank you also to Marie-Claire in Belfast, too.

Thanks to my athletics coach Richard Rodgers, for keeping me on the straight and narrow, and his rational wisdom. Thank you to my early years running mentor, Kerry O'Flaherty. Thanks to my extended McPhilemy family for all the happy memories and especially to my grandparents, for imbuing us all with kindness. Thanks to the Williamson family for always being upbeat. Thank you to my Mourne running companions, Andrew Annett, Lindsay Gordon, Zak Hanna, Patrick McNiff and David O'Flaherty - there is nothing quite like a twenty mile run in

Tollymore Forest Park, with 2,000 ft of climbing, to let off some steam.

Thanks are due to my mother, Bronagh, whose humble intellect, quiet determination and appreciation for all things quiet and subtle, is second to none. You have at times had to remind me of my Mourne roots and have always been there to centre me. To you I owe everything. For my father, Joe, from whom I have learned what it means to be loyal to a fault, diligent and resilient, despite the odds. For my little brother, Brendan, who has surpassed me in so many ways, such that I now think of you as my elder: I look up to you.

Above all, thank you to Milena, my person. In 2020 you came into my life and brought love, joy and hope beyond my wildest dreams. At this point it is difficult to discern who is the rock and who is the birch tree. You light up my world. Guess what?

Institutional

This research was funded by the Clarendon scholarship of Oxford University Press and supported by the UK National Environmental Research Council Doctoral Training Partnership in Environmental Research. My thanks are due to them. I am particularly grateful for short-term financial support through the COVID-19 Scholarship Extensions Fund (CSEF), and the mineral physics group PhD Covid-19 Hardship Fund through the Mineralogical Society.

The majority of seismic data used in this research was collated using obspyDMT, an open-source resource for instantaneous data retrieval from data centres accessible through the International Federation of Digital Seismic Networks (FDSN). A subset of the data used in this study supplemented regional seismic coverage of the Japanese Islands and surrounding east Asian margin via the Japanese nationwide broadband seismograph network, F-NET, installed by the National Research Institute for Earth Science and Disaster Resilience (NIED): I have very much enjoyed working with this data. Forward modelling simulations of the seismic wavefield and sensitivity kernels were calculated on the ARCHER and ARCHER2 UK national high performance supercomputers as part of the NERC mineral physics consortium. Test simulations were also carried out on the Oxford Advanced Research Computing services (ARC).

Abstract

This thesis aims to present the data measurement process, waveform modelling, full waveform sensitivity measurements, and inversion workflow, required to produce a P-wave tomography of the upper mantle, including the mantle transition zone, down to 1000km depth.

Improved seismic velocity models are needed: many tomography models do not include regional travel-time datasets. This is because the first arrivals identified in travel-time datasbases are not enough on their own to seismically sample the mantle transition zone. Sharp velocity gradients at the top (410km) and bottom (660km) of the mantle transition zone induce triplications in body waves. This means that there is more than one possible path between source and receiver for a given waveform: these can range from a topside reflection off the 410km discontinuity, through to refraction at the base of the 660km discontinuity. It is therefore difficult to attribute the first arrival time in a body waveform to its true path in an automated manner, as needed for tomography. This is heightened by discrepancies between the assumed reference background model for data processing and inversion, with respect to the true background model: therefore, seismic travel-times must be measured relative to synthetic data based on full waveform modelling. A limited number of regional body wave velocity models based on the full seismic waveform exist, which can provide sufficient seismic illumination of the mantle transition zone, a known barrier for subducting oceanic lithosphere.

In this study I present JEABOX, a P-wave tomography of the western Pacific upper mantle, using the joint inversion of existing teleseismic P-wave travel times based on multifrequency cross-correlation, with regional P-wave measurements between 14-30 degrees epicentral distance. I calculate Born sensitivity kernels for these latter triplicated data using the MC Kernel software based on the spectral element solver, Axisem. I showcase the integration of these novel triplicated data and their sensitivity kernels into a tried-and-tested finite-frequency tomography workflow, to perform joint inversion of teleseismic data and Dahlen kernels with regional travel-times and MC Kernels, to produce a hybridised P-wave velocity model based on Axisem, the first tomography of its kind.

The resulting model corroborates several major seismic structures observed across western Pacific subduction zones in previous studies, including what appears

to be slab stagnation beneath the Kuril and Japan trenches, and steep subduction under the Izu-Bonin trench. In the southern hemisphere, seismic signatures imply protracted subduction beneath the Sunda-Java trench under Borneo and surrounding area. Future work will tectonically interpret the JEABOX model in full.

Contents

List of Figures **xi**
List of Abbreviations **xix**
1 Introduction **1**
1.1 Motivation 1
1.2 Overview 5
1.2.1 Triplicated body waves and ray theory 5
1.2.2 Applying regional body waves to improve tomography resolution 14
1.3 History of upper mantle seismology using triplications 14
1.4 Objectives 16
1.5 Outline 19
2 Data, Measurements and Modelling **21**
2.1 Overview 22
2.2 Body wave dataset for the western Pacific 22
2.3 Multifrequency travel-time measurements 23
2.3.1 Synthetic seismograms using Instaseis 23
2.3.2 Source time functions 24
2.3.3 Cross-correlation measurements 28
2.3.4 Results 35
2.4 Future Work 37
2.4.1 Multitaper spectral estimation: a motivation and an overview . 37
2.4.2 (Numerical) Implementation 42
2.4.3 Examples 43
2.4.4 Using coherence to improve cross-correlation measurement success 43
2.5 Modelling 45
2.6 Axisem wavefields 47
2.6.1 Overview of method 47
2.7 Sensitivity kernels 49
2.7.1 Rationale 49
2.7.2 Theory 50
2.7.3 Database of kernels 52
2.7.4 Kernel visualisation 60
2.7.5 Performance 60
2.7.6 Limitations of the method and future directions 61

3 Tomography **67**
3.1 Overview . . . 68
3.2 Common corrections . . . 68
3.3 Combining paraxial and full waveform sensitivity measurements . . . 70
3.3.1 Motivation: joint inversion using Dahlen (paraxial) and MC (full waveform) kernels . . . 70
3.4 Setting up the inverse problem . . . 71
3.4.1 Winnowing of MC Kernel source and receiver values using ray theory . . . 71
3.4.2 Setting up the inverse problem . . . 74
3.4.3 Solving the inverse problem . . . 77
3.4.4 Weighting of different travel-time datasets . . . 81
3.5 Results and visualisation of the JEABOX model . . . 82
3.5.1 Limitations to the JEABOX model . . . 85
3.5.2 Kuril Trench . . . 99
3.5.3 Japan Trench . . . 99
3.5.4 Izu-Bonin Trench . . . 100
3.5.5 Subduction in the southern hemisphere . . . 106
3.5.6 Taiwan and the southern Ryukyu Arc . . . 107
3.6 Resolution Tests . . . 107
3.6.1 Overview of workflow . . . 107
3.6.2 Targeted resolution tests . . . 113
3.7 Discussion and Outlook . . . 115
3.7.1 Japan Trench . . . 115
3.7.2 Kuril Trench . . . 119
3.7.3 Izu-Bonin Trench . . . 120
3.7.4 Possible origins of variable slab dip in the Japanese Islands region 121
3.7.5 JEABOX in the southern hemisphere . . . 121
3.7.6 Depth-dependent contouring of the JEABOX model . . . 122
4 Discussions and Conclusions **145**
4.1 Discussion . . . 145
4.1.1 Japan and Izu-Bonin Slabs . . . 145
4.1.2 Southeast Asia-Australia . . . 150
4.1.3 Linking upper and lower mantle anomalies beneath east Asia . 154
4.2 Summary . . . 158
4.3 Future work . . . 161
Appendices
A Appendix **165**
References **267**

List of Figures

1.1 Triplication bow-ties for regional body waves imposed on multiples and depth phases 6
1.2 Synthetic reduced time-distance record section of triplicated body waves in an IASP91 background model 7
1.3 Synthetic reduced time-distance record section of triplicated body waves in an M311 background model, with a 525km discontinuity and depressed 690km discontinuity 8
1.4 TauP ray plots of distance-dependent multipathing of regional P-waves for a 30km source depth 9
1.5 TauP ray plots of distance-dependent multipathing of regional P-waves for a 105km source depth 10
1.6 TauP ray plots of distance-dependent multipathing of regional P-waves for a 600km source depth 11
1.7 Reduced time-distance/bow-tie plots of arrival times of regional P-waves as a function of source depth 12
1.8 SubMachine votemaps of positive velocity anomalies from global P-wave models in the western Pacific 13

2.1 Real and synthetic reduced travel-time record section for Mw 6.3 earthquake in Taiwan. 24
2.2 Instaseis-based synthetic reduced time-distance matrix plot for specific earthquake, accounting for the event source time function 26
2.3 Measured reduced time-distance matrix plot for specific earthquake . 27
2.4 High quality inverted source time function and focal mechanism for an intermediate depth earthquake 29
2.5 Modest quality inverted source time function and focal mechanism for a shallow depth earthquake 30
2.6 Onset time determination from broadband seismogram clusters during source time function inversion pre-processing 31
2.7 Multifrequency travel-time cross-correlation measurement workflow using Instaseis 32

2.8 Multifrequency travel-time cross-correlation measurement workflow using Instaseis- alternative figure 33
2.9 Gabor filters used in the frequency-dependent cross-correlation process. 34
2.10 Example of a Gabor-filtered multifrequency cross-correlation travel-time measurement 36
2.11 Travel-time histograms of regional P-waves as a function of dominant frequency 38
2.12 Random subset of approximated grazing paths (410km) of regional P-waves representative of mantle transition zone coverage 39
2.13 Random subset of approximated grazing paths (660km) of regional P-waves representative of mantle transition zone coverage 40
2.14 Random subset of approximated grazing paths (410km) with event focal mechanisms, plate boundaries and topography 41
2.15 Example of Slepian tapers applied to regional body-waves 44
2.16 Slepian-filtered Instaseis regional synthetic seismogram 45
2.17 Spectral windows associated with Slepian tapers 46
2.18 Example of cross-correlation of real and synthetic data using Slepian tapers 47
2.19 Out-of-plane and top-down view of an Axisem-derived full waveform sensitivity kernel (MC Kernel) beneath Japan, projected onto an irregular mesh 60
2.20 Cross-sectional view of a 70° sensitivity kernel 61
2.21 Sum over travel-time sensitivity (MC) kernels as a function of epicentral distance 62
2.22 A regional MC sensitivity kernel illuminating the mantle transition zone. 64
2.23 A regional MC sensitivity kernel illuminating the mantle transition zone. 65

3.1 Map of stations used to construct the JEABOX model 72
3.2 Slice of coverage and seismicity-informed mesh through a dense region of the inversion grid 75
3.3 Sample of sparse and dense regions of the JEABOX inversion grid . . 76
3.4 Kernel coverage supplemented by regional P-wave travel-time measurements and their sensitivity measurements using MC Kernel . . . 77
3.5 Misfit:roughness (resolution) curve for the JEABOX model 83
3.6 Posterior velocity distribution for the JEABOX model 84
3.7 Posterior lateral hypocentre distribution for the JEABOX model . . 84
3.8 Posterior earthquake origin time distribution for the JEABOX model 85
3.9 Targeted cross-section through Aceh. 86
3.10 Targeted cross-section through west Sumatra and Malaysia. 87
3.11 Targeted cross-section through south Sumatra. 88

3.12 Targeted cross-section through west Java and west Borneo. 89
3.13 Targeted cross-section through west Java and west Borneo. 90
3.14 Targeted cross-section through east Java. 91
3.15 Targeted cross-section through Bali. 92
3.16 Targeted cross-section through Sulawesi. 93
3.17 Targeted cross-section through eastern Sulawesi. 94
3.18 Targeted cross-section through eastern Sulawesi. 95
3.19 Targeted cross-section through Sulawesi. 96
3.20 Targeted cross-sectional slice of the JEABOX tomography model in the Japan subduction zone: slice 1 of 5. 101
3.21 Targeted cross-sectional slice of the JEABOX tomography model in the Japan subduction zone: slice 2 of 5. 102
3.22 Targeted cross-sectional slice of the JEABOX tomography model in the Japan subduction zone: slice 3 of 5. 103
3.23 Targeted cross-sectional slice of the JEABOX tomography model in the Japan subduction zone: slice 4 of 5. 104
3.24 Targeted cross-sectional slice of the JEABOX tomography model in the Japan subduction zone: slice 5 of 5. 105
3.25 3D rendering of Gaussian resolution test across the western Pacific down to 400km 109
3.26 [3D rendering of Gaussian resolution test across the western Pacific down between 400km and 800km 110
3.27 Comparison of recovered resolution from Gaussian test at upper mantle and mantle transition zone depths with and without regional P-wave data 111
3.28 Comparison of recovered resolution from Gaussian test at upper mantle and mantle transition zone depths with and without regional P-wave data 112
3.29 Synthetic input slab-targeted resolution test under the Japan trench 116
3.30 Recovery of synthetic input slab-targeted resolution test under the Japan trench using teleseismic data only. 117
3.31 Recovery and synthetic input for slab-targeted resolution test under the Japan trench for the JEABOX model 118
3.32 Recovery and synthetic input for slab-targeted resolution test under the Izu-Bonin trench 119
3.33 Recovery and synthetic input for slab-targeted resolution test under the Izu-Bonin trench 120
3.34 Contoured fast and slow velocity anomalies for the JEABOX model, 90km, 180km, 280km 123

3.35 Contoured fast and slow velocity anomalies for the JEABOX model, 370km, 460km, 550km 124
3.36 Contoured fast and slow velocity anomalies for the JEABOX model, 650km, 740km, 830km 125
3.37 Contoured fast velocity anomalies for the JEABOX model, 920km, 1020km, 1110km and 1200km 126
3.38 Contoured fast velocity anomalies for the JEABOX model, inset of southeast Asia at 90km, 180km and 280km 127
3.39 Contoured fast velocity anomalies for the JEABOX model, inset of southeast Asia at 370km, 460km and 550km 128
3.40 Contoured fast velocity anomalies for the JEABOX model, inset of southeast Asia at 650km, 740km and 830km 129
3.41 Inverted view of contoured fast velocity anomalies for the JEABOX model, inset of southeast Asia at 90km, 180km and 280km 130
3.42 Inverted view of contoured fast velocity anomalies for the JEABOX model, inset of southeast Asia at 370km, 460km and 550km 131
3.43 Inverted view of contoured fast velocity anomalies for the JEABOX model, inset of southeast Asia at 650km, 740km and 830km 132
3.44 Contoured fast velocity anomalies for the JEABOX model, inset of southeast Japan at 90km, 180km and 280km 133
3.45 Contoured fast velocity anomalies for the JEABOX model, inset of southeast Japan at 370km, 460km and 550km 134
3.46 Contoured fast velocity anomalies for the JEABOX model, inset of southeast Japan at 650km, 740km and 830km 135
3.47 An inverted view of contoured fast velocity anomalies for the JEABOX model, inset of southeast Japan at 90km, 180km and 280km 136
3.48 An inverted view of contoured fast velocity anomalies for the JEABOX model, inset of southeast Japan at 370km, 450km and 550km 137
3.49 An inverted view of contoured fast velocity anomalies for the JEABOX model, inset of southeast Japan at 650km, 740km and 830km 138
3.50 Contoured fast velocity anomalies for the JEABOX model, inset south of Taiwan at 90km, 180km and 280km 139
3.51 Contoured fast velocity anomalies for the JEABOX model, inset south of Taiwan at 370km, 460km and 550km 140
3.52 Contoured fast velocity anomalies for the JEABOX model, inset south of Taiwan at 650km, 740km and 830km 141
3.53 An inverted view of contoured fast velocity anomalies for the JEABOX model, inset south of Taiwan at 90km, 180km and 280km 142
3.54 An inverted view of contoured fast velocity anomalies for the JEABOX model, inset south of Taiwan at 370km, 460km and 550km 143

3.55 An inverted view of contoured fast velocity anomalies for the JEABOX model, inset south of Taiwan at 650km, 740km and 830km 144

4.1 Plane view slices of JEABOX down to 550km. 146
4.2 Plane view slices of JEABOX down to 900km. 147
4.3 Plane view slices of JEABOX down to 1500km. 148
4.4 Plane view slices of JEABOX clipped at anomaly magnitudes of 1%. 148
4.5 Votemap depth slices of high velocity structures in the western Pacific, compared with JEABOX, to 600km depth. 155
4.6 Votemap depth slices of high velocity structures in the western Pacific, compared with JEABOX, to 750km depth. 156

A.1 JEABOX south-north trending cross section along 98°E 166
A.2 JEABOX south-north trending cross section along 100°E 167
A.3 JEABOX south-north trending cross section along 102°E 168
A.4 JEABOX south-north trending cross section along 104°E 169
A.5 JEABOX south-north trending cross section along 106°E 170
A.6 JEABOX south-north trending cross section along 108°E 171
A.7 JEABOX south-north trending cross section along 110°E 172
A.8 JEABOX south-north trending cross section along 112°E 173
A.9 JEABOX south-north trending cross section along 114°E 174
A.10JEABOX south-north trending cross section along 116°E 175
A.11JEABOX south-north trending cross section along 118°E 176
A.12JEABOX south-north trending cross section along 120°E 177
A.13JEABOX south-north trending cross section along 122°E 178
A.14JEABOX south-north trending cross section along 124°E 179
A.15JEABOX south-north trending cross section along 126°E 180
A.16JEABOX south-north trending cross section along 128°E 181
A.17JEABOX south-north trending cross section along 130°E 182
A.18JEABOX south-north trending cross section along 132°E 183
A.19JEABOX south-north trending cross section along 134°E 184
A.20JEABOX south-north trending cross section along 136°E 185
A.21JEABOX south-north trending cross section along 138°E 186
A.22JEABOX south-north trending cross section along 140°E 187
A.23JEABOX south-north trending cross section along 142°E 188
A.24JEABOX south-north trending cross section along 144°E 189
A.25JEABOX south-north trending cross section along 146°E 190
A.26JEABOX south-north trending cross section along 148°E 191
A.27JEABOX south-north trending cross section along 150°E 192
A.28JEABOX west-east trending cross section along 15°S 193

A.29JEABOX west-east trending cross section along 13°S 194
A.30JEABOX west-east trending cross section along 11°S 195
A.31JEABOX west-east trending cross section along 9°S 196
A.32JEABOX west-east trending cross section along 7°S 197
A.33JEABOX west-east trending cross section along 5°S 198
A.34JEABOX west-east trending cross section along 3°S 199
A.35JEABOX west-east trending cross section along 1°S 200
A.36JEABOX west-east trending cross section along 1°N 201
A.37JEABOX west-east trending cross section along 3°N 202
A.38JEABOX west-east trending cross section along 5°N 203
A.39JEABOX west-east trending cross section along 7°N 204
A.40JEABOX west-east trending cross section along 9°N 205
A.41JEABOX west-east trending cross section along 11°N 206
A.42JEABOX west-east trending cross section along 13°N 207
A.43JEABOX west-east trending cross section along 15°N 208
A.44JEABOX west-east trending cross section along 17°N 209
A.45JEABOX west-east trending cross section along 19°N 210
A.46JEABOX west-east trending cross section along 21°N 211
A.47JEABOX west-east trending cross section along 23°N 212
A.48JEABOX west-east trending cross section along 25°N 213
A.49JEABOX west-east trending cross section along 27°N 214
A.50JEABOX west-east trending cross section along 29°N 215
A.51JEABOX west-east trending cross section along 31°N 216
A.52JEABOX west-east trending cross section along 33°N 217
A.53JEABOX west-east trending cross section along 35°N 218
A.54JEABOX west-east trending cross section along 37°N 219
A.55JEABOX west-east trending cross section along 39°N 220
A.56JEABOX west-east trending cross section along 41°N 221
A.57JEABOX west-east trending cross section along 43°N 222
A.58JEABOX west-east trending cross section along 45°N 223
A.59JEABOX west-east trending cross section along 47°N 224
A.60JEABOX west-east trending cross section along 49°N 225
A.61JEABOX west-east trending cross section along 51°N 226
A.62JEABOX west-east trending cross section along 53°N 227
A.63JEABOX west-east trending cross section along 55°N 228
A.64Inverted view of contoured fast velocities of the JEABOX model, down to 550km depth 229
A.65Inverted view of contoured fast velocities of the JEABOX model, from 650km down to 1100km depth 230

A.66 Inverted view of contoured slow velocities of the JEABOX model, down to 550km depth 231
A.67 Inverted view of contoured slow velocities of the JEABOX model, from 650km down to 1100km depth 232
A.68 Contoured fast velocities of the JEABOX model along the Kuril trench 233
A.69 Supplementary randomised coverage subsets of 410km grazing regional P-wave paths for band one (filtered with a 30s dominant period Gabor filter) 234
A.70 Supplementary randomised coverage subsets of 410km grazing regional P-wave paths for band two (filtered with a 21s dominant period Gabor filter) 235
A.71 Supplementary randomised coverage subsets of 410km grazing regional P-wave paths for band three (filtered with a 15s dominant period Gabor filter) 236
A.72 Supplementary randomised coverage subsets of 410km grazing regional P-wave paths for band four (filtered with a 10s dominant period Gabor filter) 237
A.73 Supplementary randomised coverage subsets of 410km grazing regional P-wave paths for band five (filtered with a 7.5s dominant period Gabor filter) 238
A.74 Supplementary randomised coverage subsets of 410km grazing regional P-wave paths for band six (filtered with a 5s dominant period Gabor filter) 239
A.75 Supplementary randomised coverage subsets of 660km grazing regional P-wave paths for band one (filtered with a 30s dominant period Gabor filter) 240
A.76 Supplementary randomised coverage subsets of 660km grazing regional P-wave paths for band two (filtered with a 21s dominant period Gabor filter) 241
A.77 Supplementary randomised coverage subsets of 660km grazing regional P-wave paths for band three (filtered with a 15s dominant period Gabor filter) 242
A.78 Supplementary randomised coverage subsets of 660km grazing regional P-wave paths for band four (filtered with a 10s dominant period Gabor filter) 243
A.79 Supplementary randomised coverage subsets of 660km grazing regional P-wave paths for band five (filtered with a 7.5s dominant period Gabor filter) 244

A.80 Supplementary randomised coverage subsets of 660km grazing regional P-wave paths for band six (filtered with a 5s dominant period Gabor filter) . . . 245
A.81 Raw colour-coded record section of broadband data and Instaseis synthetics. . . . 246
A.82 Raw colour-coded record section of broadband data and Instaseis synthetics. . . . 246
A.83 Coherence-weighted stacks used during the finite-frequency measurement process. . . . 247
A.84 East-West cross-section through DETOX P1 at 8°N . . . 248
A.85 East-West cross-section through DETOX P1 at 10°N . . . 249
A.86 East-West cross-section through DETOX P1 at 12°N . . . 250
A.87 East-West cross-section through DETOX P1 at 14°N . . . 251
A.88 East-West cross-section through DETOX P1 at 16°N . . . 252
A.89 East-West cross-section through DETOX P1 at 18°N . . . 253
A.90 East-West cross-section through DETOX P1 at 20°N . . . 254
A.91 East-West cross-section through DETOX P1 at 22°N . . . 255
A.92 East-West cross-section through DETOX P1 at 24°N . . . 256
A.93 East-West cross-section through DETOX P1 at 26°N . . . 257
A.94 East-West cross-section through DETOX P1 at 28°N . . . 258
A.95 East-West cross-section through DETOX P1 at 30°N . . . 259
A.96 East-West cross-section through DETOX P1 at 32°N . . . 260
A.97 East-West cross-section through DETOX P1 at 34°N . . . 261
A.98 East-West cross-section through DETOX P1 at 36°N . . . 262
A.99 East-West cross-section through DETOX P1 at 38°N . . . 263
A.100 East-West cross-section through DETOX P1 at 40°N . . . 264
A.101 East-West cross-section through DETOX P1 at 42°N . . . 265
A.102 5s multifrequency measurements from an earthquake located in the Komandorsky Islands region. . . . 266

List of Abbreviations

ARC . . . . . Oxford Advanced Computing Research services.

ARCHER(2) . UK National Supercomputers.

Axisem . . . . The spectral element full waveform modelling fortran code used in this study to produce the synthetic seismic wavefields required for full waveform tomography.

Instaseis . . . This is used to interact with Green's function databases which are based on Axisem wavefields.

ISC . . . . . International Seismological Centre

HFS . . . . . Hierarchical File System (HFS).

HPC . . . . . High Performance Computing.

JEABOX . . . The name of the P-wave velocity model presented in this study, and encapsulates Japan East Asia Banda Oxford, which describes the geographical extent of the model, and the research group from which it originated.

JPTRIPP20 . The name of the discrete inversion mesh created for the JEABOX tomography model.

MC Kernel . . This is the fortran-based software which uses convolution over Axisem synthetic wavefields to create volumetric sensitivity kernels corresponding to specific time-windows yielded from cross-correlation between real and synthetic data.

MTZ . . . . . Mantle Transition Zone.

NAS . . . . . Network Attached Storage.

ObspyDMT . An open source Python toolbox used to retrieve large earthquake waveform datasets.

PyFFProc . . Python Finite Frequency Processing, the Python-based workflow used to amass cross-correlation based travel-time measurements between real and synthetic seismograms.

Ray Matrix . The fortran procedure used to assimilate finite frequency kernels based on paraxial ray bundles.

RBW . . . . . Regional Body Waves

(Self) Adjoint This refers to the time-reversed velocity seismogram or displacement seismogram (context-dependent), back-propagated from the receiver towards the source.

TICC . . . . . The extant finite-frequency tomography workflow used by the Oxford seismology research group.

Where there's music, someone chose to make a song/
over all other things on this earth.

— Brenda Shaughnessy's *'Blueberries for Cal' from 'The Octopus Museum'*

1 Introduction

Contents

1.1 Motivation **1**
1.2 Overview **5**
1.2.1 Triplicated body waves and ray theory 5
1.2.2 Applying regional body waves to improve tomography resolution 14
1.3 History of upper mantle seismology using triplications **14**
1.4 Objectives **16**
1.5 Outline **19**

1.1 Motivation

The western Pacific has a long-lived subduction history. For example, in the southern hemisphere, Indonesia has origins related to the closure of former oceans dating back to 100Ma (Hall, 2012). Recent seismic tomography of the region bears the hallmarks of persistent south-north subduction from Sumatra in the west, right through to Java in the east, as well as east-west subduction along the Banda arc, that extends from the upper to the lower mantle (Zenonos et al., 2019). Further north, the Izu-Bonin and Marianas slabs appear to subduct at a steep subduction angle along the boundary between the Philippine Sea and Pacific plates (Fukao & Obayashi, 2013; Tao et al., 2018). If one examines ocean trenches further north

again, tomography of Japan and Kuril trenches evidences significant accumulation of subducted oceanic lithosphere near the globally documented 660km discontinuity (Kennett & Engdahl, 1995), the lower limit of the mantle transition zone, extending laterally over several thousand kilometres (Fukao & Obayashi, 2013; Chen et al. 2015; Tao et al., 2018): the upper mantle and transition zone anomalies are believed to be subducted Pacific oceanic lithosphere dating back more than 50 million years, while uppermost lower mantle seismically fast velocity anomalies in the region are believed to be the Izanagi plate, the subducted conjugate margin of the Pacific plate (Seton et al., 2015; Wu et al, 2022). Between the Eurasian and Pacific margin, the relatively young Philippine Sea plate presents within 80-60Ma origins, and evidences a dichotomy between its eastern and western flanks, separated by the Kyushu-Palau ridge (Lallemand, 2016). Relatively younger subduction of the Philippine Sea plate is observed beneath southwestern Japan, along the Ryukyu trench. Here, the Philippine Sea slab is believed to exhibit variable subduction behavior in the upper few hundred kilometres of the mantle, including: a slab window leeward of the Shikoku Basin; steep subduction at the Ryukyu trench leeward of the West Philippine Basin; and subduction down to the base of the mantle transition zone at the Gagua ridge, oblique to the Ryukyu trench (Pownall et al., 2017).

Irrespective of the scale of subduction across the western Pacific, the mantle transition zone, demarcated seismically by the 410km and 660km discontinuities (Kennett & Engdahl, 1995), appears to play a significant role in the evolution of subduction. Regarding the relatively young subduction of the Philippine sea plate beneath southwestern Japan, mentioned above, its deepest extent appears to have reached the base of the mantle transition zone, where it appears to be impinged e.g. Tao et. al (2018). To the east, the Izu-Bonin slab exhibits evidence of piling and buckling as it dives deeply into, and makes contact with the 660km discontinuity e.g. (Porritt & Yoshioka, 2016). At the Japan subduction zone, protracted accumulation of subducted lithosphere extends westward under the Eurasian continent for between 3,000km-5,000km (Wu et. al, 2022); geodynamic modeling suggests that buckling of subducted lithosphere is a likely scenario for

moderately-diving slab, such as the Japan slab e.g. Cizkova & Bina (2013). In many instances, when subducted lithosphere is identified in the uppermost lower mantle (between 800-1200km), there is often a seismically resolved fast velocity gap between subducted material at the base of the mantle transition zone, and the fast anomalies beneath e.g. (Tao et al., 2018).

There are many outstanding questions related to the interaction between subducted lithosphere, the mantle transition zone and the driving forces behind plate tectonics: to what extent do the resistant forces encountered by subducted lithosphere at the base of the mantle transition zone determine plate motions at the surface? For example, Seton et al. (2015) propose that the driving forces of plate tectonics, related to the subduction of the Izanagi ridge 50 million years ago along the Eurasian margin, was sufficient to reorganise the motion of the Pacific plate. Another question is: what are the exhibited behaviours of subducted lithosphere in the mantle transition zone and under what conditions do they take place? For example, Garel et al. (2014) argue that the relative plate age between subducting and overriding plates plays a role in the buoyancy forces of the slab, relative to the ambient mantle, which has an effect on the subduction angle into the mantle transition zone.

A critical question, pertinent to this thesis is: to what extent are tomography studies of the mantle transition zone resolved, and are the methods used for tomography suitable? It is only in the last decade that full waveform modelling of synthetic data, and subsequent fitting for seismic inversion, has been implemented for continental and global tomography datasets e.g. (Chen et al., 2015; Bozdag et al., 2016). This is required to successfully resolve seismic velocity anomalies in the mantle transition zone, due to scattering and multipathing of seismic waves by the 410km and 660km discontinuities. Another added problem is the need to adequately account for both the volumetric and topographic perturbation to velocity structure relative to a starting background model. For example, Koroni et al. (2017) identified that topography in velocity models, unaccounted for during inversion, will map into the observed velocity structure. This was also identified by Tao et al. (2018) in their tomography: here, they did not interpret their resolved model within 50km of the

660km discontinuity. This is difficult to implement and automate for a large-sized tomography dataset containing many hundred of thousands to millions of data. This poses another outstanding question to be asked of tomography: is there a sweet spot between data redundancy in large datasets and the methods used for tomography, that can mitigate for the limitations in resolution at mantle transition zone depths?

Across the western Pacific, many of the seismically fast tomography features pose outstanding questions. While many body wave velocity models have been performed on a global scale that include the entire western Pacific (from the Kuril arc in the north through to Indonesia in the south) in their study region, there are fewer models that target the region. Furthermore, while Tao et al. (2018) provide a state of the art, full waveform body wave velocity model of east Asia near the Japan, Ryukyu and Izu-Bonin trenches, in addition to the subsurface beneath China, their study does not extend further south. Furthermore, few tomography studies of southeast Asia have been done in a full waveform-based framework; therefore, there is an opportunity to perform full waveform-based tomography in this region, integrated into a tomography of the Japanese Islands and east Asian margin to the north.

In this thesis I present JEABOX, a P-wave velocity model that jointly inverts for teleseismic data using finite-frequency kernels based on the method of Dahlen et al. (2000a), in addition to inverting for regional P-waves, using full waveform-based travel-time measurements and sensitivity kernels (Nissen-Meyer et al., 2014; Stähler et al., 2012, in prep. The former travel-time dataset draws from a subset of the multifrequency measurements used by Hosseini & Sigloch (2015) and in Hosseini et al. (2019), reprojected onto the tomographic inversion grid used in this study. An outstanding question regarding tomography resolution at mantle transition zone depths is whether combined full waveform-based and Dahlen-type sensitivity kernels will improve this resolution, producing better resolved features. This is important for estimating the volume of subducted slabs at different subduction zones, that penetrate the MTZ. While slab sinking rates for vertically sinking slab, estimated at roughly 10 millimetres per year (e.g. Sigloch & Mihalynuk, 2013) are used to infer former plate locations, the lateral accumulation of subducted

lithosphere in the mantle transition zone complicates this paradigm. In light of this, tomography models, with high fidelity resolved mantle transition zone features, can be applied on a case-by-case basis to integrate upper and lower mantle tomotectonic interpretations. This is important for relatively new subduction zones younger than 50 million years, where accurate location of upper mantle and transition zone slab is critical in estimating palaeo-trench locations and time of inception for subduction, with sufficient resolution.

1.2 Overview

In this chapter I review a ray-theory consideration of regional triplicated body waves and highlight the limitations of this approach for body wave tomography. From here, I motivate the method presented in this thesis, which invokes full waveform based travel-time measurements and sensitivity kernels as the means by which to harness triplications for body wave tomography. Next, I provide a short history of the use of triplications in targeted waveform studies and relate the progression of the research field to current state-of-the-art full waveform inversion methods. From here I state the objectives of this thesis before providing a brief chapter outline.

1.2.1 Triplicated body waves and ray theory

While this study goes beyond ray theory to use regional body waves in a full waveform-based framework, it is useful to consider regional P-waves in this context in order to be able to understand the multipathing of body waves by upper mantle discontinuities. What follows is a quantified consideration of triplication bow-ties as laid out in Shearer (2009). Assume seismic wave propagation is confined to an infinitesimally thin path. Distance and travel times are governed by

$$X(p) = 2p \int_0^{z_p} \frac{dz}{(u(z)^2 - p^2)^{\frac{1}{2}}} dz \tag{1.1}$$

$$T(p) = 2 \int_0^{z(p)} \frac{u^2(z)}{(u(z)^2 - p^2)^{\frac{1}{2}}} dz \tag{1.2}$$

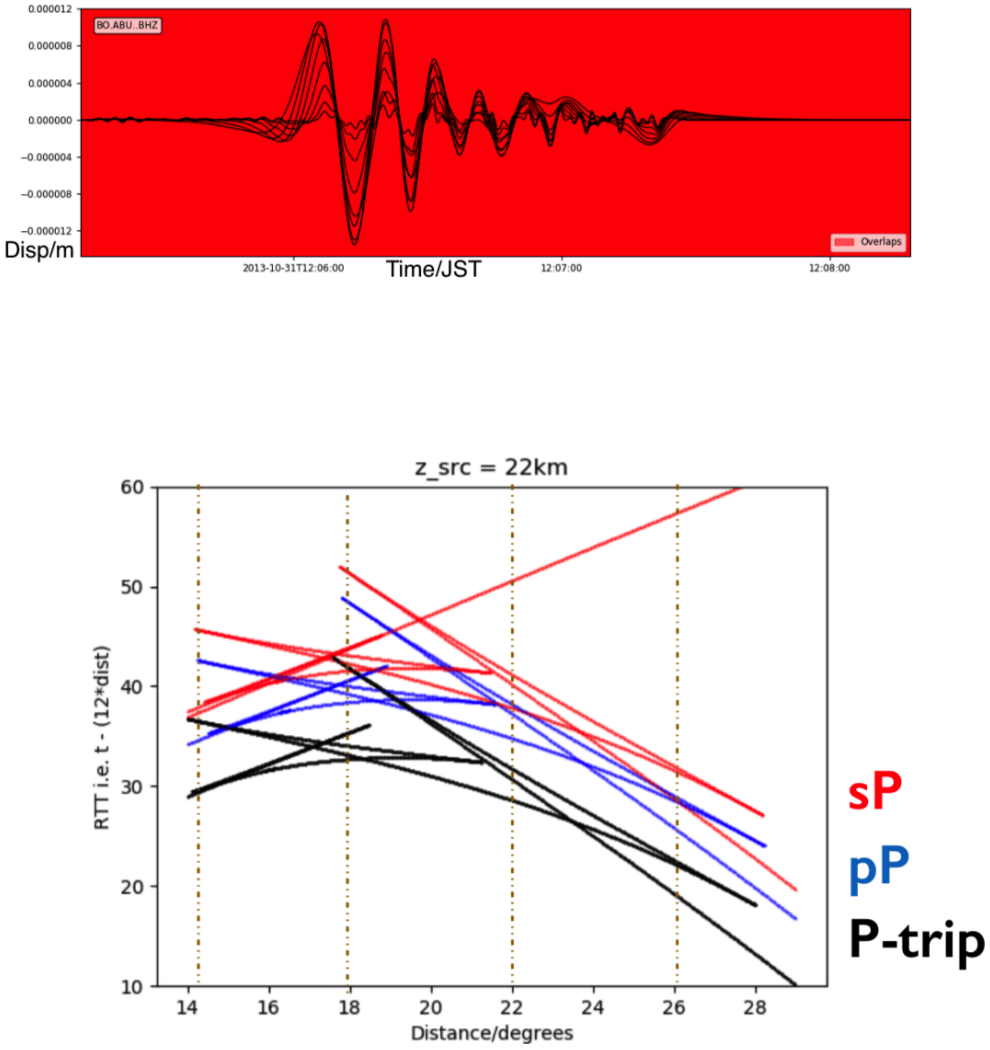

Figure 1.1: Triplication bow-ties for regional body waves imposed on multiples and depth phases. The bottom panel shows predicted triplication patterns for regional P-waves from a source located at 22km depth. Also interposed on the figure are sP and pP arrivals, which at times overlap with the P-waves as well. The top figure shows a regional body wave coda filtered using Gabor filters as will be detailed in chapter 2. Later-arriving triplications are often subsumed into the dominant first arrival. A frequency-dependent measurement approach allows these later arrivals to influence travel-time measurements obtained by cross-correlation.

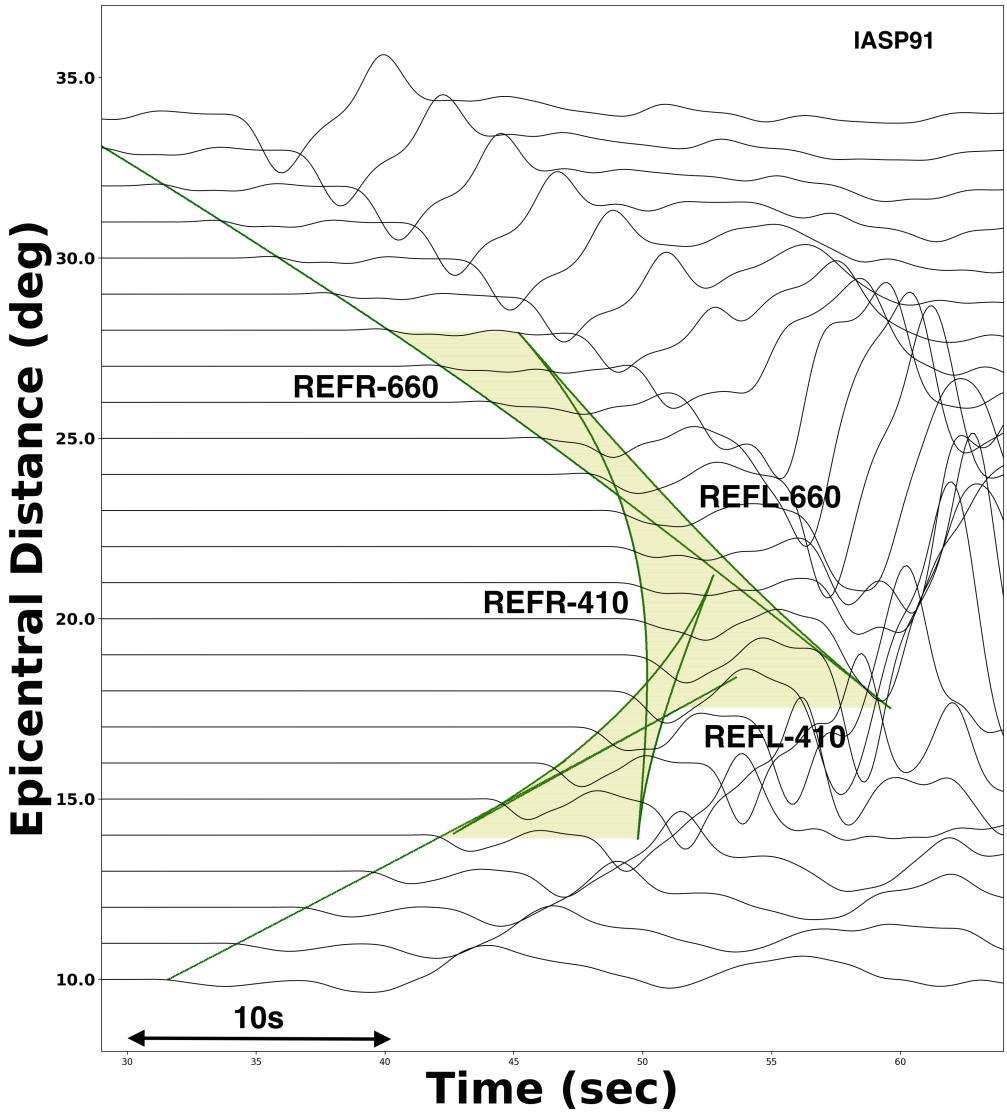

Figure 1.2: Reduced time-distance plot for the IASP91 model. Shown are regional, vertical component, synthetic waveforms, for a 100km deep explosion. Synthetic waveforms (black lines) were produced using Instaseis, based on the spectral element forward modelling code, Axisem. Waveforms are extracted from a stored global Green's function database, which is accurate up to five seconds period. P-waveforms exhibit multipathing (triplicated) effects, from roughly 14-28° epicentral distance. Green line: the major phases which constitute the P-wave coda (REFL: reflection, REFR: refraction), induced by MTZ seismic discontinuities (410km and 660km). Filled yellow area: P-wave coda envelope, followed by depth phases, which are also triplicated.

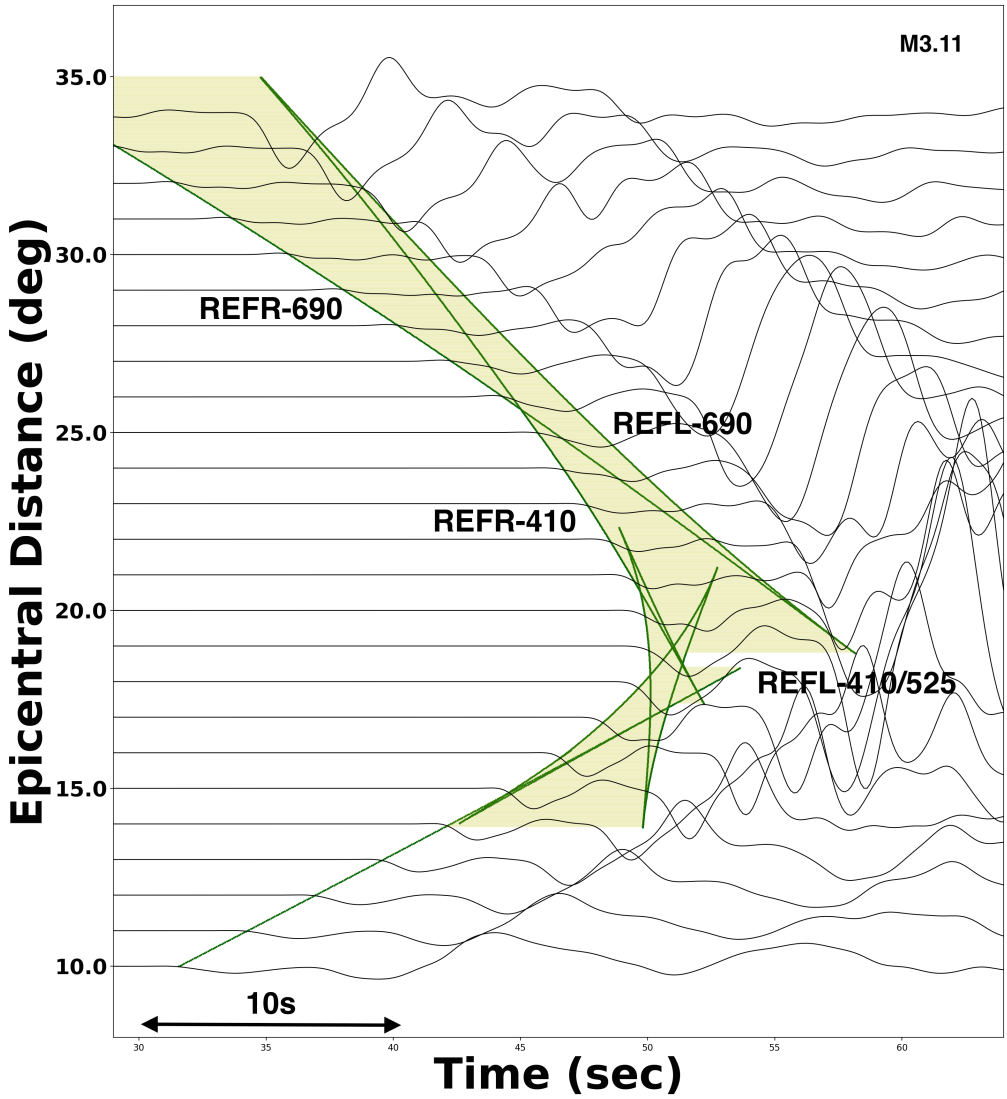

Figure 1.3: As above for the M.311 background model. Differences with respect to IASP91 are: i) a +1.5% discontinuity in velocity (525km) ii) +3% seismically fast, 525-660km iii) a 30km depression of the 660km discontinuity down to 690km. Note the modulation of the P-triplicated coda, whose reflected and refracted branches (690km) extend right out to 35°.

where the ray parameter, p, is given by

$$p = usin\theta \tag{1.3}$$

with u the seismic slowness and θ the ray take-off angle relative to the horizontal. One therefore anticipates that a steeper ray take-off angle will increase the distance at which it is detected, upon return to the surface. For a simple 1-D seismic velocity model, one expects velocity to increase with depth: from the above, ray

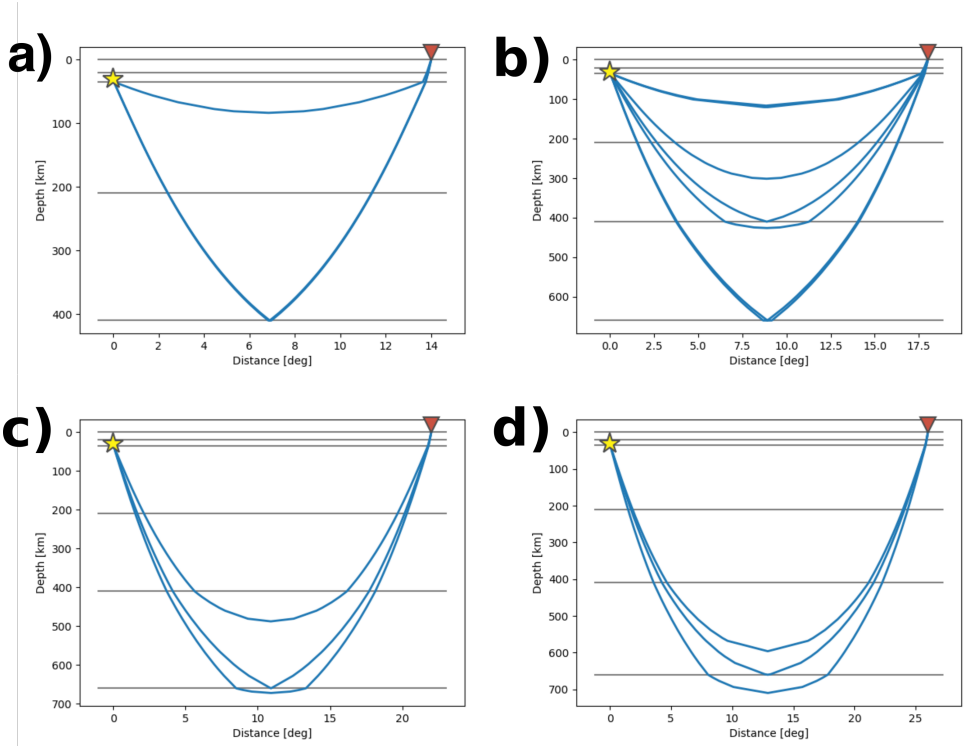

Figure 1.4: TauP ray plots of distance-dependent multipathing of regional P-waves for a 30km source depth. a) 14° epicentral distance b) 18° epicentral distance c) 22° epicentral distance d) 26° epicentral distance. At the shorter end of the triplication distance range, only triplications from the 410km discontinuity are observed. At mid-triplication distances (b) and c)), triplications are expected to be induced by both the 410km and 660km discontinuity, whilst beyond 22° distance, triplications are solely induced by the 660km discontinuity, as the seismic waves interact with the 410km discontinuity at a steep angle relative to the horizontal.

parameter decreases with depth. By extension, there is inverse proportionality between X(p),the propagation distance and ray parameter. Here, $\frac{dX}{dP} < 0$. This is the retrograde branch of the travel-time curve. Sharp or discontinuous, positive velocity gradients can render $\frac{dX}{dP} > 0$. More deeply diving rays may thus be detected at shorter epicentral distances. The portion of the ray turning or bottoming in this depth-velocity interval is termed the prograde branch. A prograde $\rightarrow$ retrograde $\rightarrow$ prograde evolution in $\frac{dX}{dP}$ yields a triplicated body wave arrival i.e. multiple arrivals of the same seismic phase, at a given distance, at different times. In this study, the 410km and 660km discontinuities define the bounds within which the sharp average velocity jump occurs, in addition to being velocity jumps themelves.

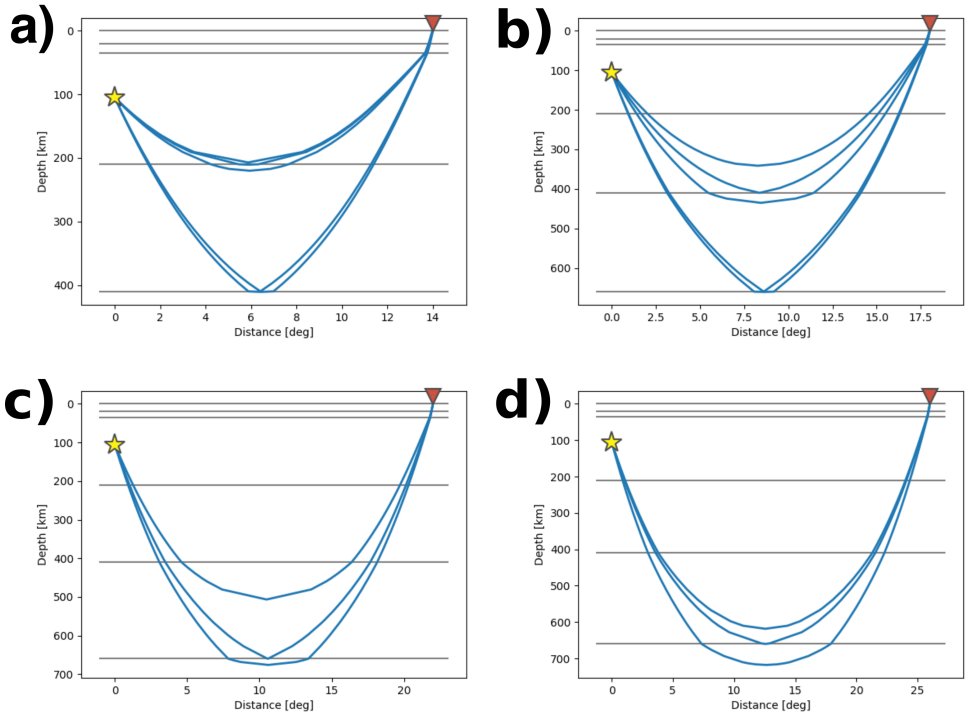

Figure 1.5: (TauP ray plots of distance-dependent multipathing of regional P-waves for a 105km source depth. a) 14° epicentral distance b) 18° epicentral distance c) 22° epicentral distance d) 26° epicentral distance. This figure should be compared with the previous figure, because it demonstrates how source depth modulates the expected temporal triplication patterns and the propagation paths to which they can likely be attributed.

There are limitations to this approach: the archetypal bow-tie geometry of the time-distance curve (figure 1.1) is observed solely for a laterally homogeneous seismic discontinuity, with clearly identifiable caustics ($dX/dP = 0$). For discontinuous velocity gradients the time-distance curve quickly becomes non-unique. This is likely to be encountered on a non-negligible number of occasions in a real earth model. Nonetheless, the approach has been used previously to good effect in Japan. Tajima & Grand (1995) characterised triplicated-P waveforms as a function of epicentral distance, source depth and source-receiver backazimuth to optimally fit 1-D velocity models for the Japanese subduction zone, identifying a distinct partition between the northeast and southwest. In the former, they anticipated the 660km discontinuity to be depressed to 690km.

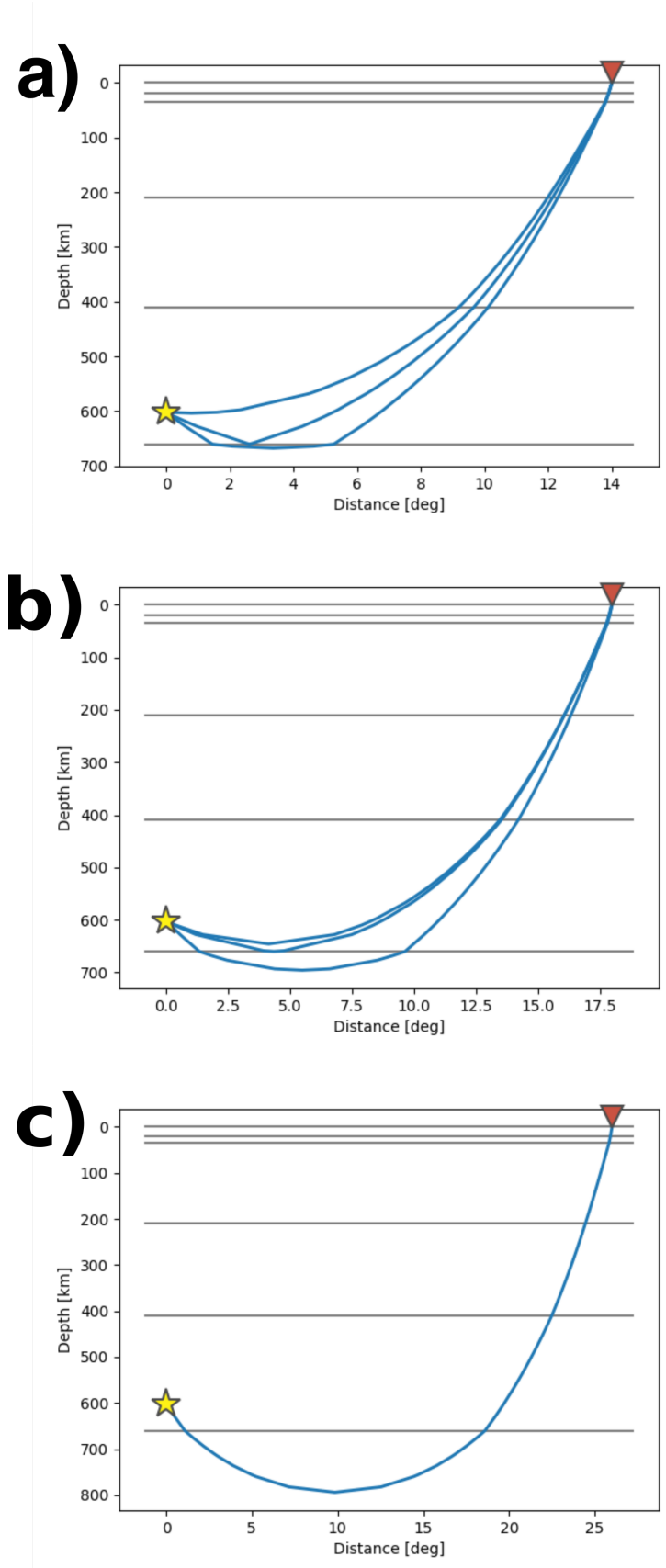

Figure 1.6: TauP ray plots of distance-dependent multipathing of regional P-waves for a 600km source depth. a) 14° epicentral distance b) 18° epicentral distance c) 22° epicentral distance d) 26° epicentral distance. No triplications from the 410km discontinuity are expected for this source depth, when considered in a ray theory paradigm. Triplication of regional P-wave ceases entirely by 26° distance.

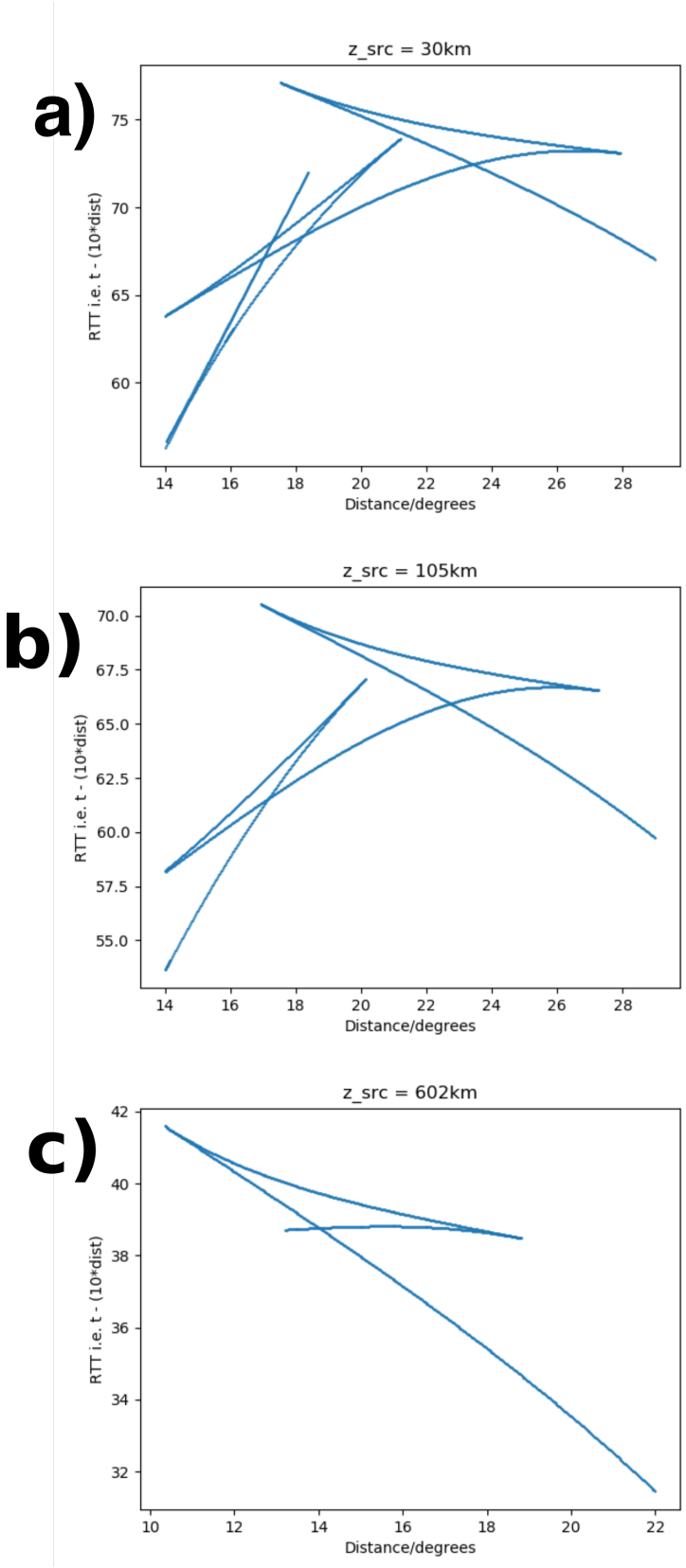

Figure 1.7: (Reduced time-distance/bow-tie plots of arrival times of regional P-waves as a function of source depth, corresponding to the TauP ray plots a) for a source depth of 30km b) a source depth of 105km and c) a source depth of 600km.

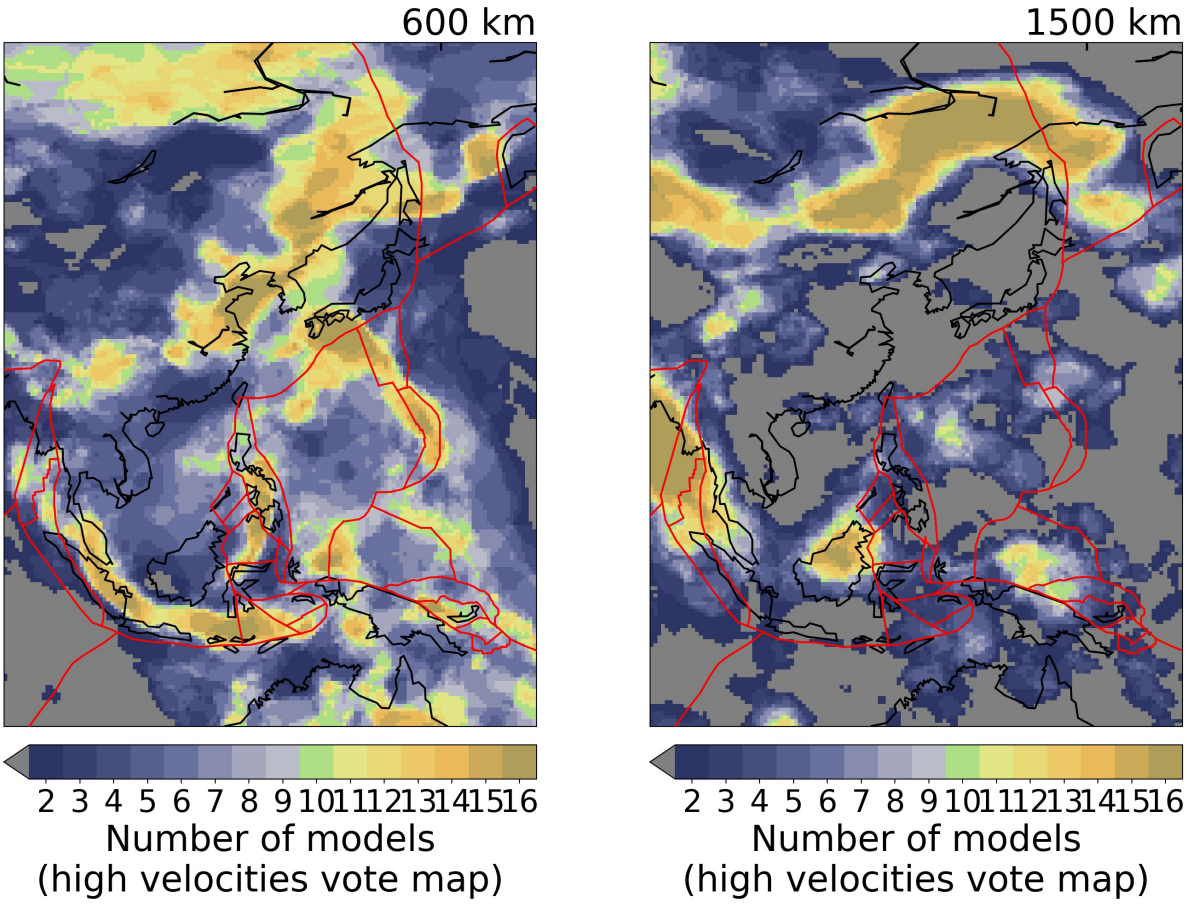

(a) 600km **(b)** 1500km

Figure 1.8: SubMachine votemaps of positive velocity anomalies from global P-wave models in the western Pacific. A suite of global P-wave tomography models are contoured at a threshold of +1% with respect to an IASP91 background model. Figures are colour-coded by the number of models with common overlap at a given location.

In light of subduction phenomena, low velocity zones and lateral velocity heterogeneity, one expects that infinitely many changes in slope of $\frac{dX}{dP}$ yield many arrivals of the same phase, spawned by an infinite suite of possible velocity models. Therefore, in order to allow regional body waves, which turn in the MTZ, to provide improved mantle transition zone resolution, measurements based on the full seismic waveform are required. Finite frequency theory attributes sensitivity of seismic waves over a volume instead of an infinitesimally thin ray path, assuming that energy scattering is predominantly in the direction of propagation.

1.2.2 Applying regional body waves to improve tomography resolution

Relative to teleseismic body waves, regional body waves (RBW) ($\tilde{1}4$ - 29°) exhibit superlative lateral sampling of the 410-690km MTZ depth range (see figures 1.4-1.7), whereas the former dive steeply, inhibiting resolution. This is desirable given that the MTZ is cited as a critical control on upper-lower mantle mass transfer. Additionally, the signal-noise-ratio (SNR) of RBWs is typically greater than that of other seismic phases used to sample the MTZ such as receiver functions and PP or SS reflections (Stähler et al., 2012).

This study is timely given recent watershed advances in the workflow of finite-frequency tomography. Sensitivity kernels, a proxy for the volume over which a given source-receiver path renders the earth visible, can now be calculated from the complete wavefield (Nissen-Meyer et al., 2014). Previously, Dahlen sensitivity kernels (Dahlen et al., 2000a) improved on ray theory (infinite frequency approximation) using an envelope of many thousands of rays to yield finite volume sensitivity kernels. Amplitudes near caustics cannot be done justice in this framework. Axisem, a spectral element code for modelling the full seismic wavefield, exploits the axisymmetry of the earth in one-dimensional background models. Its computational efficacy makes feasible the calculation of sensitivity kernels across the broadband spectrum (Nissen-Meyer et al., 2014). Furthermore, this expands the horizon of free parameters for which one may solve during seismic inversion. Amplitudes are a case in point, paving the way for amplitude kernels in addition to travel-time kernels, based on the full waveform. With methods based on ray theory, on the other hand, triplications (multiple arrivals of the same seismic phase, at different times, for a given distance) can yield infinite, unusable amplitudes.

1.3 History of upper mantle seismology using triplications

The use of triplicated body waves to constrain upper mantle and transition zone structure has been in use for more than forty years, and has been applied across a

range of versatile tectonic settings. As early as 1983, Grand and Helmberger (1983) used regional S-waveforms to deduce the velocity structure of the Canadian shield, inferring the depths of, and velocity jumps across, the upper and lower mantle transition zone discontinuities beneath the shield, in addition to seismic velocities within the shield as a function of depth.

Song et al. (2004) identified a low velocity lens atop the 410km discontinuity beneath the western United States, constraining its thickness from 20-90km across the Pacific northwest. This study is of indirect relevance to this thesis because it reconciled the low velocity seismic signals with expected velocities for partial melt layers related to historical subduction and back-arc extension.

Among the most relevant waveform-based study of triplications to this thesis comes from the work of Tajima & Grand (1995;1998), who fit triplicated body waves to synthetic models as a function of fractional velocity perturbation to the starting background model and depth of mantle transition zone discontinuities, across the Japanese Islands region. Tajima & Grand (1995) revealed the presence of a 525km discontinuity and depression of the 660km discontinuity down to 690km beneath the southern Kurile subduction zone. They also deduced that the observed velocities conformed to the hypothesis of slab flattening in the transition zone in this region. In a follow-up study (Tajima & Grand, 1998), they extended this approach to the Izu-Bonin and Ryukyu regions.

Figures 1.2 and 1.3 use the starting model and 1-D model solution, model M3.11 from Tajima & Grand (1995) to motivate how a slight change in 410km and 660km discontinuity topography can significantly modulate the observed triplication pattern in a seismic record section, using full waveform modelling using Axisem (Nissen-Meyer et al., 2014) and Instaseis (vanDriel et al., 2015). Of chief importance is the observation of the extension of the 660km triplication branches out from 29o to as much as 35 degrees. Similarly, complex bow-tie patterns are observed

at mid-triplicated distances, introduced by the accounting for a 525km discontinuity.

The majority of these targeted triplication waveform studies reconcile observed seismic data with synthetic waveforms produced using workflows predicated on ray theory. While the approach is exceptionally elegant and informative when the correct data is chosen, it has its limitations. For example, it does not account for the effects of the scattering of seismic waves manifest in the seismograms. In addition, a given triplication bow-tie pattern can be produced from more than one background model, such that the solution is non-unique. Also, very large amplitudes are predicted near the caustic points, observed at source-receiver distances where two branches of the triplications meet, in this framework. This has traditionally prohibited the use of triplicated data in seismic tomography studies. This has mandated the need to appraise triplicated waveforms in a full waveform-based framework.

State of the art waveform modelling of triplication patterns is exemplified in Tao et al. (2017;2018), who used waveform fitting by cross-correlation of SPECFEM3D-modelled (Komatitsch & Tromp, 2002) synthetic waveforms to match observed S-waveforms in east Asia. This yielded high fidelity synthetic template matches of S-waveforms, which implied high amplitude fast seismic velocity anomalies with sharp boundaries contained within the mantle transition zone, which the authors attributed to stagnant subducted slab.

1.4 Objectives

Even though there have been several incarnations of adjoint tomography models over the past decade (e.g. the EARA model of Chen et al., (2015), followed by the FWEA model of Tao et al. (2018), which used EARA as its starting model), there are still relatively few continental and global scale tomography models available in seismology, which are based on data measurements and sensitivity calculations

derived from the full seismic waveform. In addition to this, the majority of the models in existence use the well-maintained and highly benchmarked SPECFEM3D software based on the method of Komatitsch & Tromp (2002), for this purpose. While SPECFEM has the capability to reproduce upper mantle triplications in seismic waveforms for any three-dimensional background model, it is computationally expensive (e.g. Bozdag et al. (2016)).

There are a limited number of alternative frameworks to incorporate triplications into tomography workflows. Recent applications have used the direct solution method (Fuji et al., 2010) to illuminate upper mantle and transition zone velocity structure. One example of this is the triplicated S-wave dataset of Borgeaud et al. (2019), used in a targeted study of the Cocos slab beneath the Gulf of Mexico. Here I contend that there is an opportunity to improve our understanding of the mantle transition zone using regional body waves which are likely to have been triplicated during their passage through the upper mantle, using full waveform modelling based on the spectral element solver, Axisem (Nissen-Meyer et al., 2014). Axisem has been shown to be several orders of magnitude more efficient with respect to SPECFEM when waveforms are modelled at a given, like-for-like dominant frequency.

The computational efficacy of Axisem is also conducive to a data-driven approach to tomography. The majority of adjoint tomography inversions calculate one sensitivity kernel per earthquake, referred to here as an event kernel. This is a logical approach in the context of the adjoint method and when solving in a three-dimensionally heterogeneous background model; however, it comes at the cost of being able to assess a given source-receiver travel-time measurement and compare it to its individual sensitivity measurement.

An example of where this has been implemented is Hosseini et al. (2020), who use a massive dataset of frequency-dependent travel-time measurements and paraxial ray-based sensitivity kernels (Dahlen et. al., 2000a) to produce DETOX, a global

model of P-wave velocity using P, PP and P-diffratced arrivals. The workflow used in that study allows one to retrieve and visualise a given source-receiver sensitivity kernel and assess its value at every point on the inversion grid.

Sensitivity kernels are calculated based on waveforms modelled in Axisem using the fortran-based MC Kernel software (Stahler et al., in prep). Because of the relative computational efficiency of calculating these Axisem-based kernels, it is possible to embed these kernels in existing tomography frameworks, which already use massive finite-frequency travel-time datasets and their Dahlen-based sensitivity kernels. The main objective of this thesis is to present a joint inversion of regional P-wave measurements and their Axisem-based (MC) sensitivity kernels with tried-and tested teleseismic P-wave measurements and Dahlen sensitivity kernels.

A specific summary of the objectives of this thesis is as follows:

- to produce the first ever seismic tomography model based on sensitivity kernels calculated using full seismic waveforms using Axisem, by calling on the MC Kernel software, in addition to using Axisem-based multifrequency cross-correlation measurements of regional P-waves
- to develop and present a prototype framework for a massive data pipeline which incorporates these sensitivity kernels into TICC, a tried-and-tested finite-frequency tomography workflow
- to jointly invert these regional P-wave travel times with teleseismic travel-times and their Dahlen-based sensitivity kernels, for a study region which spans the entire western Pacific region. This includes the Kuril, Japan, Izu-Bonin and Ryukyu trenches in the north of the study region (where the regional P-wave dataset predominantly supplements upper mantle resolution) and extends through to the Sunda-Java and Banda arcs in the southern hemisphere
- to compare the resultant model of P-wave velocity, JEABOX, with existing tomography models that encompass the western Pacific (see figure 1.8)

- to test the resolution of the JEABOX model using targeted synthetic data which replicate observed velocity features that bear the hallmarks of subduction zones
- to suggest future work based on the main features present in the JEABOX model.

1.5 Outline

Chapter two, the data and measurement section, outlines the seismic data acquisition, the methodology underpinning the travel-time measurement process, which entails the frequency-dependent cross-correlation of regional P-wave seismograms with synthetic waveforms. These are modelled in a full waveform framework using the spectral element code, Axisem (Nissen-Meyer et al., 2014), and stored as an Instaseis Green's function database (vanDriel et al., 2015). This chapter also details the means by which explicit source time functions are estimated for earthquakes used in this study using the method of Sigloch & Nolet (2006). This chapter closes by proposing future means by which the triplication content of regional P-waves might be best harvested, such that each and every triplication is both identified and utilised.

Chapter three details the theory underpinning the MC Kernel software, which calculates Born sensitivity kernels by convolving forward and reversed seismic wavefields modelled in Axisem. From here I detail the workflow needed to calculate sensitivity kernels for each and every source-receiver travel-time measurement accumulated in chapter two, on high performance computing resources. I also highlight the limitations to the workflow and the need to limit the size of the MC kernel dataset used in this study.

Chapter four outlines the static corrections applied to multifrequency travel-time measurements accumulated in chapter two, accounting for the ellipticity of the earth and topography, in addition to crustal corrections. Thereafter I

detail the means by which a discrete inversion grid is created based on regional seismic coverage in the western Pacific, in addition to the LSQR-based inversion scheme used for this tomography. I support this with a documentation of the different component datasets which contribute to the overall inversion and the regularisation of the dataset, specifically:

- regional P-wave travel-times based on frequency-dependent cross-correlation with Instaseis-generated waveforms and their Axisem-based (MC) sensitivity kernels
- teleseismic P-wave travel-times based on frequency-dependent cross-correlation with Instaseis-generated waveforms, originally amassed as part of the global tomography of Hosseini et al. (2020) and their paraxial finite-frequency Dahlen kernels (Dahlen & Nolet, 2000a), which are based on the Born approximation.
- teleseismic travel-time picks from the International Seismological Centre bulletin (Weston et al., 2018).

From here I go on to showcase the resulting JEABOX model (Japan East Asia Banda Oxford, an acronym which attempts to do justice to the geographical span of the model space across the entire western Pacific subduction margin) model of P-wave velocity through visualisation, outlining some of the key features. I also present the results of resolution tests, including generic Gaussian spike tests and targeted resolution tests, the latter of which attempt to replicate and recover some of the major features of the JEABOX model. I close by proposing future work.

The abandoned palace is full of treasure glowing underground.

— Stephen Sexton's *'Yellow Switch Palace' from 'If All the World and Love Were Young'*

2

Data, Measurements and Modelling

Contents

2.1 Overview **22**
2.2 Body wave dataset for the western Pacific **22**
2.3 Multifrequency travel-time measurements **23**
2.3.1 Synthetic seismograms using Instaseis 23
2.3.2 Source time functions 24
2.3.3 Cross-correlation measurements 28
2.3.4 Results 35
2.4 Future Work **37**
2.4.1 Multitaper spectral estimation: a motivation and an overview 37
2.4.2 (Numerical) Implementation 42
2.4.3 Examples 43
2.4.4 Using coherence to improve cross-correlation measurement success 43
2.5 Modelling **45**
2.6 Axisem wavefields **47**
2.6.1 Overview of method 47
2.7 Sensitivity kernels **49**
2.7.1 Rationale 49
2.7.2 Theory 50
2.7.3 Database of kernels 52
2.7.4 Kernel visualisation 60
2.7.5 Performance 60
2.7.6 Limitations of the method and future directions 61

2.1 Overview

This chapter presents the workflow use to amass finite-frequency based travel-times based on cross-correlation of collated regional body-wave data with full waveform forward modelled seismograms. I begin by laying out the data retrieval steps using the ObspyDMT software. Next I outline the methodology underpinning the Green's function database used to generate synthetic waveforms for the cross-correlation measurement process. Next I lay out the explicit source time function estimation process used in this study, to convolve into synthetic Green's functions. From here I lay out the workflow for the cross-correlation measurement process before providing a quick overview of histograms of regional body wave travel times. I close the chapter by briefly touching upon alternative means by which triplicated body waves could be harvested in the future, including multitaper meaurements and waveform stacking approaches.

2.2 Body wave dataset for the western Pacific

I harvested three-component, broadband seismic waveforms via *ObspyDMT* (Hosseini & Sigloch, 2017), a python-based code which automates interaction with data centres and associated data exchange. The catalogue of events are based on that of the Global Centroid Moment Tensor, which extends from 2018 back to 2005. I standardised the cropping of waveforms: for a given documented earthquake origin time, I spliced the data at 300 seconds before the predicted P-wave onset time, based on ray-predicted travel-times from *Tau-P*, in an *IASP91* background model (Kennett & Engdahl, 1995), with an end time of 3600 seconds after the P-predicted onset. Correction for instrument response was also implemented by deconvolution in *ObspyDMT* with a water level of 600 decibels.

I used earthquakes with a minimum moment magnitude (Mw) of 5.8. This allowed for calculations of explicit source time function estimates using the method of Sigloch & Nolet (2006), such that the signal-to-noise ratio (SNR) of teleseismic

waveforms is sufficient (greater than 1).

The east Asian and general western Pacific margin is arguably one of the most densely instrumented regions on earth, with data from more than 1500 stations publicly available via the International Federation of Digital Seismic Networks. We supplemented these data with broadband waveforms retrieved from the Japanese *F-net* Broadband Seismograph Network. Figure 2.14 shows the broad distribution of earthquakes used in this study and the corollary seismic coverage. While we present measurements based on full waveform modeling and sensitivity, ray-approximated coverage conveys a first order sense perception of coverage in the upper mantle and transition zone. Coverage is still skewed due a less than ideal distribution of sources, of which one example is a relative paucity of earthquakes on the Chinese mainland. While this is somewhat mitigated by a significant contribution of earthquakes in Taiwan through to Indonesia, source-receiver distribution is far from the desired closed circuit of sources. I do note, however, that the data contributed by the NorthEast China Extended SeiSmic Array (NECESS Array) project (Tang et al., 2014) somewhat mitigated for this, by improving the azimuthal station coverage towards the northwest of the study region presented in this thesis.

2.3 Multifrequency travel-time measurements

2.3.1 Synthetic seismograms using Instaseis

I computed synthetic waveforms, complementary to our broadband dataset, based on the full waveform spectral element code *AxiSEM* (Nissen-Meyer et al., 2014). Examples are shown in figures 2.1 and 2.3 respectively, as well as comparative real data in figure 2.2. *AxiSEM* allows dexterity during our measurement process due to its computational efficiency. By limiting wavefield calculation to spherically-symmetric background models, waveform propagation is effectively collapsed to two dimensions, the third being calculated analytically. A consequence of this is an order-of-magnitude CPU reduction for a given walltime, compared with other spectral element codes (Nissen-Meyer et al., 2014).

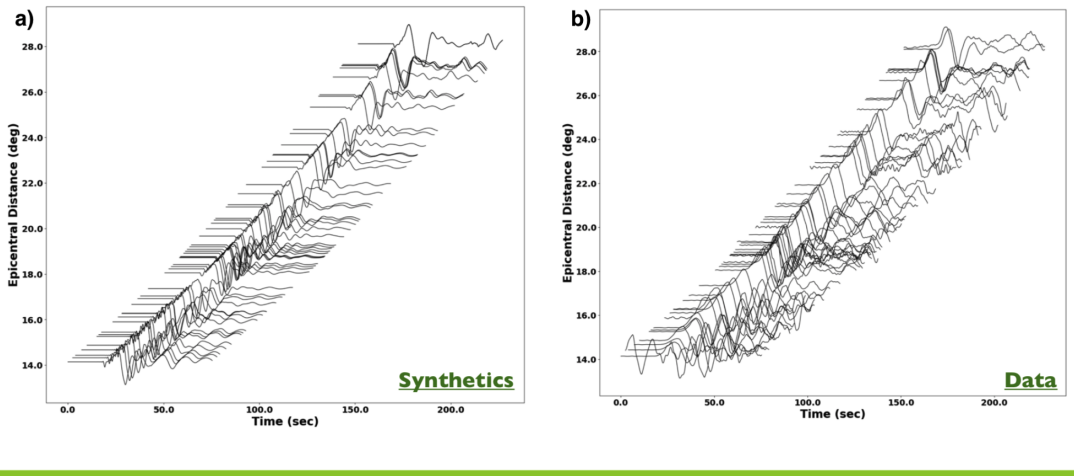

Figure 2.1: Real and synthetic reduced travel-time record section for Mw 6.3 earthquake in Taiwan. a) Instaseis-modelled waveforms with convolved event source time function included in the waveforms b) real observed broadband data.

We created a Green's function database using *Instaseis* (van Driel et al., 2015), also based on *AxiSEM*, which enables the gathering of whole-Earth databases at feasible computational cost, by using the reciprocity theorem. Our velocity model of choice was IASP91 (Kennett & Engdahl, 1995) with embedded PREM attenuation (Dziewonski & Anderson 1981), which accounted for instrinsic attenuation during the cross-correlation measurement process. This has been used previously to good effect for global (Hosseini et al., 2020) and targeted teleseismic tomography (Sigloch et al., 2008; Tsekhmistrenko et al., in prep.). This enabled me to instantly retrieve synthetic Green's functions, modelled up to 5 seconds dominant seismic period.

2.3.2 Source time functions

The workflow presented in this study adopts the matched filter approach of Sigloch & Nolet (2006) for source time function estimation, combines it with Axisem and applies both method to triplicated body waves. The workflow gives dual priority to semi-automated, explicit earthquake source time function (STF) estimates and *Instaseis* Green's functions, when calculating synthetic seismograms for arbitrary

source-receiver paths. I consider the use of explicit source time functions to be essential, given the length scales over which I intend to perform regional tomography (epicentral distances between roughly 10 and 40°), delivering seismic mantle resolution up to 1000km depth, including the ~410-690km mantle transition zone (MTZ). In order to mitigate signal suppression by incoherent noise, I analysed events with a moment magnitude (Mw) in the range of 5.0-7.0, to ensure sufficient waveform signal-to-noise noise ratios (SNR) of >1 were obtained. These events are anticipated to exhibit source rupture times on the order of 10^0 - $2x10^1$ seconds (Stähler et al., 2012). Here it is assumed that an observed broadband waveform is effectively the convolution of the source time function with the along-path, true Green's function. It can be expected that the STFs act as a low pass filter on the temporally compact suite of triplicated body wave arrivals (Stähler et al., 2012), whose maximum envelope duration is not expected to exceed 10s.

My choice of misfit was a relative time-shift, yielded from cross-correlation between frequency-filtered real and synthetic waveforms. Given that I evidently sought to maximise the number of measurements for tomography input, I argue that the use of explicit STFs is needed for several reasons: I) the effect of signal overlap between the triplicated body wave phases of interest and depth phases, the latter of which propagate energy vertically from the source, reflect off the earth's surface before propagating to the receiver. These are themselves triplicated. II) the role which the moment tensor plays in modulating waveform amplitudes and polarities. To best honour the contribution of the triplicated body wave coda and the STF to the overall waveform, we used the tried-and-tested method of Sigloch & Nolet (2006), as mentioned above. These contain signal which manifests in all regional seismograms. Typically, the tails of these signals have multiple changes in slope, further modulating waveform amplitudes, which may not be honoured using approximate Gaussian or triangular STFs. In what follows I provide a brief overview of the source time function workflow.

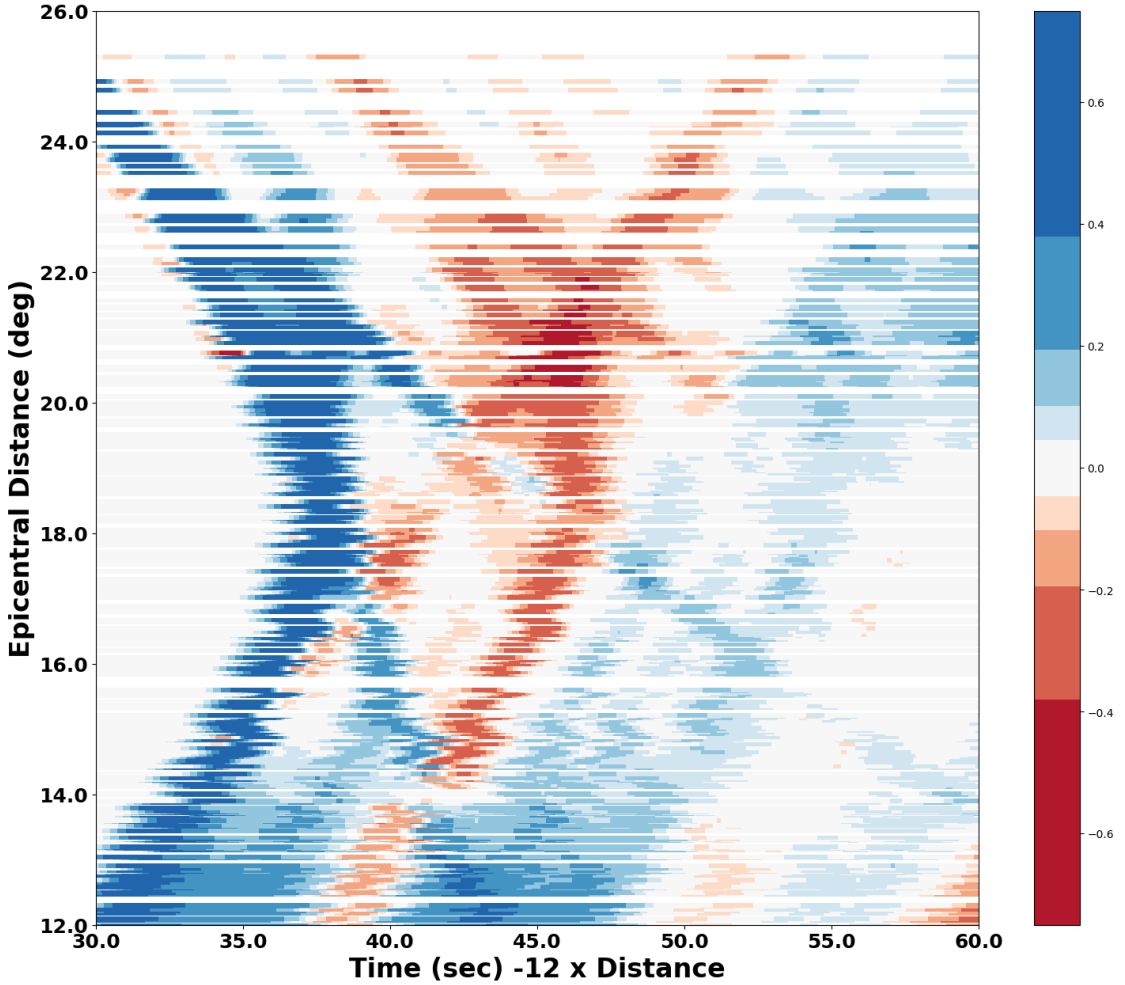

Figure 2.2: Instaseis-based synthetic reduced time-distance matrix plot for specific earthquake, accounting for the event source time function, replicating a Mw 6.6 earthquake from the Queen Charlotte Islands region (2008-01-05, 11:01am), as detected across the US Array (TA), Shown is a record section, extracted from an Instaseis Green's function database, based on full waveform modeling, accurate to 0.5Hz, as computed for the IASP91 reference model. At the time of the event, the array extended due south, from eastern Montana to southwest Texas. 410/660 sampling is beneath the US northwest. Arrival times are late relative to model-predicted travel times.

While the multifrequency measurement dataset presented in this study is augmented for regional-scale tomography, I predicate STF estimates on broadband waveforms detected at teleseismic distances, from the II,IU,GE and G permanent international seismic networks. Azimuthal station distribution is adequate for the east Asian margin and western Pacific subduction zones. I argue that STF estimation based on data independent of our waveform dataset is in fact desirable because this avoids the introduction of possible bias, from spatially correlated regional

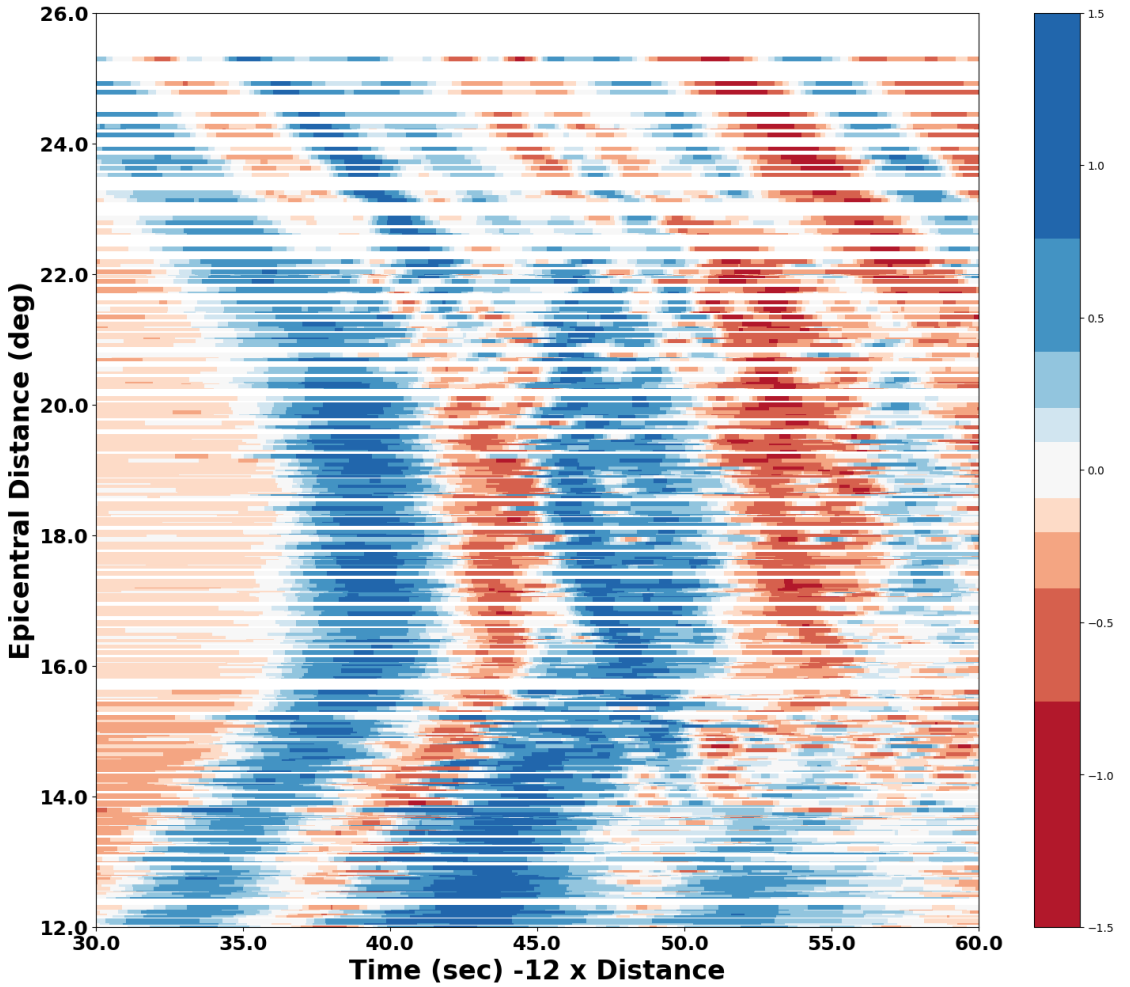

Figure 2.3: Measured reduced time-distance matrix plot for specific earthquake. Broadband P-triplicated record section for a shallow, Mw 6.6 earthquake from the Queen Charlotte Islands region (2008-01-05, 11:01am), as detected across the US Array (TA).

waveforms, as highlighted by Stähler et al. (2012). For detailed methodology, I direct the reader to Sigloch & Nolet (2006) and only provide an abridged workflow summary below.

For a given earthquake, synthetic broadband waveforms pertaining to each station were calculated via the WKBJ approximation as per Chapman (1978), modulated by the catalogued earthquake moment tensor. Joint deconvolution of Green's functions out of the broadband waveforms yielded a starting STF estimate.

An update for the moment tensor was then carried out using LSQR inversion, which allowed for station-by-station waveform amplitude correction. An update of the STF marks a new iteration of the above steps, which is repeated until convergence or break criteria are met: the convergence criterion is dictated by an RMS misfit between data and synthetics, and the break criteria the development of a negative source time function tail, at the same time as an unsatisfactory change in RMS misfit was observed. This entire process is repeated for a suite of possible earthquake depths (2km bins for shallow catalogued events, $<$ 50km; reasonable deviations from reported depths for deeper events) before selecting the overall best estimate of the STF. This is judged by the operator on the grounds of: I) the physical appearance of the STF time series II) reasonable overall STF negativity, ideally $<$ 10%. Figures 2.4-2.6 show examples of the source time workflow for both a high quality deep event and modest quality shadow event, in addition to an example of the azimuthally distinct waveform clustering included in the STF estimation process.

For this study I calculated 150 of these explicit source time functions globally, to contribute to the overall source time function bank of the Oxford Seismology Research Group, which totals more than 4,000 source time functions.

2.3.3 Cross-correlation measurements

I utilised the *Python Finite Frequency Processing* (*PyFFProc)* protocol, pioneered by Hosseini & Sigloch (2015) to produce my dataset of finite frequency travel-time measurements from P-triplicated time windows. Figures 2.7 and 2.8 present an overview of the workflow. Here I present a brief summary.

I batch processed broadband waveforms on an event-by-event basis. For an endmember waveform pertaining to a given source-receiver path, I retrieved the associated Green's function , which accounted for source depth and moment tensor effects on the waveform. This Green's function was convolved with its explicit

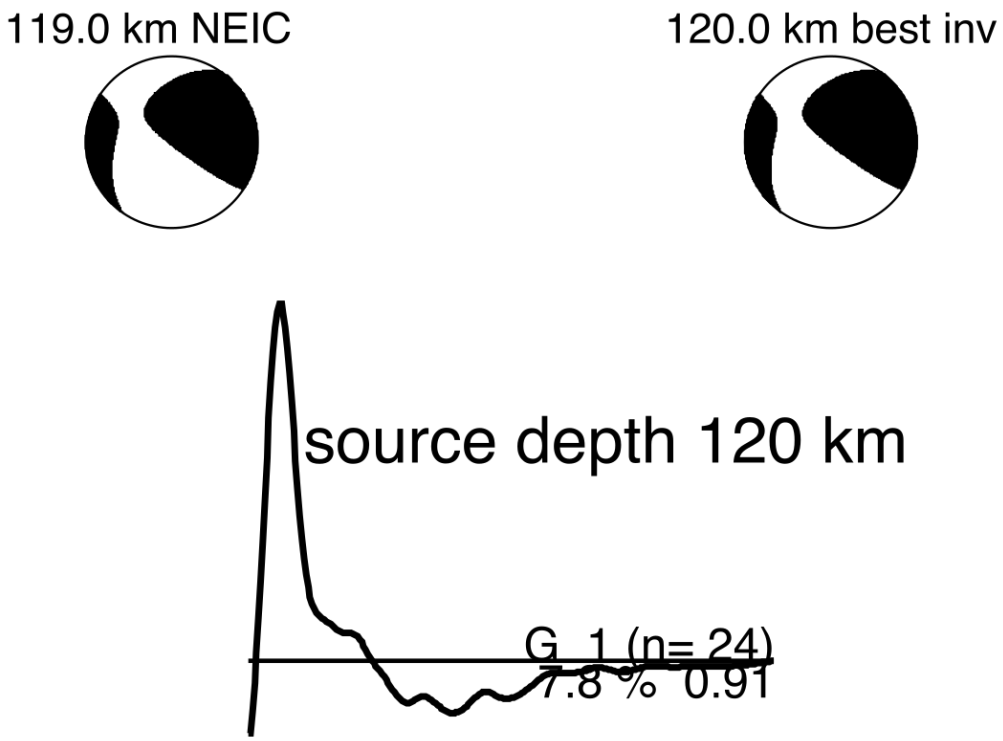

Figure 2.4: High quality inverted source time function and focal mechanism for an intermediate depth earthquake. The inverted source time function has a high cross-correlation factor (> 0.9) and tails with negative amplitudes which constitute less than 10% of the entire source time function.

source time function estimate, calculated as highlighted in the above section. This produced the synthetic waveform, also known as the 'matched filter' (Sigloch & Nolet, 2006), which was taken forward for cross-correlation.

I then passed the broadband waveforms and matched filters through the same suite of frequency filters. Currently, Gabor filters are the tool of choice, however, future work will investigate whether the use of multitaper spectral estimation (Percival & Walden, 1993) using Slepian tapers can improve the harvest for frequency

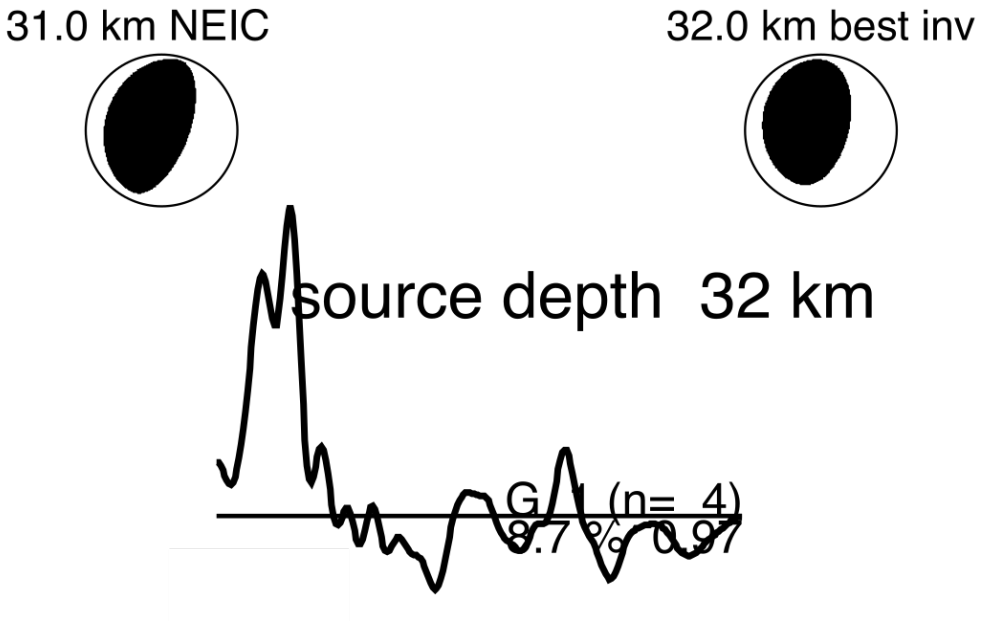

Figure 2.5: Modest quality inverted source time function and focal mechanism for a shallow depth earthquake.

content extraction from triplicated body waves. This would further conform to the 'arbitrary phase' school of thought advocated in the adjoint tomography and full waveform inversion communities e.g. Stähler et al. (in prep).

Six overlapping passbands with centre periods from 30 through ∼5 seconds, stepping down in $\sqrt{2}$ second increments, were chosen to cover the range of wavelengths of interest for tomography i.e. on the order of 100-500km (figure 2.9). This lends up to 12 degrees of freedom to a waveform observation, one for travel-time and amplitude ratio between real and synthetic waveform, in each frequency band. Amplitudes ratios are calculated in *PyFFProc* as documented in Sigloch & Nolet (2006). Prior to cross-correlation, waveforms are proportionally cropped with respect to the impulse response (IR) of a given filter, such that the time-window used for cross-correlation, T_{window} is given by

$$T_{window} = T_{PRE} + 1.5 * IR + T_{OFF} \tag{2.1}$$

. T_{PRE} and T_{OFF} are preset and offset times padded onto cross-correlation windows to ensure that the entire P-triplicated envelope is captured (here they were 7s and 2s

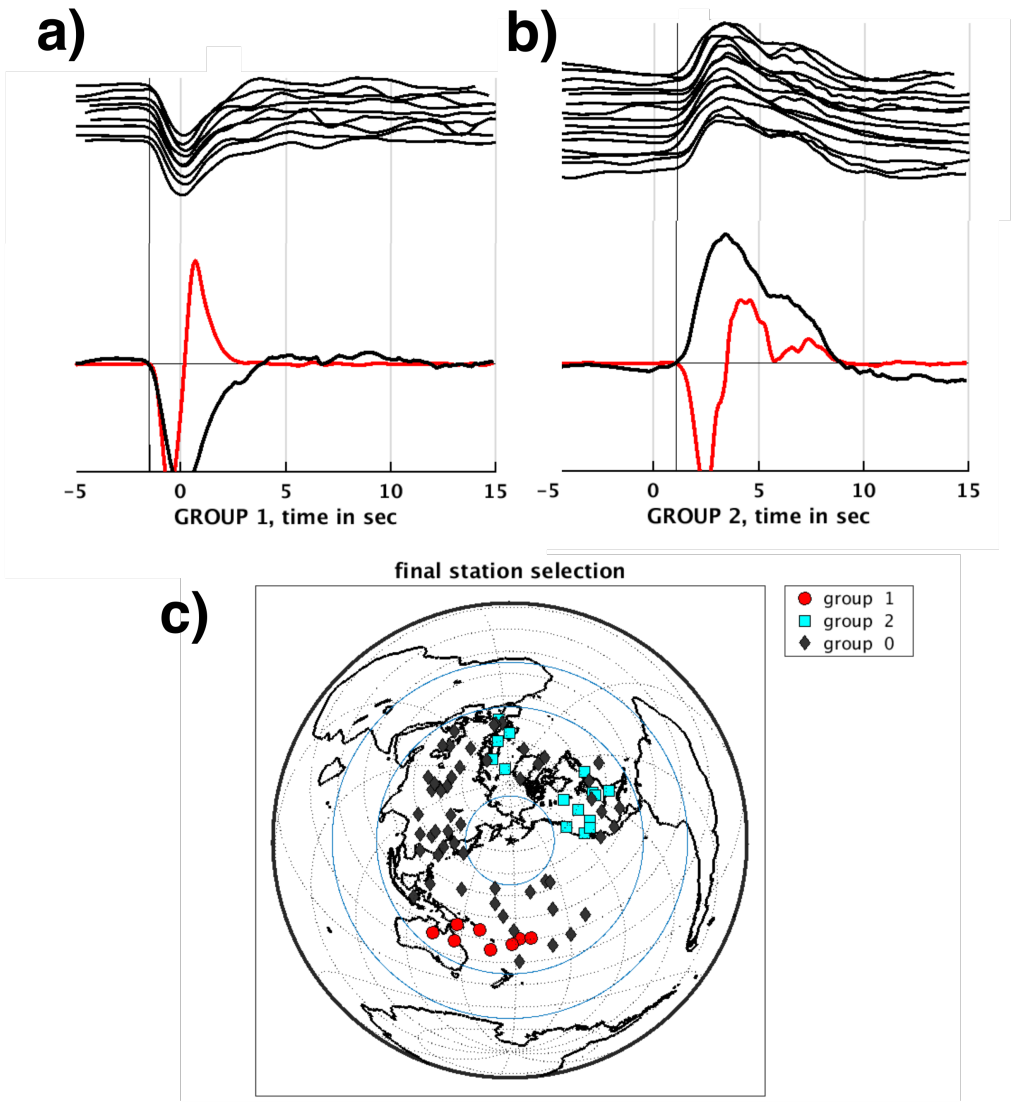

Figure 2.6: Onset time determination from broadband seismogram clusters during source time function inversion pre-processing. a) and b) show the two waveform clusters which naturally divide into two azimuthally distinct groups. c) shows the location of the receivers corresponding to those waveforms, colour-coded by group. Black diamonds denote all receivers where waveforms were of low SNR or did not cohere with other well-correlated waveforms. These were subsequently discarded.

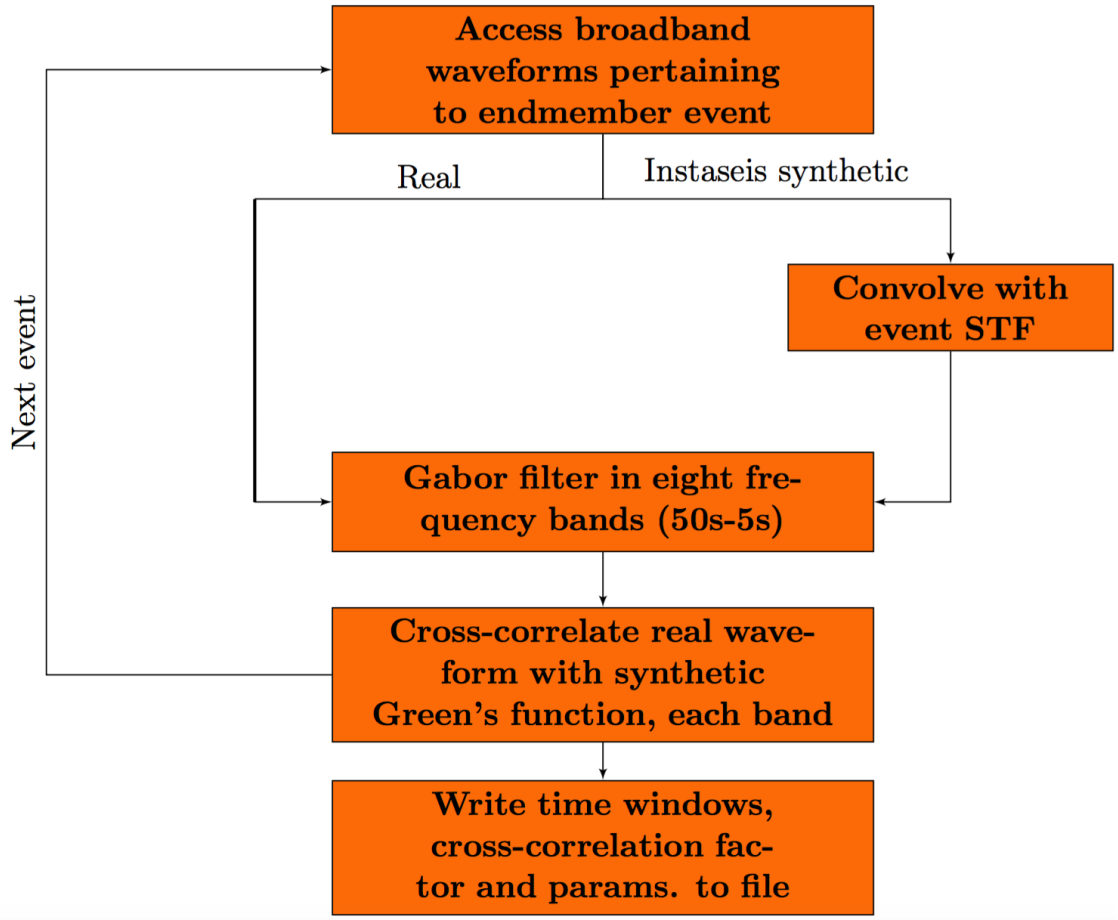

Figure 2.7: Multifrequency travel-time cross-correlation measurement workflow using Instaseis.

respectively), in addition to promoting stability during fourier transform operations for filtering purposes. I chose these time windows carefully, in order to ensure that sensitivity kernels calculated based on cross-correlation measurements deliver the best results from seismic inversion. This required a trade-off when setting the entire cross-correlation window time, to ensure that the signal of interest was contained in the time window, without lengthening the time window such that the overall successful cross-correlation measurement yield was reduced.

I performed cross-correlation between Gabor-filtered real waveforms and matched filters. This entailed calculating the cross-correlation function at all possible time shifts, dT. The dT and associated time window over which cross-correlation

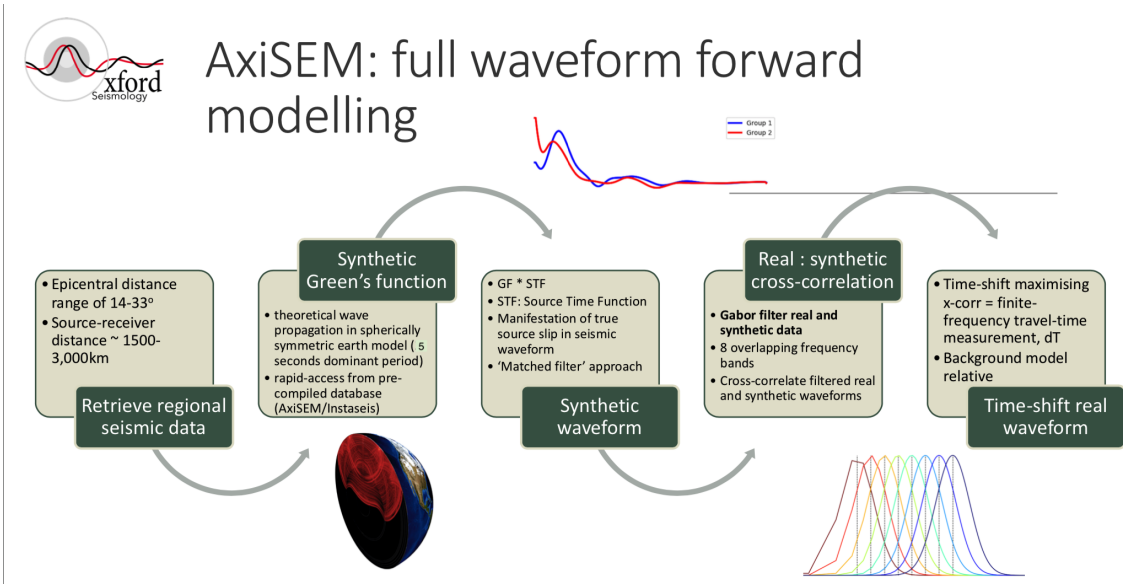

Figure 2.8: Multifrequency travel-time cross-correlation measurement workflow using Instaseis- shown is an alternative visualisation of the previous figure. Sphere representing waveform propagation is from Nissen-Meyer et al. (2014).

was performed, that maximised the cross-correlation function, and exceeding an empirically defined threshold of 0.8, was banked as input for the corresponding sensitivity kernel calculation. Both were then retained for least-squares inversion for P-wave velocity in the upper mantle and transition zone (the seismic inversion workflow will be presented in chapter four).

Cycle skip mitigation

The likelihood of encountering cycle skipping increases proportionally with frequency when performing cross-correlation based travel-time measurements (Zaroli, 2010).

We adopted several measures to mitigate the risk of stray, cycle-skipped measurements being taken forward for inversion. Firstly, the cross-correlation process evolves in a two-step manner, as in Hosseini et al. (2015). A larger, 'blanket' time-shift ceiling is allowed for the lowest frequency-band of $\sim$ 30 seconds. Subsequent, higher frequency bands are subject to much more strict criteria $\leq$ 3 seconds relative to the blanket time-shift. I contend that this is a sufficiently long time lag to capture

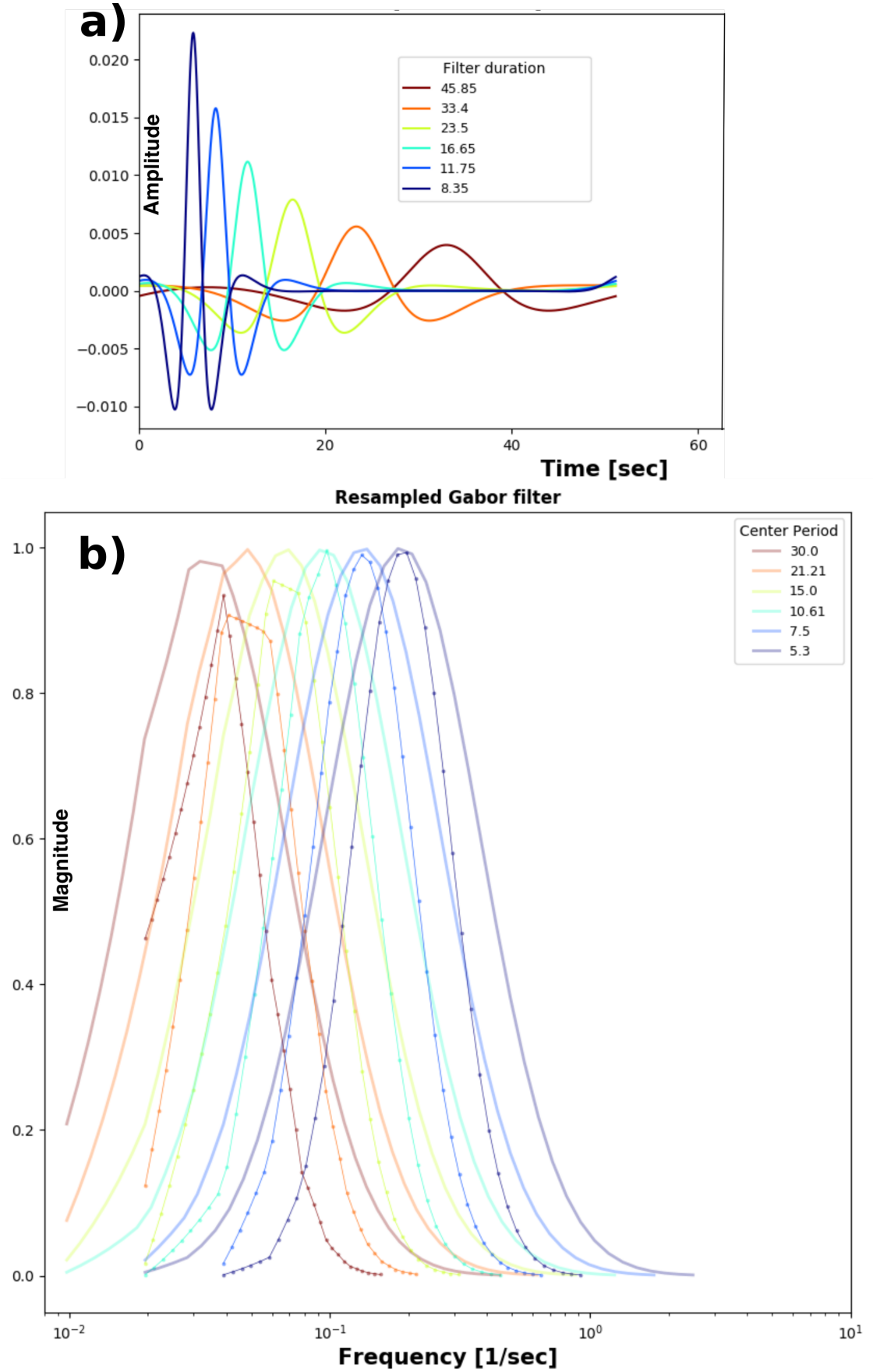

Figure 2.9: Gabor filters used in the frequency-dependent cross-correlation process. a) Impulse responses of filters b) Gabor filters in frequency space.

any frequency-dependent dispersion that might be observed for P-triplicated waves, without increasing the risk of cycle-skipping. Secondly, I contend that there is still a role to play for the operator, albeit a subjective one. *Matplotlib* plot panels output by *PyFFProc* allowed me to scrutinise, for a given dubious measurement I) whether event-by-event measurements from neighbouring stations fell vastly short of the cross-correlation threshold II) whether time shifts for broadly similar waveforms were markedly out of agreement, and allowed me to take action accordingly.

As an additional check for cycle skipping, I calculated several additional misfit functions, based on the method of Ritsema & Van Heijst (2002), giving an overall measure of fit, using an average of $F1(\tau)$, the least squares misfit of data with respect to synthetics at time lag, τ and $F2(\tau)$, the waveform similarity, also at time lag τ i.e.

$$F3(\tau) = \frac{F1(\tau) + F2(\tau)}{2} \tag{2.2}$$

Full definitions of $F1(\tau)$ and $F2(\tau)$ can be found in Ritsema & Van Heijst (2002). I note that the above criteria were used as misfit measures of choice in other finite-frequency based tomography studies e.g. Zaroli et al. (2010): in their work, a value of $F3(\tau)$ at time lag τ that exceeds a value of 0.7 and is distinguishable as the primary function optimum, is considered a successful measurement, devoid of cycle skipping. Given that there are inevitable differences in the respective finite-frequency measurement workflows,I solely utilise the latter criterion. The matched filter approach used here appears to generically satisfy misfit criteria from independent studies, even performing relatively well for failed measurements which do not exceed our cross-correlation factor threshold i.e. picking the time shift corresponding to the optimum value of the Ritsema & Van Heijst (2002) function.

2.3.4 Results

Figure 2.11 shows travel-time histograms amassed from the multifrequency measurement process detailed in the previous sections, for the targeted regional P-wave dataset presented in this study. A total of approximately **150,000** cross-correlation

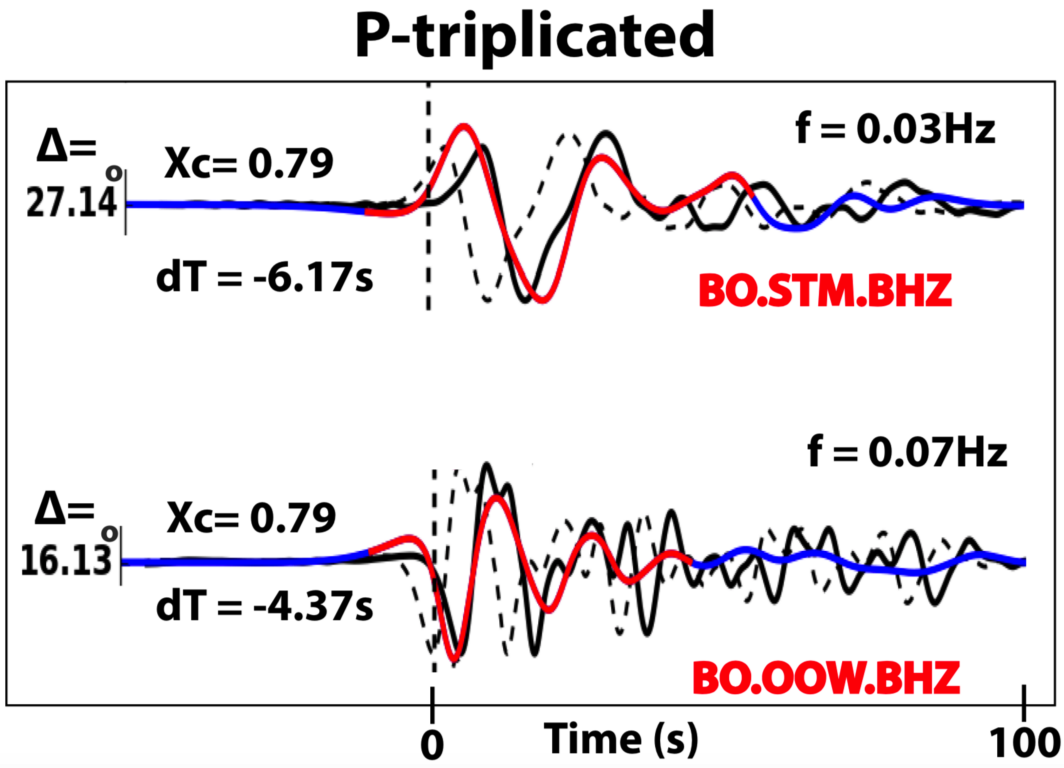

Figure 2.10: Example of a Gabor-filtered multifrequency cross-correlation travel-time measurement.

travel-times were obtained with a cross-correlation factor greater than 0.79. **95860** of these were provided by the first three frequency bands of 30s, 21s and 15s dominant period respectively. This is important as only these first three bands were taken forward for inclusion in the inversion process due to time, computing and storage constraints. Of these **95860** measurements, there was essentially a 1:1 split between measurements contributed by the open source Japanese broadband FNET network and the rest of the open source data available across the western Pacific.

This dataset was then combined with an existing teleseismic multifrequency travel-time dataset amassed by Hosseini et al. (2020) as part of a global P-wave tomography study. This tomography model had three incarnations, with each successive iteration of the model adding novel data types, including PP and PDiff measurements. Here I utilise a western Pacific subset of the DETOX-P1 model

from this global tomography, which only used teleseismic P-waves. I extracted multifrequency travel-times from this dataset at 30s, 15s, 7.5s and 3.8s period respectively. In chapter four I outline the steps to re-calculate the Dahlen sensitivity kernels required for these teleseismic measurements, and their re-projection onto the specific inversion grid used for this study. In total, the western Pacific DETOX-P1 data subset provided an approximately extra **1 million** multifrequency travel-time measurements to be taken forward for inversion. Figures 2.12 and 2.13 show to first order the mantle transition zone added resolution from the successful cross-correlation measurements amassed as presented in this chapter. Random subsets are plotted, thus I also direct the reader to figures A.69-A.80 for examples of alternative randomised scrambles of mantle transition zone coverage.

2.4 Future Work

2.4.1 Multitaper spectral estimation: a motivation and an overview

The target destination for exploration of triplicated body waves and for triplication tomography, is to be able to obtain an independent travel time and amplitude measurement, corresponding to each and every constituent triplicated arrival, within the context of measurements based on full waveform modelling. Multitaper spectral estimation is thus well-suited to multifrequency travel time measurements and conducive to extracting the frequency dependence of the different triplication branches of the body wavetrain. Percival & Walden (1993) showed that correlation between separate eigenspectra of time series measurements can be mitigated if one uses a set of orthogonal data tapers. One example is Discrete Prolate Spheroidal Sequences, more commonly referred to as Slepian tapers (Percival & Walden, 1982), for which each and every taper strongly sample the majority of the trace in the time domain. While not orthogonal in frequency, they are orthogonal in the time-bandwidth product (Sigloch, pers. comm, 2019) As such, a stack or weighted average of these measurements ought to approach full replication of the true frequency content of the waveform, from multiple independent measurements,

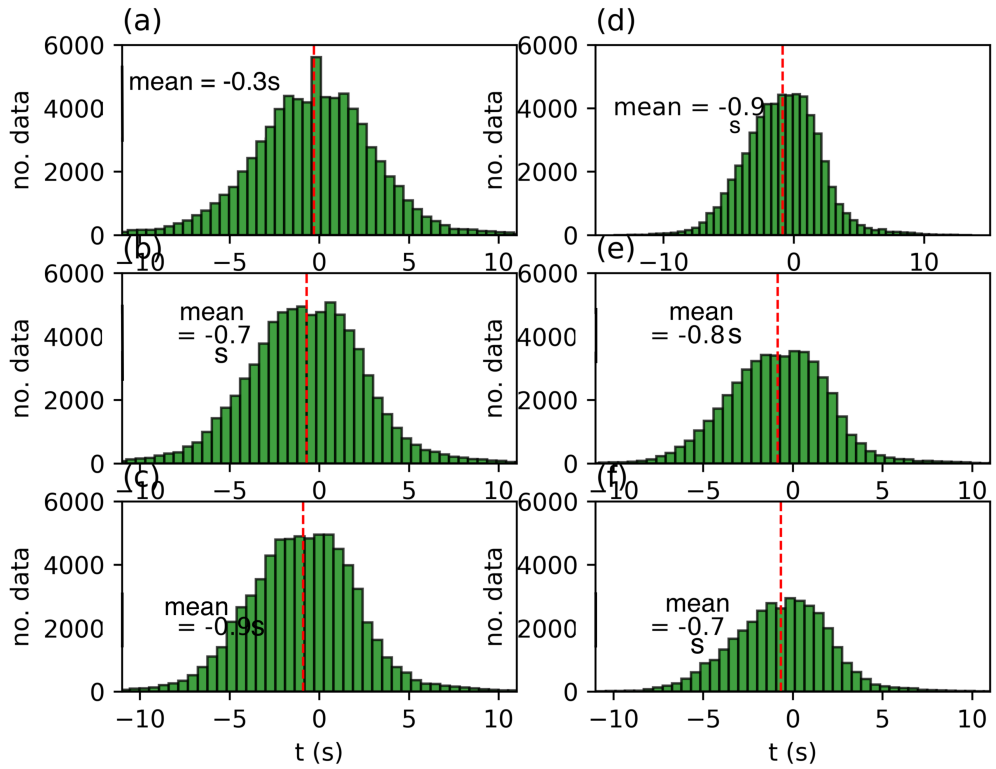

Figure 2.11: Travel-time histograms of regional P-waves as a function of dominant frequency, for the western Pacific. a) 30 seconds dominant period b) 21 seconds dominant period c) 15 seconds dominant period d) 10 seconds dominant period e) 7 seconds dominant period and f) 5 seconds dominant period. The lowest frequency band for this data set is approximately zero-mean, while the subsequent frequency bands have a mean of roughly 1 second. There is no significant dispersion as a function of frequency observed for this dataset.

provided that they span the appropriate time-bandwidth space. In light of this, I propose the following hypotheses:

- Dynamic, waveform-by-waveform weighted average multitaper spectral estimation (MSE) of triplicated body waves can produce higher cross-correlation measurement success between data and synthetic time series, compared to statically set log Gabor filters

- A linear combination or weighted average of these measurements ought to replicate the true frequency content of a triplicated waveform, from multiple independent measurements that span the appropriate time-bandwidth space

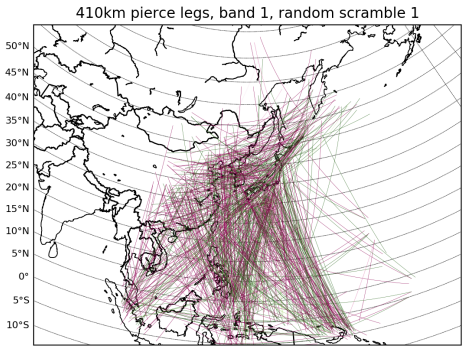

(a) Band 1 30s

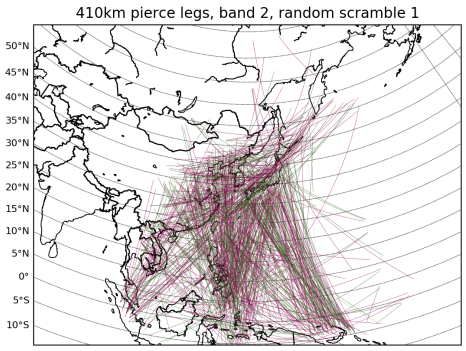

(b) Band 2 21s

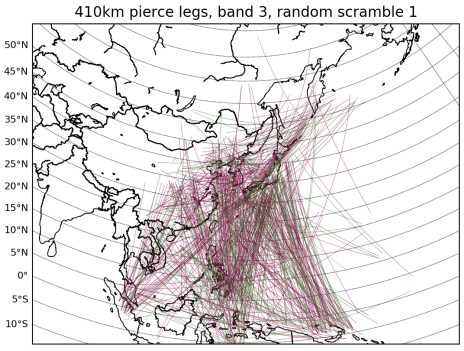

(c) Band 3 15s

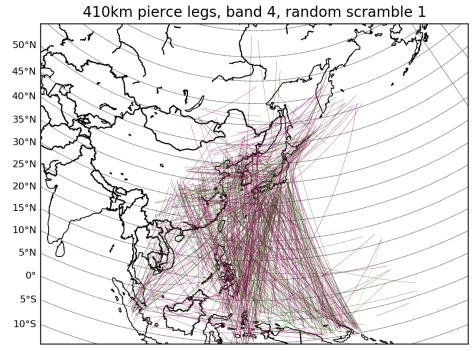

(d) Band 4 10s

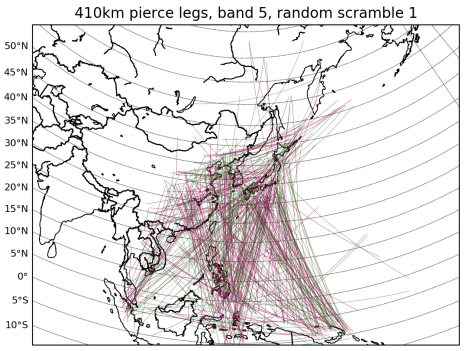

(e) Band 5 7s

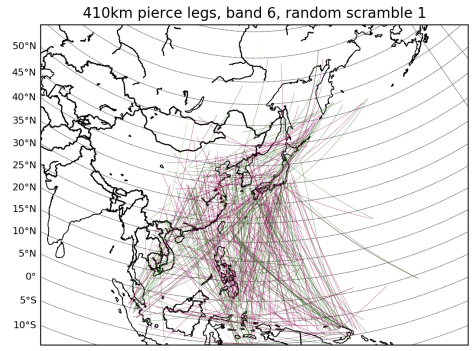

(f) Band 6 5s

Figure 2.12: Random subset of approximated grazing paths (410km) of regional P-waves representative of mantle transition zone coverage. The figure shows point-to-point transition zone segments based on the entrance and exit point of a hypothetical ray path to and from the 410km discontinuity in an IASP91 backgorund model. The colour of the rays is a random scramble, utilised to bring out ray coverage. Ten realisations of a subset of measurements, randomly chosen for each realisation, are implemented to fully demonstrate the extent of coverage. Shown here is the first random scramble implemented for each frequency band.

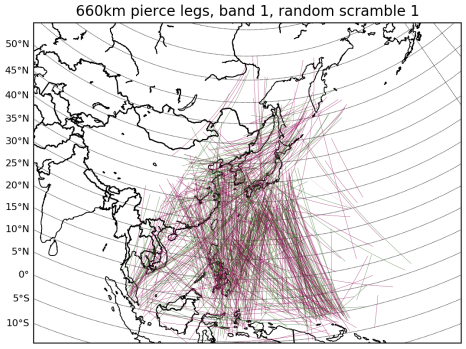

(a) Band 1 30s

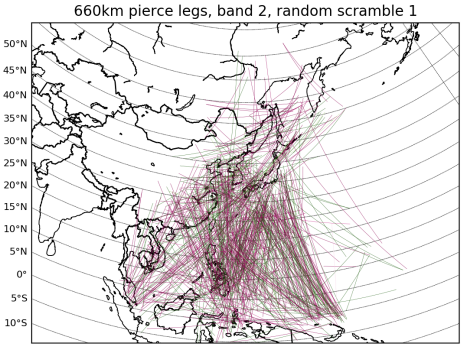

(b) Band 2 21s

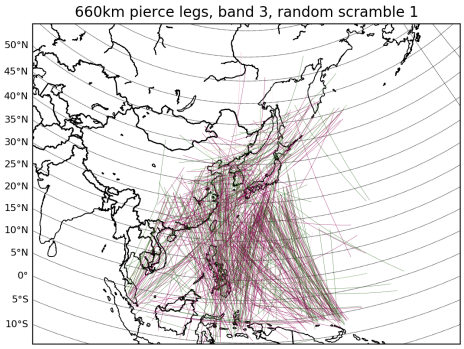

(c) Band 3 15s

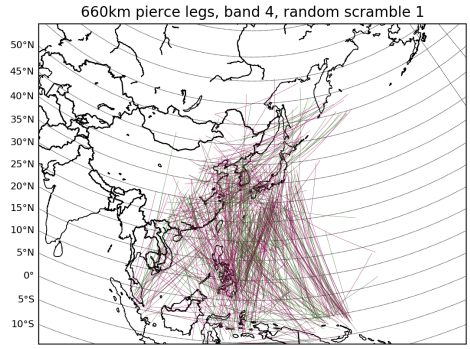

(d) Band 4 10s

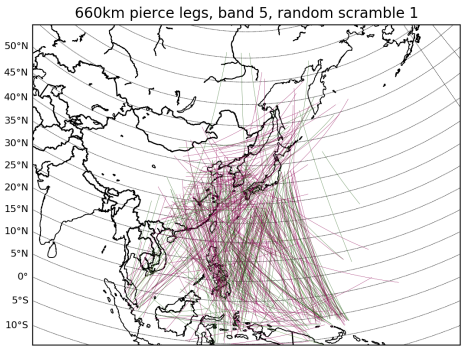

(e) Band 5 7s

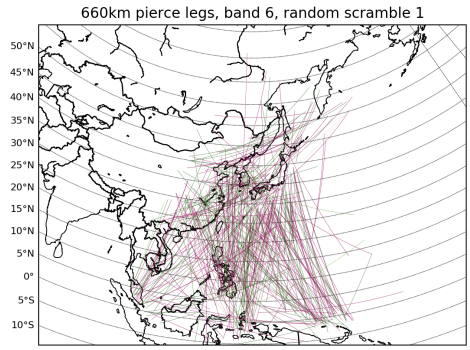

(f) Band 6 5s

Figure 2.13: Random subset of approximated grazing paths (660km) of regional P-waves representative of mantle transition zone coverage. The figure shows point-to-point transition zone segments based on the entrance and exit point of a hypothetical ray path to and from the 660km discontinuity in an IASP91 backgorund model. The colour of the rays is a random scramble, utilised to bring out ray coverage. Ten realisations of a subset of measurements, randomly chosen for each realisation, are implemented to fully demonstrate the extent of coverage. Shown here is the first random scramble implemented for each frequency band.

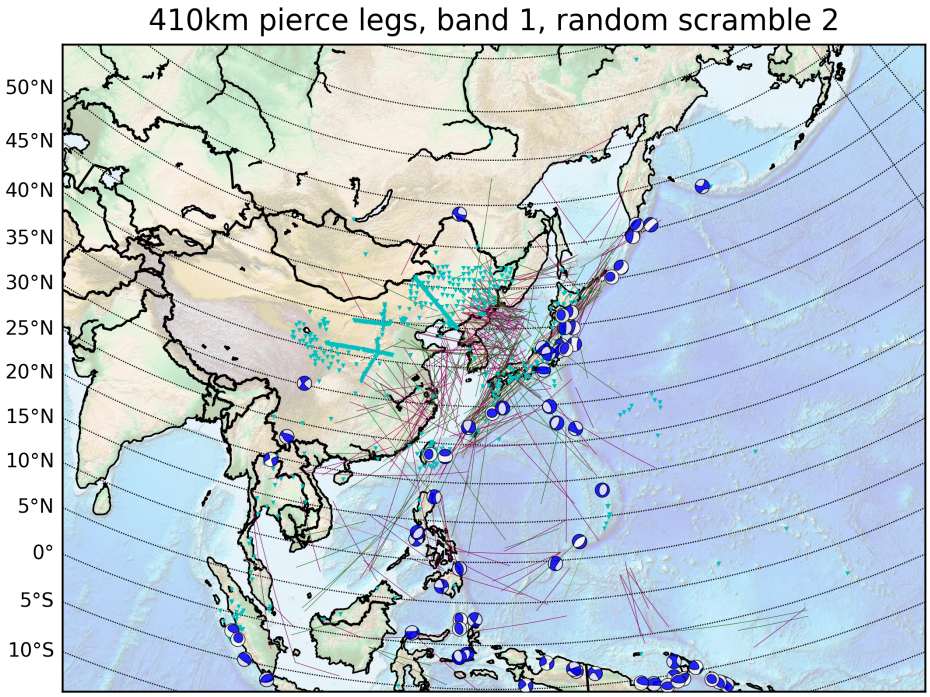

Figure 2.14: Added bathymetry and a selection of regional seismicity (beachballs) for a random subset of approximated grazing paths (410km) with major plate boundaries also visible.

- Bias mitigation and overall variance reduction using MSE of a broadband waveform can improve travel time measurements based on the corresponding data tapers and can limit the propagation of uncertainties to successive steps of a tomography workflow

- Differences in travel-time measurements, based on successively higher order Slepian tapers might be used to distinguish separate time-distance triplication branches.

Here I provide a brief summary of the multitaper measurement workflow used in this study, which is strongly based on the recipe of Percival & Walden (1993).

Definition of spectra, tapers and spectral windows

2.4.2 (Numerical) Implementation

I cropped each broadband waveform using a 60 second time window containing the triplicated P-wave arrivals and subsequent P-wave multiples and depth phases, with an approximately 10 second preset to the first manifest arrival. The Nyquist frequency and fundamental Fourier frequency are defined as

$$f_{alias} = \frac{1}{2\Delta t} \tag{2.3}$$

and

$$f(N) = \frac{1}{N\Delta t} \tag{2.4}$$

respectively, where Δt is the waveform time step and N the number of data samples in the time window. The best estimate of the waveform's 'true' frequency spectrum, $S^{mt}(f)$, is constructed from k many data tapers, $h_{t,k}$ such that

$$S^{(mt)}(f) \equiv \Delta t \left| \sum_{t=1}^{N} h_{t,k} X_t e^{-i2\pi f t \Delta t} \right|^2 \tag{2.5}$$

where X_t denotes the waveform value at the tth timestep. I want each constituent eigenspectrum to be uncorrelated and thus use the Slepian tapers discussed above for this purpose. We created these on the fly using the open source python code *mtspec* (Krischer, 2016), based on the method of Slepian (1978), which can be expressed as

$$h_{t,k} \equiv \begin{cases} v_{t-1,k}(N,W), & t = 1, ...N; \\ 0, & otherwise \end{cases} \tag{2.6}$$

where $v_{t-1,k}$ denotes the tth value of the kth taper and W the half resolution bandwidth (see Percival & Walden (1993) for further reading). Complementary spectral windows for the tapers are given as

$$H_k(f) = \Delta t \left| \sum_{t=1}^{N} h_{t,k} e^{-i2\pi f t \Delta t} \right|^2 \tag{2.7}$$

for which the side lobe level determines the extent of signal leakage.

Workflow for triplicated body waves

I calculated the resolution bandwidth, 2W, where

$$W = \frac{j}{N\Delta t} \tag{2.8}$$

and

$$0 < W < \frac{1}{2\Delta t} \tag{2.9}$$

. I set j = 4. For a typical time window sampled at 20Hz, this yields W = $\frac{1}{15}$Hz and resolution bandwidth of $\frac{2}{15}$ Hz. Percival & Walden (1993) note that favourable variance reduction with higher W poses the risk of smoothing out small wavelength features: as such, a trade-off choice in W must be made. I then computed k eigenspectra using Slepian tapers based on the above parameters, such that k does not exceed the Shannon number,K, where $K = 2NW\Delta t$ and $k \leq K - 1$.

2.4.3 Examples

In what follows, figures 2.15-2.18 lay out an example multitaper measurement as applied to regional body wave codas, including the Slepian tapers applied, the associated spectral windows for a subset of the data tapers and the outworkings of these during cross-correlation.

2.4.4 Using coherence to improve cross-correlation measurement success

What follows is based on discussions and collaboration with Schwarz (pers. comm, 2017). Coherent stacking: triplications could be classed as coherent signals of interest of low amplitude and contaminated with random noise (Schwarz & Gajewski, 2017). Due to low signal-to-noise ratios and overall complexity that can be observed in triplicated body wave codas, cross-correlation travel-time measurements of triplicated phases can be difficult to perform, leading to a low yield of measurements above a successful cross-correlation threshold (Schwarz, pers. comm). By utilising the proximity of neighbouring stations, one option is to link spatially correlated measurements by means of coherence and wave front arguments to collectively

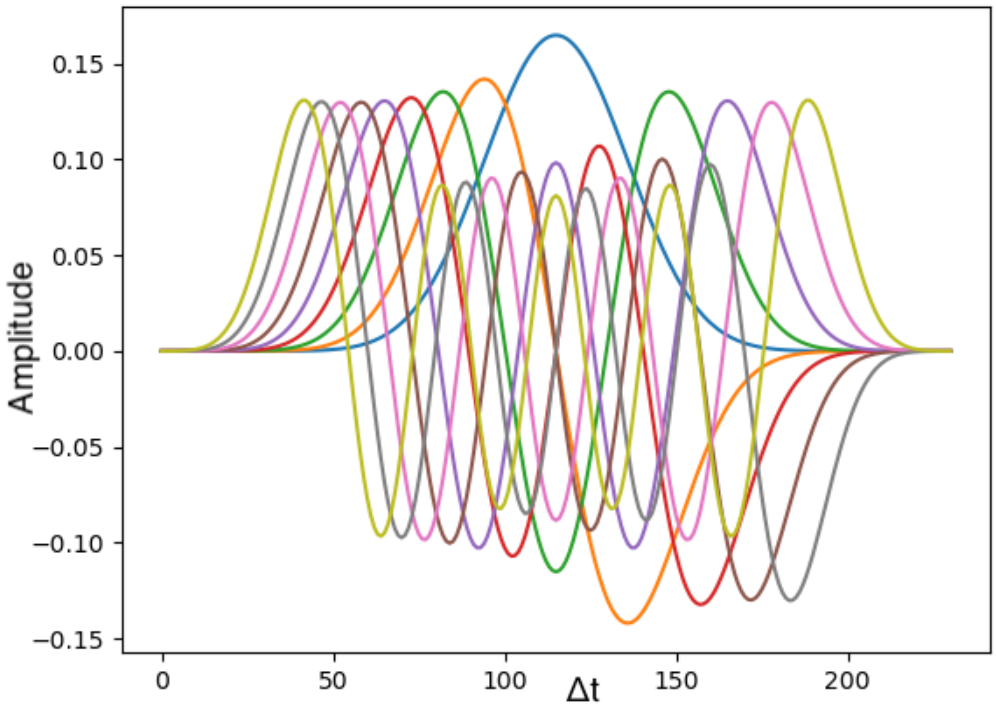

Figure 2.15: Example of Slepian tapers applied to regional body-waves. Shown are the first ten orthogonal data tapers. Note that most applications of Slepian tapers to time series data generally use only the first four tapers.

inform the time window selection for cross-correlation. In the appendix of this thesis can be found supporting figures for the coherence-based stacking process outlined briefly below.

- For a given waveform, we performed a stack over all neighbouring traces within a 500km window, normalized by the number of neighbouring traces.
- We computed the complementary semblance, to produce a coherence-weighted stack.
- Slope and curvature attributes at each point were used to characterise emerging wavefronts for every data sample using the BEAM Julia software package (Schwarz and Gajewski, 2017).

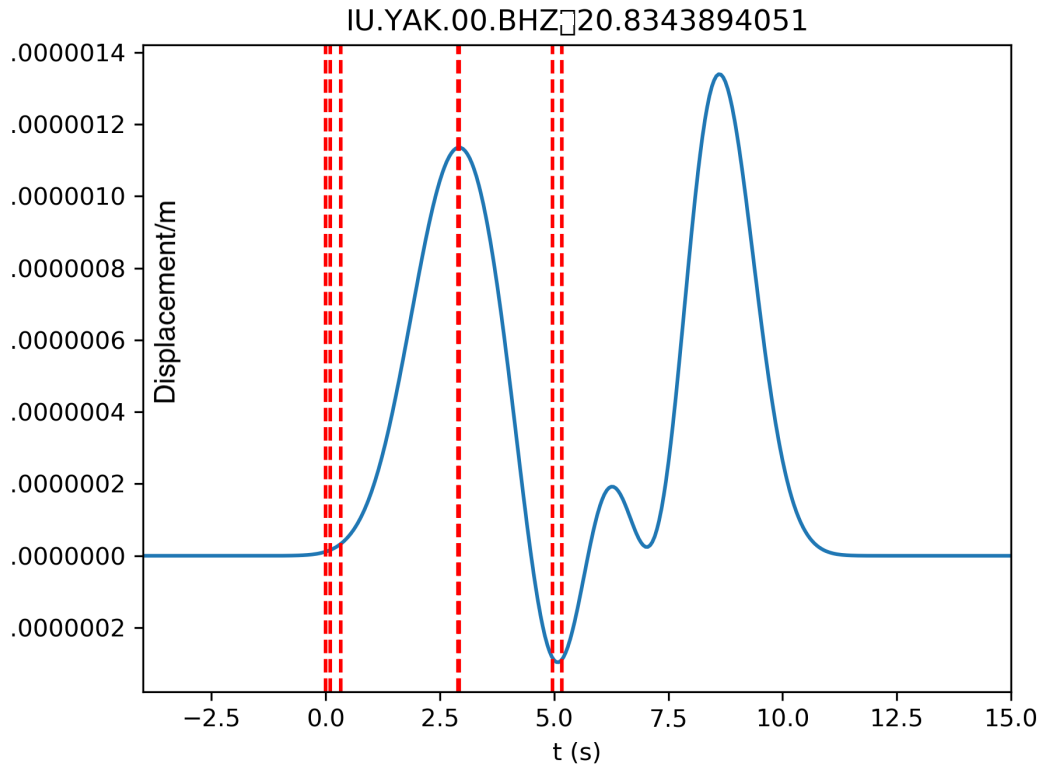

Figure 2.16: Slepian-filtered Instaseis synthetic seismogram for a source-receiver distance of 20 degrees. Shown is a waveform filtered using the fifth taper shown in the previous figure. Red dashed lines represent TauP-predicted arrival times in an IASP91 background model, which is expected to be triplicated. It can be seen that the first break in energy, in addition to the peak and trough of the first order feature of the first waveform cycle, line up with the TauP-predicted arrivals. Future work will focus on reproducibility for a variety of waveforms across a range of epicentral distances.

- This appeared to improve cross-correlation measurement success with respect to unstacked regional P-wave waveforms

Future work will aim to explore the usefulness of coherence analysis in suppressing uncorrelated noise and interfering phases to further improve access to the triplicated wave field. I refer the reader fo figures A.81, A.82 and A.83 for trial applications of the process outlined above.

2.5 Modelling

The rest of this chapter details the accumulation of the bank of full waveform-based sensitivity kernels for each and every regional multifrequency travel time

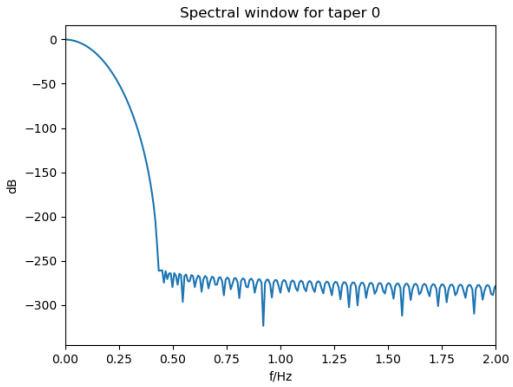

(a) Spectral window 1

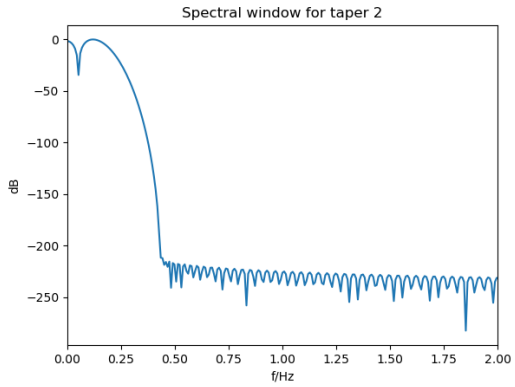

(b) Spectral window 3

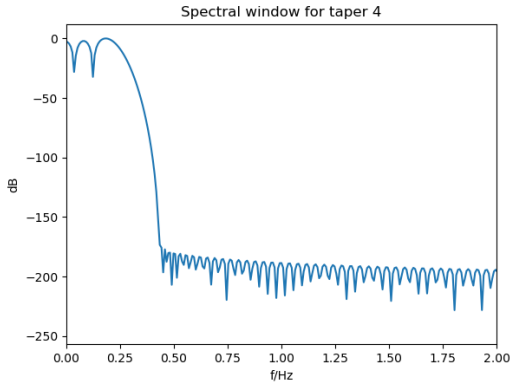

(c) Spectral window 5

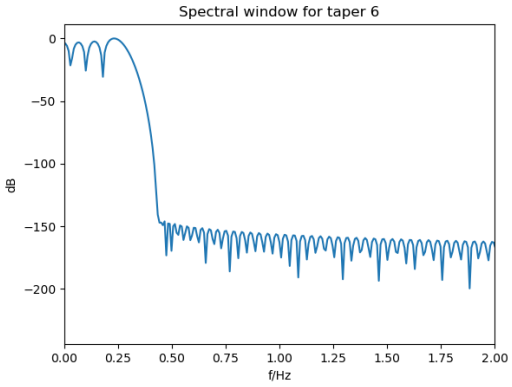

(d) Spectral window 7

Figure 2.17: Some examples of spectral windows associated with Slepian tapers.

yielded in chapter 2, to be embedded in an extant finite-frequency tomography workflow. I begin with a quick review of the spectral element code, Axisem and provide an explanation for calculating sensitivity kernels based on Axisem using the MC Kernel software. Next, I provide a brief overview of the theory of travel-time sensitivity kernels, which are essentially the cross-correlation-informed, time-integrated mathematical convolution of forward and backward Axisem wavefields. From here I detail the measurement winnowing process required to create a feasible sensitivity kernel bank on high performance computing resources, in addition to the protocol for this. From here, I demonstrate briefly the performance of the MC kernel code and supplement this with visualisation of some sensitivity kernels, before briefly addressing the limitations of the method, and proposing future directions for Axisem-based full waveform tomography.

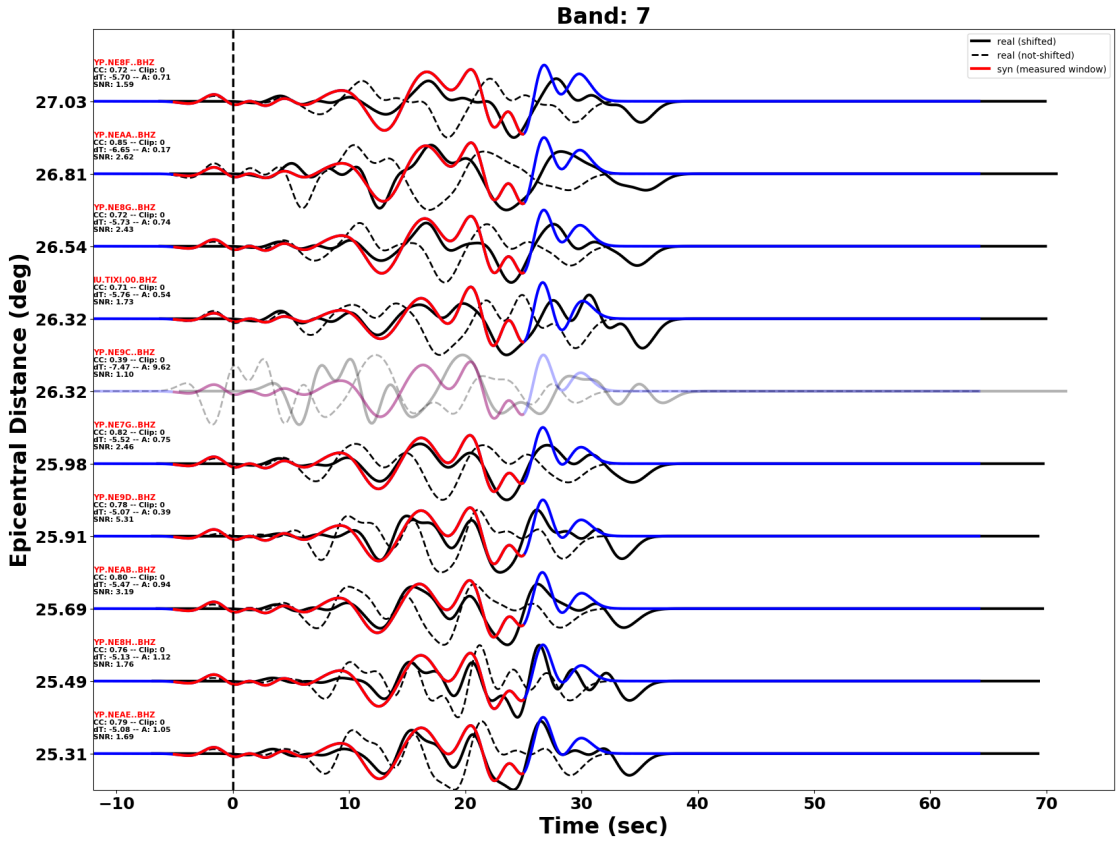

Figure 2.18: Example of cross-correlation of real and synthetic data using Slepian tapers in the Pyffproc workflow. Note that this is a trial experiment and that the first break of energy does not occur until 10 seconds in this time-record section. Red lines are synthetic Instaseis data and black lines the real Slepian-filtered data. There is a high success rate for cross-correlation measurements shown in this figure, such that secondary arrivals appeared to be captured well. Future work will look to reproduce measurement success and suppress any sources of artificial noise introduced into the workflow.

2.6 Axisem wavefields

2.6.1 Overview of method

Here I present a summary of the method outlined by Nissen-Meyer et al. (2014). The spectral element solver is used to produce the wavefield bank, required to compute full-waveform based Fréchet derivatives, to be taken forward for tomography. Each Fréchet derivative, or sensitivity kernel, requires one 'adjoint' wavefield i.e. a point force back-propagated from receiver to source location, and a forward wavefield with full moment tensor source, at its correct depth. The forward global wave propagation bank must contain runs at source depths sufficiently representative of

the catalogue used in this study (see 3.2.3 for an elaboration on the decision-making process for the number of forward runs).

The unique selling point of the axisymmetric spectral element method, as implemented by the AxiSEM software, is its tactful use of moment tensor and point force sources, which effectively collapses the wave propagation domain to two dimensions (Nissen-Meyer et al., 2014), on a semi-circle positioned along the central axis of the, to all intents and purposes, spherical Earth. Corrections for the ellipticity of the earth are addressed in chapter 4. This is required to maintain source radiation pattern symmetry. This enables the azimuthal dimension of the wavefield to be computed analytically.

In order to be consistent with the Green's function database used to gather multifrequency measurements, forward simulations of global wave propagation are carried out in an IASP91 1-D or radial background model (Kennett, 1995). This study aims to deliver continental-regional scale body wave tomography, to investigate what is known to be both a volumetrically and topographically heterogeneous MTZ. I consider the choice of a radially symmetric background model to be fit for purpose, due to linearity between cross-correlation based travel-time measurements and perturbations to the starting velocity model. Mercerat and Nolet (2013) observed cross-correlation delay times to remain linear with perturbations of up to 10% in body wave velocity. Such perturbations are within the realm of P-wave velocity perturbations observed in other full-waveform based regional tomography, which was up to 5% (e.g. Tao et al., (2018). Below is a ten-step roadmap through the AxiSEM workflow for a typical tomography-augmented modeling of the wavefield, as outlined in Nissen-Meyer et al. (2014).

- Posing the 3D weak form of the wave equation
- Decompose source radiation patterns into constituent responses to each element of the moment tensor, Mij, expressed as a function of azimuth, respectively for monopoles, dipoles and quadrupoles (m=0,1,2)
- Address the solution to step 1

- Multiply all wavefields at all locations in domain
- Map reference co-ordinates, upon which any derivatives are computed, to the physical dimension, related by the Jacobian.
- Expand the wavefield, element-wise to the 4th/5th/6th order, using Lagrange polynomials
- Gather all element operations and assemble mass and stiffness matrices
- Temporally discretize the wavefield as an ordinary differential equation system, solved using a second order Newmark scheme.
- Account for the source time function. Here I use a Gaussian for the purposes of tomography.
- Assemble the response to the full moment tensor by summing over the constituent radiation patterns and convolving with the (2D) Green's function (eqs. 8 through 12 in Nissen-Meyer et al., 2014).

Note that four independent simulations of the wave equation can explain all six elements of the moment tensor. This is due to azimuthal equivalence.

2.7 Sensitivity kernels

2.7.1 Rationale

The rationale of this study is to investigate the means by which triplicated body waves (which are in essence a temporally compact packet of body waves) can be harnessed to improve tomographic resolution in the upper mantle and transition zone. In order to achieve this, I use sensitivity kernels that strike a balance between sufficiently capturing the realistic physics of the upper mantle while enabling a flexible workflow, that promotes quality control over multiple data and its pre-processing.

Here I seek to demonstrate the suitability of MCKernel (Stähler et al., in prep.) for this purpose, which calculates kernels as the convolution of the frequency-filtered

forward and receiver-to-source back-propagated seismic wavefields, which were forward modelled using the spectral element code, AxiSEM. Given the use of the full seismic waveform, the kernels are similar to the event kernels used in gradient-based adjoint tomography: however, they also inherit the dexterity of ray-based, finite-frequency sensitivity kernels (e.g. Dahlen & Nolet, 2000a; Hosseini et al., 2020; Tsekhmistreno et al., 2019), in that a kernel for each source-receiver path can be calculated and subsequently analysed. This is especially useful for the mantle transition zone, in that a given kernel, calculated over a time window unique to a given finite-frequency measurement, can be interpreted in terms of volumetric sensitivity. In this study I focus solely on volumetric sensitivity kernels, calculated in a spherically symmetric 1-D background model, with fixed mantle transition zone topography as per the IASP91 background model.

Sensitivity kernels can be considered to be a mapping function between observations of body wave arrival times and the seismic velocity profile of the solid Earth, within the volume over which those body waves have propagated. In other words, they represent the change in seismic travel time with respect to the perturbation of model parameters, i.e. P-wave velocity, in this study.

2.7.2 Theory

The *Axisem*-based, frequency-filtered cross-correlation measurements, performed on triplicated body wave time windows, were taken forward to compute three-dimensional, exact Fréchet sensitivity kernels using *MC Kernel* (Stähler et al., in prep.). This uses forward and self-adjoint wavefields from *Axisem*, where 'self-adjoint' refers to the time-reversed velocity seismogram, back-propagated from the receiver. The unique selling point of this scheme is that kernels are projected onto irregular inversion grids, whose density is dictated by apparent ray coverage, based on the multifrequency measurement dataset. In this study, meshes are created using the method of Persson and Strang (2004). Kernel projection is via Monte Carlo integration: as such, precision of each discretised kernel value was dictated by the regional coverage (Stähler et al, in prep).

Travel time kernels represent the change in seismic arrival time (δt) , yielded from multifrequency travel time measurements, with respect to perturbation in model parameters, δm(x), distributed over a volume between source and receiver. In essence, this requires a convolution of the forward and backward (self-adjoint) wavefields. Here we assumed the Born approximation. This assumes that a given scatterer predominantly projects energy in the direction of seismic wave propagation, to first order (Dahlen et al., 2000a). This has exhibited strong performance when accounting for the scattering of seismic energy on the regional-global scale in previous studies (Dahlen et al., 2000a; Chen et al.,2015).

In this section we present an abbreviated version of the kernel formalism as documented in Stähler et al. (in prep.). Under the assumption of an isotropic Earth, Stähler et al. (2012) define the perturbation to the seismic waveform, written in terms of the wavefield tensors as

$$\delta u = -\int_V \left[\delta\rho \overrightarrow{v_i}.\overleftarrow{v_i} + \overrightarrow{E_{ii}}.\overleftarrow{E_{jj}}\delta\lambda + 2\overrightarrow{E_{ij}}.\overleftarrow{E_{ij}}\delta\mu\right] \mathbf{d^3r} \tag{2.10}$$

where λ and μ indicate the Lamé constants, $\mathbf{E}$ the strain tensor and $\mathbf{v}$ the velocity field. Left and right facing arrows denote the forward and backward-propagating field quantities respectively. This can be related to the unperturbed seismogram by

$$\begin{aligned}\delta u_i(t,x) = -\int_T\int_V (\delta\rho(x')G_{ij}(x,x',t-t')\partial_t^2 u_j(x',t') + \\ \delta c_{jklm}(x')\partial_k G_{ij}(G_{ij}(x,x',t-t').\partial_l u_m(x',t'))d^3x'dt'\end{aligned} \tag{2.11}$$

where $G_{ij}(x,x',t-t')$ denotes the endmember Green's function and c_{jklm} the stiffness tensor. x' and t' are the reciprocal locations and times of x and t as per reciprocity theorem. We express the travel-time measurement, as per Stähler et al. (in prep), as

$$\delta T = \int_V K_X^{\delta T}\delta X(x)d^3x \tag{2.12}$$

where $K_X^{\delta T}$ is the physical parameter kernel e.g. compressional or shear-wave velocity. This is underpinned by kernels in the fundamental parameters as defined by Fichtner (2011). The travel time kernel is the product of the physical or

'waveform' kernel with the velocity seismogram, integrated over the endmember cross-correlation time window, normalised by the squared velocity seismogram, integrated over the same time window.

$$K_X^T = \frac{\int_{T_1}^{T_2} K_X(t)\dot{u}(t)dt}{\int_{T_1}^{T_2} u^2(t)dt} \tag{2.13}$$

2.7.3 Database of kernels

Axisem wavefield source depths

The ideal scenario for tomography using sensitivity kernels based on the full seismic waveform, is to calculate a forward wavefield, whose source depth represents the inferred or 'true' wavefield depth, pertaining to each waveform for each event, at the highest possible frequencies. In relation to the multifrequency measurement dataset used in this study, this depth is given by that calculated for the source time function convolved into the synthetic Green's function, upon which the measurement is based. In the event that the inverted source time function is not of sufficient quality, the source depth is the catalogued NEIC depth: however, this would require calculating a forward wavefield for each unique depth occurrence in the earthqauke database, using AxiSEM. This protocol is ill-advised, if not intractable, due to

- (High performance) computing costs
- Storage requirements on disk, both in terms of magnitude and temporal duration of storage
- Post-processing time
- Knock-on effects on kernel compute time and (HPC) resources
- Latency in intra- and inter-network data transfer and file handling.

Already, at this period, even with the use of depth binning, roughly 84 forward and one backward wavefield would need to be calculated for the event database used in this study. Given the HPC environment in which we predominantly implement this workflow (Oxford Advanced Resource Computing with SLURM, ARCHER,

the UK national supercomputing service, with Torque scheduler, and ARCHER2, its successor, also with SLURM), a ceiling storage maximum of 5TB is available for use, without incurring significant financial costs for long-term storage. Each wavefield would require roughly 1.2TB of disk space for the initial calculation and post-processing steps. Up to 50TB of disk space would be required to store the post-processed wavefields in perpetuity and at the very least, for the life-cycle of this study. In addition, the cumulative post-processing time commutes to three weeks (550 hours). If the dominant period were to be upscaled to two seconds, the above values would grow exponentially (Nissen-Meyer et al., 2014). This vastly increases the compute time required for each kernel.

Two possible approaches to mitigate for this data-intensive bottleneck are

- Coarsen the AxiSEM depth bins used to amass the forward wavefield database. This would introduce or heighten multiple artefacts in the tomography for the following reasons.

- Keep the AxiSEM depth bins as suggested but only compute a forward wavefield, if a given depth bin represents the source depth for a number of events, above a given threshold i.e. such that multifrequency measurements based on these events contributes meaningfully to seismic inversion.

Here I opt for the first approach, using coarse source depth bins to represent the seismic wavefield, for every source depth occurring in my catalogue. I computed forward wavefields in Axisem at intervals of 2km between 0-100km, at intervals of 5km between 100-200km, and 10km for depths greater than 200km. This resulted in a total of approximately 80 forward modelled seismic wavefields, in addition to one backward propagated seismic wavefield. Each wavefield was modelled accurate to roughly 8s period.

Opting for the latter approach, I set a threshold of ten events in a given depth bin, for all events above 150km depth, in order to compute a forward AxiSEM wavefield. This results in 28 crust and uppermost mantle forward runs. I handpick a select number of event bins greater than 150km depth, giving a total of 38

forward runs to be calculated. This collapsed the hot storage required for all seismic wavefields, prior to post-processing, to roughly 10TB . Long term storage for HPC/NAS resources was reduced to 10 TB after post-processing (including the resultant sensitivity kernels calculated from the seismic wavefields).

Depth choice

A forward modelled seismic wavefield, with dominant period of 7.5 seconds, is computed for each earthquake depth bin, whose decrements are informed by the multifrequency travel time measurement dataset. In the upper 50km, spanning the earth's crust and uppermost mantle, bins aggregate in 2km decrements. This is justified by the tradeoff between the measurement of the travel time by cross-correlation, the known range of seismic velocities at crustal depths and the required accuracy of the travel time measurement i.e. a 1km difference between the inverted source time function depth and the Axisem bin depth commutes to a change of roughly 0.1s arrival time within the 10-50° epicentral distance range, which is on the order of 1 x 10^{-4} % of the aggregate travel time of the P-waves. I invoked a similar argument when computing Axisem wavefields between 50-100km depth, keeping the bin width at 2km.

In addition, the change in source time function pulse shape between the inverted STF depths and the pulse shape for inverted source depth (2km above and below this) is minimal, and the decision on the final STF is often made subjectively by the user. Nonetheless, it is important to take this into account because the Instaseis-based cross-correlation measurements are informed by the source time function.

Due to the distribution of earthquake source depths (there are typically fewer with increasing depth), both generally and for the catalogue used in this study, Axisem wavefield depths are modelled in 5km depth bins between 100-200km depth, and 10km resolution below 200km depth.

Subjective Parameter Choices: Axisem source types for MC Kernel wavefields

At the time of running, Axisem inserts a source at the origin. In this study I seek to strike a balance, between computing forward wavefields that are fit purpose for the calculation of seismic sensitivity kernels, whilst ensuring that novel additions to the existing seismic tomography workflow are integrated as seamlessly as possible. Contiguity between the frequency filters used to calculate paraxial, ray-based Dahlen kernels in previous tomography, and the filters used in this study to calculate MC sensitivity kernels, is of chief importance.

At the ray matrix step of the TICC tomography workflow (i.e. the fortran procedure used to assimilate finite frequency kernels based on paraxial ray bundles), Gabor filters, as used in chapter 2, were used to calculate the frequency-filtered, Instaseis-relative cross-correlation travel time measurements: however, event-specific inverted source time functions were not subsequently convolved with those Gabor filters. Instead, for every Gabor filter, the source time function passband was flat (Sigloch, pers. comm). In this context, the cutoff frequency of the filter used to calculate the paraxial ray-based Dahlen kernels, was the cutoff frequency of the Gabor filter response itself, for which its energy was tapered off using an approximated slope.

In this study, I seek to compute as high fidelity seismic wavefields as possible. Crucially, I seek to mitigate for the presence of artificial noise in both the forward modelled and filtered seismic wavefields, whilst aiming to calculate a wavefield that presents as broadband as possible (Sigloch, pers. comm; Nissen-Meyer, pers. comm ; van Driel et al., 2015). One example of artificial noise is aliasing, which can arise from an inappropriate choice of source time function. In the context of the resolution of the numerical mesh, a Dirac-delta or narrow Gaussian (1Hz) source on a mesh with resolution «1Hz would be inappropriate (here I only model the seismic

wavefield to 7.5s dominant period).

In light of the above, I use a Gauss-0 type source in Axisem. This is a Gaussian source time function, whose period is the resolution of the mesh, upon which the wavefield is forward modelled. Here, we calculate wavefields on a 7s mesh, densified near the major model discontinuities of the IASP91 background model (Kennett,1995).

As outlined in van Driel et al. (2015), the falloff slope in the amplitude spectrum, both of the source and seismogram, should be sufficiently large, such that the lowest possible sampling rate, subject to the constraints of the mesh, can be used, to avoid aliasing of the signal. In this study, I adhere to their advised minimum sampling resolution of 4 samples per period, when forward modeling Axisem wavefields for calculating sensitivity kernels.

In addition, accounting for the effects of attenuation on the seismic wavefield results in little to no change in shape of the sensitivity kernels, for like-for-like source-receiver paths (Stähler, pers. comm. 2020). Running Axisem without attenuation enables a wavefield to be forward modelled in approximately 50% of the wall time: thus, in the interests of computational efficacy, I opt for this line of approach in this study.

Calculation of Wavefields on HPC Resources

Axisem wavefields were mainly calculated on a CRAY XC30 MPP supercomputer, maintained by ARCHER, the UK National Supercomputing Service. Computing nodes on ARCHER have dual 12-core Intel Ivy Bridge series processors, which commutes to 24 CPUs per node, each of which has 64GB of memory (this later became 128 CPUs per node, with 128GB memory).

Computing resources are finite: it is in this context that a subjective choice on the number of Axisem forward wavefields, their dominant source period and their post-processing protocol, was determined. I envision that the tomography workflow, as outlined in this thesis, could best approach full or near automation in future studies, although here I present a protocol study, with each component step laid out with the potential to be automated. In light of this, I batch compute each Axisem wavefield bin using job arrays on ARCHER. Job arrays run the spectral element solver multiple times in parallel, modified for each earthquake source depth. This preempts the need for manual, sequential submission of more than 50 forward simulations.

Storage

Given that wavefields are to be retained for posterity, the raw computed seismic wavefields were transferred by remote data syncing, from the ARCHER compute nodes (work directory) to storage resources, whose source resides at the workstation level. Specifically, I use a Western Digital 14TB Elements Desktop Drive New Technology File System (NTFS), connected to workstation reosurces by USB 3.0. This enables data transfer rates of up to 5GB/s., network transfer rate permitting. Future studies will clone this dataset to Network Attached Storage systems and cloud computing resources, if the latter becomes available. Currently, steps to ensure data posterity include using the Oxford Hierarchical File System (HFS). This service retains the two most recent copies of each seismic wavefield on the desktop drive and backs up up to 400GB per day, from NTFS to HFS.

Post-processing

I capitalise free local computing resources, and post-process Axisem wavefields on a local workstation, rather than post-processing the wavefields on HPC resources. This requires operations be performed on each component part of the wavefield, in order to sum, weight and rotate each component part of each endmember forward wavefield accordingly. Wavefields then undergo a rechunking operation to allow them to be read as contiguous time series. Once this is done this enables the calculation of sensitivity kernels for each time-dependent and informed

multifrequency measurement.

After post-processing, a typical forward run of Axisem, with time sampling of four points per period, without accounting for the effects of attenuation and honouring seismic periods up to 7s, occupies approximately 80GB of storage. This is comprised of four ordered netcdf files for each subrun (i.e. wavefield source depth), from which the weighted sum produces a wavefield excited by any seismic moment tensor (Stähler et al., in prep.)

Following on from this, an Axisem wavefield bank containing roughly 80 source depths should is representative of most terrestrial seismicity catalogues. This equates to a modest net storage requirement on the order of 5-10TB. To put this in context, this is a fraction of most NAS resources and cloud storage currently available to the geoscientific community i.e. the entire database can be stored on an external hard disk if needed, incurring modest hardware costs on the order of several hundred pounds.

The wavefield bank is suitable for this study because it enables the incorporation of regional P-wave finite frequency travel time measurements into an existing, tried-and-tested tomography workflow: crucially, it allows for the inversion of a dataset containing periods up to 10s-15s, in line with previous tomography, implemented on the global scale (Hosseini et al., 2020; Mohammadzaheri, 2021).

Bottlenecks in the subset workflow

While the long term storage of Axisem wavefield bins is modest, the post-processing of hot copies of each forward simulation requires that much larger, unprocessed netcdf files be temporarily stored, typically on the scale of a few days to several weeks. While I observe that the entire Axisem wavefield bin could be computed as a single batch job array on ARCHER HPC resources, in several of hours and at modest computational cost, this is prohibited by constraints imposed by available

disk space. My current quota of 5TB at the time of writing is much above the default 1TB allocation for ARCHER users. Nonetheless, a mini-batch job array of 5 Axisem wavefields occupies roughly 800GB of storage space before post-processing. In addition, the Extraction, Transformation and Loading (ETL) of this mini-batch is further constrained by local storage, albeit a generous 14TB, therefore, the ETL must be staggered over the entire database. This entails:

- Data transfer (from HPC to local resources) of the mini-batch
- Post-processing of the wavefield mini-batch (4n wavefields must undergo a field transform, where n is the number of source depths in the mini-batch)
- Quality checking that post-processing for the mini-batch has been successfully completed, before deleting the unprocessed wavefields, and storing the processed copies for subsequent tomography steps (i.e. for calculating sensitivity kernels)
- Computing and transferring the next mini-batch after space has been made available on local and HPC resources.

Protocol for kernel calculation

Sensitivity kernels are computed in batches. Akin to the workflow used to calculate Axisem wavefields on HPC resources, I use the job array functionality on ARCHER to run multiple kernel calculations in parallel. One job submission pertains to a given Earthquake, with a kernel being calculated for each successful multifrequency travel time measurement, in different frequency bands, for every receiver.

Each event is assigned to a given batch based on the depth of its source. Each batch corresponds to its endmember Axisem forward run. Where the moment tensor solution, which is used as an input parameter to MC Kernel and contains information regarding the source depth, presents with a depth, either calculated from source time function inversion or that stated in the NEIC catalogue, that lies between two Axisem bin depths, that event is assigned to the batch corresponding

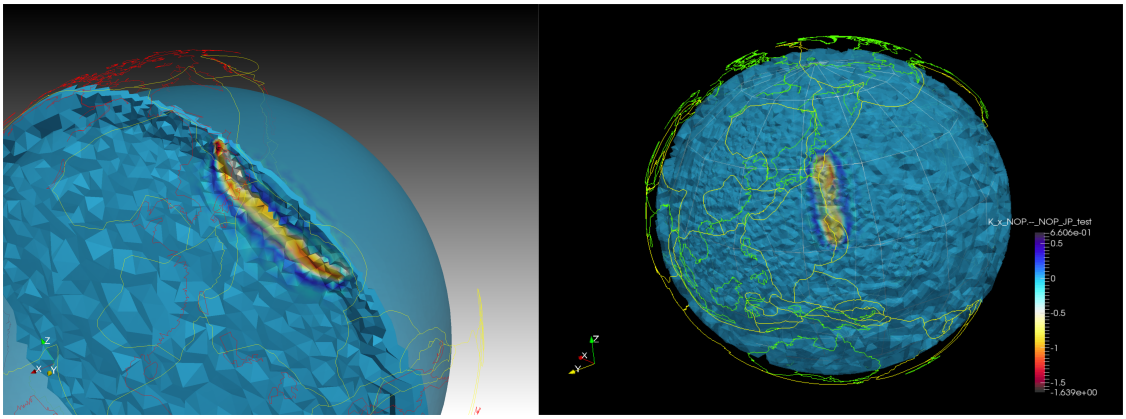

Figure 2.19: Out-of-plane and top-down view of an Axisem-derived full waveform sensitivity kernel (MC Kernel) beneath Japan, projected onto an irregular mesh.

to the nearest bin depth. This provides the advantage of only having to transfer one Axisem wavefield to HPC resources at a time. In this study, this allows me to order data input to the ensuing tomography in a tractable manner i.e. one can iteratively add measurements and kernels to successive inversions of the dataset by depth and track the model evolution or change in resolution, using synthetic feature recovery.

2.7.4 Kernel visualisation

This short section shows a mini gallery (figures 3.1 and 3.2) of sensitivity kernels calculated using MC Kernel and projected onto the JPTRIPP20 inversion mesh used in this study. I direct the reader to chapter four for an overview of the steps taken to create the inversion mesh based on the seismicity coverage in the western Pacific. Seismic illumination of the mantle transition zone at regional distances is evidenced in figures 3.4 and 3.5.

2.7.5 Performance

Figure 3.3 shows the sum over all values for MC sensitivity kernels as a function of epicentral distance. The magnitude of these sums is expected to approach the travel-time of the seismic phase of interest (Nolet, pers. comm; Sigloch, pers. comm) as shown here. Godwin (2020) showed that this also applies for Axisem wavefields where a heterogeneous layer (with respect to the background model) is present. If one considers two sensitivity kernels with the same source depth and source-receiver

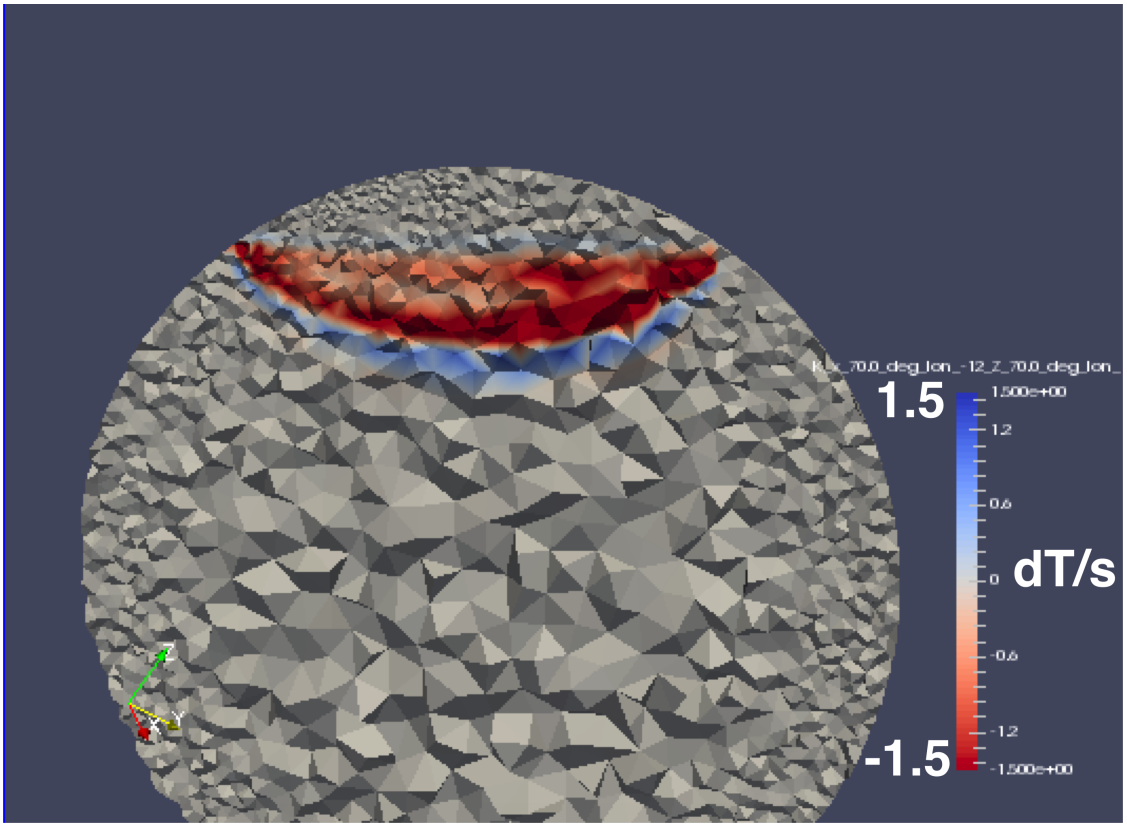

Figure 2.20: Cross-sectional view of a 70° sensitivity kernel.

distribution, one with a heterogeneous anomaly along the seismic energy propagation path and the other calculated in the ambient background model, by differencing the sum over all values between the two kernels, one expects to yield the travel-time anomaly induced by the along-path heterogeneity. This is important when considering the definition of the sensitivity kernel, which is a convolution operation integrated over the time window yielded from cross-correlation measurements.

2.7.6 Limitations of the method and future directions

In this short section I address the limitations of the approach used to calculate sensitivity kernels based on the full waveform. This thesis uses kernels based on seismic wavefields based on Axisem, which calls upon spherically symmetric background models, such that they are one-dimensional in the radial direction.

Here I use wavefields based on an IASP91 background model. The adjoint

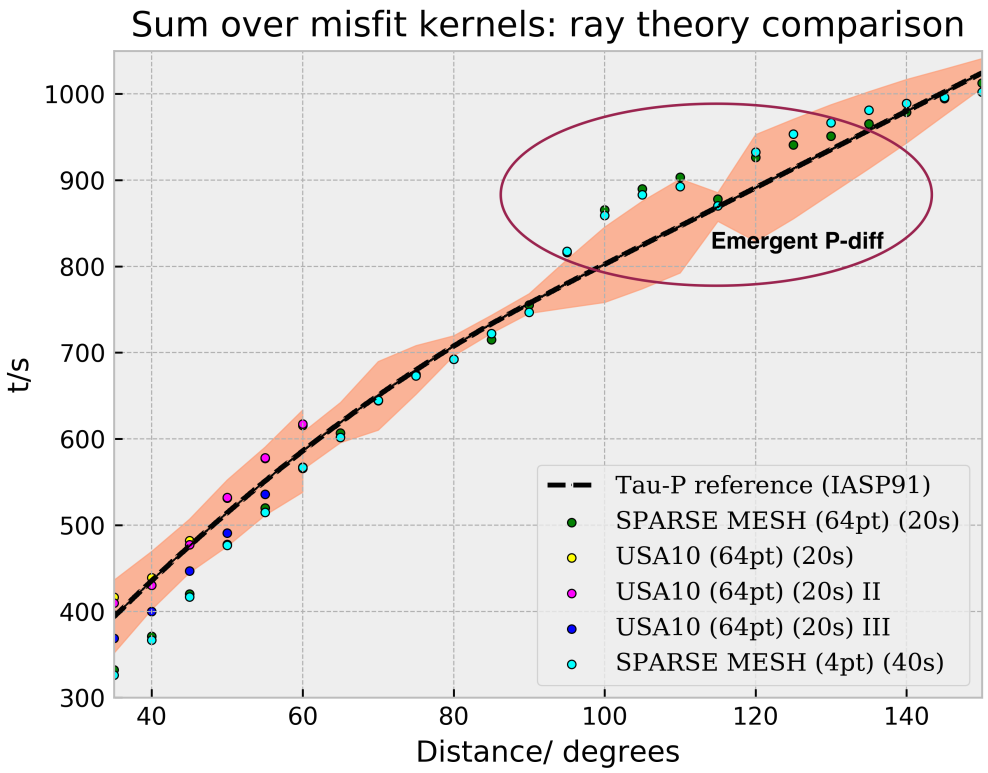

Figure 2.21: Sum over travel-time sensitivity (MC) kernels as a function of epicentral distance. Plotted are the predicted travel-times in an IASP91 background model (black dashed) for a succession of runs of the MC kernel software, on several inversion grids, with both sparse and coarse meshes, and at different azimuths on those grids. Points on the plot denote the individual sums over kernels for a given endmember run. The orange shaded regions denote the 95% confidence intervals calculated for the data in Python.

tomography community typically calculate three-dimensional event kernels for seismic wavefields propagated in fully three-dimensional background models e.g. Chen et al., 2015. There are advantages to this latter approach, in that by using a 3-D starting model, and provided it is to first order close to the true earth model, one is able to produce models with improved waveform fits that take into account measurements based on three-dimensional synthetic waveforms; however, it is also possible that an inadequate exploration of model space during inversion results in a solution that is trapped in local minima, rather than the true solution minimum.

In this study the topography along the major seismic discontinuities which distinguish the upper (410km) and lower (660km) bounds of the mantle transition

zone is smooth, whereas other state-of-the-art tomography models in the region invert based on 3-D topography (Tao et al., 2018). This topography is fixed during the inversion, however, the authors note that they do not interpret their model approximately 50km above and below the base of the mantle transition zone.

Related to the above, Koroni et al. (2017) show that travel-times of seismic waves can be decomposed into elastic and topography-induced components. Here I acknowledge that future studies using MC kernel should explore this line of approach. The Axisem-based methodology for calculating topography kernels has been implemented and benchmarked by Colombi et al. (2012) but is yet to be amalgamated as an additional functionality of the MC Kernel software. This will enable means by which to set up discontinuity topography as an additional free parameter during seismic inversion, using the extant TICC tomography workflow (i.e. the workflow used in this study).

Future studies should also account for the modulation of the sensitivity kernel by the source radiation pattern as dictated by the earthquake moment tensor. Currently, while the moment tensor is taken into account during the Instaseis-based cross-correlation measurement process in PyFFProc, moment tensors are fixed as explosions when calculating sensitivity kernels.

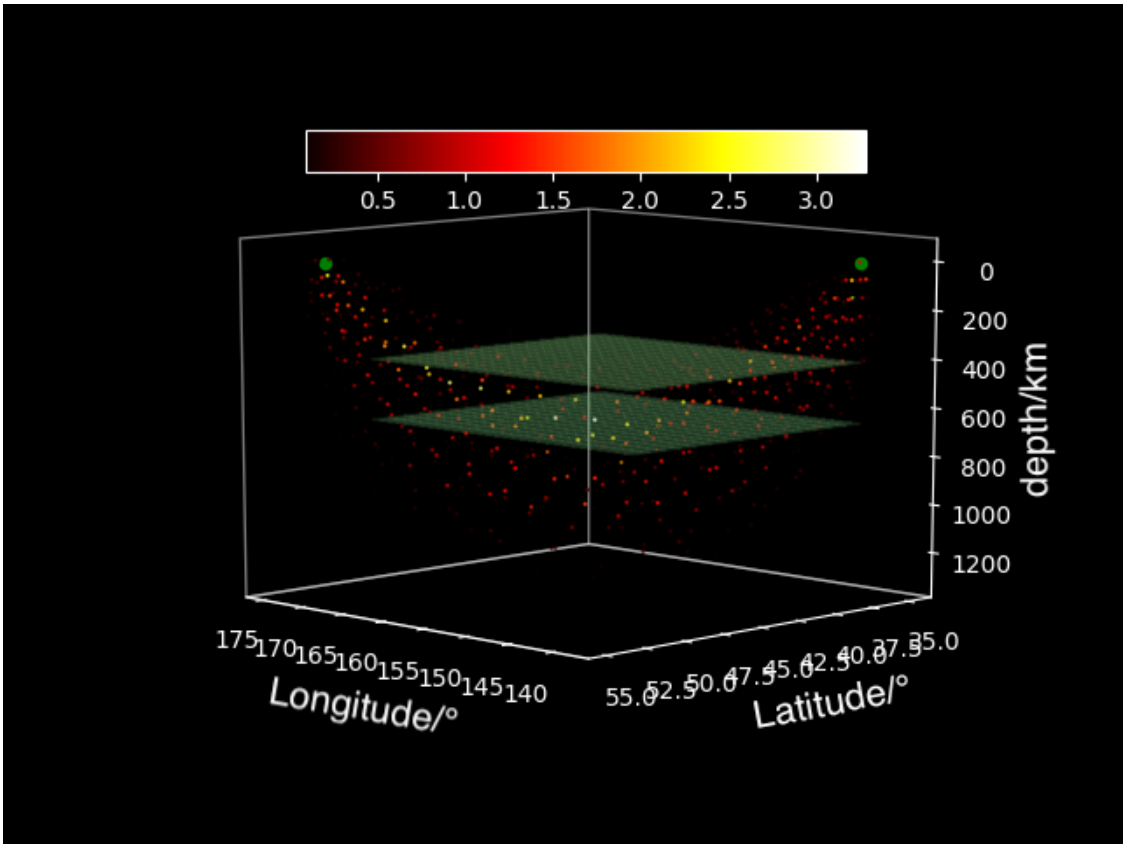

Figure 2.22: A regional MC sensitivity kernel illuminating the mantle transition zone. Visible is peak sensitivity between the 410 and 660km (green sheets).

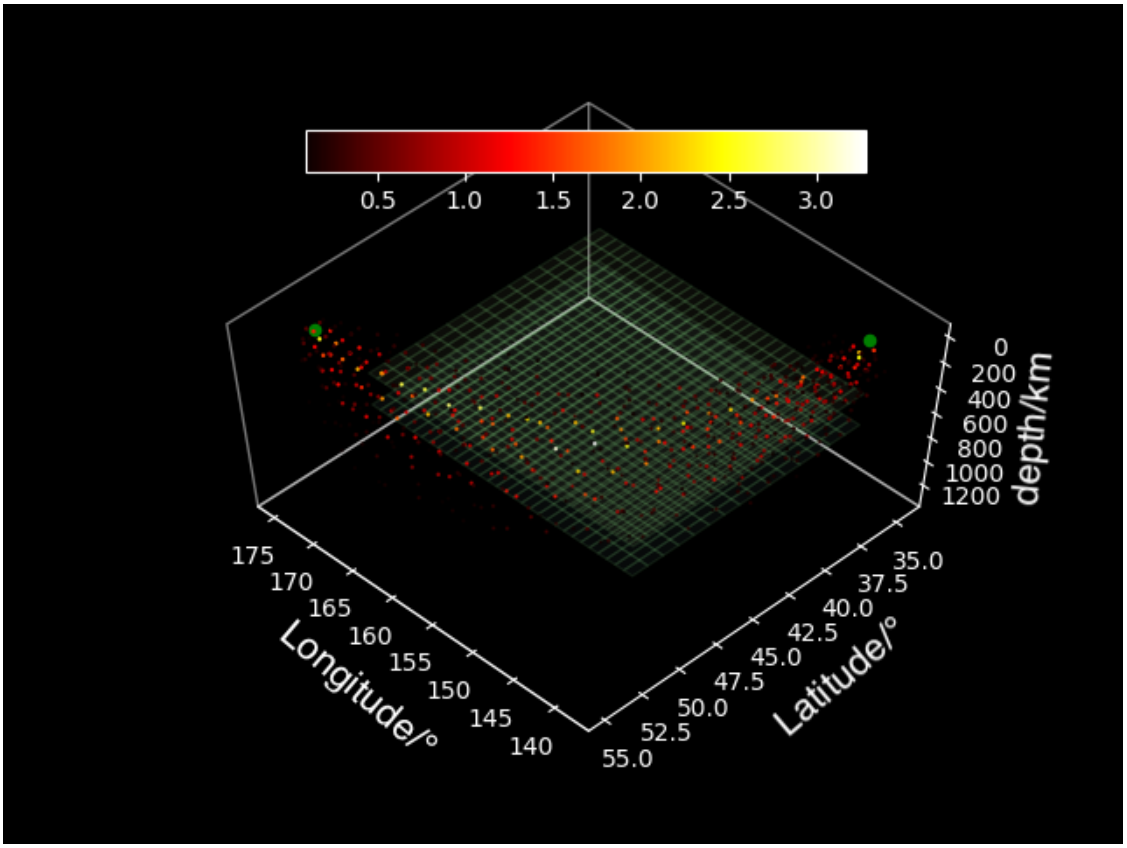

Figure 2.23: A regional MC sensitivity kernel illuminating the mantle transition zone. Visible is peak sensitivity between the 410 and 660km (green sheets). Thus supports the previous figure by showing the kernel from a different vantage point.

Five miles deep,/ on the Japan Trench floor/, the forecast is the same today/ as for the last million years:/ near freezing, cave-black,/ five tons of pressure per square inch.

— Sarah Lindsay's *'Adaptive Behavior' from 'Debt to the Bone-Eating Snotflower'*

3 Tomography

Contents

3.1 Overview **68**
3.2 Common corrections **68**
3.3 Combining paraxial and full waveform sensitivity measurements **70**
3.3.1 Motivation: joint inversion using Dahlen (paraxial) and MC (full waveform) kernels 70
3.4 Setting up the inverse problem **71**
3.4.1 Winnowing of MC Kernel source and receiver values using ray theory 71
3.4.2 Setting up the inverse problem 74
3.4.3 Solving the inverse problem 77
3.4.4 Weighting of different travel-time datasets 81
3.5 Results and visualisation of the JEABOX model **82**
3.5.1 Limitations to the JEABOX model 85
3.5.2 Kuril Trench 99
3.5.3 Japan Trench 99
3.5.4 Izu-Bonin Trench 100
3.5.5 Subduction in the southern hemisphere 106
3.5.6 Taiwan and the southern Ryukyu Arc 107
3.6 Resolution Tests **107**
3.6.1 Overview of workflow 107
3.6.2 Targeted resolution tests 113
3.7 Discussion and Outlook **115**
3.7.1 Japan Trench 115
3.7.2 Kuril Trench 119
3.7.3 Izu-Bonin Trench 120
3.7.4 Possible origins of variable slab dip in the Japanese Islands region 121
3.7.5 JEABOX in the southern hemisphere 121

3.7.6 Depth-dependent contouring of the JEABOX model . . . 122

3.1 Overview

This chapter presents the inversion workflow used in this study to deliver the JEABOX model, a hybrid Dahlen and MC kernel-based finite-frequency P-wave tomography of the western Pacific (with a principal focus on the Japanese Islands and minor focus on Indonesia) based on an amalgamated regional and teleseismic P-wave dataset. This is the first ever Axisem-based seismic tomography.

I start by outlining the steps taken for corrections to cross-correlation travel-time measurements, including corrections for crust, ellipticity and topography. Next I lay out the parameterisation of the inversion grid, before addressing the merging of the new regional P-wave dataset from chapter 2, with an existing teleseismic dataset, based on a western Pacific subset of the DETOX-P1 global model. From here I briefly address the regularisation of the model, before visualising the output of JEABOX. Next I present a limited number of targeted resolution tests for the Japanese Islands and Indonesia subduction zones. I close with suggestions for future resolution testing of a model space that spans all subduction margins in the entire western hemisphere, and propose some tectonic applications for the JEABOX model.

3.2 Common corrections

It is highly unlikely that the magnitude of the multifrequency cross-correlation measurements, as amassed in section 2.4, are solely attributed to the along-path upper mantle seismic heterogeneities, which we seek to resolve. The properties of the crust beneath each station must be taken into account, particularly for the east Asian continent, and especially for the Japanese Islands. For example, the lithology in which the Japanese FNET seismic network is situated, spans more than 250Myr of protracted subduction (Moreno et al., 2016), ranging from

Pliocene sandstone, through to granitic and metamorphosed rocks. Here I outline the steps taken to correct for the effects on the observed travel-times due to the ellipticity of the Earth, its topography and the properties of the crust beneath the receiver, for each measurement.

In some instances, the effects of the crust may dominate the travel time related to the signal of interest. An overview of the procedure implemented here is detailed in section 13.3 of Nolet (2008). In brief, the crust-corrected travel-time is given by differencing the travel-times between the spherically symmetric background model and a given 3D crustal model, over the 3D model local crustal thickness. This differencing is done assuming a vertical trajectory beneath the station

$$\delta t_{crust} = \tau_{3D} - \tau_{BG} \tag{3.1}$$

where τ is given by a sum over crustal segments, such that

$$\tau = \sum \sqrt{1 - p^2 c^2 / r^2} dr \tag{3.2}$$

. Here, c and p denote the velocity and slowness, for crustal corrections according to the crustal model CRUST1.0 (Laske et al., 2013), which bins approximated corrections in 1 degree x 1 degree segments, across the globe.

In addition, cross-correlation delays were measured relative to synthetic seismograms using Instaseis, which were generated in a spherically symmetric background model: thus, measurements must be corrected for the ellipticity of the Earth. We direct the reader to section 13.1 of Nolet (2008) for an overview of this process. The net altitude of the stations (local topography less the station overburden) must also be taken into account. Again, Nolet (2007) shows that the net effect of topography is to modulate the source-receiver epicentral distance by $\delta\Delta$, resulting in a modulation of the original travel time (δt) measurement,$\delta\tau$, such that

$$\delta\tau = \delta t - p\delta\Delta \tag{3.3}$$

where p is the slowness of the ray-theory approximated trajectory, assuming like-for-like slowness over the short lengthscales of the excess topography, relative to the net path.

3.3 Combining paraxial and full waveform sensitivity measurements

3.3.1 Motivation: joint inversion using Dahlen (paraxial) and MC (full waveform) kernels

The finite-frequency travel time seismic tomography workflow presented in this study has been used to good effect on the global scale (Hosseini et al., 2020), in addition to the transcontinental (Mohammadzaheri et al., 2021), continental (Sigloch et al., 2008) and regionally supplemented (Tsekhmistrenko et al., 2021) scales. The corresponding datasets utilised cross-correlation based multifrequency teleseismic travel times and hand-picked P-wave travel times from the ISC-EHB catalogues (Weston et al., 2018), for which P-wave velocity was solved, in a weighted, joint inversion. I build on these workflows by using a combination of full waveform based sensitivity kernels for regional distances, in addition to Dahlen sensitivity kernels and rays based on hand-picked ISC-EHB travel times.

While the study presented here requires full waveform-based sensitivity kernels to incorporate triplicated P-wave measurements, I opted to use a (weighted) joint inversion, in order to complete tomographic resolution, above and below mantle transition zone depths. In addition to amalgamating hand-picked travel times with full waveform-based regional multifrequency P-wave measurements (and sensitivity kernels), I computed Fréchet kernels based on the method of Dahlen et al. (2000a), for source-receiver epicentral distances outside of the anticipated triplicated range. These use ray theory, in tandem with the single scattering (Born) approximation, to express the sensitivity of a finite-frequency measurement. In this context, the sensitivity volume is constructed as the sum of all possible ray trajectories from the source (and trajectories back-propagated from the receiver) to each Born scatterer, in proximity to the ideal, central ray (Dahlen et al., 2000a). I refer to these hereafter as Dahlen kernels and direct the reader to Dahlen et al. (2000a) for an in-depth overview of 'Banana-Doughnut' theory.

In order to calculate the relevant Dahlen kernels for the study region of East Asia and the western Pacific, I use a subset of the multifrequency cross-correlation measurements used to construct the DETOX-P1 global P-wave velocity model created by Hosseini et. al. (2020). In order to select only the most relevant data, I threshold multifrequency measurements from this dataset by source location in the western hemisphere i.e. Flinn-Engdahl region. In addition, measurements for DETOX-P1 were originally performed in eight overlapping frequency passbands from 30.0s to 2.7s, sequentially stepping through in steps of $\frac{1}{\sqrt{2}}$s. Here I only take forward every second passband, resulting in the use of four passbands of 30s, 15s, 7.5s and 3.7s respectively. This approximately contributed an extra **1 million** travel-times to the overall dataset.

3.4 Setting up the inverse problem

3.4.1 Winnowing of MC Kernel source and receiver values using ray theory

It has been well documented in full waveform tomography and adjoint tomography literature that parameterised elements of a given sensitivity kernel, proximal to source and receiver, can present with values up to several orders of magnitude larger/greater than their neighbours. For example, Tape et al. (2007) applied a Gaussian smoothing operator (at sub-wavelength scale with respect to the dominant period resolved by the numerical simulation) to omit large amplitudes near source and receiver. Tao et al. (2018) regularise their posed conjugate gradient algorithm with Gaussian spheres around source and receiver for each earthquake, to mitigate for the very large gradients. Similarly, Nissen-Meyer and Fournier (unpublished) detailed a loss of symmetry between source and receiver. They attributed this to the effects of source radiation patterns and near-field effects, inherent in the synthetic wavefields, upon which sensitivity calculations are based. Here I present the steps used to replace offending elements and a summary of the procedure, which I carried out as a post-processing step after batch calculation of Axisem-based MC kernels for the targeted regional P-wave dataset.

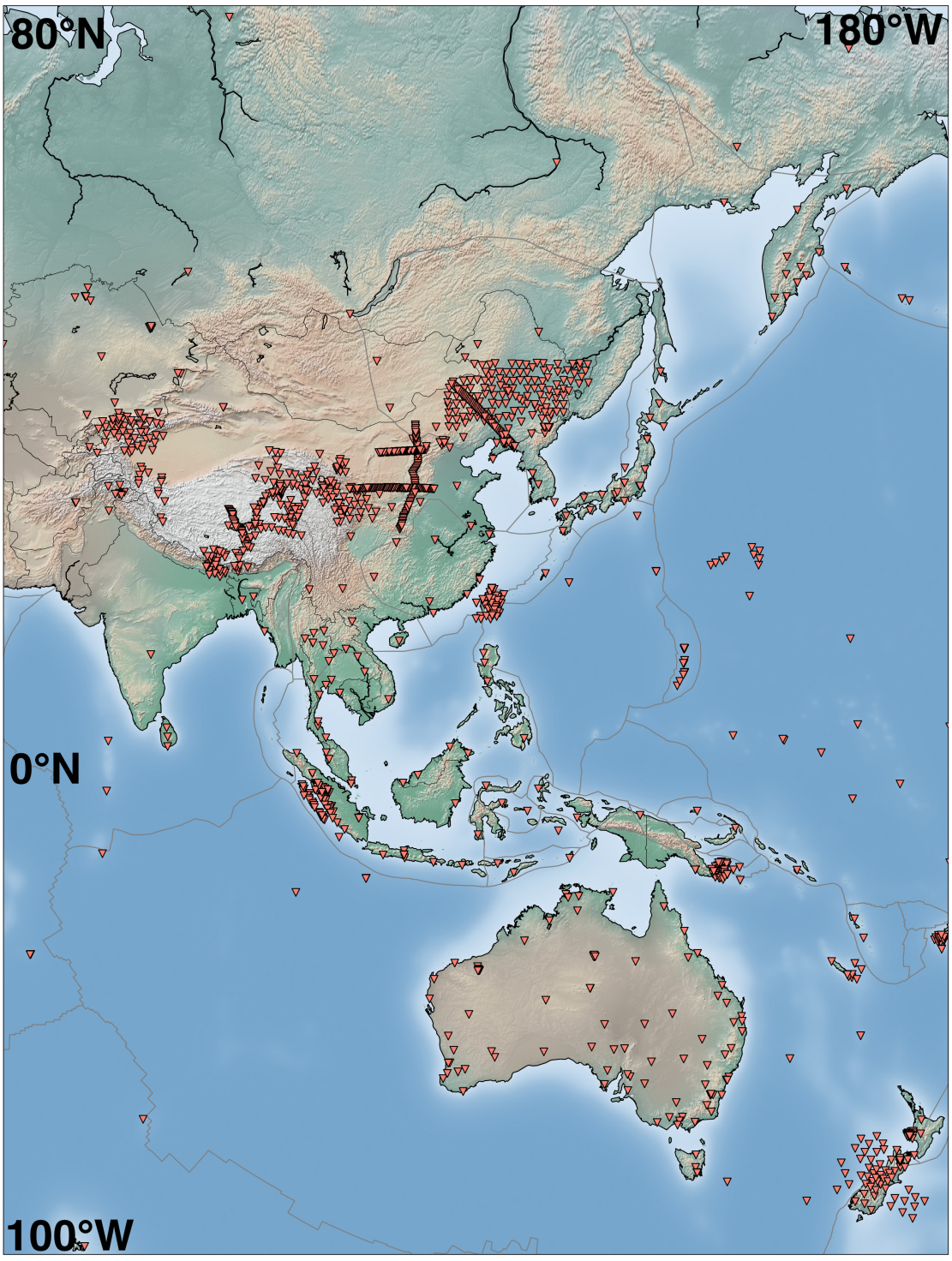

Figure 3.1: Map of the stations used to construct the JEABOX model. Plotted are all seismic stations contained in the multifrequency P-wave cross-correlation travel-time measurements from the western hemispherical subset of the DETOX-P1 model, in addition to the targeted regional P-wave cross-correlation travel-time measurements of east Asia, the Japanese Islands, Phillippine Sea plate and surrounding vicinity. Visible are several isolated stations in the middle of the Philippine Sea plate, and an isolated cluster of stations east of the Izu-Bonin trench, in the Pacific Ocean. It is noted that resolved velocity structures that appear to be artefacts spatially correlate with these stations. Given the coverage-informed meshing procedure used in this study, this may imply a slight overfitting of the JEABOX dataset, in these parts of the inversion grid, where voxel edge lengths can exceed 300km.

Projection of the correct travel time at each vertex of the inversion grid follows a revision of the workflow as described for the Paraxial Dahlen kernels in Dahlen et al. (2000a). For full waveform kernels, only the source and receiver are flagged as singular points.

- The central ray trajectory is discretised between source and receiver at a finite number of nodes in space.
- For each node, the midpoint is set with respect to the previous ray step. From there, the average seismic (P-wave) velocity is calculated over the segment as , where is the seismic velocity at the ith node.
- The distance of the ray node from each singular point is calculated. If the distance is within a user-defined threshold radius (rthresh) (typically 20-50km in a Dahlen kernel context, a placeholder variable is set as 50km.
- The position of the scatterer in the quadrature plane (the disk which bounds all possible detour times at a given point on the central ray and whose size is within the Fresnel zones of interest). This step is defunct for ray theory: by definition, the scatterer's position lies at the centre of the disk, on the central ray.

At this point, the sensitivity matrix , is populated by

- Finding the tetrahedron of the inversion grid which bounds the ray node under consideration
- Retrieving the tetrahedron's four spatial node interpolation coefficients, each corresponding to a vertex, and projecting appropriately. I direct the inclined reader to chapter 12.2 of Nolet (2008) for a summary of local parameterisation.

For each vertex, a weighted ray-theory sensitivity kernel value (i.e. a travel time) is assigned.

3.4.2 Setting up the inverse problem

Equation 3.3 expressed the travel time measurement as the product of the sensitivity kernel with the model parameters. This relation holds independent of whether kernels are calculated based on the full waveform, using the method of Dahlen et al. (2000a), or the infinite frequency approximation. Generalising the link between the data and model parameters takes the form (Tsekhmistrenko, 2019)

$$d_i = \int_V K_i^T(r) m(r) d^3r \tag{3.4}$$

where m(r) is the parameterised model on what is hereafter referred to as the inversion grid. This can be expressed as

$$m(r) = \sum_{j=1}^{M} m_j h_j(r) \tag{3.5}$$

where the model is defined at j many locations and h(j) are the appropriate basis functions to project from continuous to the discrete model space. In this study I use a data-driven meshing process based on the *DistMesh* (Persson & Strang, 2004) and *Quickhull* (Barber et al., 1996) software packages in MATLAB. This produces a spherical mesh of tetrahedra, whose tetrahedral density is informed by seismic coverage. Regions with better seismic coverage present with tetrahedra with smaller edge lengths with respect to regions of poor seismic coverage. This reduces the number of unknown model parameters for which to solve during seismic inversion globally, while also allowing for a sufficiently densely parameterised targeted study region. The mesh is of radius 6421km to ensure that the Earth's surface is encased by the tetrahedra. The initial mesh exhibits a homogeneous edge length of 200km before it undergoes iterative densification in regions with a large number of seismic sources and receivers. Here, this results in an inversion grid with 51,600 nodes (also referred to as vertices), with a shortest edge length of roughly 70 km in areas of peak seismic coverage.

The numerical discretisation of m(r) in equation 4.5 allows equation 4.4 to be rewritten as

$$d_i = \sum_{j=1}^{M} m_j \int_V K_i^T(r) h_j(r) d^3r \tag{3.6}$$

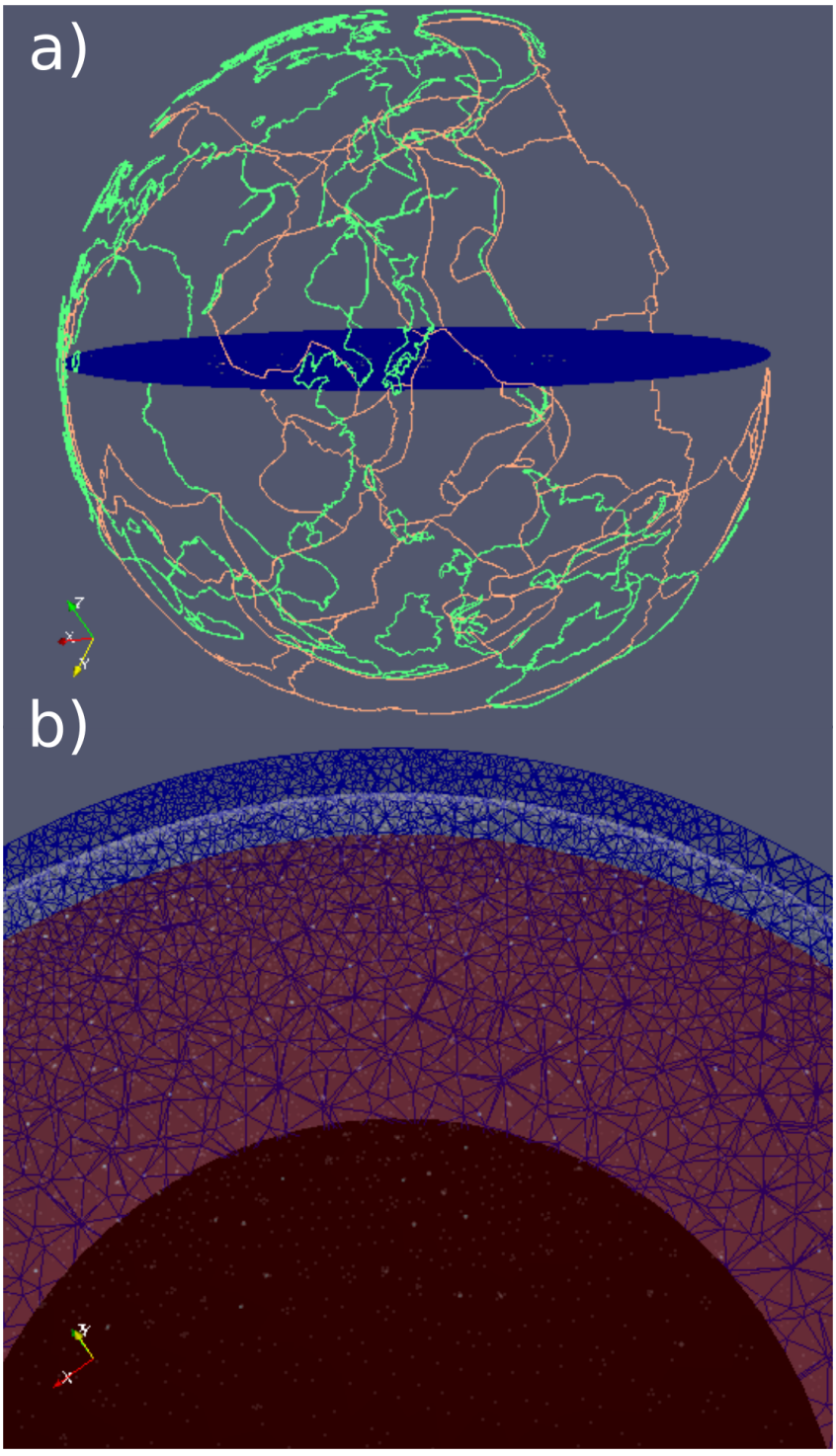

Figure 3.2 Slice of coverage and seismicity-informed mesh through a dense region of the inversion grid.

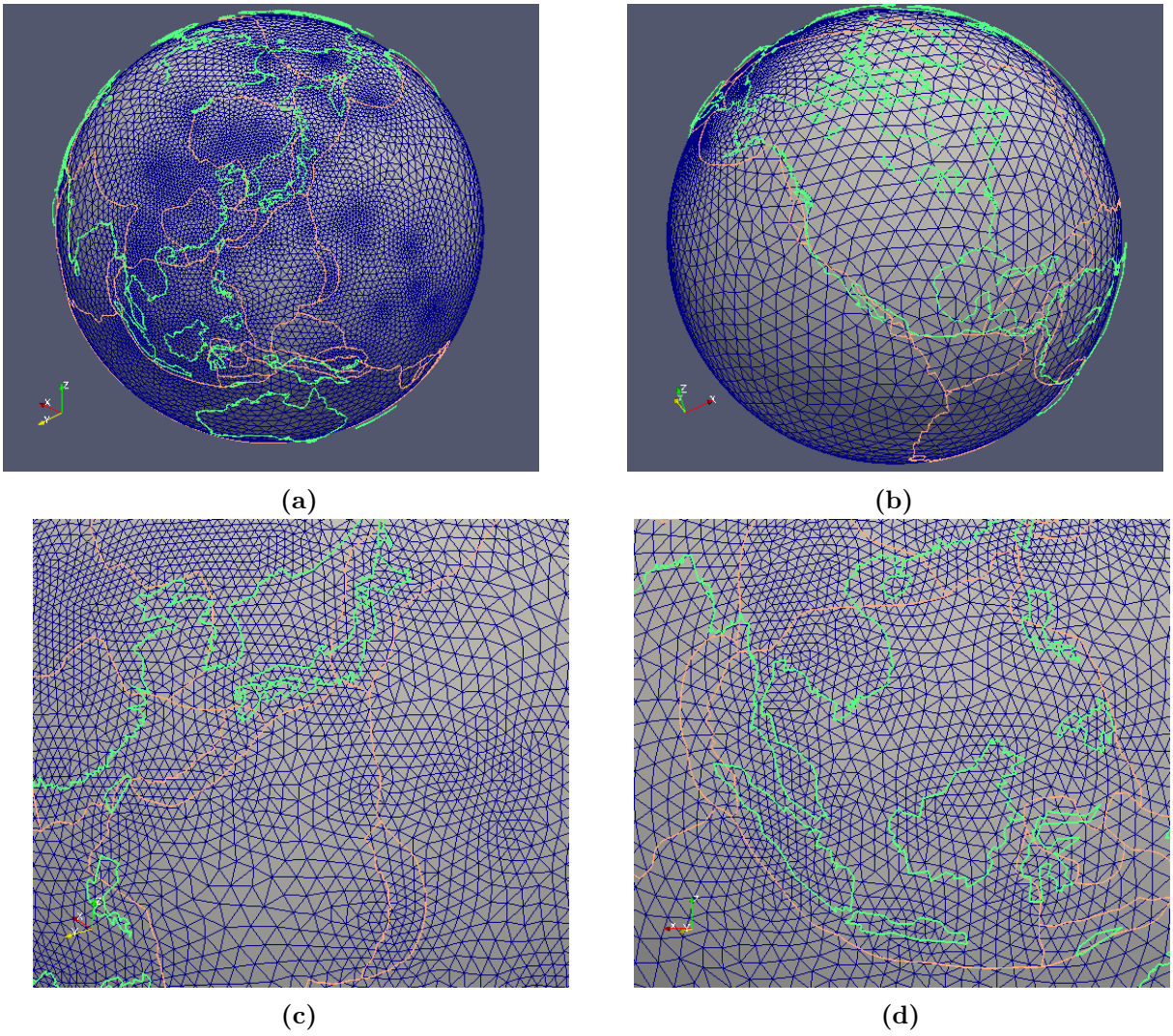

Figure 3.3: Sample of sparse and dense regions of the JEABOX inversion grid. a) Japan (dense) b) USA (sparse) c) Inset of densely sampled Japanese Islands region d) Modestly sampled southern hemisphere, Indonesia through Borneo.

. All sensitivity kernels (i.e. Axisem-based MC kernels and Dahlen kernels) used in this inversion are similarly projected on the inversion grid, such that all kernels can be represented together in a single sensitivity matrix,

$$G_{ij} = \int_V K_i^T(r) h_j(r) d^3r \tag{3.7}$$

resulting in

$$d_i = \sum_{j=1}^{M} G_{ij} m_j \tag{3.8}$$

Even though I seek to produce a model of a targeted region including, east Asia, the Japanese Islands and western Pacific, the model space is meshed globally in

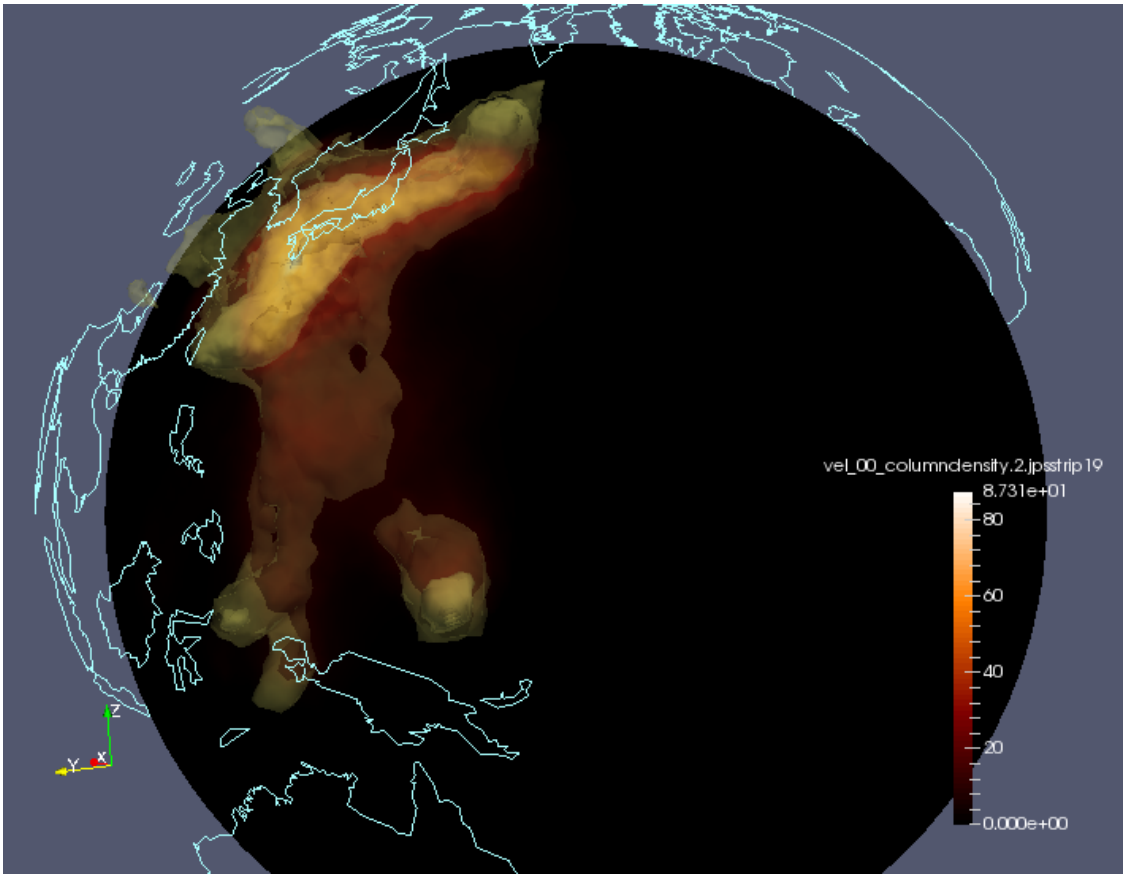

Figure 3.4 Kernel coverage supplemented by regional P-wave travel-time measurements and their sensitivity measurements using MC Kernel.

this workflow, which should mitigate for artefacts arising from boundary conditions (Tian et al., 2009).

3.4.3 Solving the inverse problem

The aim of seismic inversion is to produce a model solution of deviation of P-wave seismic velocity ($\frac{dVp}{Vp}$) from the reference background model that adequately fits the dataset whilst presenting spatial distributions of seismic velocity that conform with our understanding of regional plate tectonics and upper mantle processes. Because the number of data, N, vastly exceeds the number of model unknowns, M, ($N \gg M$) there is no model solution that fits every datum exactly. The system is overdetermined and a regularised solution must be sought. The inversion workflow

used in this study follows in broad, the least squares inversion scheme laid out in Nolet (2008), by considering a discrete model relationship between data (travel-times, amassed from cross-correlation of triplicated and teleseismic P-wave waveforms), **d** and model (P-wave velocity), **m**. Additional unknowns were introduced to the model vector to account for measurement corrections (hypocentre location, origin times and additional corrections for structure beneath receivers not accounted for by reference-model based crustal corrections).

$$\mathbf{G_1 m_1} + \mathbf{G_2 m_2} = \mathbf{Gm} = \mathbf{d} \tag{3.9}$$

$\mathbf{m_1}$ denotes model parameters corresponding to seismic velocity at each node in model space i.e. the inversion grid, with $\mathbf{m_2}$ the corollary parameters for station and event corrections. For M_1 model parameters and M_2 measurement corrections, this results in a system comprised of $M_1 + M_2 = M$ unknowns and N many data equations. When attempting to solve this system, the following must be considered:

- **Dependency between measurement rows**. A consequence of unavoidable errors in the measurements is that the system possesses no exact solution.
- **Subjective regularisation of solutions**. Small, unquantified errors, unaccounted for in data, **d**, can result in large errors in the model, **m** (Nolet,2008).

To enable regularisation the workflow applies both norm damping and smoothing. Equation 3.8 then becomes in practice (Hosseini, 2020)

$$\begin{pmatrix} C_d^{-\frac{1}{2}} d \\ 0 \\ 0 \end{pmatrix} = \begin{pmatrix} C_d^{-\frac{1}{2}} G \\ \epsilon_n I \\ c_m^{-\frac{1}{2}} \end{pmatrix} m \tag{3.10}$$

where C_d is the data covariance matrix, ϵ_n is a toggle on the extent of norm damping applied, $c_m^{-\frac{1}{2}}$ is a smoothing matrix and ϵ_s is the multiplier applied to the smoothing matrix. Here, the definition of norm damping is the introduction of artificial data with values very close to zero. This operates as a bias to direct the model solution towards the reference background model. In an effort to adequately explore the model space, a typical inversion cycle solves for a set of model solutions using a fixed

norm damping to smoothing ratio, with an increasing magnitude of regularisation applied for each successive solution. This exploration of model space becomes in essence a trade-off between the misfit of the model to the data and the roughness of the model i.e. the model L2-norm.

The misfit of observed travel times to the sensitivity kernel model product, equivalent to the predicted data (Hosseini, 2020) can be related to the misfit, and can be written as (Tian et al., 2009)

$$\frac{\chi^2}{N} = \frac{1}{N}\sum_{i=1}^{N}\Big(\frac{d_i - \sum_j K'_{ij} m_j}{\sigma_i}\Big)^2 \tag{3.11}$$

. Ideally, $\frac{\chi^2}{N} \approx 1$, with the targeted objective that data must be fit a defined range of 2σ uncertainty (Tian et al., 2009). In practice, I consider a fit of two thirds of all data within an average of 2σ uncertainty (i.e. two standard deviations) as adequate, in line with previous studies, although inversion performance is generally better than this guideline target. The model L2-norm is written as

$$||Gm - d||_2^2 \tag{3.12}$$

Having obtained a travel time sensitivity kernel for each multifrequency cross-correlation measurement, I solve the inverse problem $\mathbf{d} = \mathbf{Gm}$ using the tried and tested LSQR algorithm of (Paige and Saunders, 1982). During each exploration of model space using different norm damping and smoothing multipliers, 5000 iterations of LSQR take place to ensure that the model adequately converges.

Exploration of model space is a twofold process. The first step entails a crude inversion for seismic velocity, event hypocentre corrections, earthquake origin time corrections and tightly constrained source depth corrections, applying negligible regularisation. This is with the intention of removing outlying data from the dataset. Here I consider outliers to be those data which lie more than three standard deviations outside the general distribution. The second step is the aforementioned exploration of model space using increasing norm damping and smoothing multipliers. This has the effect of reducing the model norm, a proxy for roughness or complexity,

at the cost of increasing misfit of the data.

The second step examines the tradeoff between model roughness against misfit to construct a regularisation curve, or 'L-curve'. Equation 3.11 shows that misfit is inversely proportional to the magnitude of the standard measurement errors, σ, as highlighted in Nolet (2008). An error was assigned to each multifrequency measurement during the cross-correlation process. In an ideal scenario, where a perfect estimation of measurement uncertainty for each datum is obtained, the reduced misfit measure, $\frac{\chi^2}{N}$, would be exactly 1. This is highly unlikely for real earth datasets. Even a 10% underestimation or overestimation for σ_i, where i denotes the ith datum would result in an overestimation of 19%, or underestimation of 21%, respectively, for that individual measurement. Nolet (2008) advises that the final choice of tomography model should be within 20-30% of the target reduced χ^2_{red} of 1. It is in this context that I constructed regularisation curves, whose inflection points are expected to be close to 1 as a guide.

Figure 4.5 shows a regularisation curve, with model L-2 norm, a proxy for model roughness, plotted against the reduced model misfit. The dashed line. From here, if one chooses a slightly or less damped and smoothed solution on the vertical leg of the regularisation curve, it is observed that model complexity increases markedly, with nominal reduction in misfit. The expectation is that the visual appearance of the model will show grainy, short-wavelength features, implying that fitting more of the poorer quality data, or noise in the data, can only be achieved at the cost of high model complexity. This, inevitably, is undesirable as there is a significant underestimation of measurement uncertainty. Conversely, choosing a model solution far along the horizontal leg of the regularisation curve, where norm damping and smoothing parameters are much higher, is also undesirable. The solution presents as excessively smooth with an underfitting of the aggregate dataset, and an overestimation of errors. A viable, albeit subjectively chosen model, is one where a reduction in model complexity is observed, with a modest

reduction in L-2 norm, and a χ^2_{red} in the range of 0.7-1.3. This study chooses a solution with misfit value of 0.8, solution 8.

3.4.4 Weighting of different travel-time datasets

Given that the overall purpose of this study is to improve tomography resolution in the upper mantle, with a particular emphasis on the mantle transition zone, using regional body waves, I seek to maximise the information gain provided by the targeted regional P-wave travel-time dataset and sensitivity kernel bank. Given that the sum total of Axisem-based regional P-wave kernels is a factor of 10 smaller than the number of Dahlen kernels and is a similar factor smaller than the number of supplementing ISC travel-time picks, I opt to slightly bias the inversion scheme towards fitting the smaller, regional P-wave dataset, by upweighting the data. Relative data weighting is a subjective process, although it has been used to good effect in previous tomography studies using a variety of complementary datasets. Golos et al. (2018) performed shear wave tomography beneath the United States using both surface and body waves, the former of which provide peak coverage in the upper mantle, whilst body waves provide strong teleseismic illumination throughout the mid-lower mantle. Here I argue that the datasets presented in this study offer a similar benefit. Regional P-waves provide seismic illumination of the mantle transition zone, whilst Dahlen kernels provide more than adequate sensitivity at teleseismic distances. In addition, when calculating Axisem-based MC kernels, I extended the epicentral distance threshold for this procedure out to 50° such that there is mutual overlap between the regional and teleseismic datasets (the latter of which contains data from 32-85° epicentral distance). It is important to note that there is a risk of overfitting a given dataset if upweighted too much. During prototype inversions of this dataset, evidence that this was occurring was signified by a predominance of resolved velocity structure confined solely to the upper mantle. This does not conform to the expected model when data has been input across the entire teleseismic distance range from finite-frequency Dahlen kernels and ISC-based travel-times. In this study, I made the decision to upweight

the regional P-wave and Axisem-based MC kernel dataset by a factor of 2 relative to the rest of the data. In practice this means that two data from the regional P-wave dataset ought to be fit for every 1 datum from the Dahlen and ISC datasets. This comes at the cost of raising the relative contribution of these latter two datasets to the overall data misfit, $\frac{\chi^2}{N}$. This bore out visually in the final set of JEABOX models as the retention of resolved velocity structure in the mid-mantle, whilst sharpening the resolved features in the mantle transition zone.

3.5 Results and visualisation of the JEABOX model

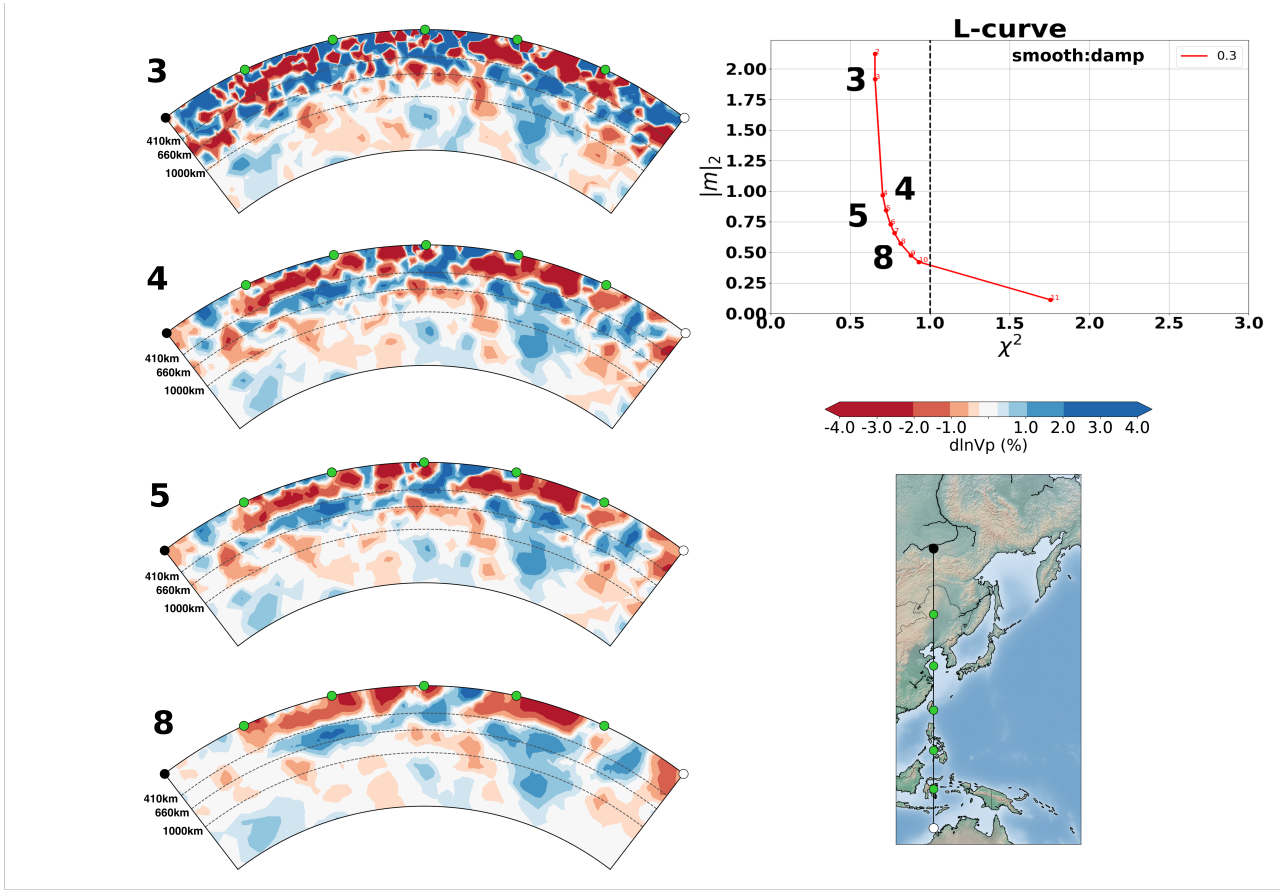

Figure 3.5: Misfit:roughness (resolution) curve for the JEABOX model. Also shown are spatially equivalent model slices for different regularisation parameters. Under-regularised models present as grainy due to the overfitting of noise. I chose solution number eight, beyond which the model changes little in appearance for a significant cost in model misfit.

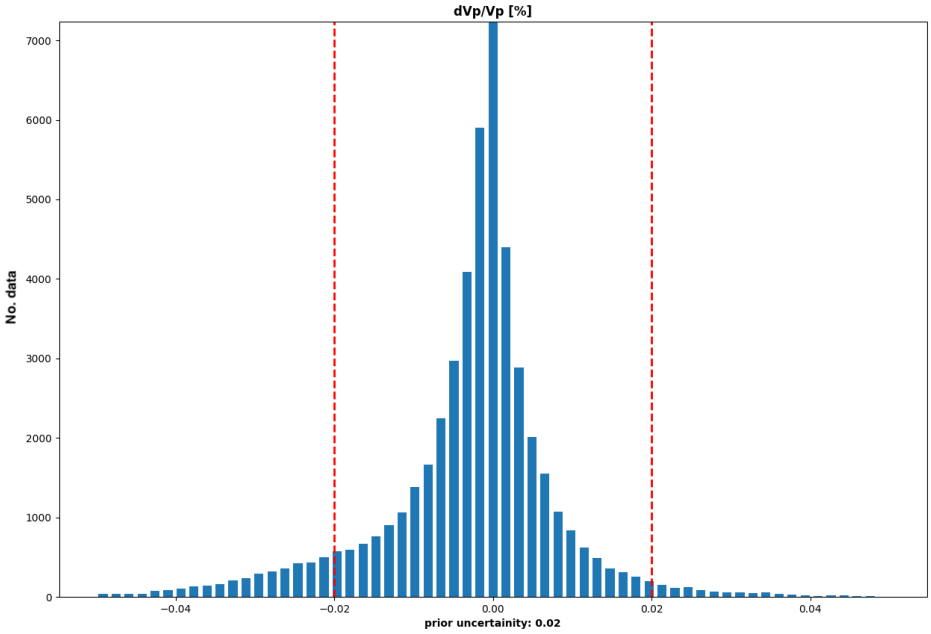

Figure 3.6: Posterior velocity distribution for the JEABOX model. Red dashed lines contain the 2-σ confidence bounds.

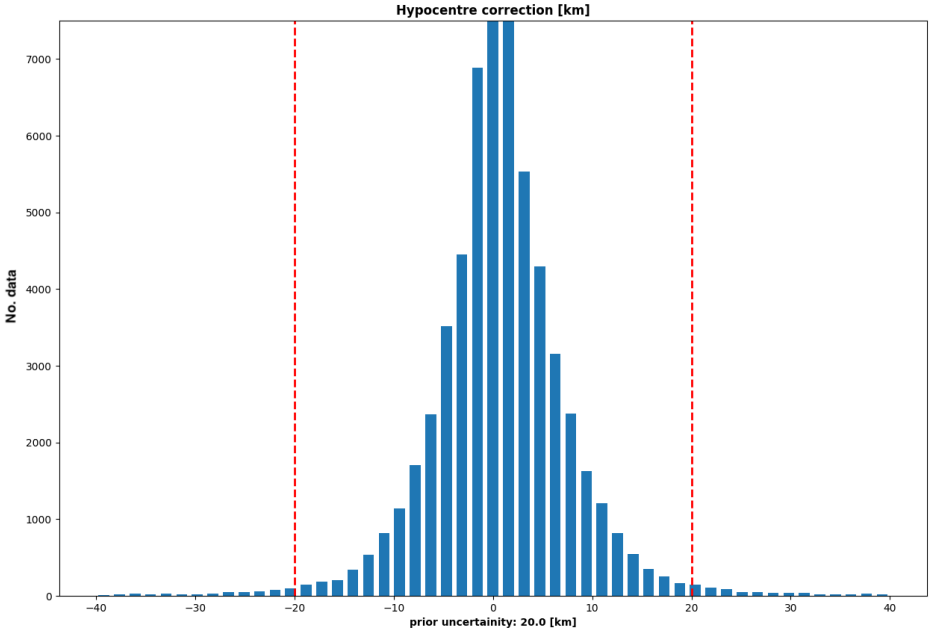

Figure 3.7: Posterior lateral hypocentre distribution for the JEABOX model. Red dashed lines contain the 2-σ confidence bounds.

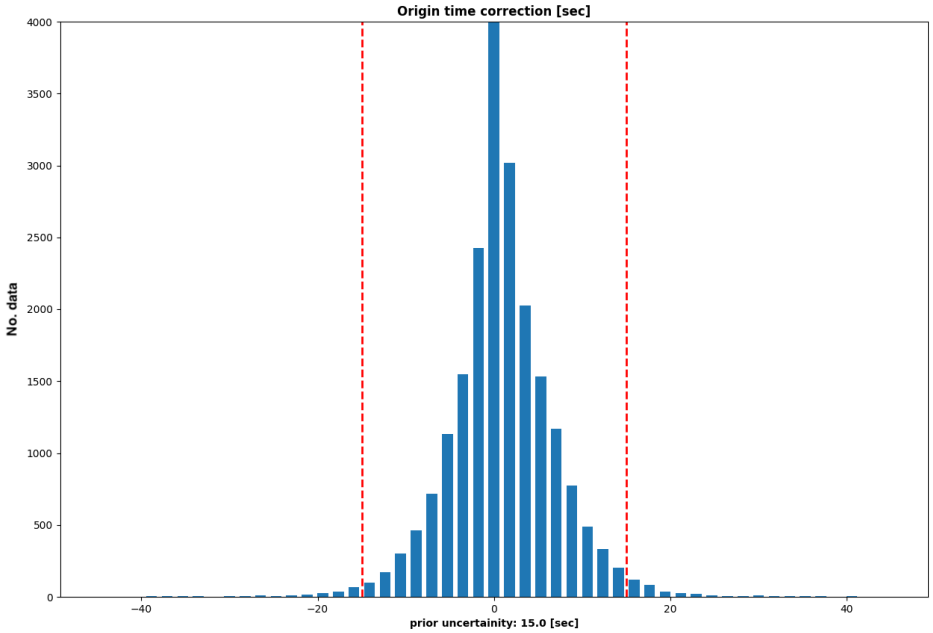

Figure 3.8: Posterior earthquake origin time distribution for the JEABOX model. Red dashed lines contain the 2-σ confidence bounds.

What follows in this section is an overview of the JEABOX P-wave model of the upper mantle, mantle transition zone and deeper to a maximum depth of 1200km. Here I present targeted cross-sectional slices and depth sections of a suite of subduction zones across the western Pacific, extending from the Kuril trench in the north, right through to Borneo in the southern hemisphere. These sections are colour-coded logarithmically. I have also included a panoply of wide slices of the JEABOX tomography in the appendix of this thesis, trending both south-to-north and east-to-west. SubMachine (Hosseini et al., 2018) cross-sections are also included in the appendix for reference, although I note that it is difficult to compare with other models, because they produce different amplitudes and are calculated on different inversion grids.

3.5.1 Limitations to the JEABOX model

It is worth noting that while western Pacific is the most seismically dense region on earth, there are still limitations to the seismic coverage, which are borne out in this

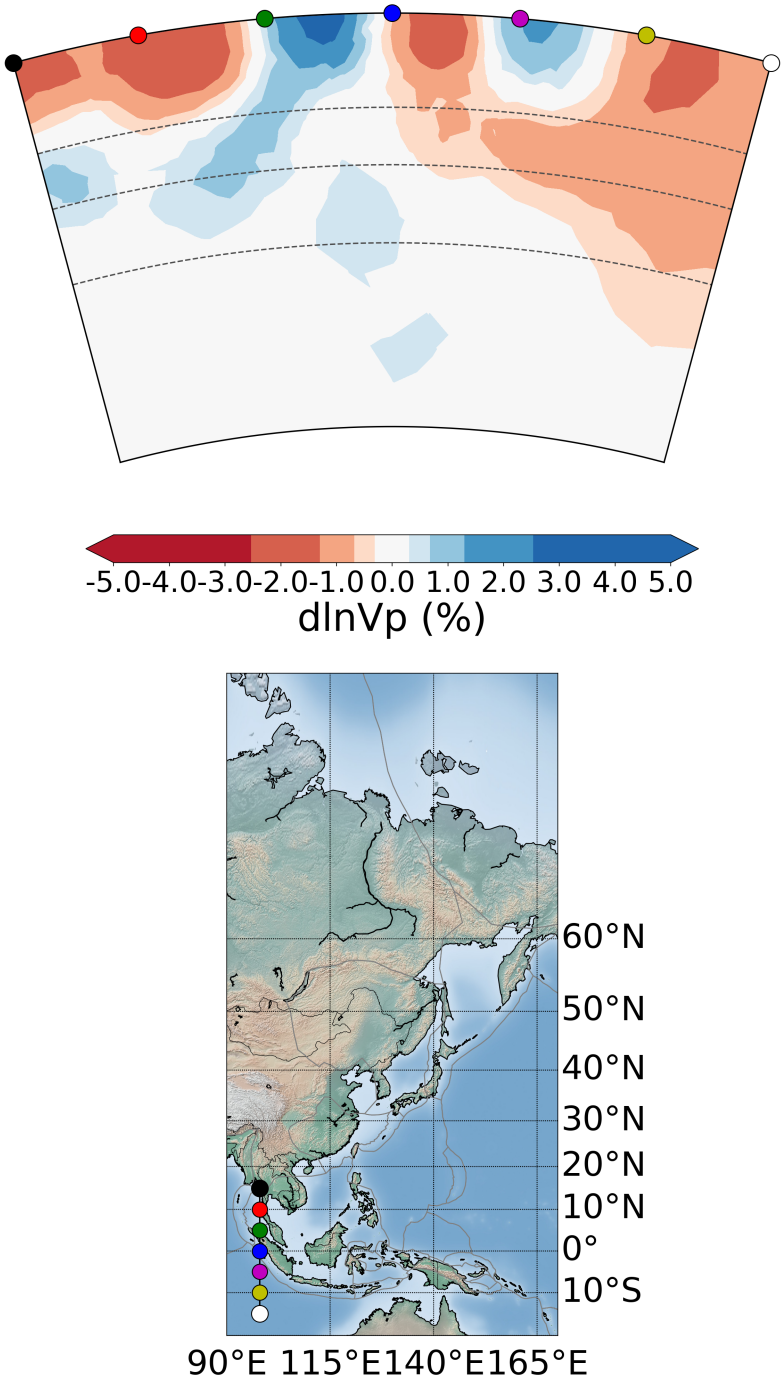

Figure 3.9: Targeted cross-sectional slice (N-S) of the JEABOX tomography model in the southern hemisphere, through Aceh.

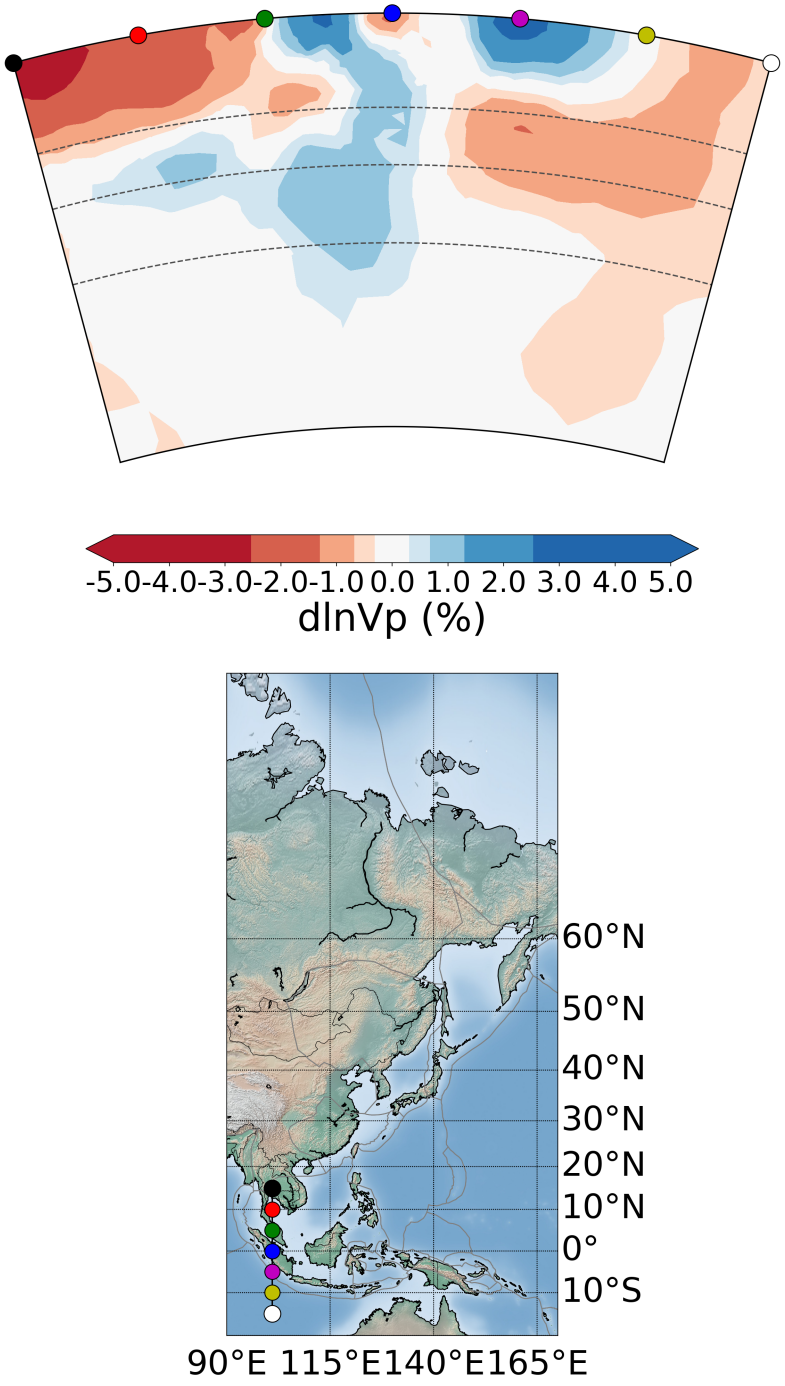

Figure 3.10: Targeted cross-sectional slice (N-S) of the JEABOX tomography model in the southern hemisphere, through west Sumatra and Malaysia.

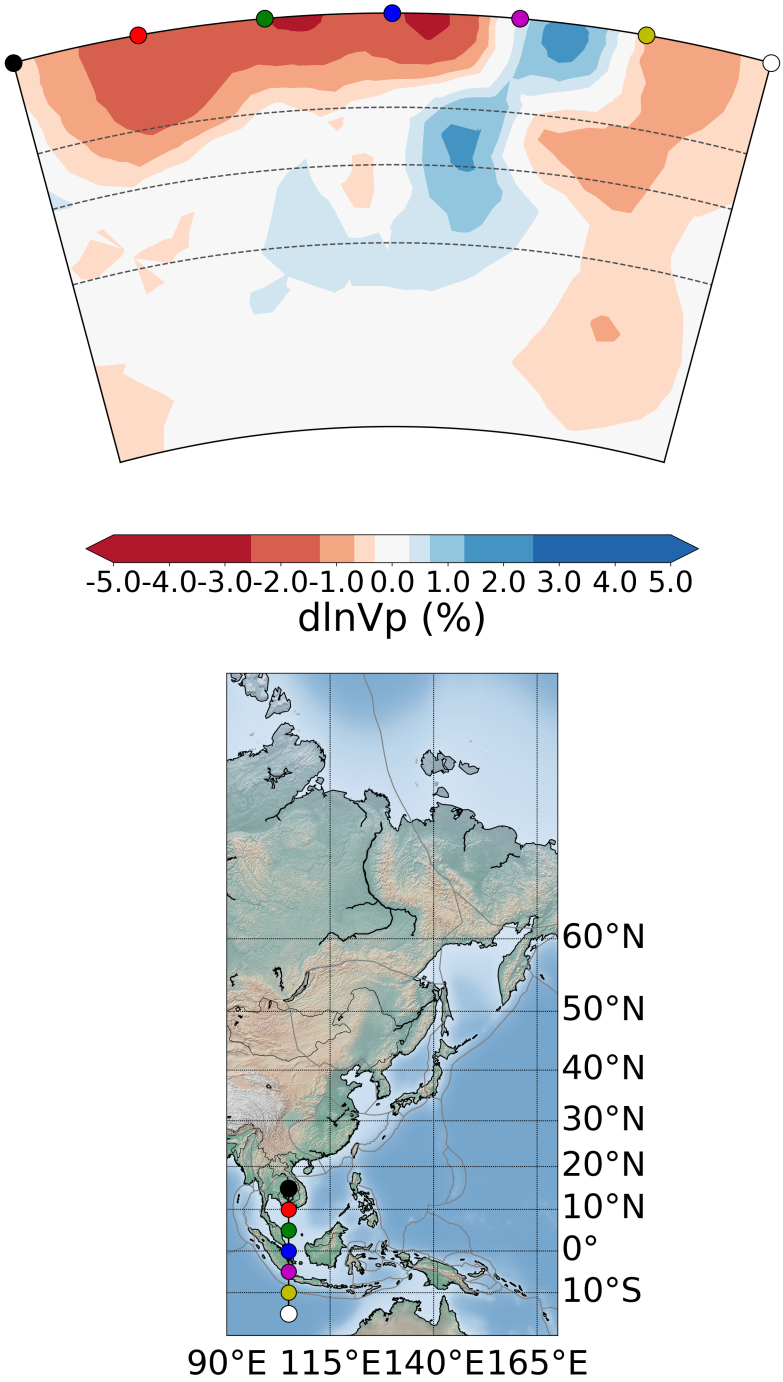

Figure 3.11: Targeted cross-sectional slice (N-S) of the JEABOX tomography model in the southern hemisphere, through south Sumatra.

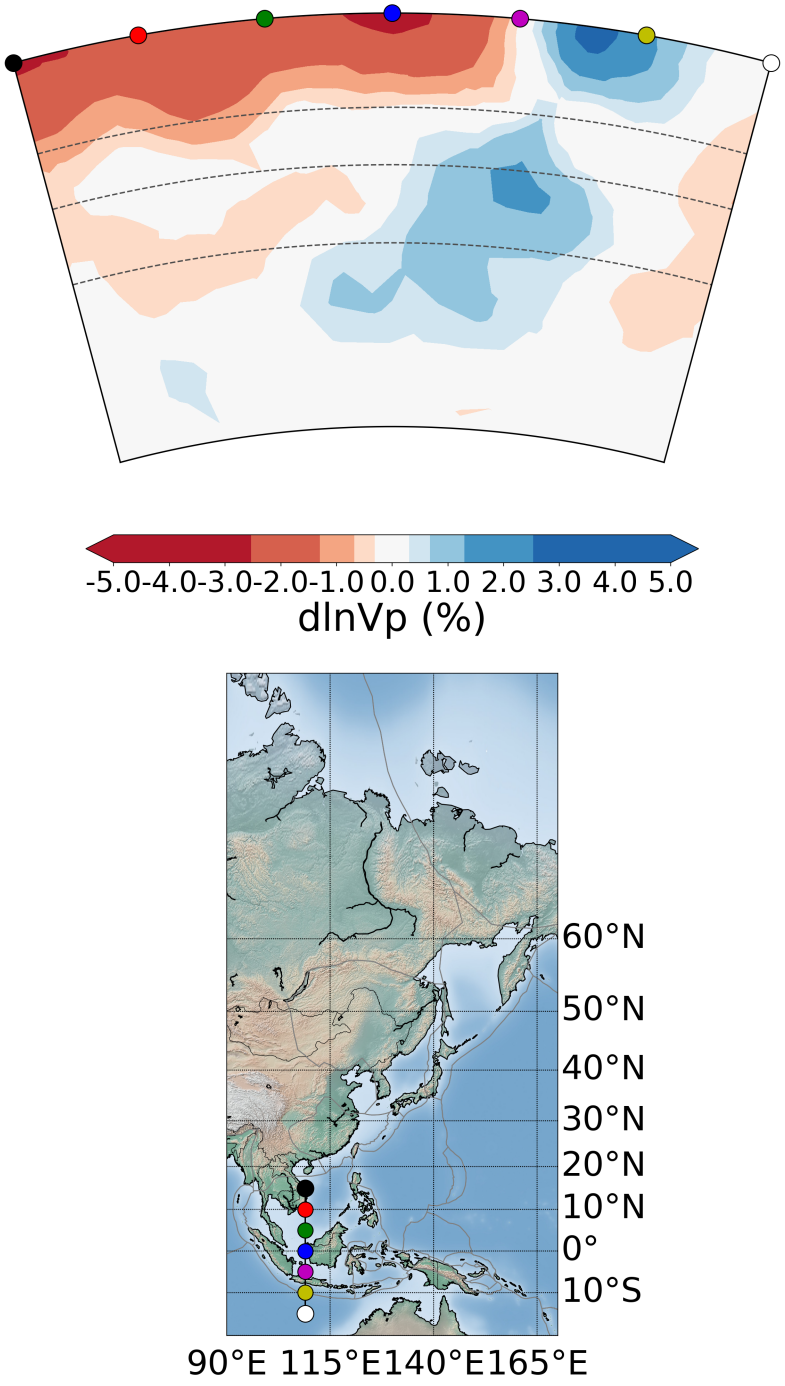

Figure 3.12: Targeted cross-sectional slice (N-S) of the JEABOX tomography model in the southern hemisphere, through west Java and west Borneo.

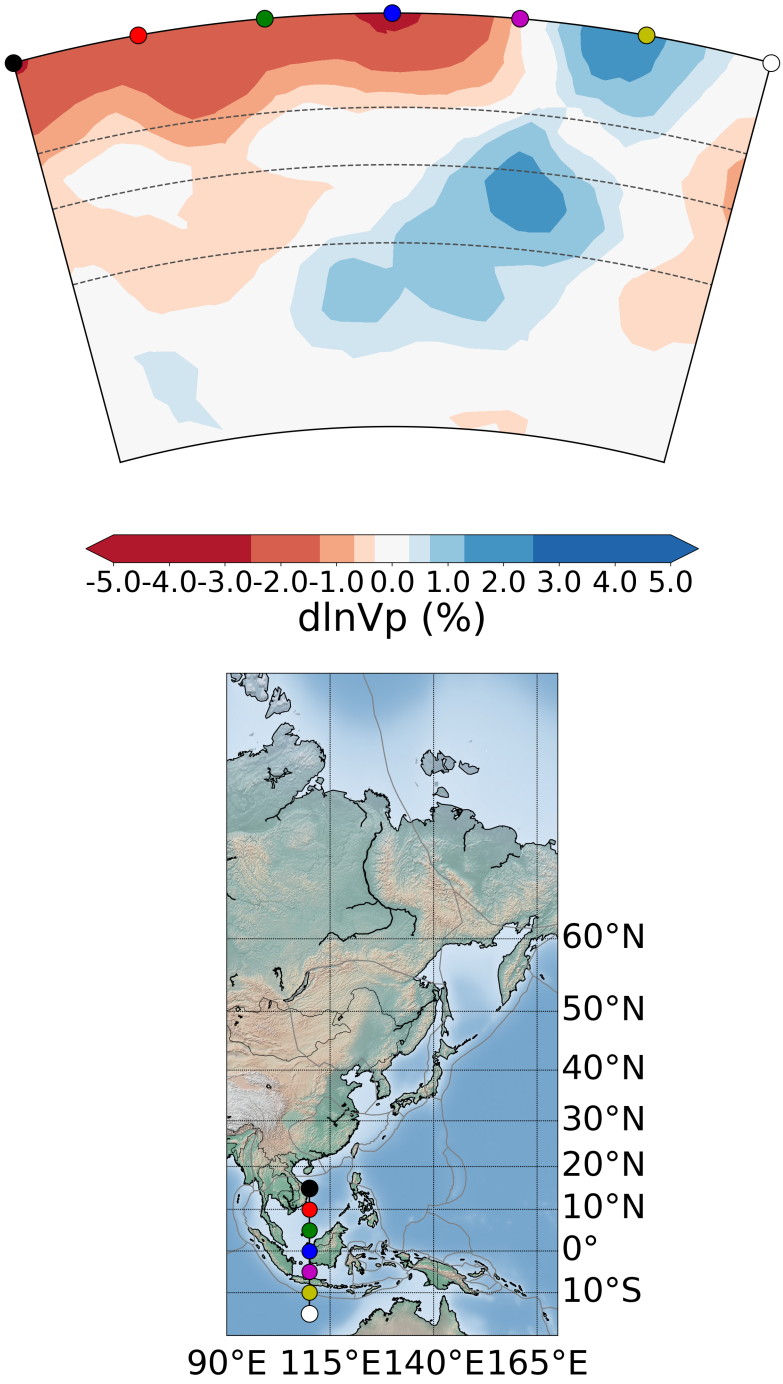

Figure 3.13: Targeted cross-sectional slice (N-S) of the JEABOX tomography model in the southern hemisphere, through west Java and west Borneo, 1 degree in longitude to the east of the previous figure.

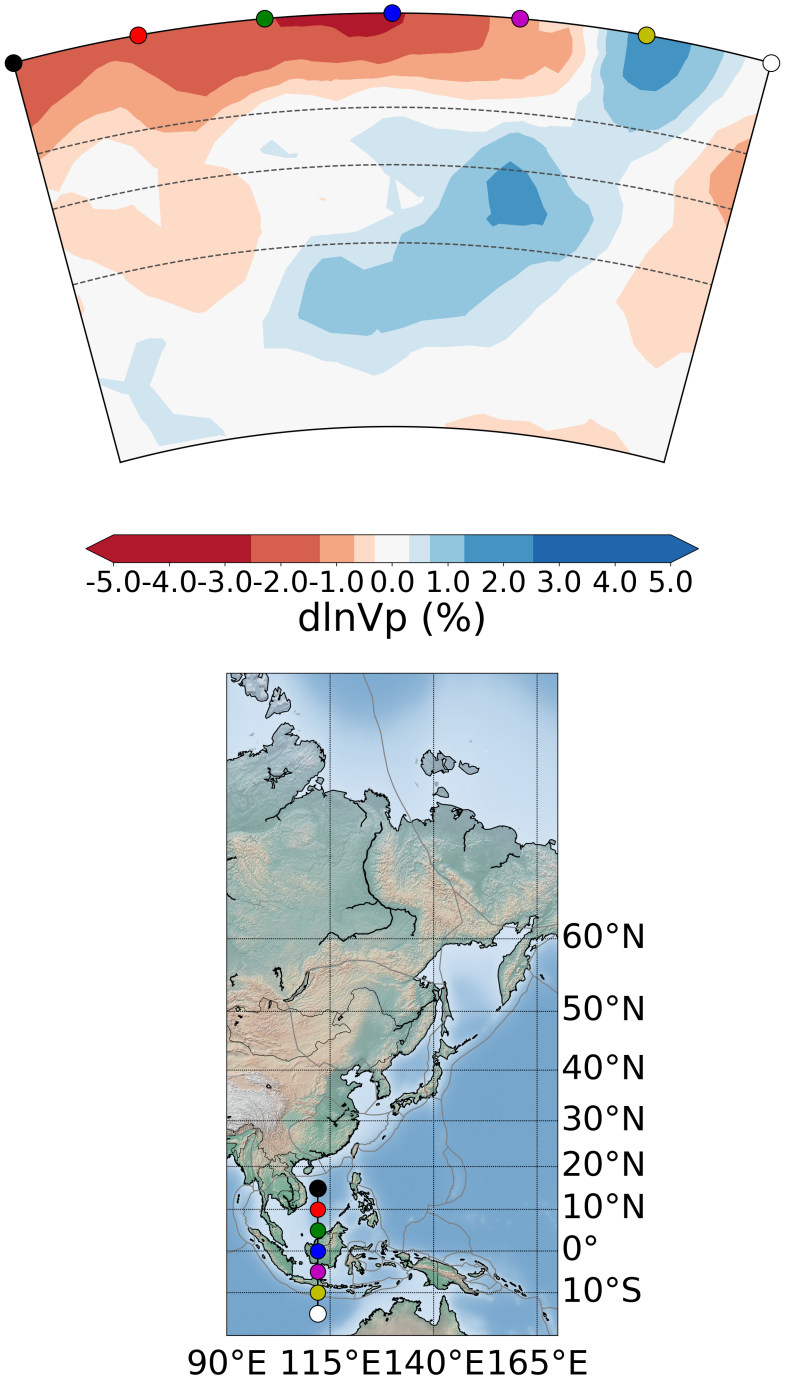

Figure 3.14: Targeted cross-sectional slice (N-S) of the JEABOX tomography model in the southern hemisphere, through west Kalimantan and east Java.

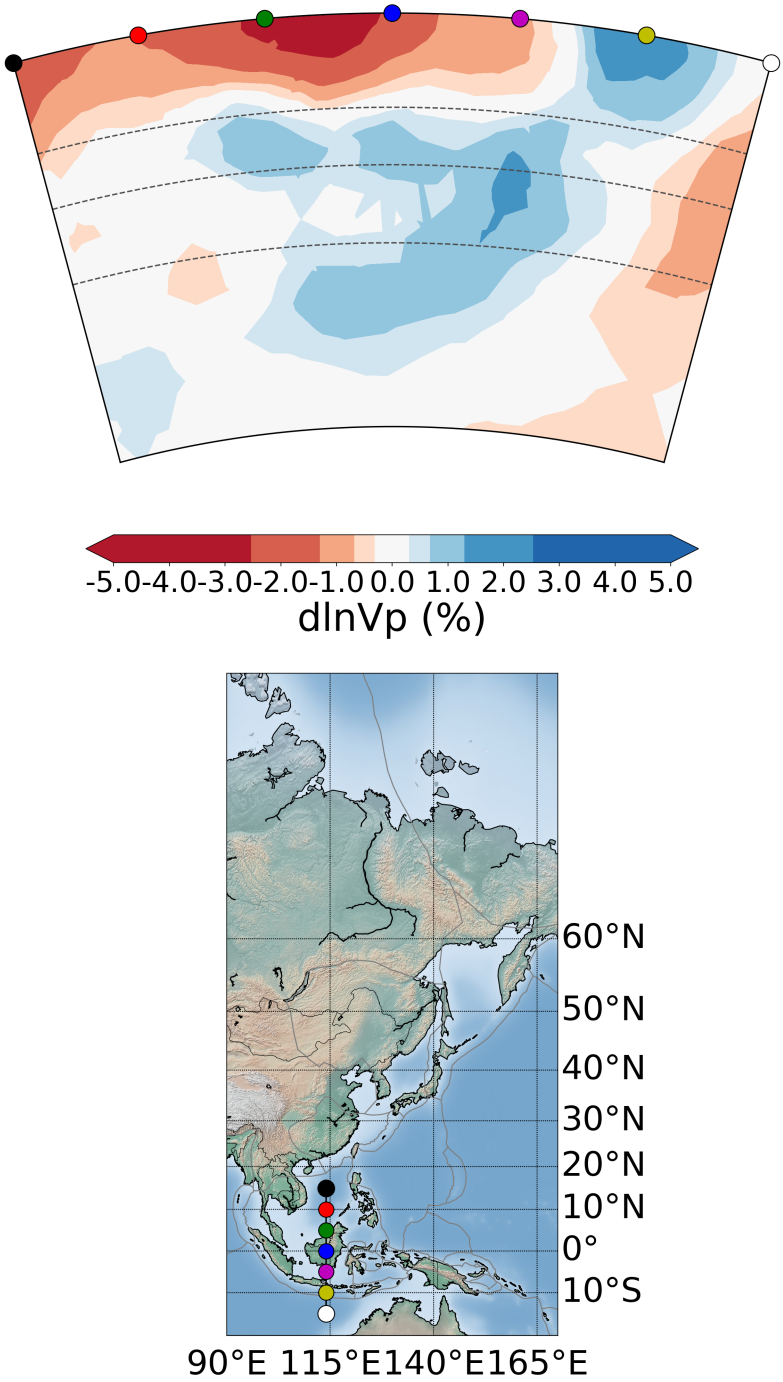

Figure 3.15: Targeted cross-sectional slice (N-S) of the JEABOX tomography model in the southern hemisphere, through Bali and central Kalimantan.

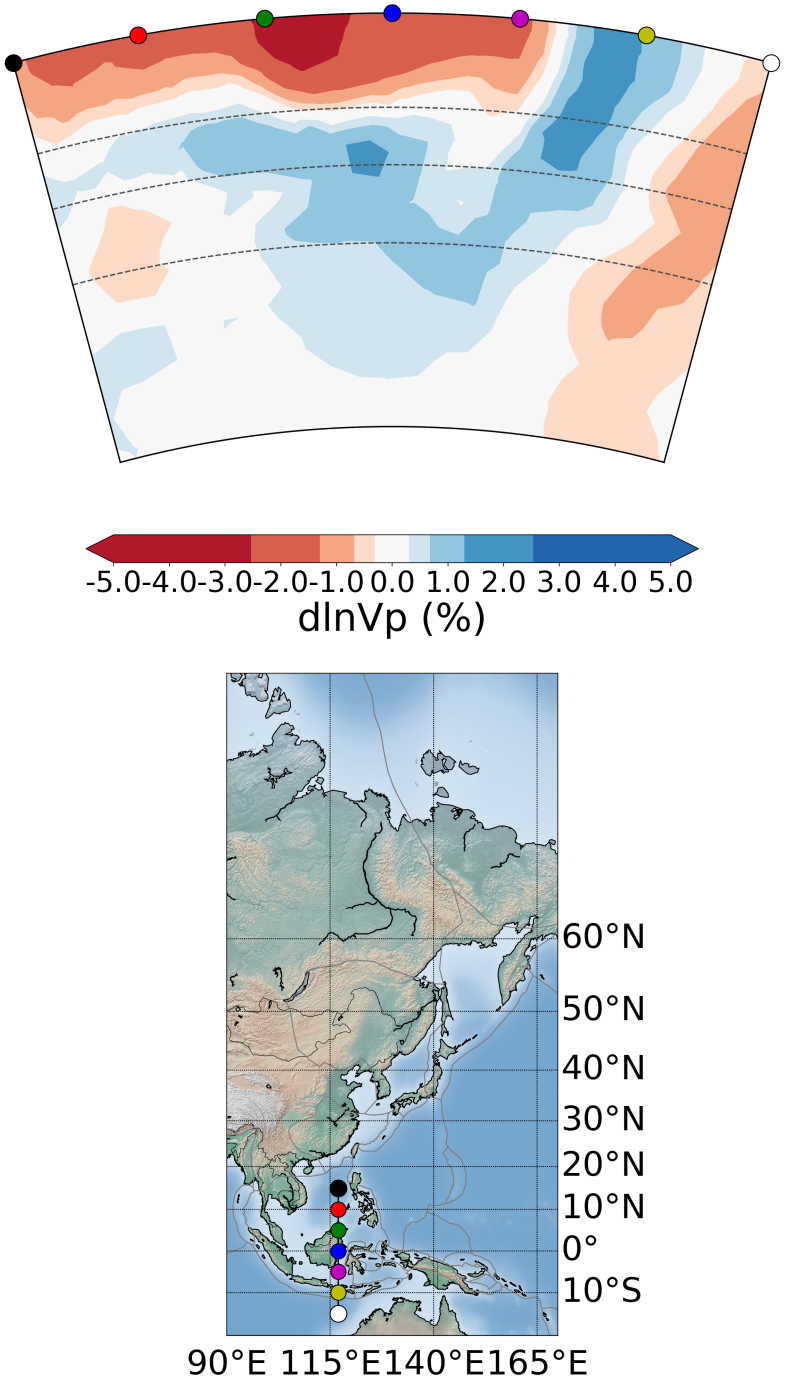

Figure 3.16: Targeted cross-sectional slice (N-S) of the JEABOX tomography model in the southern hemisphere, through eastern Borneo and Sulawesi.

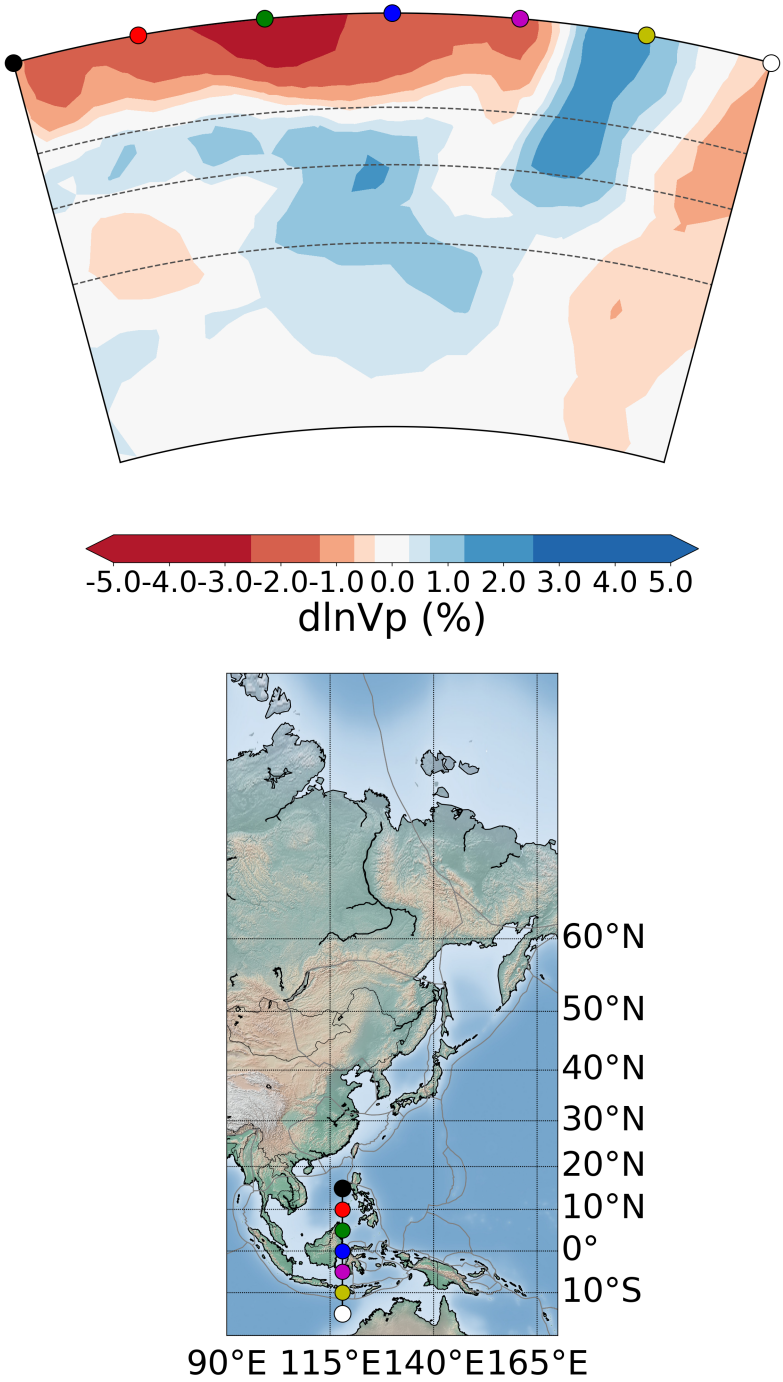

Figure 3.17: Targeted cross-sectional slice (N-S) of the JEABOX tomography model in the southern hemisphere, through eastern Borneo and Sulawesi.

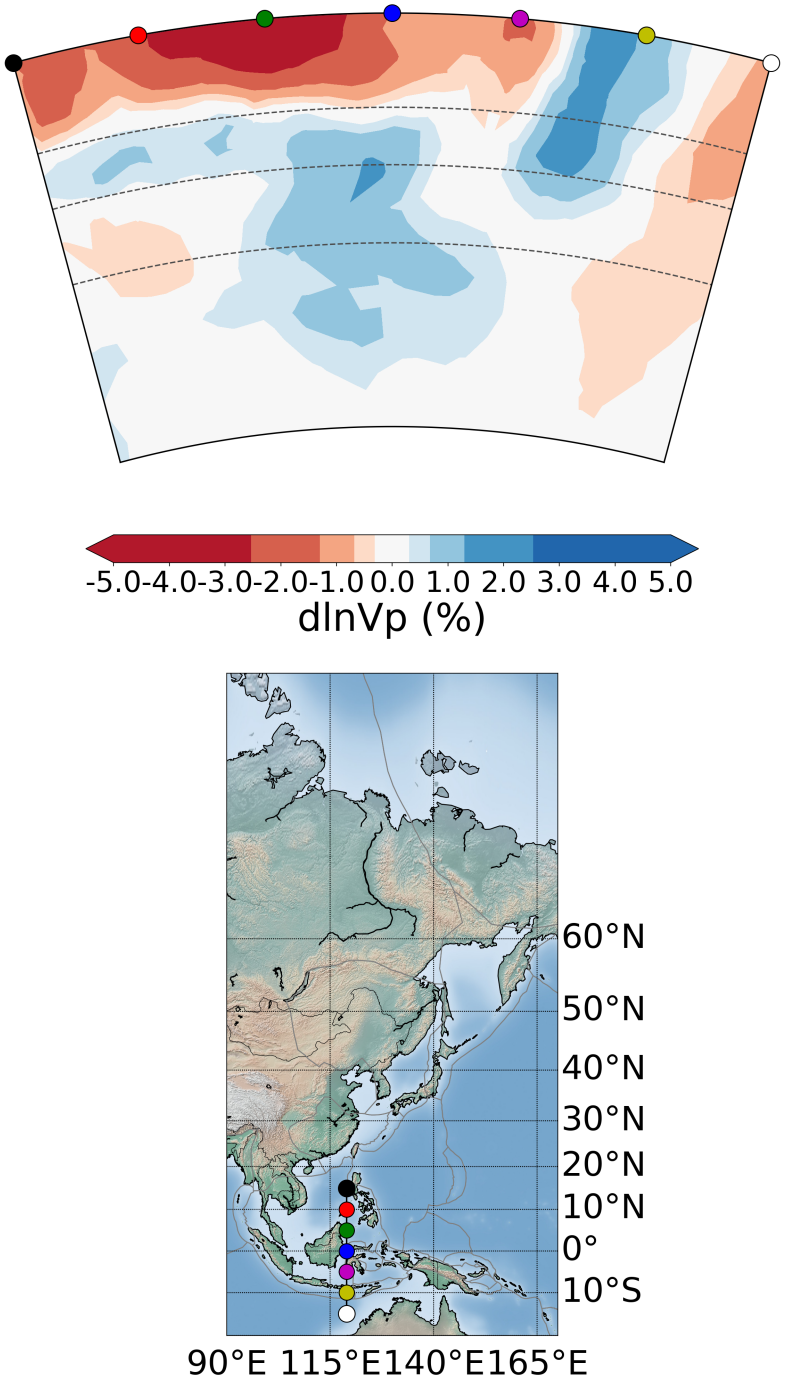

Figure 3.18: Targeted cross-sectional slice (N-S) of the JEABOX tomography model in the southern hemisphere, through eastern Borneo and Sulawesi.

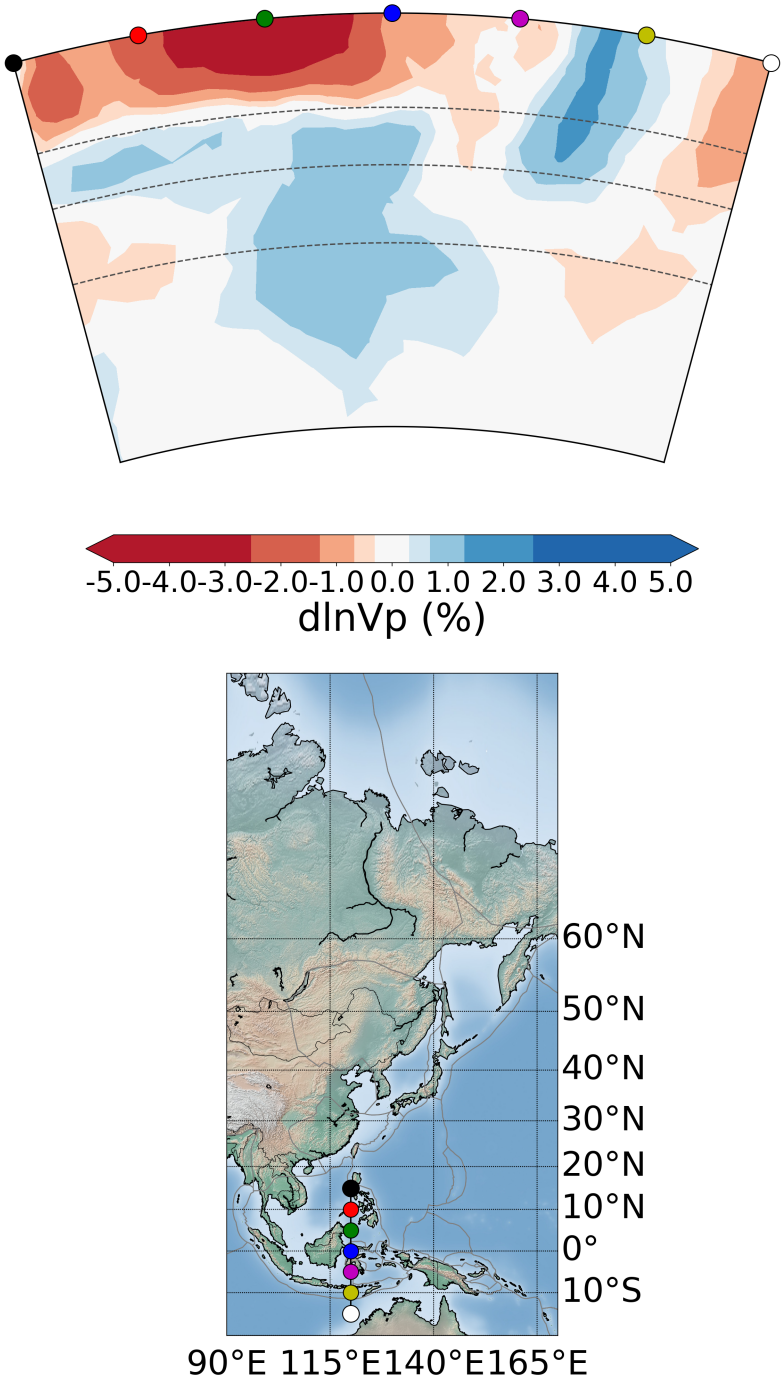

Figure 3.19: Targeted cross-sectional slice (N-S) of the JEABOX tomography model in the southern hemisphere, through eastern Borneo and Sulawesi.

study. In the Japanese Islands and Philippine Sea region, the majority of seismic stations are located westward of the predominating seismicity. In contrast, a limited number of stations are in place within the Philippine Sea plate itself. Similarly, only a handful of seismic stations are emplaced east of the Pacific subduction margin. Here I acknowledge that the performance of the JEABOX model is imperfect in the middle of the Phillippine Sea plate, where an a seismically fast anomalous P-wave velocity body is observed. I attribute this to overfitting of the data where there are relatively few seismic stations present. Here I do not attempt to seismically interpret the JEABOX model. Similarly, I do not interpret east of the Pacific subduction margin, invoking a similar argument. Future work will attempt to mitigate for this overfitting.

It is also worth noting that a large terrestrial array, located on the east Asian continent in China, is not publicly available and was not used in this study. Use of this data would likely have further constrained seismic structure beneath the east Asian margin. One instance of this is the complex Ryukyu subduction zone, where it has been documented that it is difficult to distinguish subducted Pacific slab from the relatively young Philippine Sea slab, although various studies have tried to improve understanding using a multidisciplinary approach (Pownall et al., 2017).

I also note that the regional P-wave dataset based on multifrequency cross-correlation measurements with Instaseis synthetic seismograms and Axisem-based (full waveform) sensitivity kernels provides densified seismic illumination in the Japanese Islands region. South of Japan, the relative contribution of these novel seismic data to the JEABOX model could be improved upon. Future work will seek to expand the regional P-wave dataset presented in this thesis. One means by which this could be achieved is the advancement of high performance computing resources, one example of which is the migration of the UK National Supercomputer

to a new 24-cabinet system (ARCHER2) with 128 cores per node, compared to the 24-cores per node available on its predecessor (ARCHER).

3.5.2 Kuril Trench

Figures A.24-A.26 show a close-up cross-section through the Kuril subduction zone, trending from east to west. Visible is a moderately dipping seismically fast anomaly (approximately 45 degrees), on the order of 150km thick, and of the order of 3% on average in amplitude in the upper mantle. In the mantle transition zone, this anomaly appears to connect to a thicker fast velocity body, which occupies the entire depth range of the MTZ and also appears to flatten. This thick velocity anomaly then extends far under northeast Russia for up to 1000km. This thick velocity body also appears to extend beyond the 660km discontinuity into the mid-mantle, down to roughly 900km depth. There is also an observed distinct zonation of relatively faster velocities in the centre of the thick velocity anomaly, which taper off towards the extremities of the anomaly, from greater than 3% in amplitude to approximately 1% in amplitude.

3.5.3 Japan Trench

Figures 4.20-4.24 show a close-up cross-section through the Japan subduction zone, trending from east to west. Here, in what can be assumed to be the seismological signature of the subducted Pacific slab, the fast velocity body in the upper mantle has a more modest dip which is approximately 30°, although I do note that the slab appears to subduct slightly more steeply to the north approaching Sapporo. Again, the average amplitudes of the fast velocity bodies are in the range of 2-3% and exhibit distinct zonation when plotted logarithmically, from the core of the anomalies to their boundaries. In the vicinity of the 410km discontinuity there is contiguity between the fast anomaly bodies. In the mantle transition zone, the anomaly gradually broadens out to occupy the entire MTZ. The feature extends right under east Asia, from China in the north through to beneath south Korea, at the southern limit of the Japan trench. Here the anomaly appears to terminate at the base of the mantle transition zone and is akin to resolved features in previous studies e.g. Fukao & Obayashi (2013). Based on the plots shown here, there seems

to be little to no connection between seismically fast velocity anomalies at the base of the mantle transition zone and features observed at greater depths.

3.5.4 Izu-Bonin Trench

Figures A.47-A.50 show cross-sections through the Izu-Bonin subduction zone, trending from east to west. Izu-Bonin slab appears to dive at a much steeper angle relative to its more northerly neighbour, the Japan trench. Here, it is possible to corroborate this interpretation to first order, although I acknowledge that there is significant smearing of the fast velocity feature in this region of the JEABOX model. This is likely an artefact of poor receiver distribution for resolving the Izu-Bonin slab, as encountered in other previous full waveform studies of the region (Tao et al., 2018).

Figure 4.32 shows the relative recovery for a deeply diving slab-like feature right down to the base of the mantle transition zone in this region. It appears that the effect of smearing is predominantly lateral: the recovered feature is roughly 1.5 times its original thickness, and the amplitude of the more concentrated synthetic is more evenly distributed throughout the wider recovered velocity anomaly. I observe that, based on this resolution test, there is little to no smearing in depth, which implies a depth constraint on the lower terminus of the Izu-Bonin slab. This conforms with receiver function studies and observations of the deepest documented earthquakes in the region, such as the 2015 680km deep Chichi-Jima event (Porritt & Yoshioka, 2016). Here I have used resolution testing to acknowledge the limits of the JEABOX model as a function of space, whilst advocating a link between the extent of lateral smearing in the resolution tests and what is observed in the model itself. In this region, it is also worth noting that the inversion grid is coarser when compared with other neighbouring subduction zones.

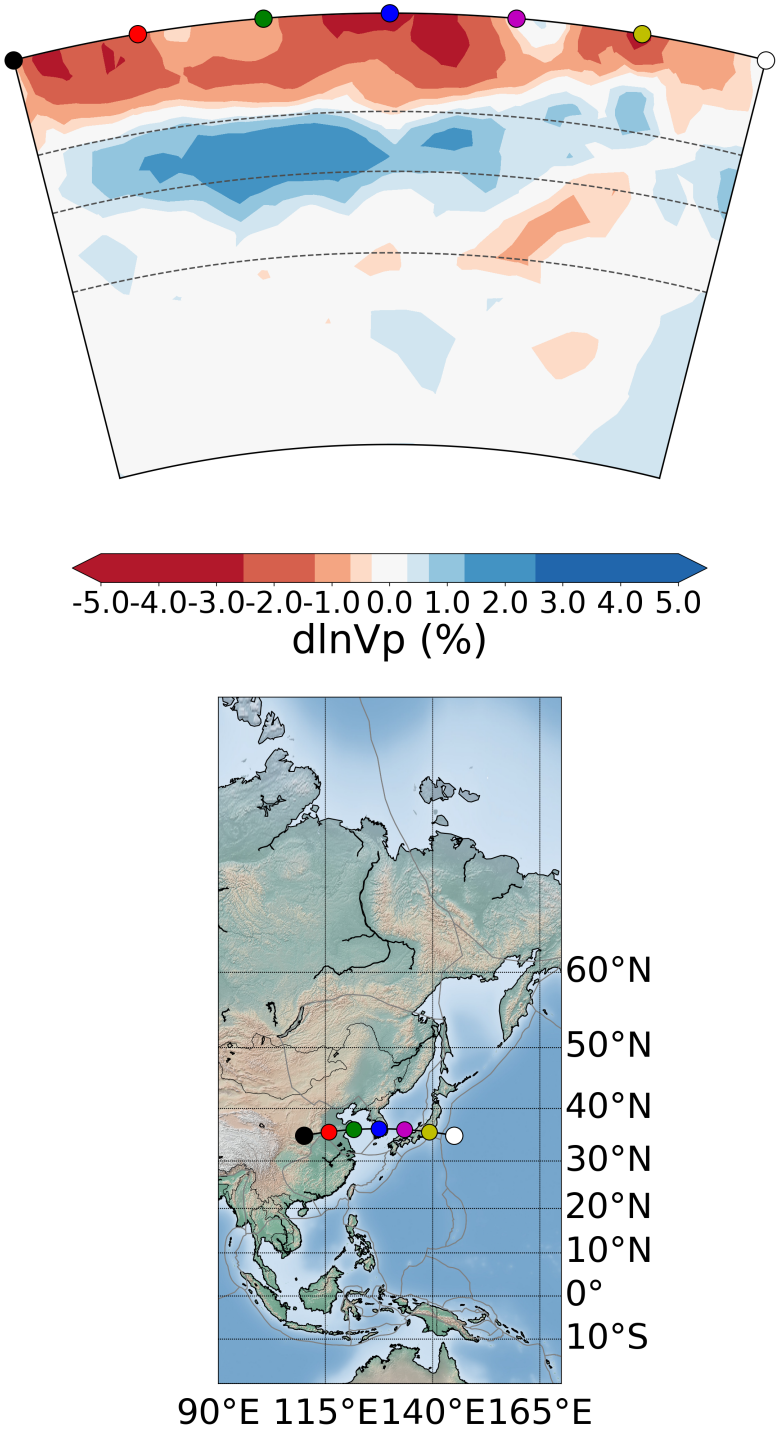

Figure 3.20: Targeted cross-sectional slice of the JEABOX tomography model in the Japan subduction zone: slice 1 of 5.

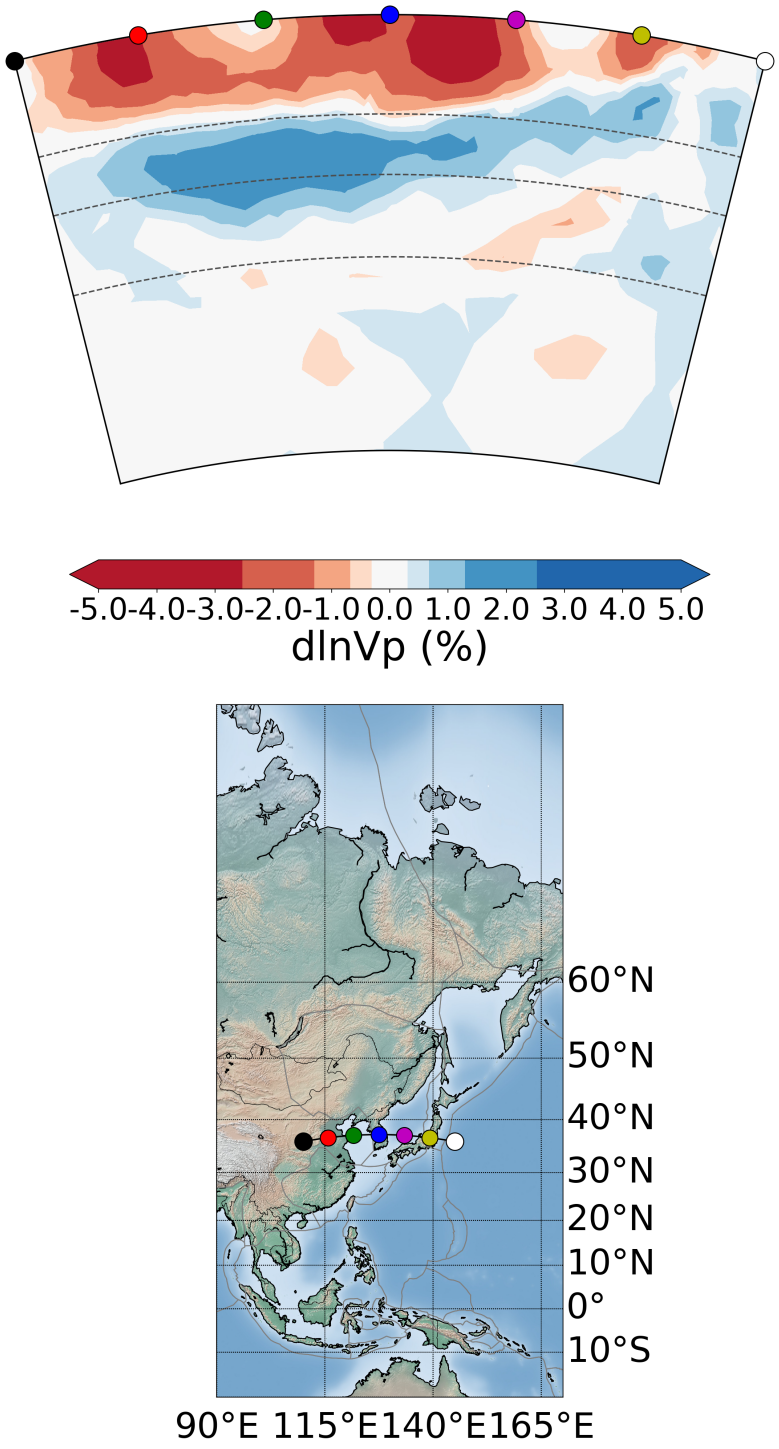

Figure 3.21: Targeted cross-sectional slice of the JEABOX tomography model in the Japan subduction zone: slice 2 of 5.

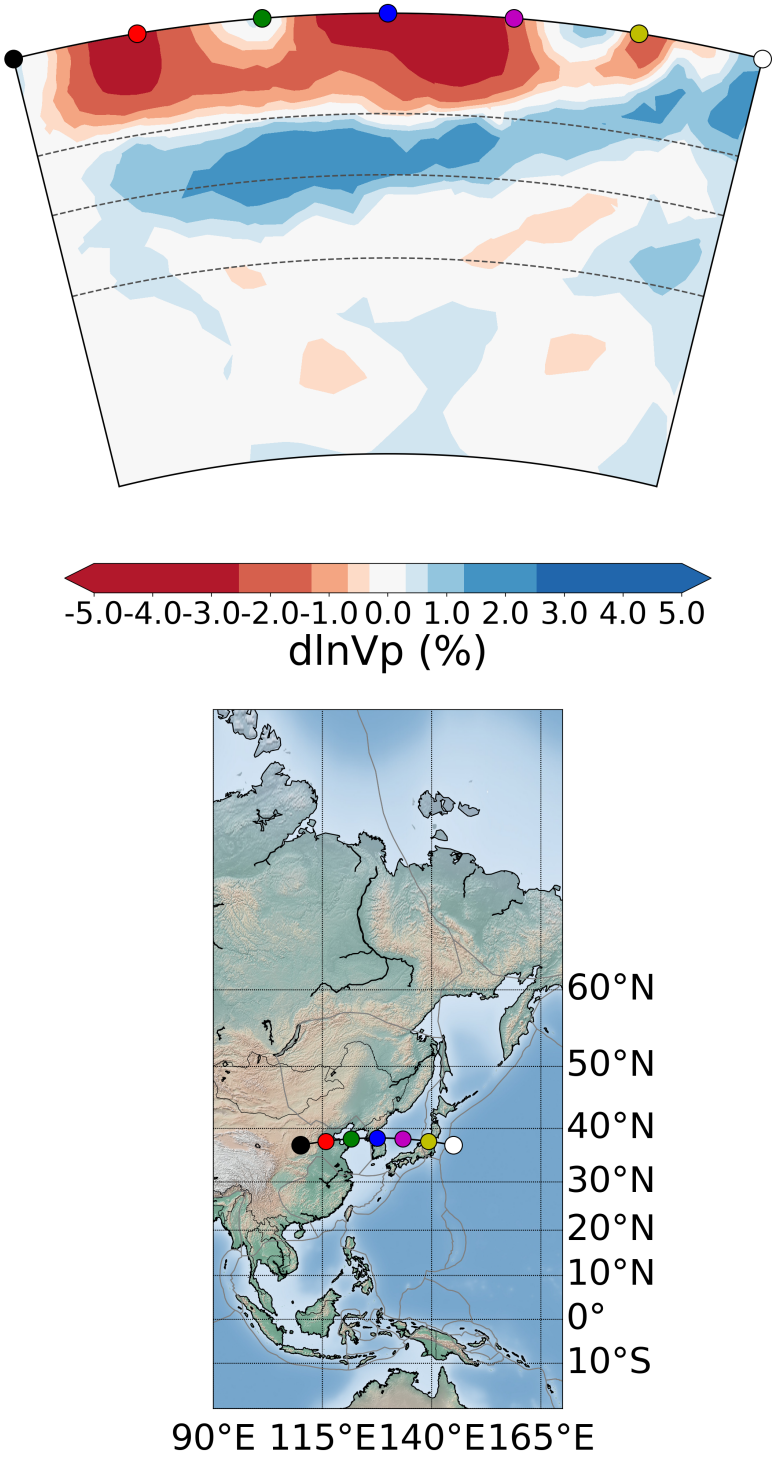

Figure 3.22: Targeted cross-sectional slice of the JEABOX tomography model in the Japan subduction zone: slice 3 of 5.

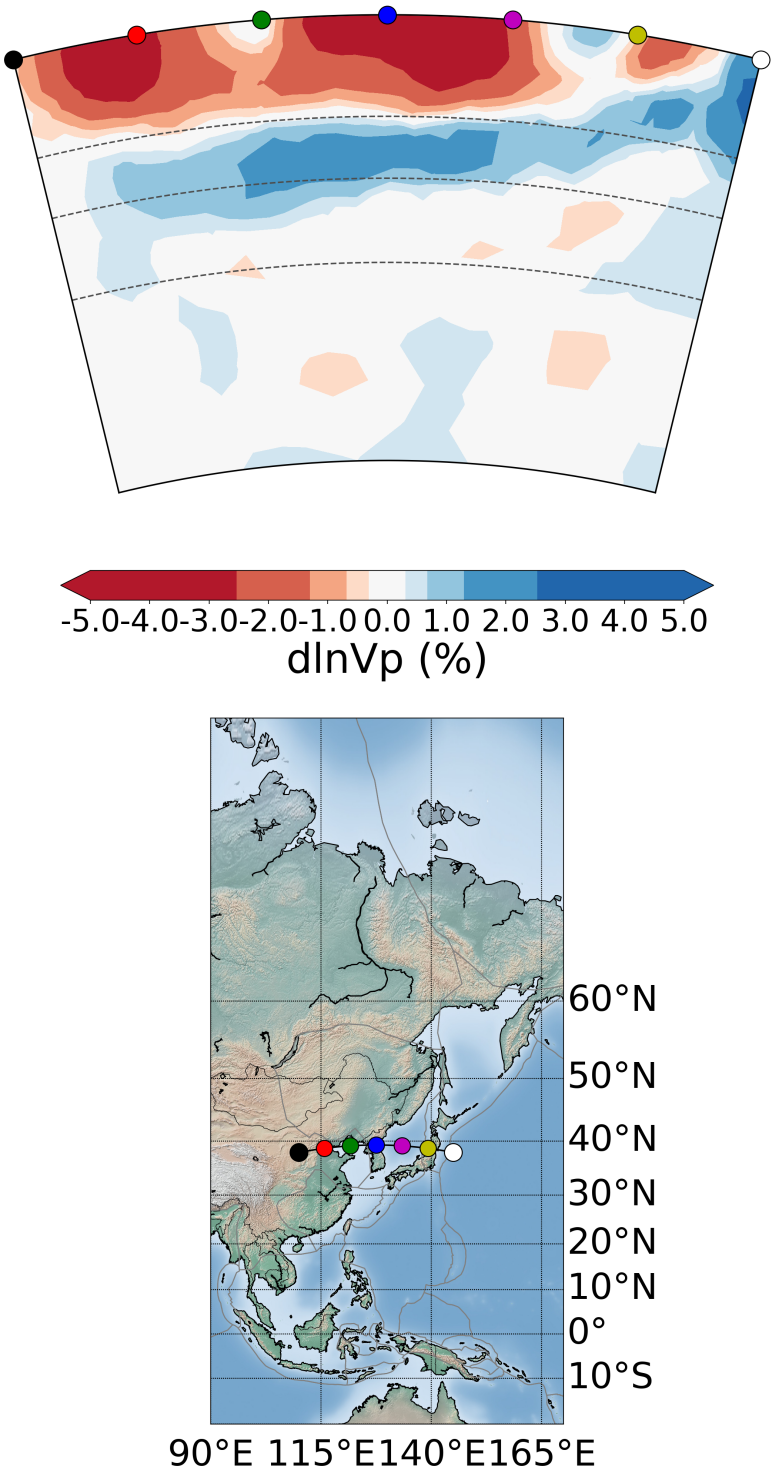

Figure 3.23: Targeted cross-sectional slice of the JEABOX tomography model in the Japan subduction zone: slice 4 of 5.

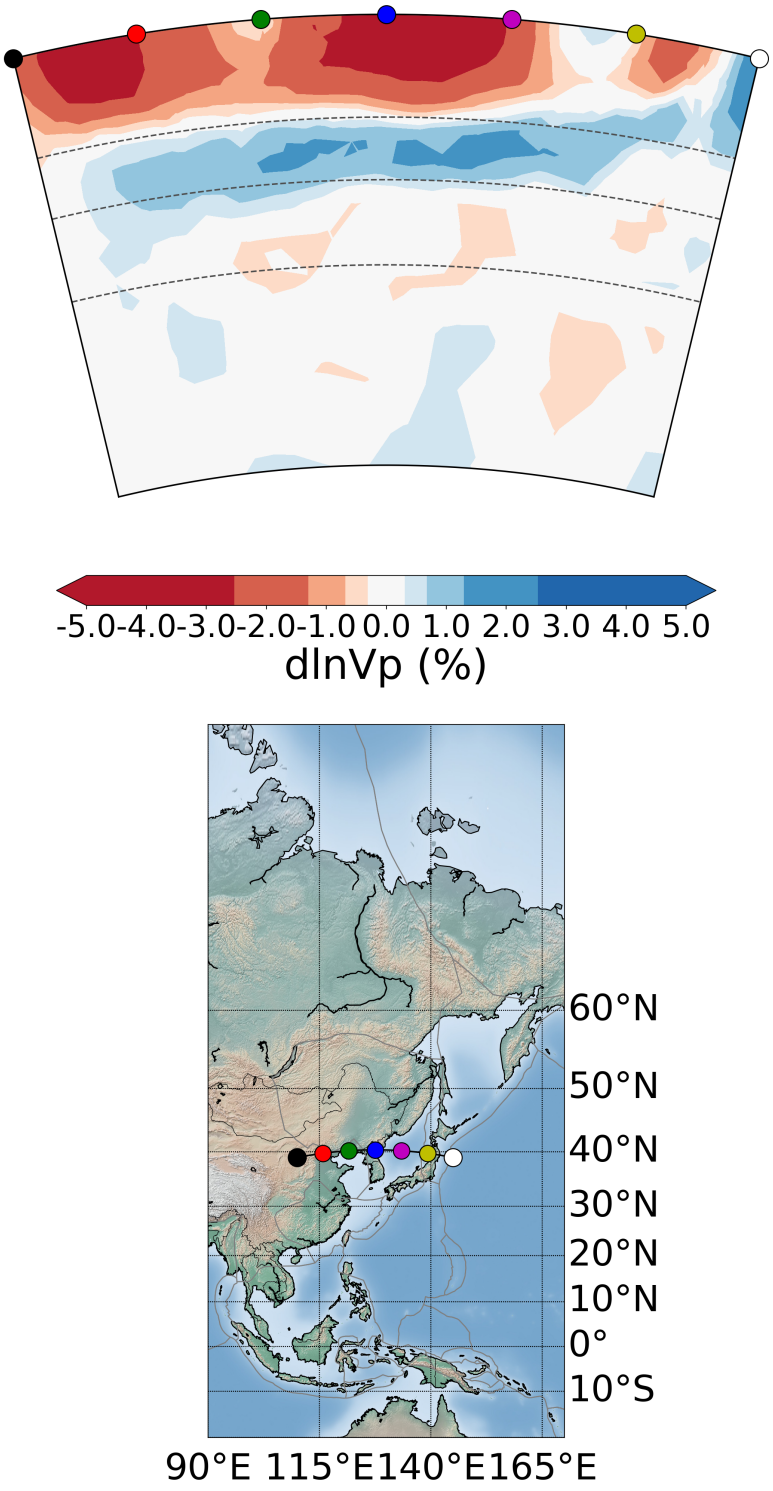

Figure 3.24: Targeted cross-sectional slice of the JEABOX tomography model in the Japan subduction zone: slice 5 of 5.

3.5.5 Subduction in the southern hemisphere

The JEABOX model reveals seismically fast features across the predominant subduction margin in the southern hemisphere, which extends from the south of Indonesia, right through Borneo and beyond the northernmost extend of Australia, whose trenches strike, to first order, east to west.

In the Aceh region, the slab is variable in appearance. With a thickness on the order of 200km, it subduction angle varies significantly along-strike. It appears to dive deeply beneath western Sumatra. Here, fast anomalies appear to be connected above and below the base of the mantle transition zone. Future work will carry out resolution tests to examine the resolving power of the JEABOX model in this region. This feature is observed more or less continuously across the Sunda trench.

There is a change in character to the fast velocity anomalies (inferred to be subducting oceanic lithosphere) beneath the Java trench. Here, the JEABOX model presents with much thicker fast velocity anomalies in both the upper mantle and transition zone, which extend deep beneath Borneo, right beyond the base of the Bullen transition regime (1000km). Trending south-north beneath mid-Borneo the seismically fast anomalies show two limbs,

- a thick main limb that extends from the upper mantle down to greater than 1000km, with a morphology that is similar to what is visible across the rest of the Java trench
- a second limb that appears to overlap or branch off from the main limb, which appears to be stagnated oceanic lithosphere in the mantle transition zone.

This feature appears to extend eastward of Borneo until the Lesser Sunda Islands and western Sulawesi region.

3.5.6 Taiwan and the southern Ryukyu Arc

From the northernmost Philippines near Luzon, through Taiwan and into the southern Ryukyu trench, I observe a contiguous fast velocity feature that continues into the mantle transition zone and extends under the east China and Yellow Seas. While I acknowledged in a previous section that seismic coverage is suboptimal in the middle of the Philippine Sea plate, I note that this feature does in fact appear to extend eastward of Taiwan for approximately 400-500km. Future work will endeavor to recover this feature using targeted resolution tests. This feature is of interest for the well-documented and complex tectonic history of the Philippine Sea plate e.g. Lallemand (2016).

3.6 Resolution Tests

3.6.1 Overview of workflow

In this study I choose a tomography model with an acceptable trade-off between model L-2 norm and data misfit, along the knee of the regularisation curve. This is subjectively chosen because of the norm damping and smoothing applied to the model. This requires that the model of choice be queried using a series of resolution tests. This entails creating a suite of synthetic starting models, from which synthetic travel-times are derived. Each datum is created based on the source-receiver distribution which constituted the original multifrequency measurement dataset gathered from the real Earth. I then invert the synthetic dataset for a given resolution test, using the sensitivity matrix created from the real Earth data. I carry this out using the same model parametrisation (i.e. on the same inversion grid), with the same smoothing and norm damping parameters, the same number of LSQR iterations, and assigning the same prior source correction bounds, as per the original inversion for the real Earth model. Because the model for the resolution test is known, one can assess the spatially dependent recovery of its features, in terms of the smallest resolvable length scale by location and depth, the bleeding of amplitude of those features, and both vertical and lateral smearing.

The following mathematical expression of this is based on the resolution and error analysis of Nolet (2008). In the resolution workflow outlined above, the inverse problem can be written as

$$d = d^{syn} + e = Gm^{test} + e \tag{3.13}$$

where d^{syn} is the dataset created based on the input resolution test model, m^{test} the starting resolution test model and **e** is an error term, also known as a noise term. Given that tomography is by its nature a generalised inverse problem, it is known that

$$G^{-1}G \neq I \tag{3.14}$$

Nolet (2008) expresses the model error $\hat{m}$ as

$$\hat{m} - m^{true} = G^{-1}d - m^{test} = (G^{-1}G - I)m^{test} + G^{-1}e \tag{3.15}$$

such that the model error is a combination of two factors: the model resolution and measurement errors in the data. The resolution test procedure presented here allows for the assessment of resolution, as well as exploration of the noise term, **e**. In what follows I present a selection of resolution tests to assess the minimum length scale resolveable across the study area and the role seismic coverage plays in recovered model amplitudes. First, I present some of the recovery from Gaussian 'spike' tests (alternating spherical fast and slow seismic model patches, with a Gaussian taper from a peak amplitude at their centres) with different radii and spacing between the spherical anomalies. This is done to choose the appropriate length scale for the next set of resolution resolution tests , with test model features of sign, amplitude and dimensions commensurate with those observed in different parts of the real Earth velocity model. Given that the western Pacific is, to first order, a convergent plate margin, these test models are mainly comprised of seismically fast features that reflect what I interpret to be subducting oceanic lithosphere in my real Earth velocity model.

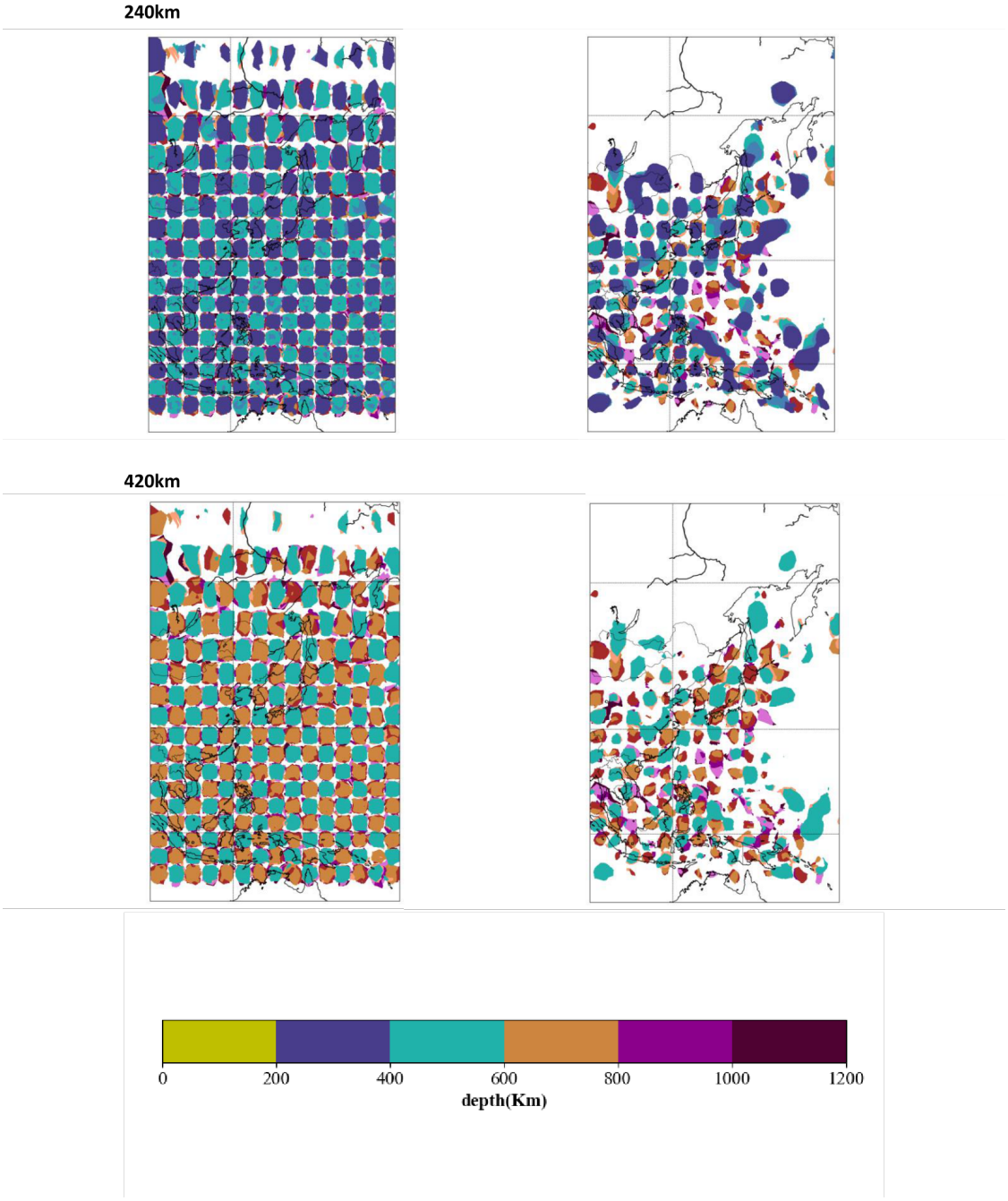

Figure 3.25: 3D rendering of Gaussian resolution test across the western Pacific down to 400km. Top panels show the input resolution test (left) and recovered features from the resolution test (right), sliced at a depth of 240km. Bottom panels show a depth slice of 400km.



Figure 3.26: 3D rendering of Gaussian resolution test across the western Pacific between 400km and 800km. Top panels show the input resolution test (left) and recovered features from the resolution test (right), sliced at a depth of 660km. Bottom panels show a depth slice of 780km.

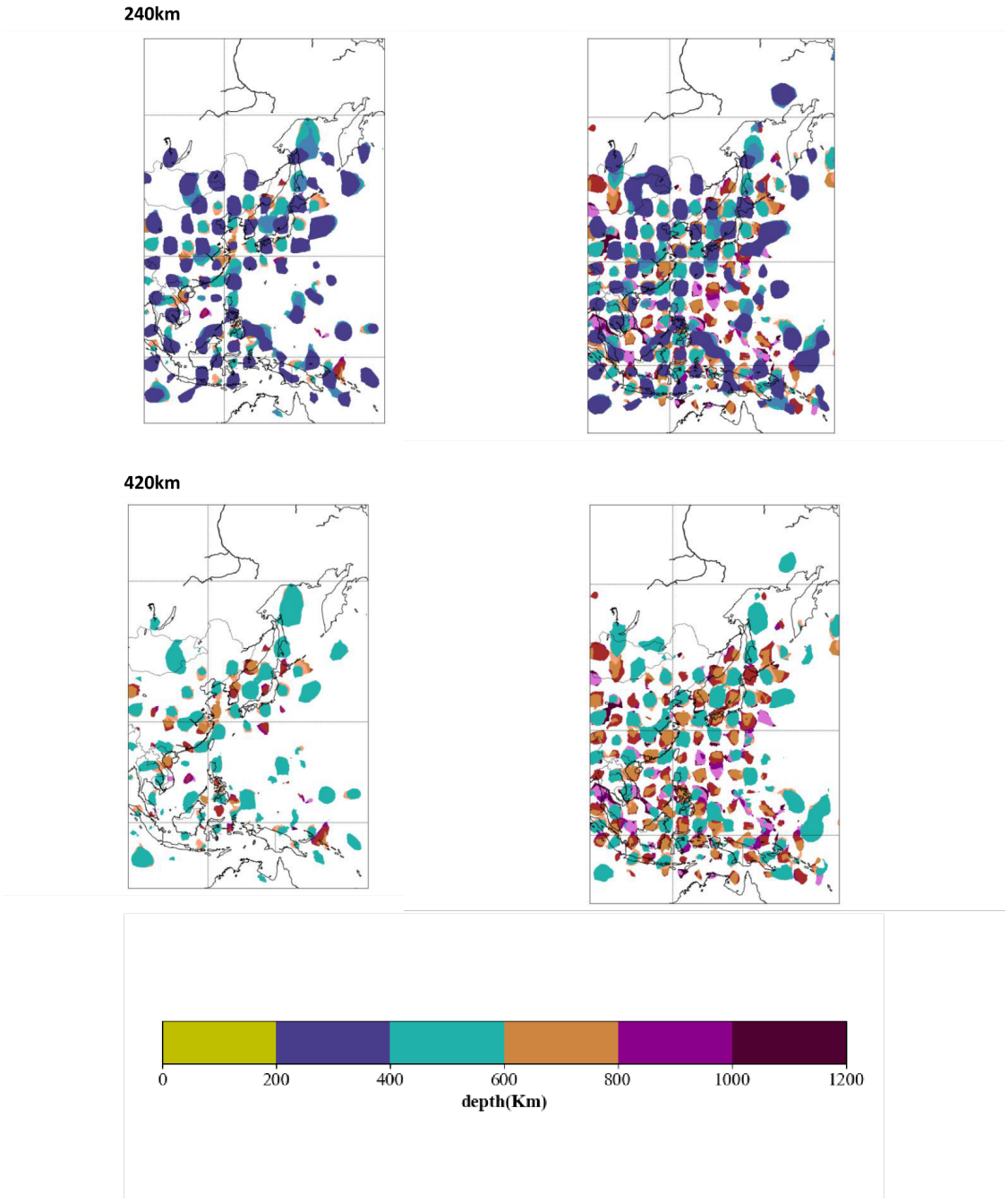

Figure 3.27: Comparison of recovered resolution from Gaussian test at upper mantle and mantle transition zone depths with and without regional P-wave data. Left columns denote teleseismic data only. The right hand columns denote resolution tests based on both teleseismic and regional coverage for the JEABOX model.

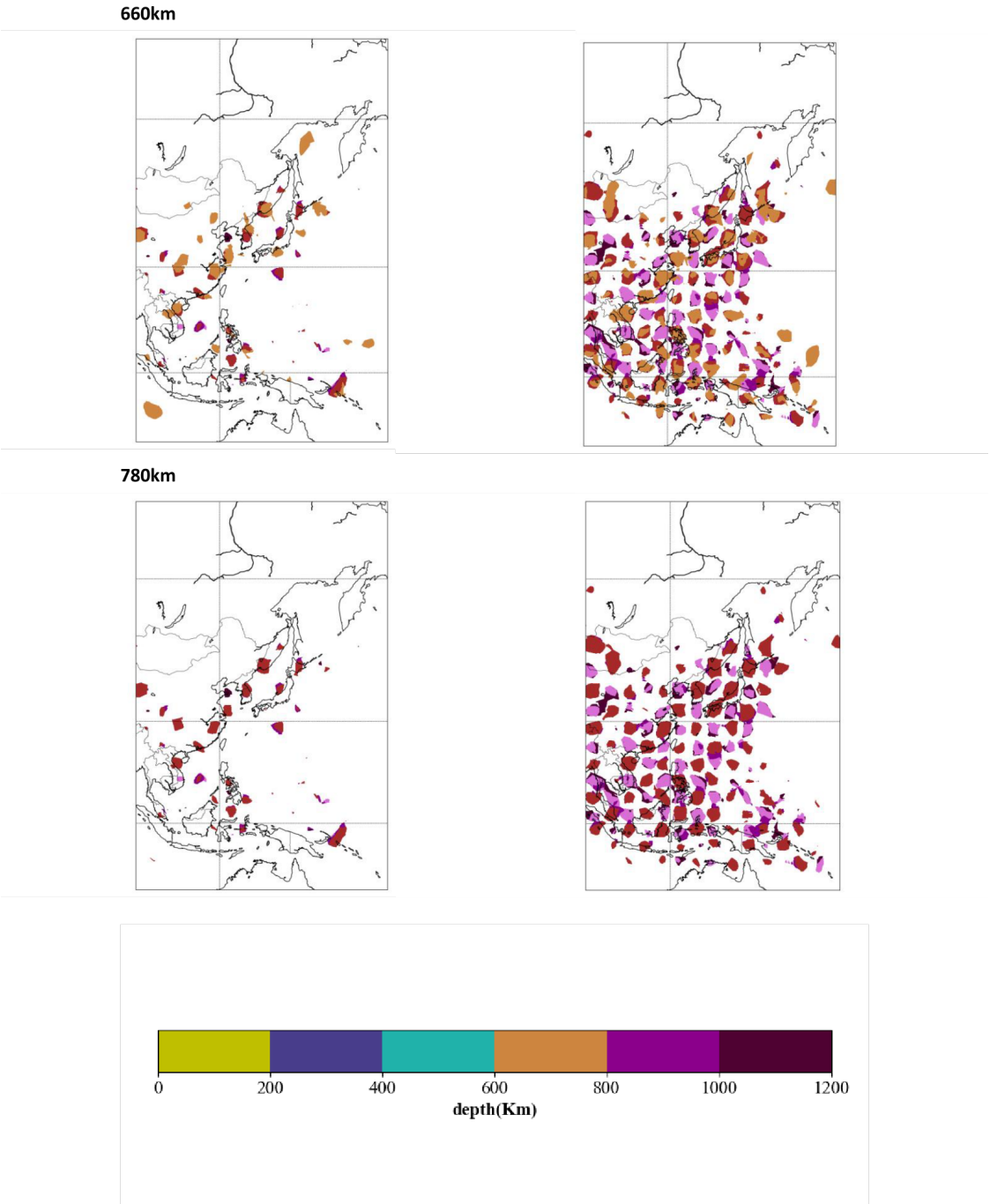

Figure 3.28: Comparison of recovered resolution from Gaussian test at upper mantle and mantle transition zone depths with and without regional P-wave data. The left hand column shows the recovered resolution...

3.6.2 Targeted resolution tests

In this section I discuss both the generalised and targeted resolution tests carried out for the JEABOX model. Figures 4.25 and 4.26 lay out the input and recovery from a Gaussian resolution test across the western Pacific. The inputs were Gaussian anomalies of alternative sign with peak amplitudes at their centres and radii of 200km. These tapered off in amplitude towards their boundaries. The figures colour code the Gaussian balls by their depth, stepping down through different depth slices, to show the depth-dependent recovery of these Gaussian spheres on a two-dimensional plot. Spheres have been contoured at +1%. Four depth slices are shown: 240km, 420km, 660km and 780km.

At 240km, there is generally good recovery of the Gaussian spheres across the region. Areas where features are smeared include east of the Japan subduction zone in the middle of the Pacific plate, in the middle of China and north of Australia. Loss of amplitude and recovery is observed in the middle of the Pacific plate and in southern Russia, to the west of the Sea of Okhotsk. At 420km recovery is better than at shallower depths. Lateral smearing of the Gaussian spheres is much less pronounced, although the amplitude loss observed in the Pacific plate and southern Russia is also observed here. This trend also repeats itself for the 660km and 780km slices.

Figures 4.27 and 4.28 compare recovery between the full JEABOX dataset, which includes regional P-waves based on full waveform sensitivity kernels calculated using MC Kernel and the recovery in their absence, using teleseismic data only. For like-for-like thresholding of the recovered Gaussian spheres, marked improvement in feature recovery is observed with the addition of the regional P-wave data. This is most pronounced across all depth slices in the middle of the Philippine Sea plate and the South China Sea.

In addition to Gaussian spheres, I performed several targeted resolution tests to scrutinise observed seismically fast features in the JEABOX model that conformed to the morphology expected to be associated with subducted oceanic lithosphere. I did this for the Kuril trench, Japan trench and Izu-Bonin trenches.

Figure 4.31 shows the input and recovery for a slab-like resolution test beneath the Japan trench, with a moderately dipping slab in the upper mantle, on the order of 150km thick and a thick body that occupies the entire mantle transition zone and extends for approximately 500km laterally. The recovered features retain their input geometry to first order, but are slightly smoother after undergoing norm damping and smoothing. What is important is that the dimensions of the recovered features are similar to first order: however, I note that the more concentrated, higher amplitude input anomalies, are more diffuse and lower in amplitude in the recovered model slices. Also included for the Japan slab is the same resolution test using teleseismic data only in figures 4.29 and 4.30 (both its synthetic input and recovery), which shows less sharp recovery, in what is a well-instrumented region of the JEABOX model space.

Figure 4.33 shows the input and recovery for a slab-like resolution test beneath the Kuril trench. Again, the recovery of the slab-like feature at mantle transition zone depths is acceptable, although there is amplitude loss in the upper few hundred kilometres of the uppermost mantle. The additional slow velocity anomaly introduced in the upper mantle was also recovered. From this test I infer that resolution beneath the Kuril trench is acceptable at mantle transition zone depths, but that further scrutiny of the model at upper mantle depths needs to be carried out in future work.

Next I address resolution beneath the Izu-Bonin trench. What follows was already referenced in the model presentation section above. Figure 4.32 shows the relative recovery for a deeply diving slab-like feature right down to the base of

the mantle transition zone in this region. It appears that the effect of smearing is predominantly lateral: the recovered feature is roughly 1.5 times its original thickness, and the amplitude of the more concentrated synthetic is more evenly distributed throughout the wider recovered velocity anomaly. I observe that, based on this resolution test, there is little to no smearing in depth, which implies a depth constraint on the lower terminus of the Izu-Bonin slab.

3.7 Discussion and Outlook

In this section I discuss some of the major features presented above for the JEABOX model and identify the future steps required in order to make JEABOX fit for tectonic interpretation.

3.7.1 Japan Trench

Cross-sections through the Japan trench, due to their flattening appearance in the mantle transition zone, provide seismic evidence for slab stagnation at and above the 660km discontinuity. This is in agreement with previous finite-frequency tomography studies of the Japan trench (Fukao et al., 2013). In addition, the peak fast P-wave velocity amplitudes ranging between 3-5% corroborate other full waveform-based tomography studies of the region (Tao et al., 2018). Furthermore, the targeted resolution test of the Japan trench provides evidence that the seismically fast body observed is real, and that its structure is accurate to first order.

Leading on from this, the anomaly thickens by roughly a factor of two to occupy the majority of the mantle transition zone, compared to the upper mantle. Coupled with this, some of the cross-sections exhibit sinuosity in the iso-contours of their velocity. Geodynamic simulations have investigated the possible rheological deformation mechanisms of subducted oceanic lithosphere in the upper mantle and transition zone e.g. Cizkova & Bina (2013), of which one example is buckling (Porritt & Yoshioka, 2016). The sinuosity in fast seismic velocities shown here for the JEABOX model may provide seismic evidence for such a phenomenon,

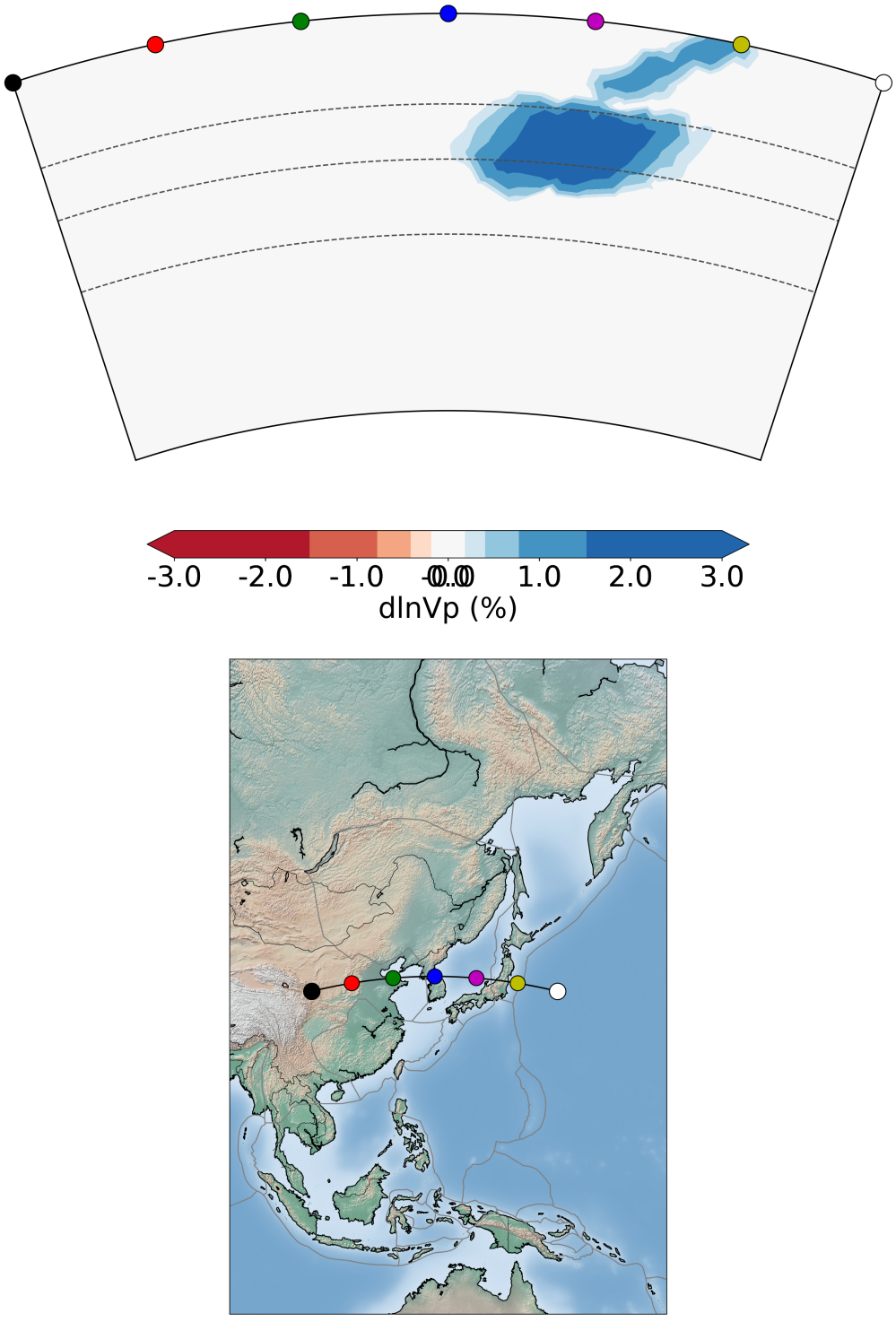

Figure 3.29: Synthetic resolution test of a modestly dipping upper mantle slab and slab stagnation in the transition zone beneath the Japan trench. The input structure is comprised of a 100km thick +3% seismic anomaly dipping at roughly 45° with respect to the Earth's horizontal between 0-400km, in addition to a 250km thick body between 400-700km, also roughly +3% in amplitude, to mimic the stagnation of subducted oceanic lithosphere in the transition zone.

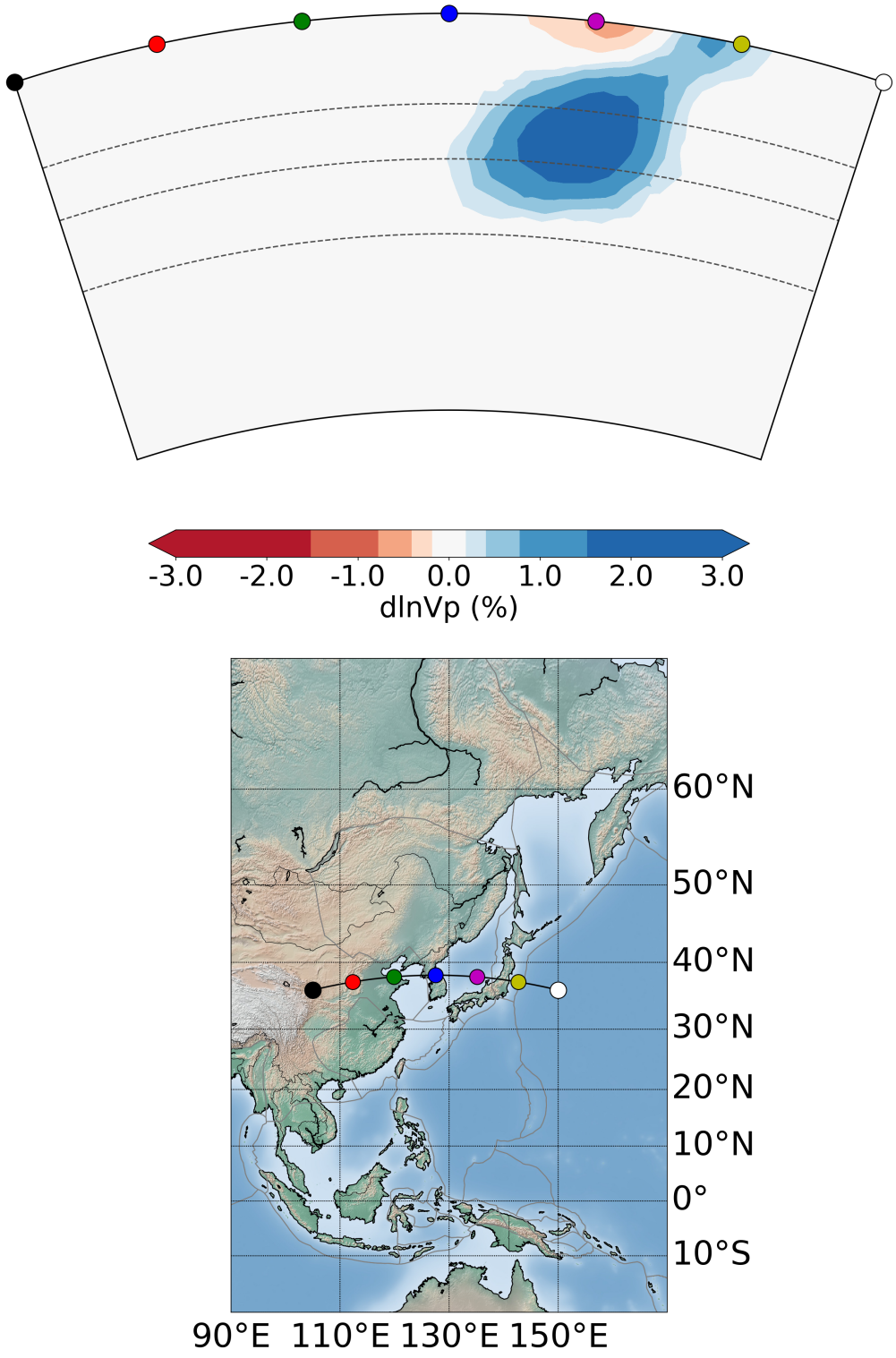

Figure 3.30: Recovered velocity structure from the synthetic resolution test of a modestly dipping upper mantle slab and slab stagnation in the transition zone beneath the Japan trench, using teleseismic data only (i.e. the DETOX-P1 model subset.).

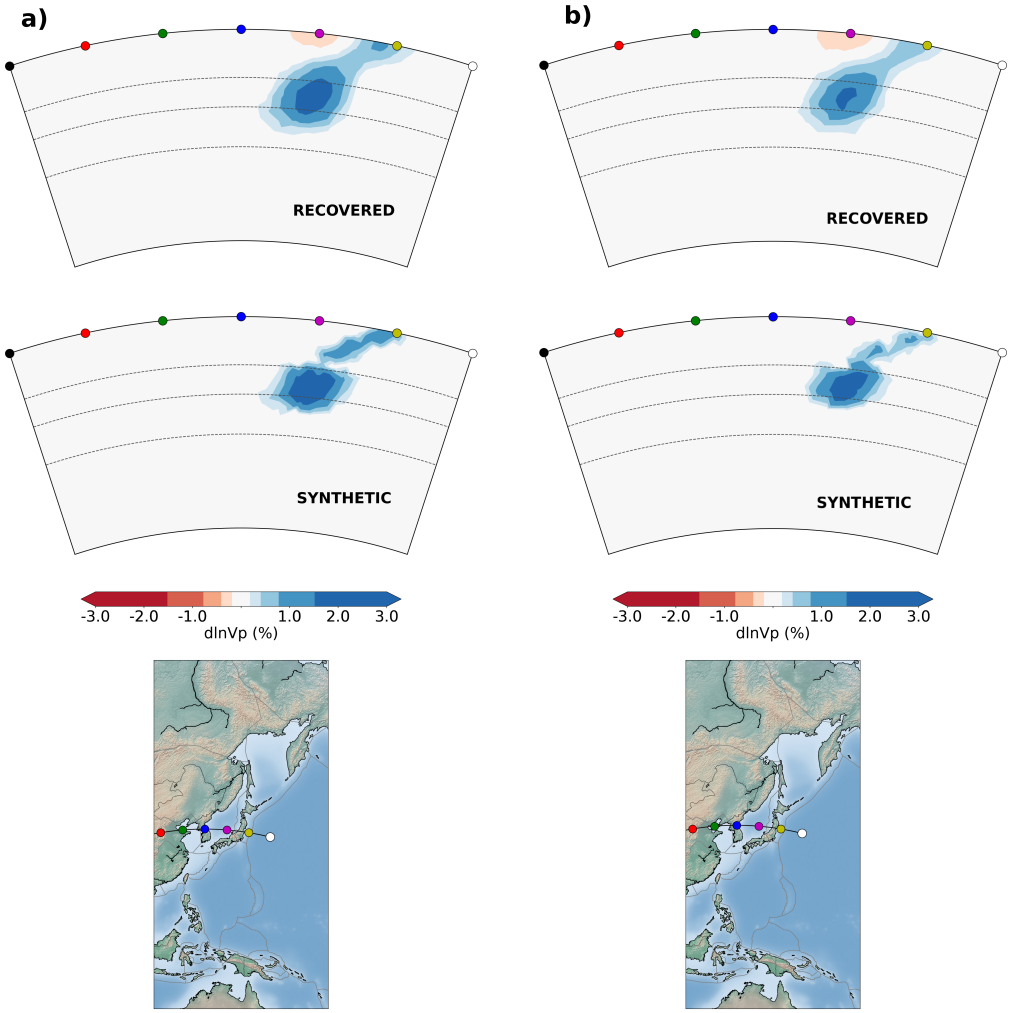

Figure 3.31: (Top) Recovered velocity structure from the synthetic resolution test of a modestly dipping slab in the upper mantle to the base of the transition zone beneath the Japan trench, based on the dataset used for JEABOX (Bottom) Synthetic. Shown are two cross-sectional slices from both the input and recovery for this resolution test. Clearly visible is the contrast between feature recovery using teleseismic data only and the addition of regional P-wave data and their complementary Axisem-based sensitivity (MC) kernels, used here. Recovered slab features are sharper and more concentrated proximal to the locus of their synthetic input locations.

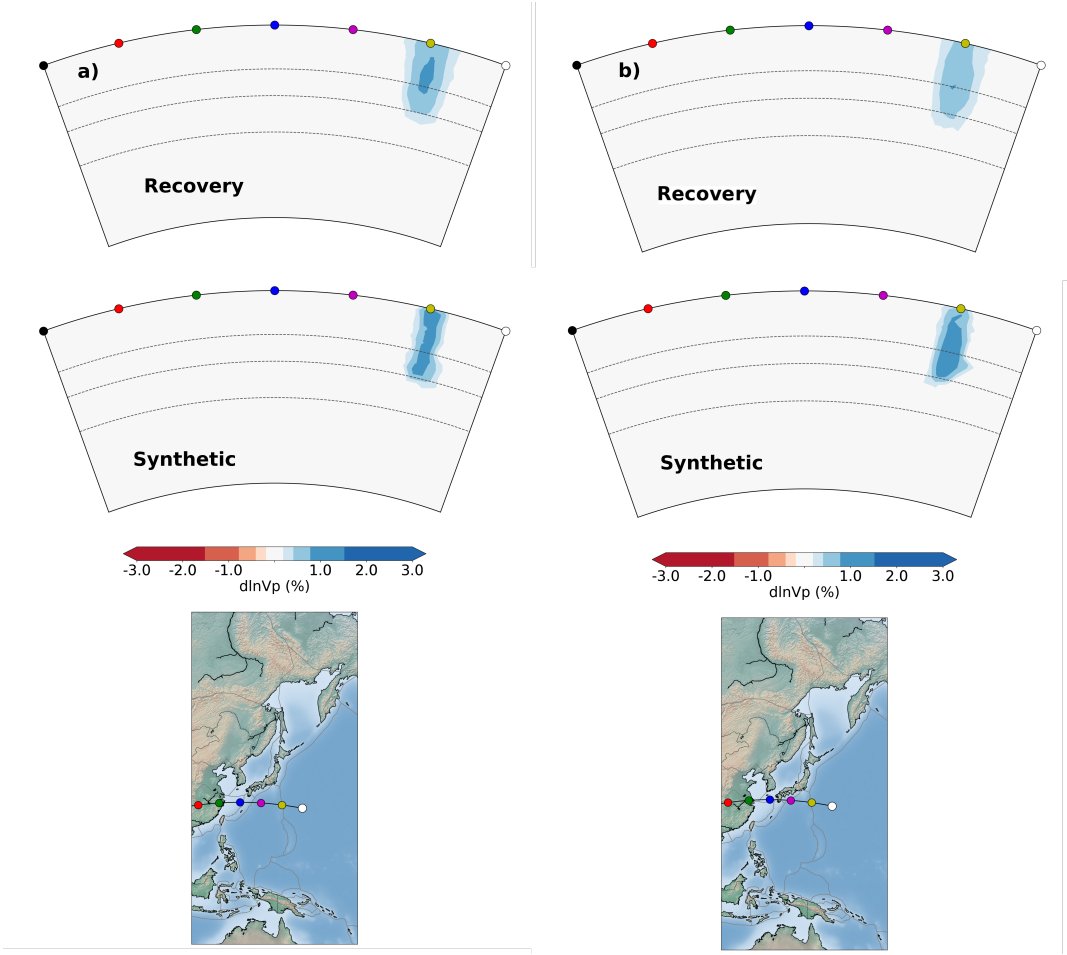

Figure 3.32: (Top) Recovered velocity structure from the synthetic resolution test of a steeply dipping slab in the upper mantle to the base of the transition zone beneath the Izu-Bonin trench, based on the dataset used for JEABOX (Bottom) Synthetic

however future work is needed to test this hypothesis. Examples of future work needed are increasing the maximum frequency of multifrequency cross-correlation measurements and MC kernels in the JEABOX dataset, and a suite of resolution tests that emulate a buckling slab. Here, it is more likely that the sinuosity observed beaneath the Japan trench is a manifestation of interpolating between the discrete points of the inversion mesh.

3.7.2 Kuril Trench

Here I also interpret cross-sections of the JEABOX model to infer that slab stagnation is also present beneath the Kuril trench. The targeted resolution tests imply that slab-like seismic structure is recoverable in the mantle transition zone,

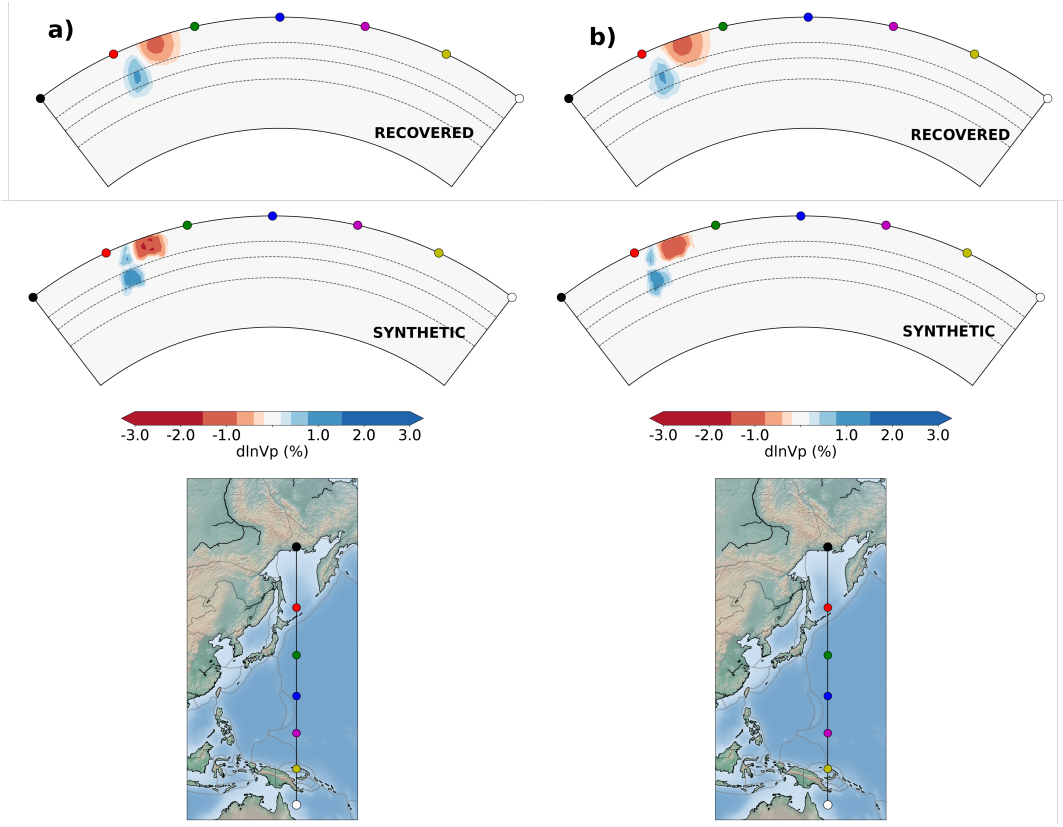

Figure 3.33: (Top) Recovered velocity structure from the synthetic resolution test of a steeply dipping slab in the upper mantle to the base of the transition zone beneath the Izu-Bonin trench, based on the dataset used for JEABOX (Bottom) Synthetic

though coverage is poorer in the upper mantle. This imperfect resolution makes sense given that Kuril is located at the northeastern fringe of the study area.

3.7.3 Izu-Bonin Trench

While the Izu-Bonin slab exhibits lateral smearing according to the targeted resolution test for the region, the same resolution test implies good depth constraint on the slab, in addition to the first order orientation of the resolved seismically fast feature. This may imply that subducted oceanic lithosphere beneath the Izu-Bonin trench is subducting at a very steep angle.

3.7.4 Possible origins of variable slab dip in the Japanese Islands region

Given the constrast in seismological signatures between the Japan and Izu-Bonin slabs outlined above, it is worth addressing the possible origins for this contrast in future work and testing these seismically. This is important because it is a perfect location on earth to examine the interplay between slab impingement in the transition zone (and their residence times), the strength of the asthenosphere and the overriding plate (e.g. Garel et al. (2014); Cerpa, pers. comm), in addition to the correlation between trench movement rates and the age of subducted slab. This is important for constraining former tectonic plate locations in the vicinity of east Asia and the Japanese Islands region, especially in the past 50Myr. This is also important in context of attempting to unravel the complex plate tectonic history of the Philippine Sea plate, which also has a north-south dimension to it, in addition to the predominant east-west subduction along both its eastern and western boundaries, which will also be the subject of future work.

3.7.5 JEABOX in the southern hemisphere

Future work will perform targeted resolution tests of slab-like features across the southern hemisphere portion of the JEABOX model. The original aim of this thesis was to produce a targeted tomography of east Asia and the Japanese Islands region, however, it was subsequently discovered that there was a large volume of regional and teleseismic data available to exploit throughout the rest of the western Pacific and its connection to Indonesia. Here I close this section with one of many possible hypotheses to be tested in future work.

Seismically fast velocity anomalies resolved near the Sunda trench exhibited P-wave velocity signatures that indicated slab accumulation in the mantle transition zone and a large body of what may be slab in the lower mantle. The connectivity between these bodies, in addition to structure resolved in the upper mantle, needs to be verified in future work. One motivation for this is that the seismic cross-sections

cover the predicted overlap in locations of the Sunda and Molucca slabs. Here, Morgan (2021) argued for a stacking of slab folds in the uppermost lowermantle at approximately 1000km depth, in addition to interaction of the Molucca slab with the Sunda slab from the west.

3.7.6 Depth-dependent contouring of the JEABOX model

I draw the reader's attention to figure 4.34 through to figure 4.55, which show the JEABOX model contoured at discrete depth slices and overlaid on top of one another, to draw attention to any depth-dependent correlation between contiguous, seismically fast velocity structures. An example of where this is important is in proximity to trenches, where the dip of the slab should be borne out in these pseudo-3D plots. In addition, by rendering the JEABOX model in this manner, it can be seen that the mantle transition zone is more or less saturated throughout the majority of western Pacific subduction zones covered by the study region.

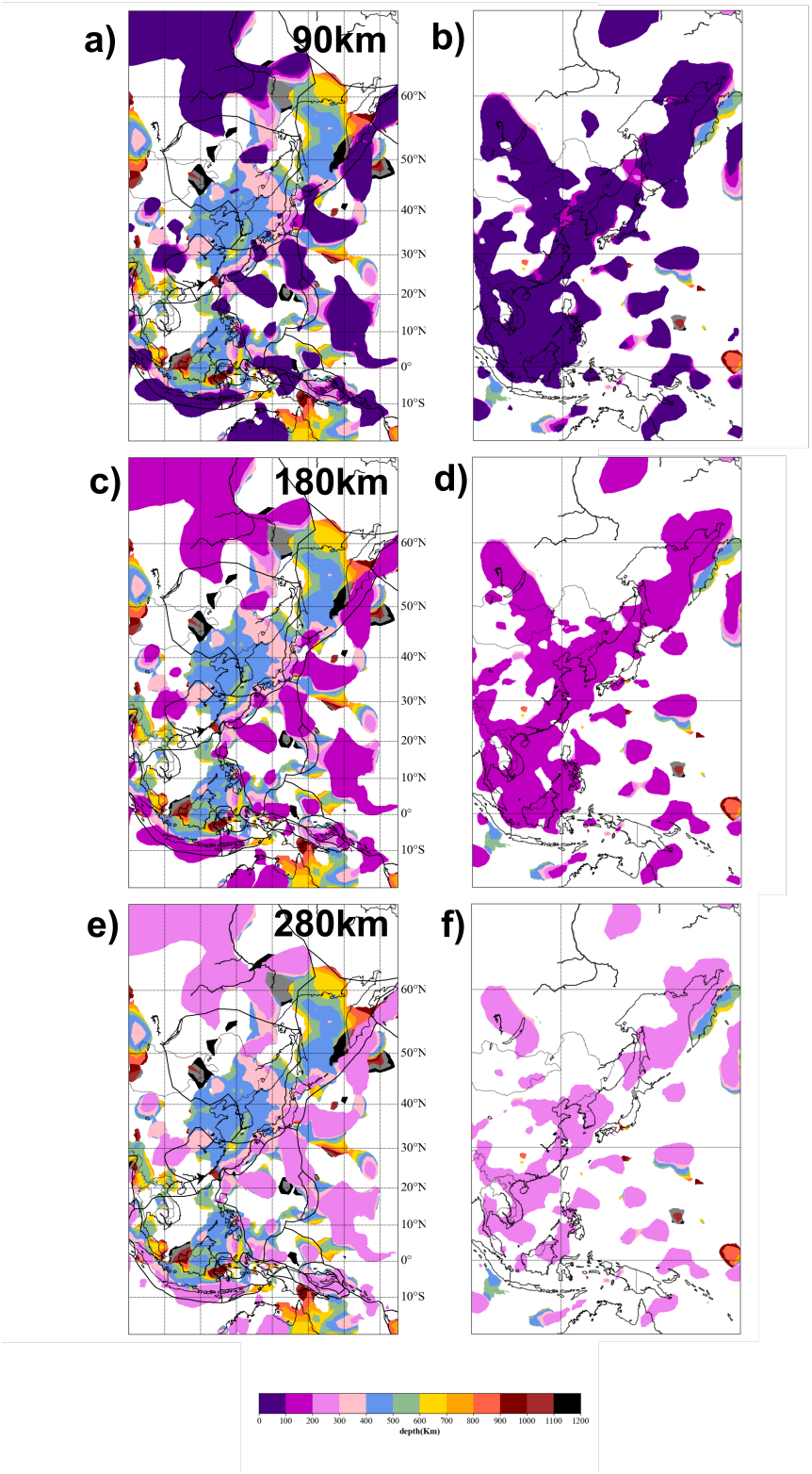

Figure 3.34: Contoured fast and slow velocity anomalies for the JEABOX model, 90km (a) and b)), 180km (c) and d)) , 280km (e) and f)). Fast anomalies are contoured for values in the JEABOX model greater than 0.375% on the left hand column. Slow anomalies are contoured in the right hand column, for seismically slow structures between 1% and 5%.

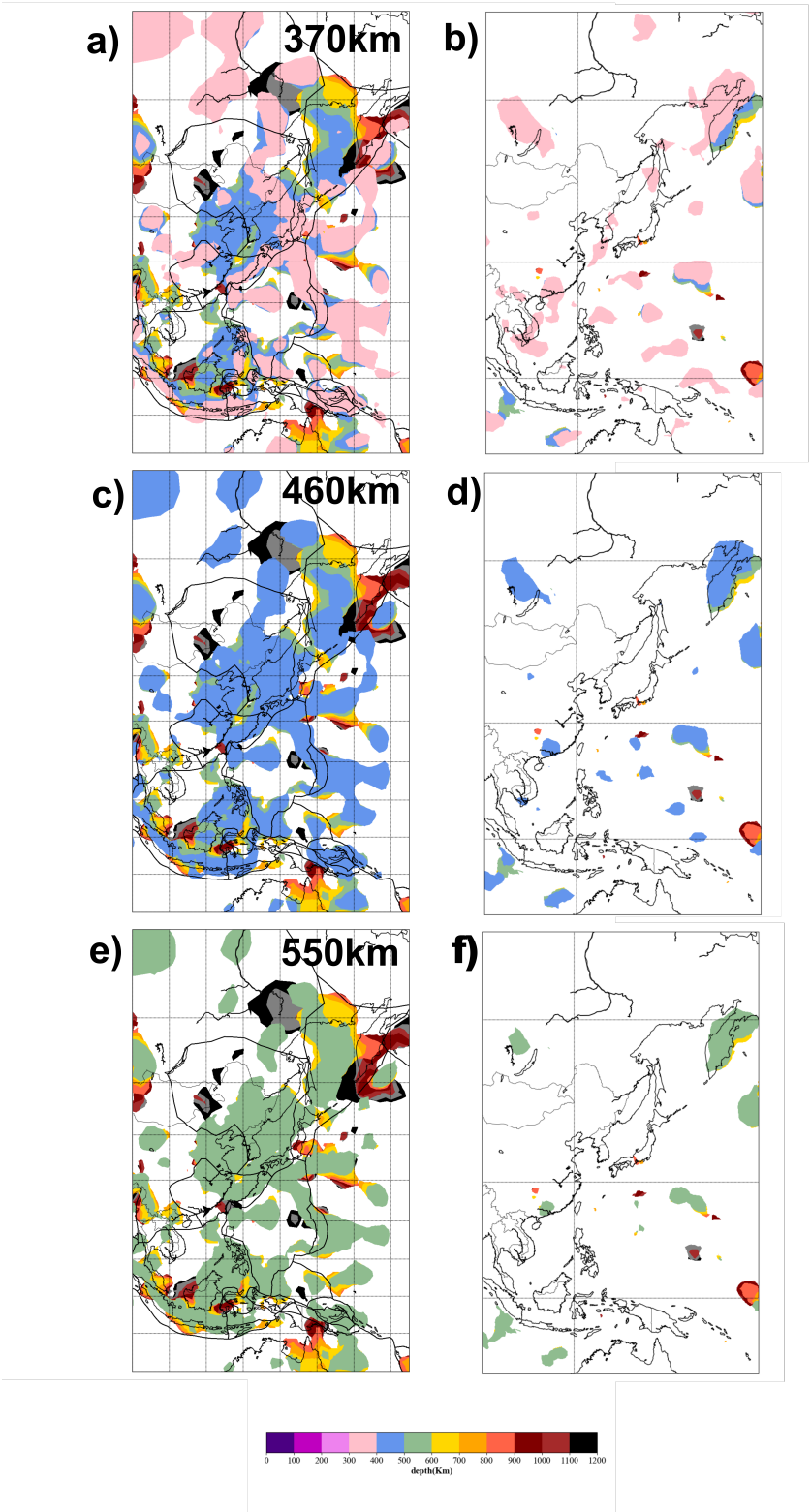

Figure 3.35: Contoured fast and slow velocity anomalies for the JEABOX model, 370km (a) and b)), 460km (c) and d)) , 550km (e) and f)). Fast anomalies are contoured for values in the JEABOX model greater than 0.375% on the left hand column. Slow anomalies are contoured in the right hand column, for seismically slow structures between 1% and 5%.

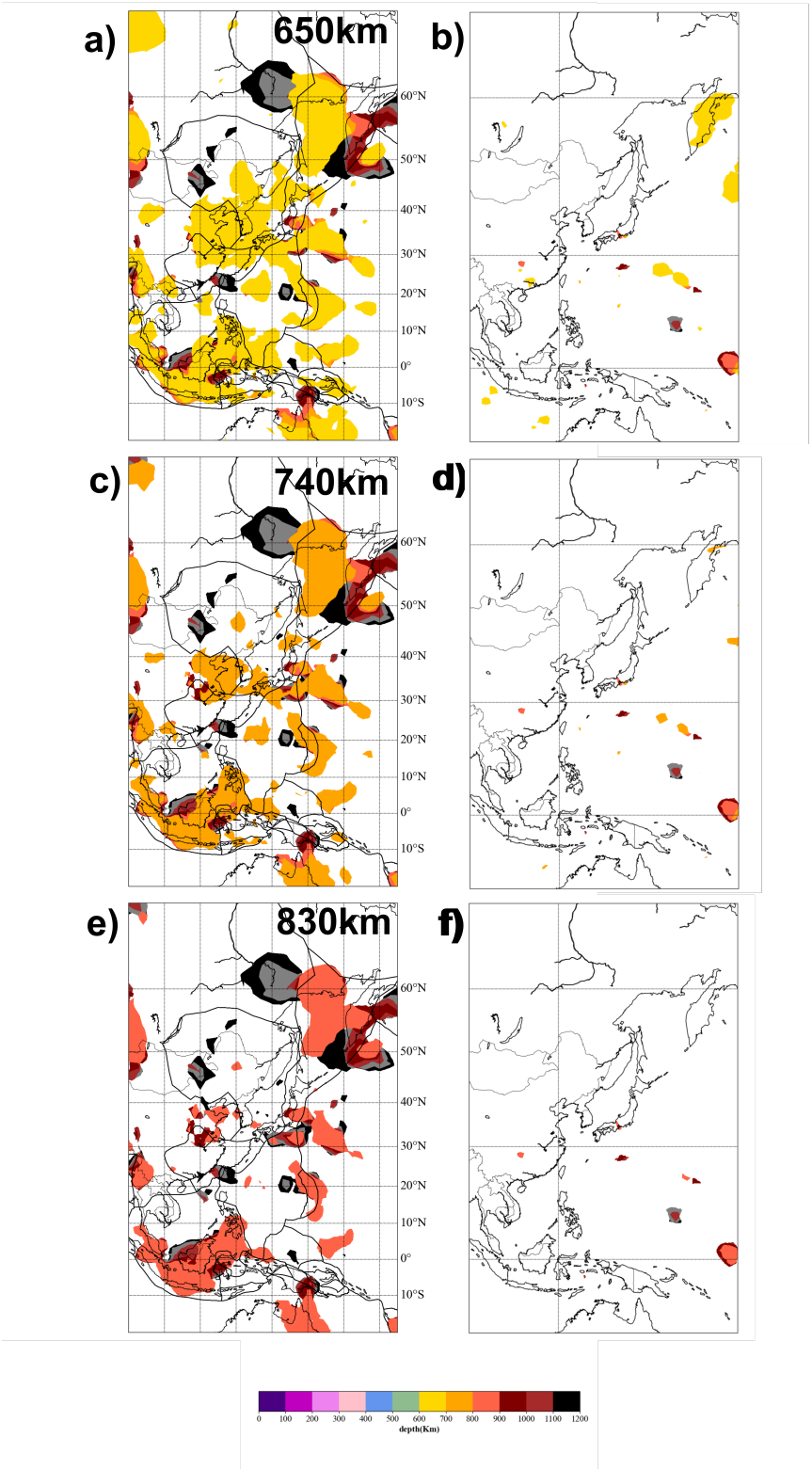

Figure 3.36: Contoured fast and slow velocity anomalies for the JEABOX model, 650km (a) and b)), 740km (c) and d)) , 830km (e) and f)). Fast anomalies are contoured for values in the JEABOX model greater than 0.375% on the left hand column. Slow anomalies are contoured in the right hand column, for seismically slow structures between 1% and 5%.

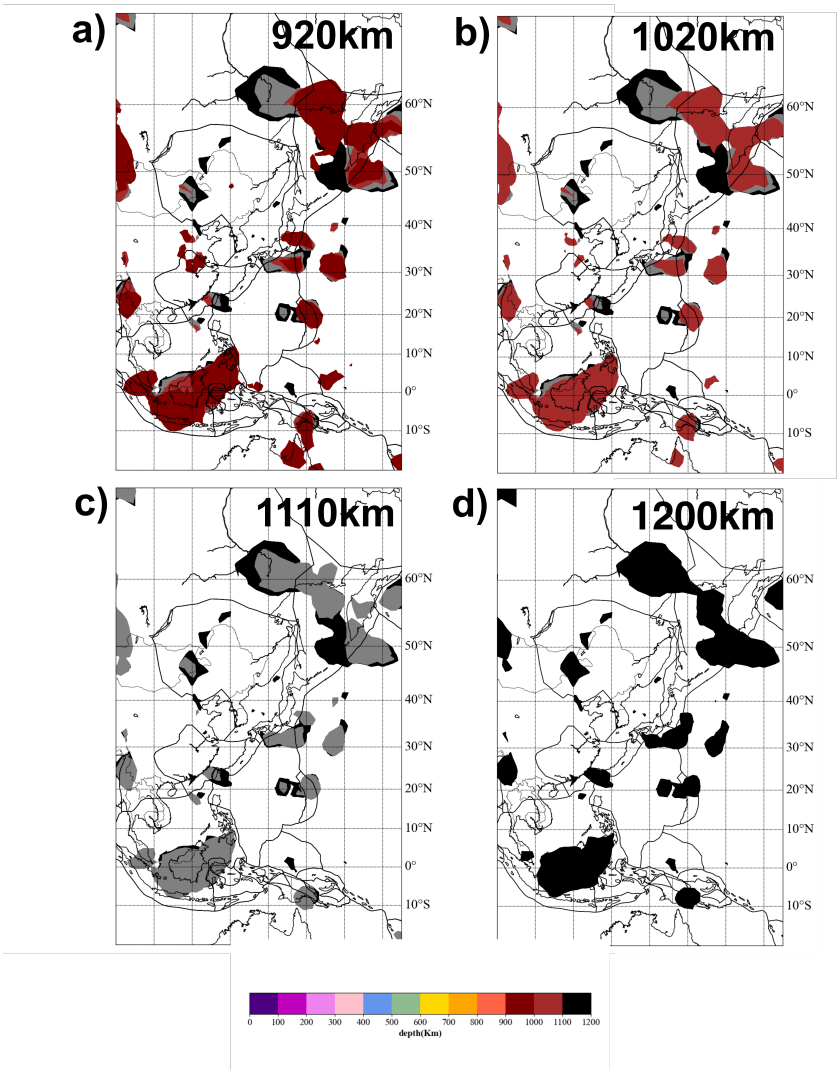

Figure 3.37: Contoured fast and slow velocity anomalies for the JEABOX model, 920km (a) and b)), 1110km (c) and d)) , 1200km (e) and f)). Fast anomalies are contoured for values in the JEABOX model greater than 0.375% on the left hand column. Slow anomalies are contoured in the right hand column, for seismically slow structures between 1% and 5%.

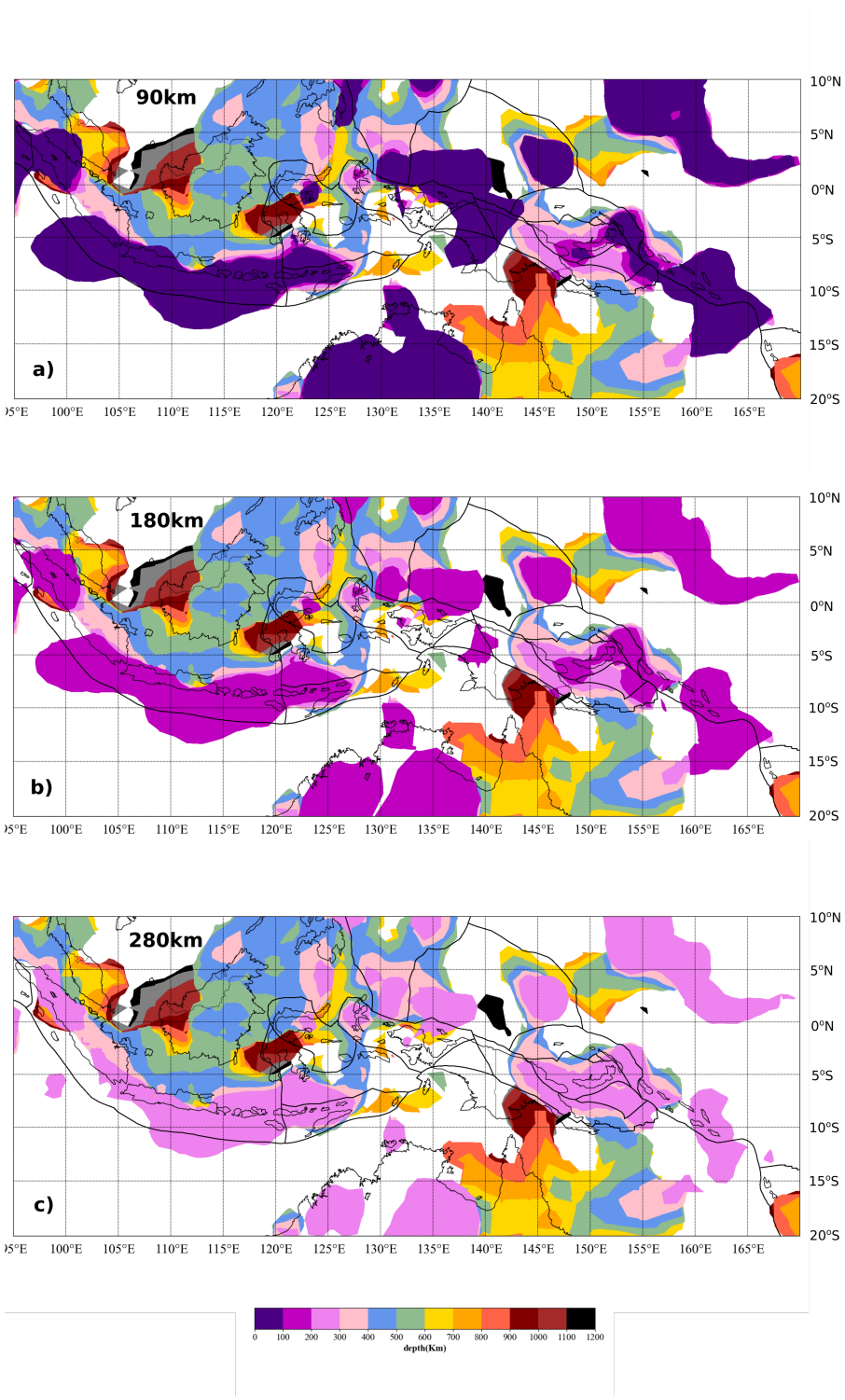

Figure 3.38: Contoured fast velocity anomalies for the JEABOX model, inset of southeast Asia at 90km, 180km and 280km. At each given depth , anomalies are contoured for values greater than +0.375%. a) 90km b) 180km and above c) 280km and above.

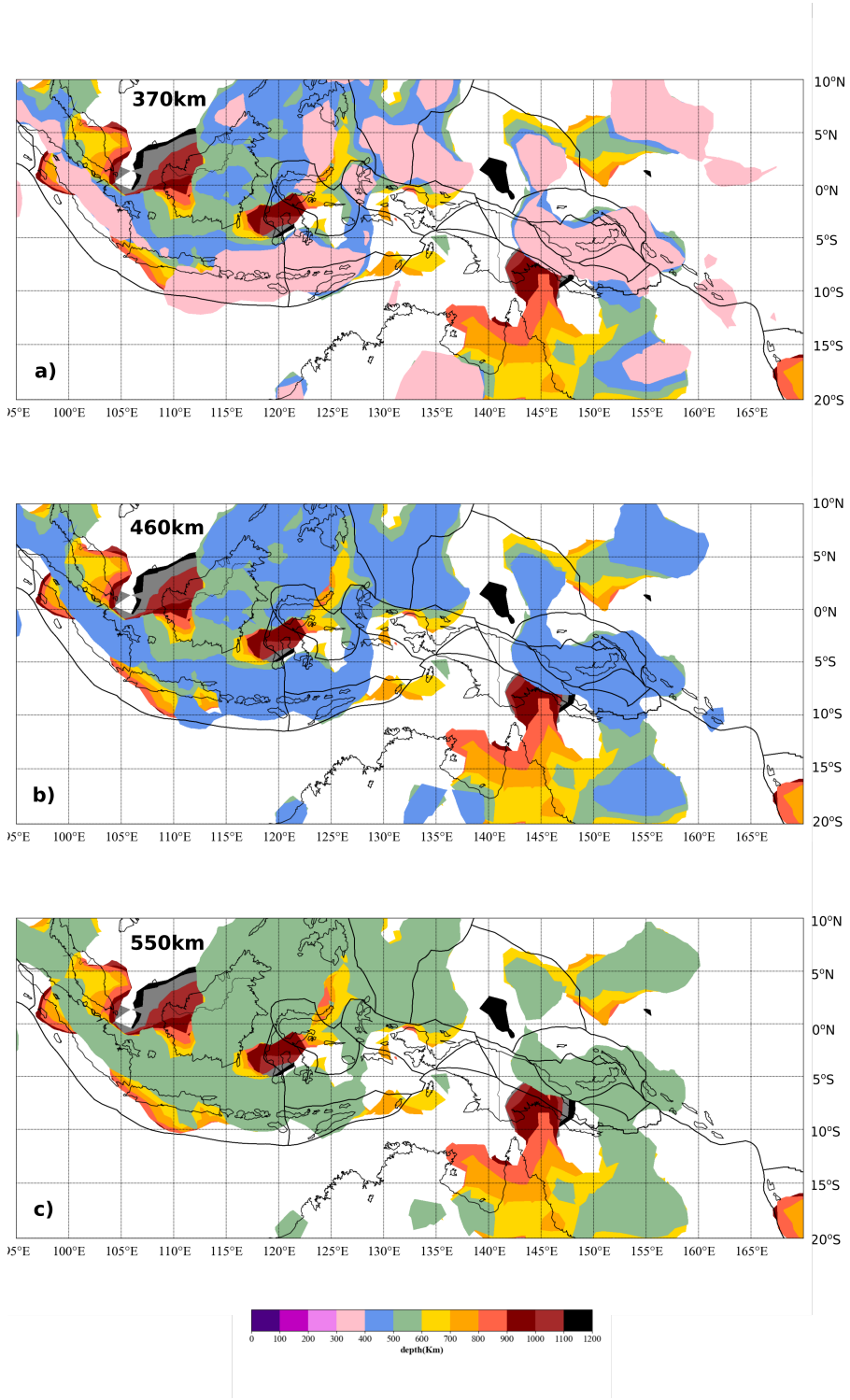

Figure 3.39: Contoured fast velocity anomalies for the JEABOX model, inset of southeast Asia at 370km, 460km and 550km. At each given depth , anomalies are contoured for values greater than +0.375%. a) 370km and above b) 460km and above c) 550km and above.

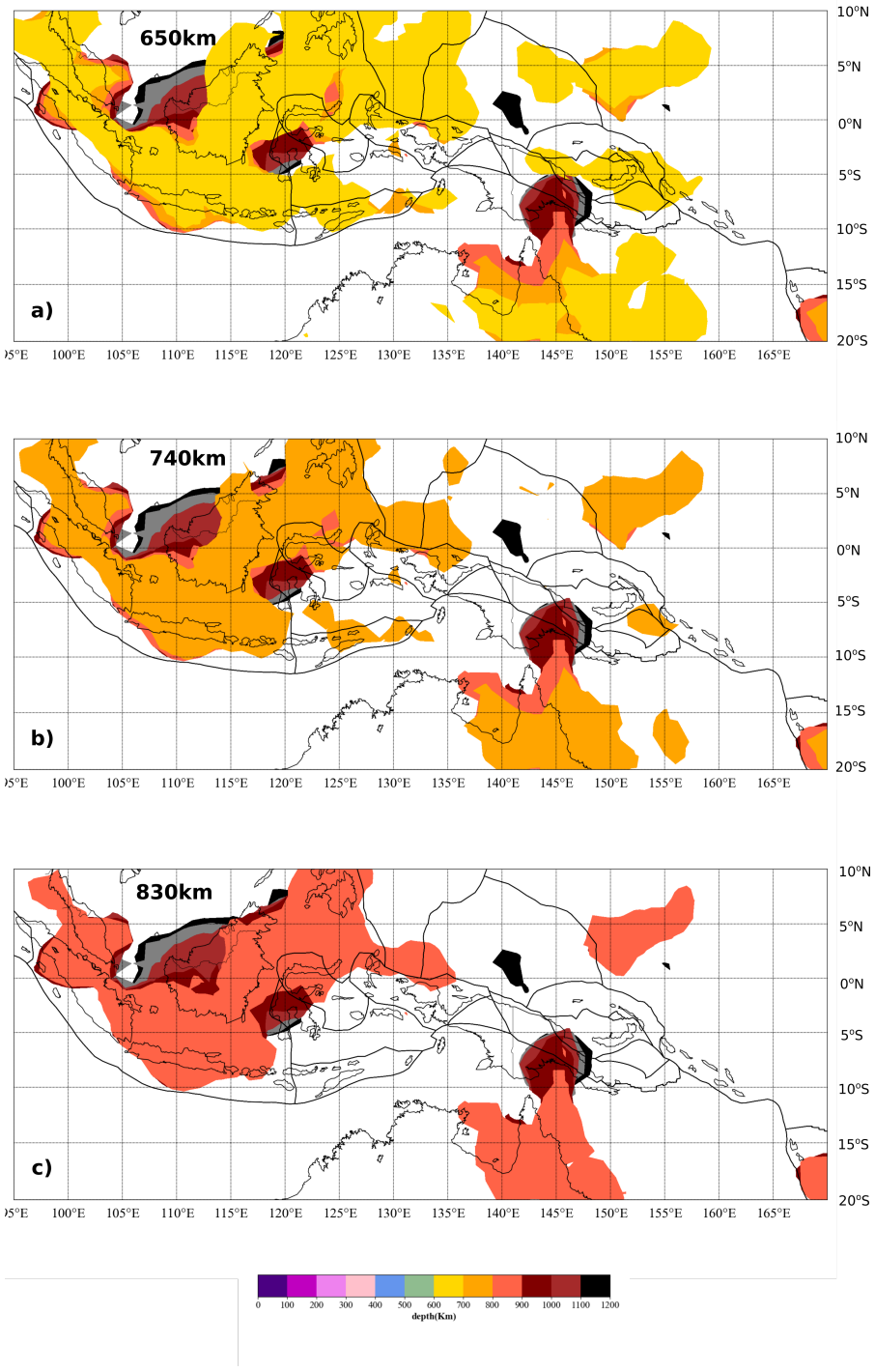

Figure 3.40: Contoured fast velocity anomalies for the JEABOX model, inset of southeast Asia at 650km, 740km and 830km. At each given depth , anomalies are contoured for values greater than +0.375%. a) 650km and above b) 740km and above c) 830km and above.

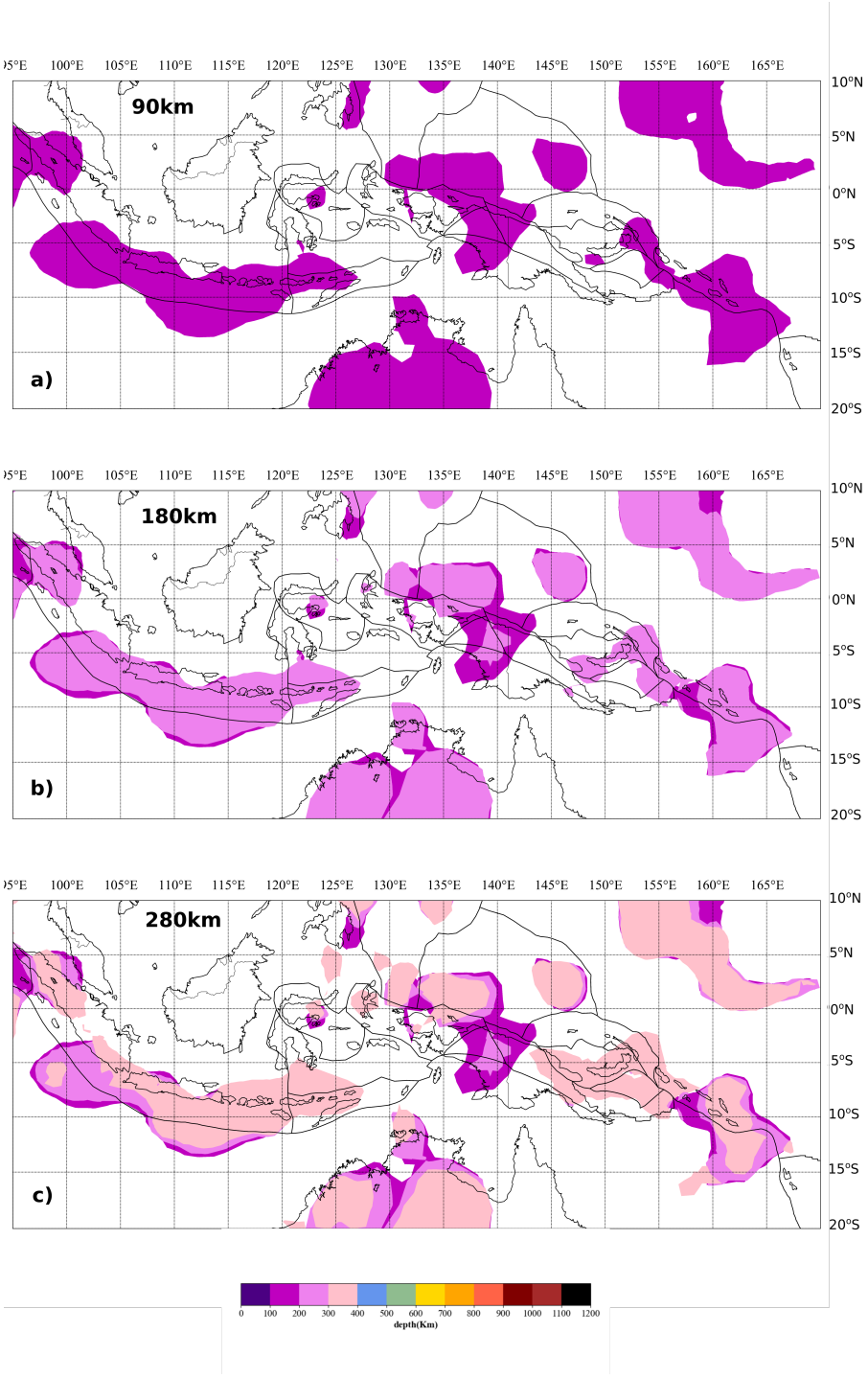

Figure 3.41: Inverted view of contoured fast velocity anomalies for the JEABOX model, inset of southeast Asia at 90km, 180km and 280km. At each given depth , anomalies are contoured for values greater than +0.375%. a) 90km and above b) 180km and above c) 280km and above.

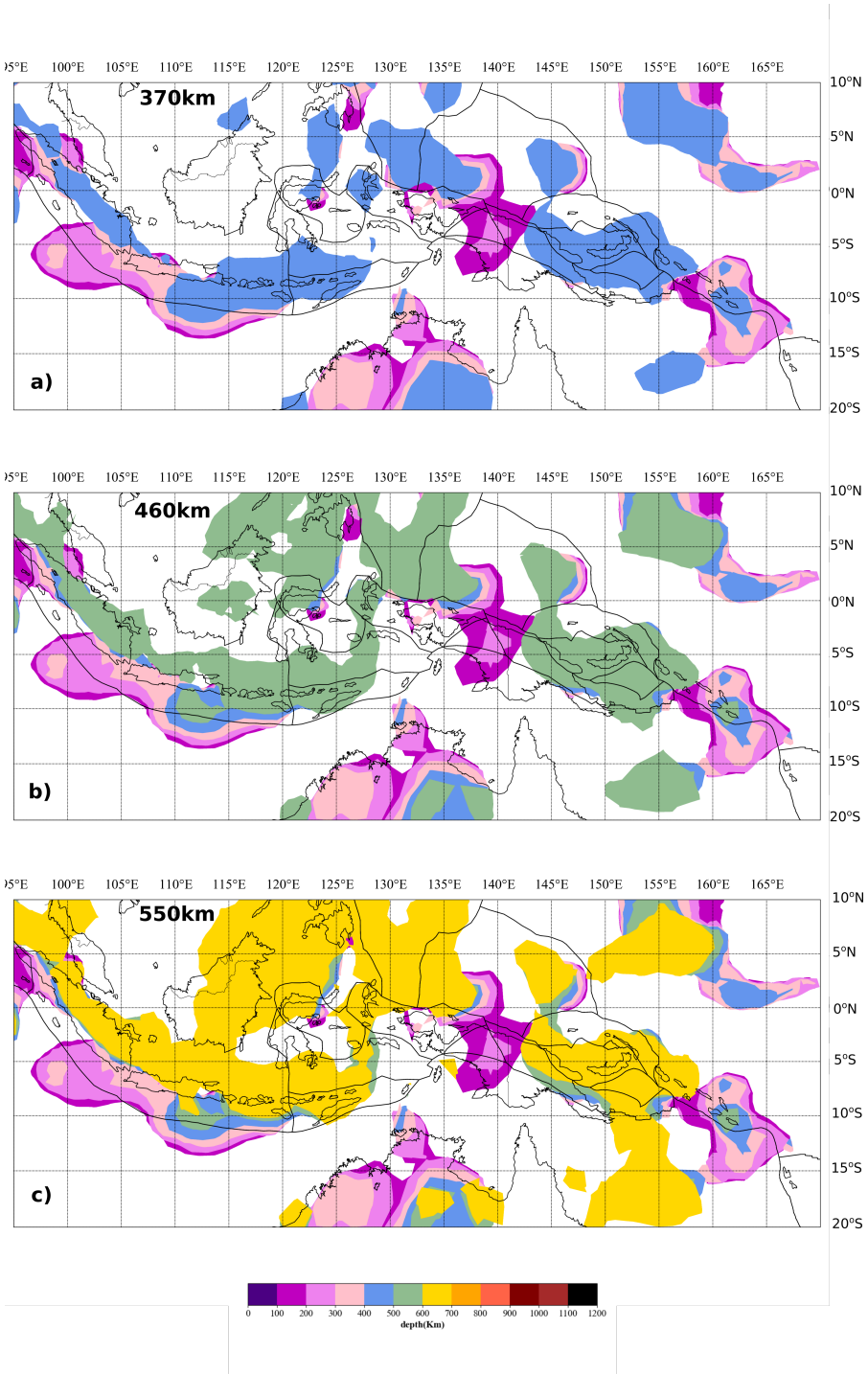

Figure 3.42: Inverted view of contoured fast velocity anomalies for the JEABOX model, inset of southeast Asia at 370km, 460km and 550km. At each given depth , anomalies are contoured for values greater than +0.375%. a) 370km and above b) 460km and above c) 550km and above.

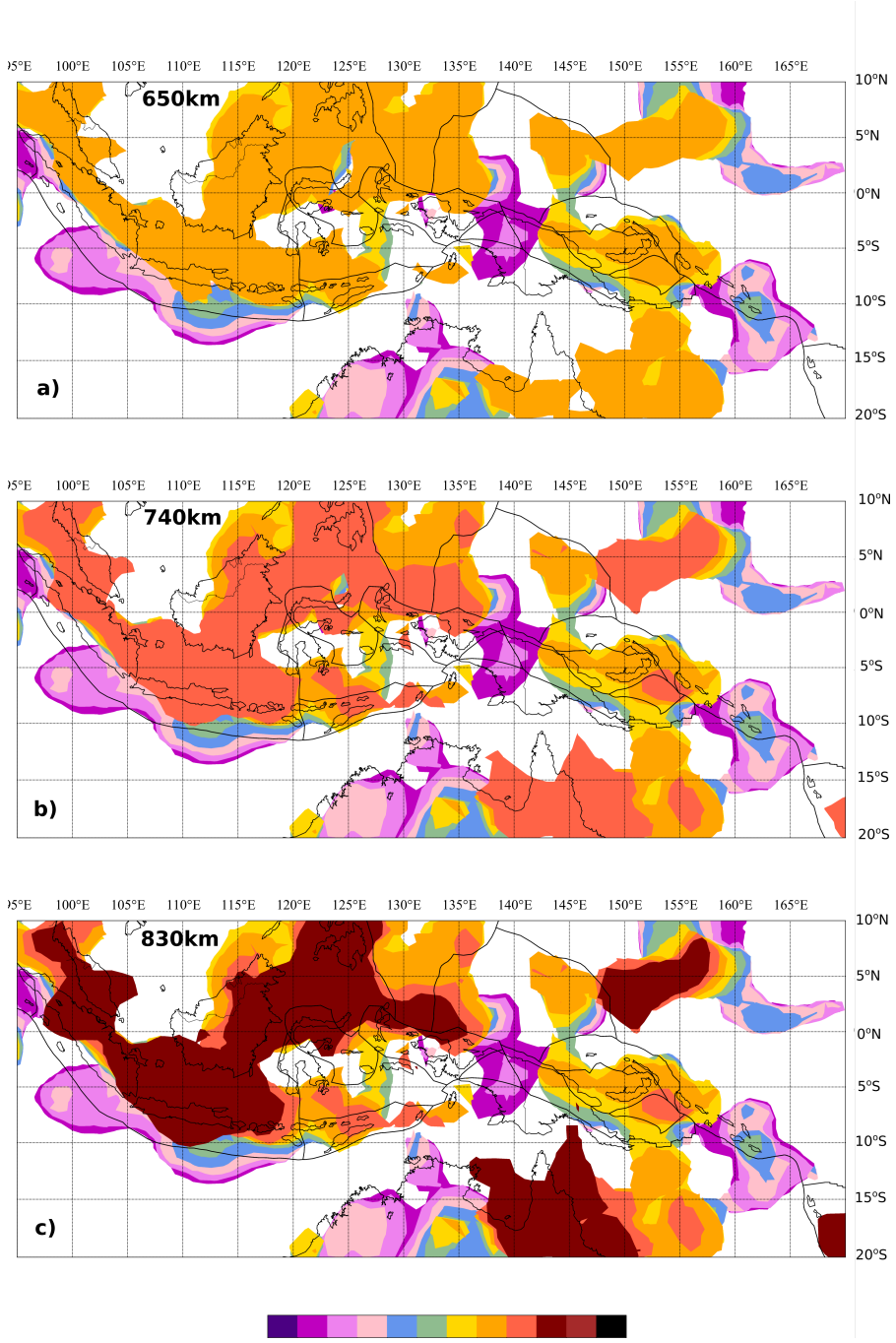

Figure 3.43: Inverted view of contoured fast velocity anomalies for the JEABOX model, inset of southeast Asia at 650km, 740km and 830km. At each given depth , anomalies are contoured for values greater than +0.375%. a) 650km and above b) 740km and above c) 830km and above.

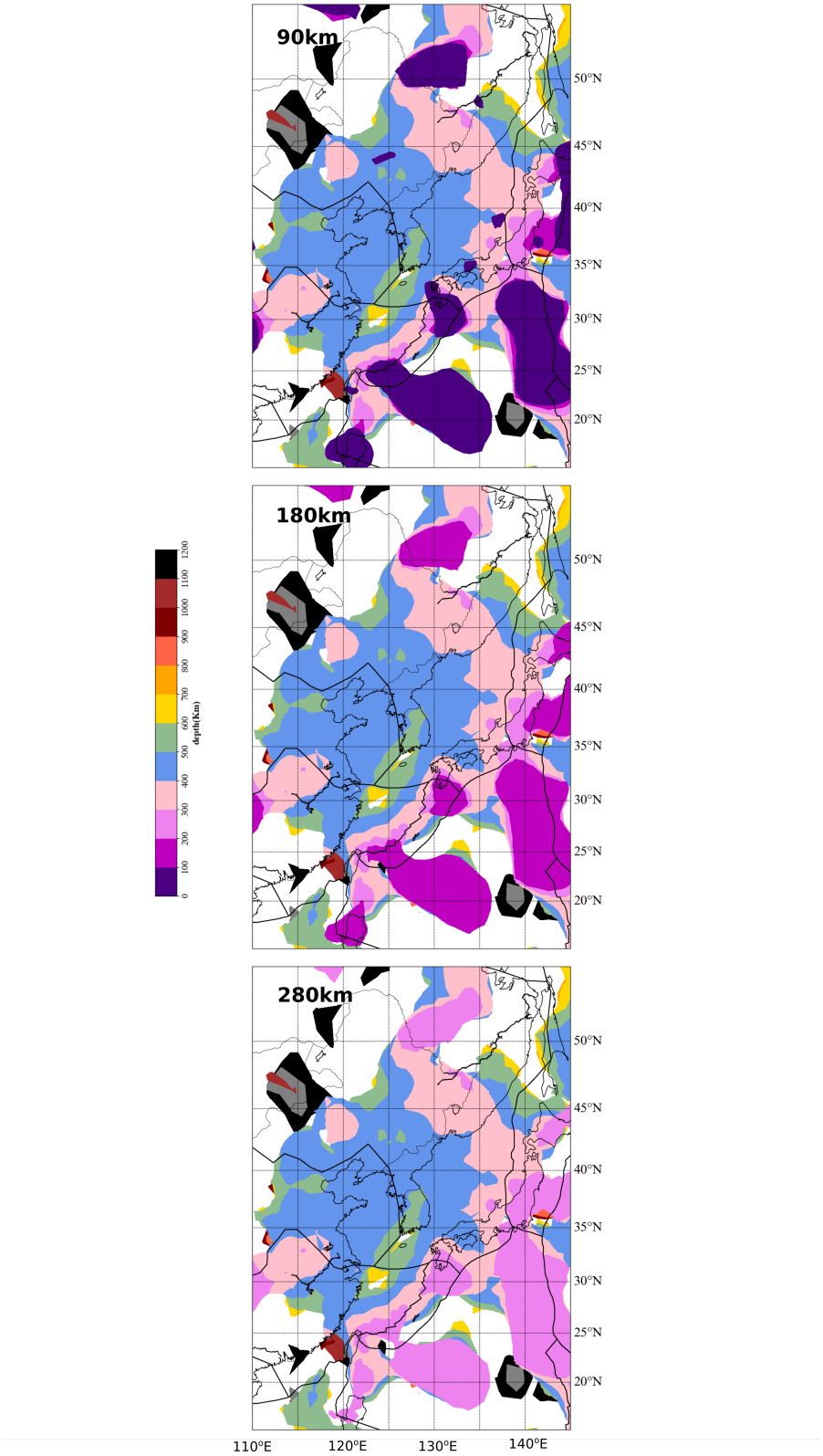

Figure 3.44: Contoured fast velocity anomalies for the JEABOX model, inset of southeast Japan at 90km, 180km and 280km. At each given depth , anomalies are contoured for values greater than +0.375%. a) 90km and above b) 180km and above c) 280km and above.

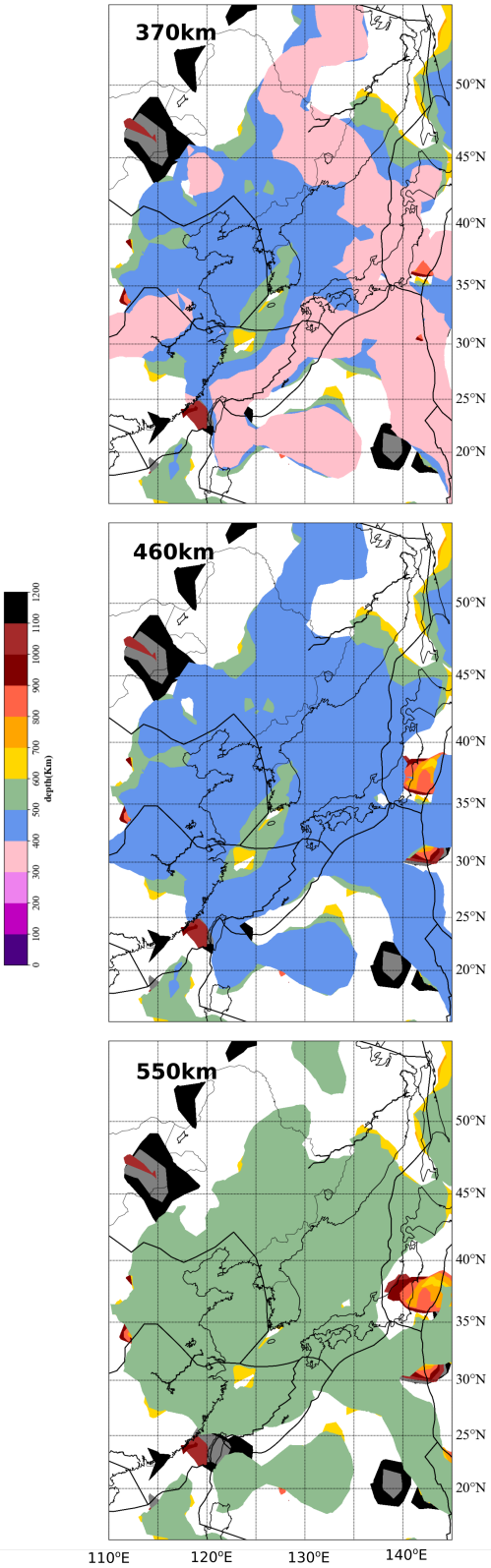

Figure 3.45: Contoured fast velocity anomalies for the JEABOX model, inset of southeast Japan at 370km, 460km and 550km. At each given depth , anomalies are contoured for values greater than +0.375%. a) 370km and above b) 460km and above c) 550km and above.

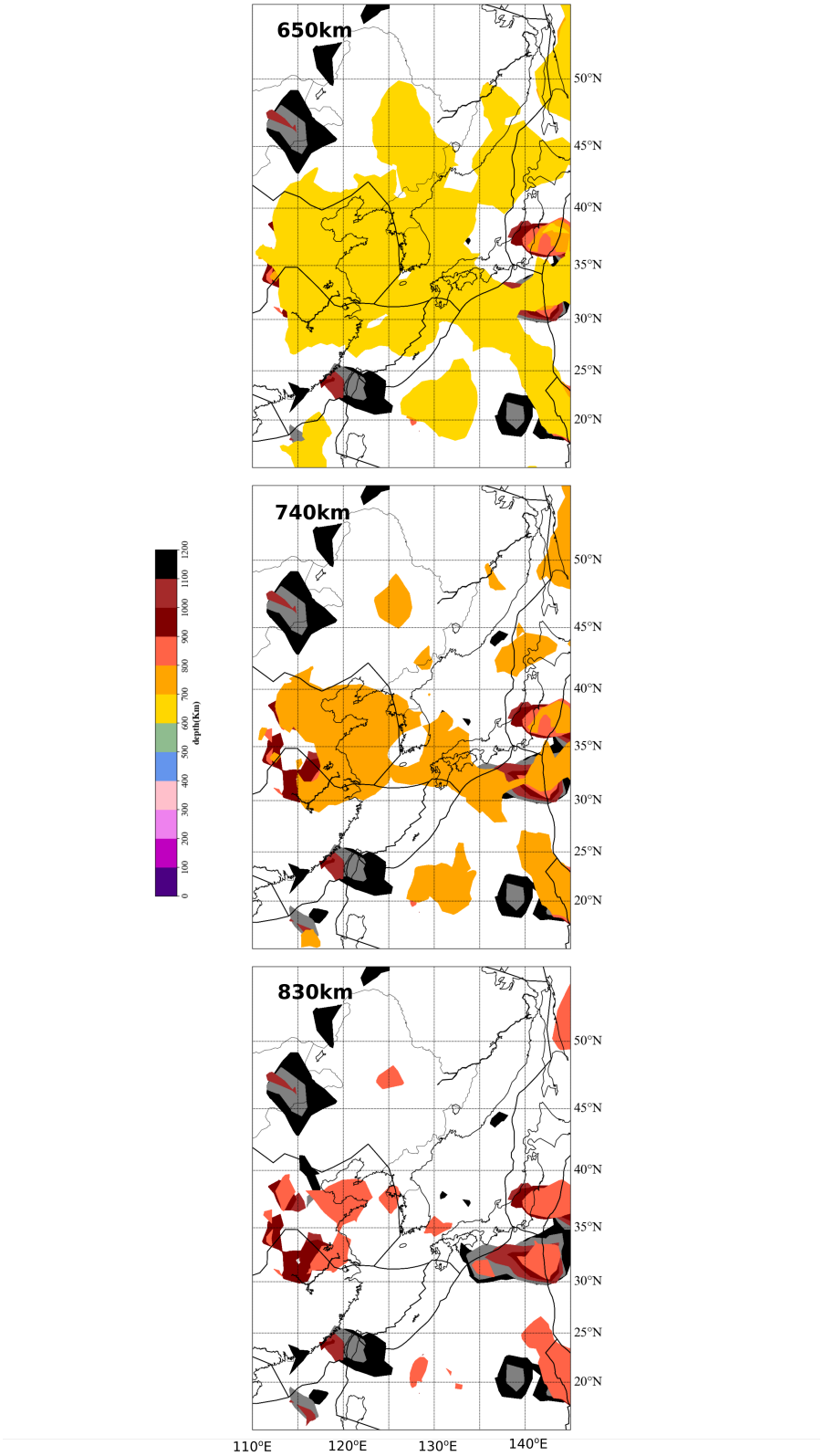

Figure 3.46: Contoured fast velocity anomalies for the JEABOX model, inset of southeast Japan at 650km, 740km and 830km. At each given depth , anomalies are contoured for values greater than +0.375%. a) 650km and above b) 740km and above c) 830km and above.

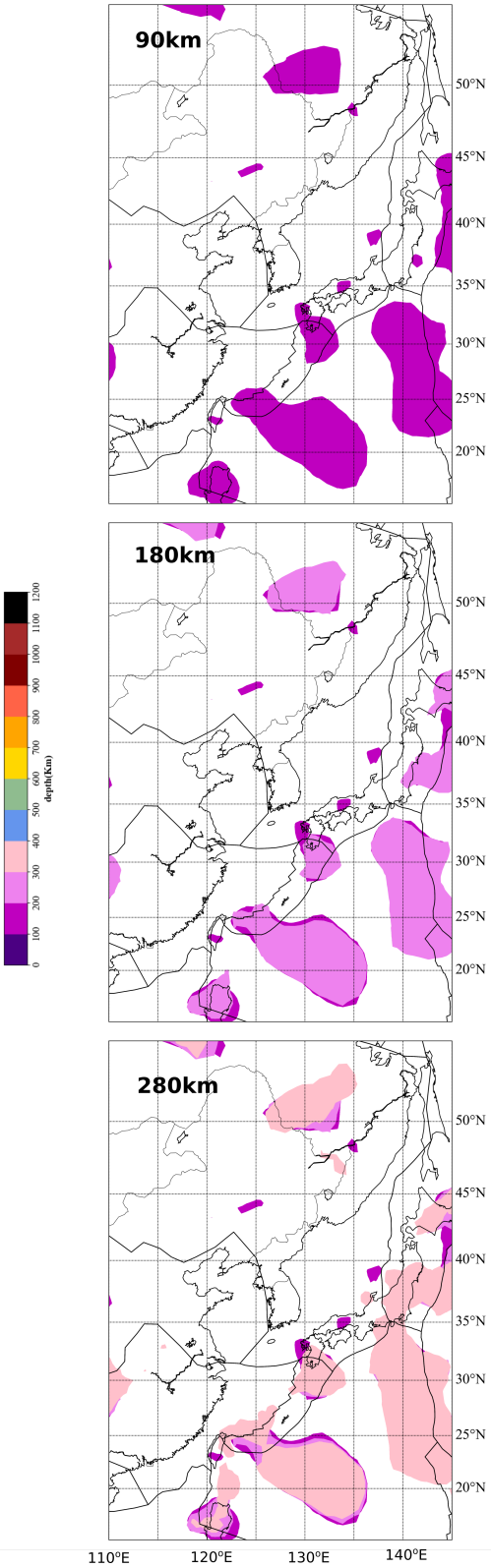

Figure 3.47: An inverted view of contoured fast velocity anomalies for the JEABOX model, inset of southeast Japan at 90km, 180km and 280km. At each given depth , anomalies are contoured for values greater than +0.375%. a) 90km and above b) 180km and above c) 280km and above.

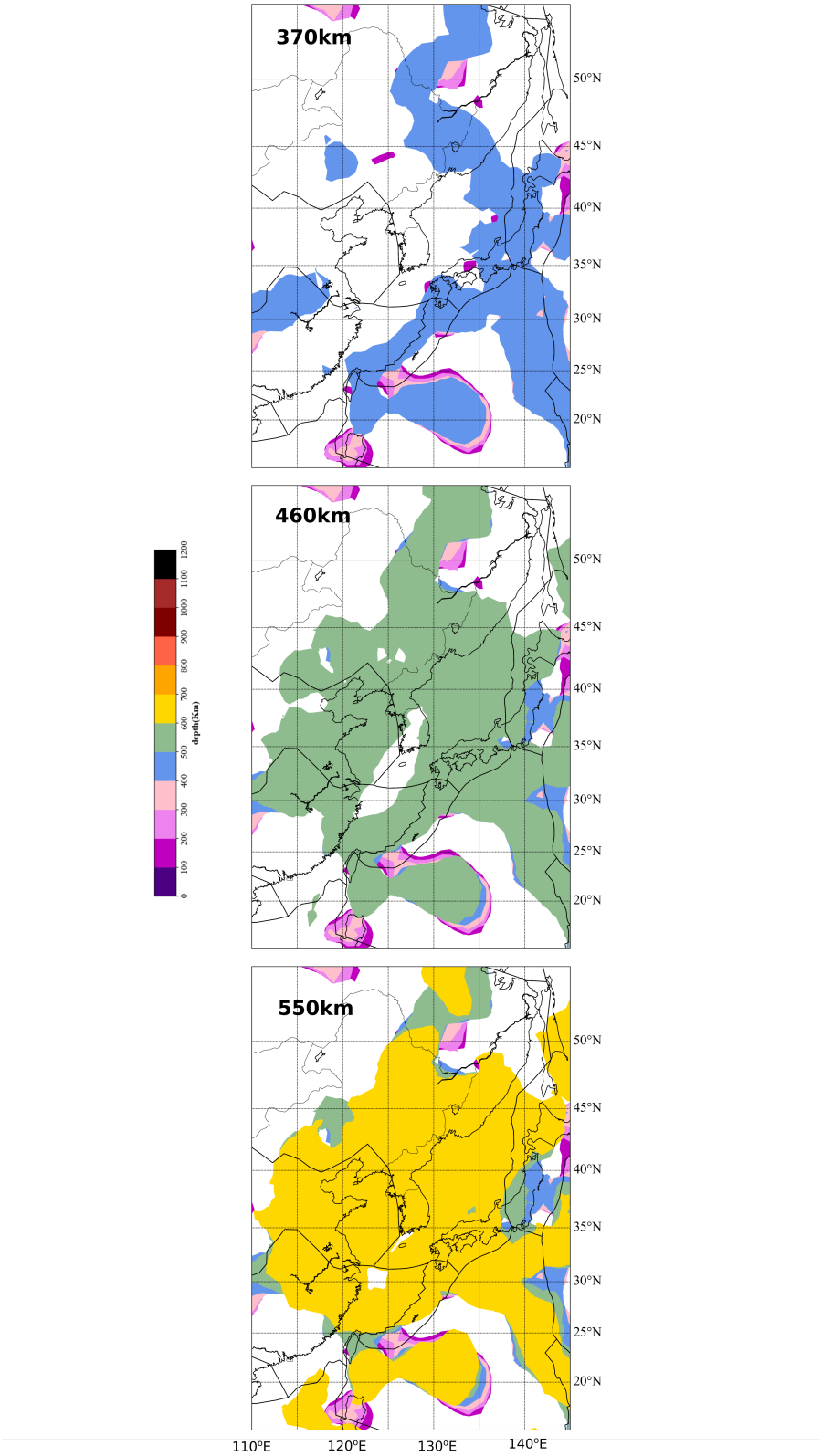

Figure 3.48: An inverted view of contoured fast velocity anomalies for the JEABOX model, inset of southeast Japan at 370km, 450km and 550km. At each given depth , anomalies are contoured for values greater than +0.375%. a)370km and above b) 450km and above c) 550km and above.

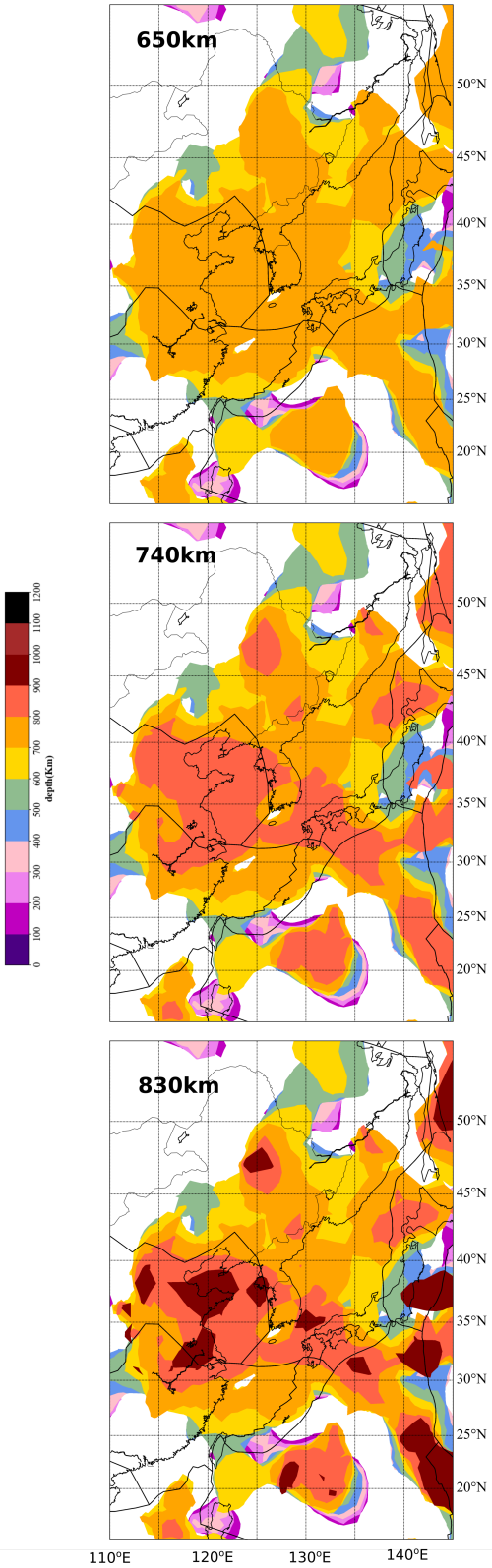

Figure 3.49: An inverted view of contoured fast velocity anomalies for the JEABOX model, inset of southeast Japan at 650km, 740km and 830km. At each given depth , anomalies are contoured for values greater than +0.375%. a) 650km and above b)740km and above c) 830km and above.

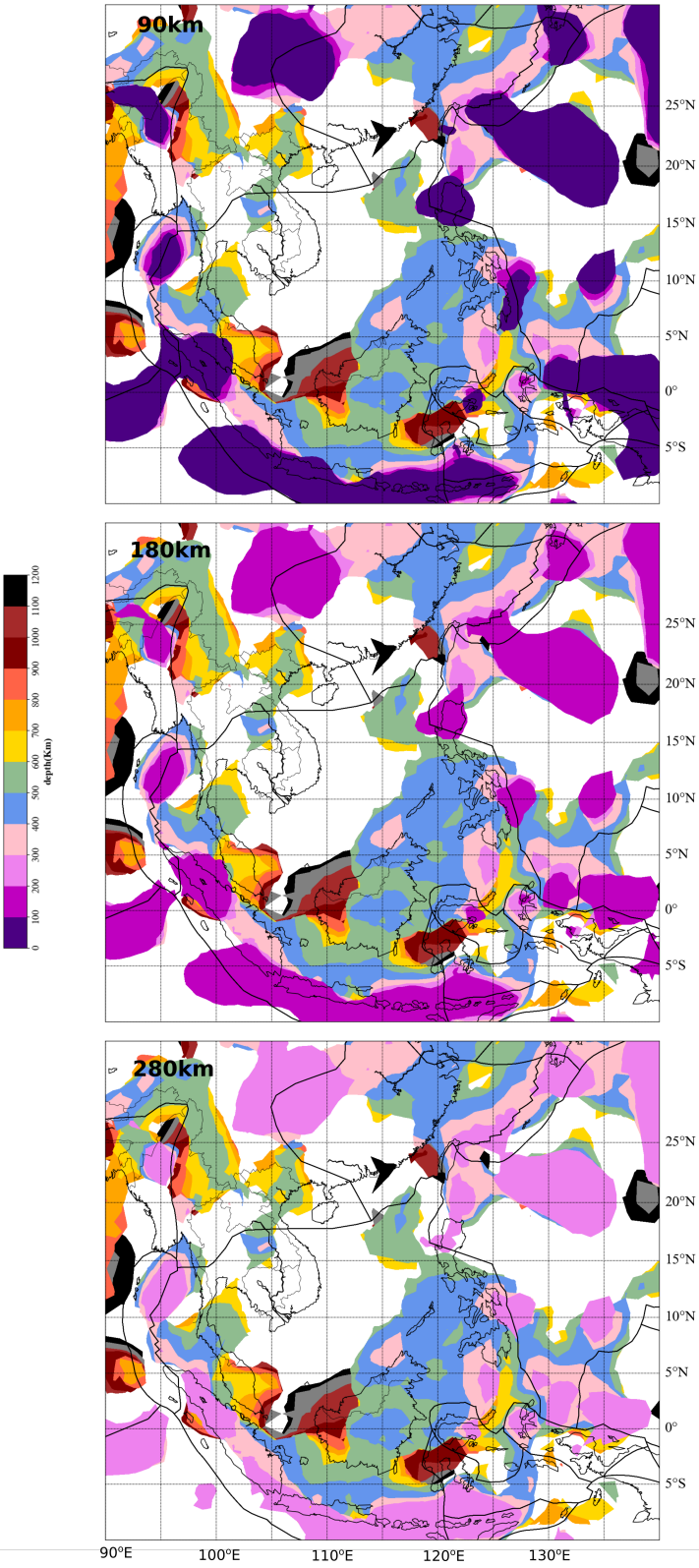

Figure 3.50: Contoured fast velocity anomalies for the JEABOX model, inset south of Taiwan at 90km, 180km and 280km. At each given depth , anomalies are contoured for values greater than +0.375%. a) 90km and above b) 180km and above c) 280km and above.

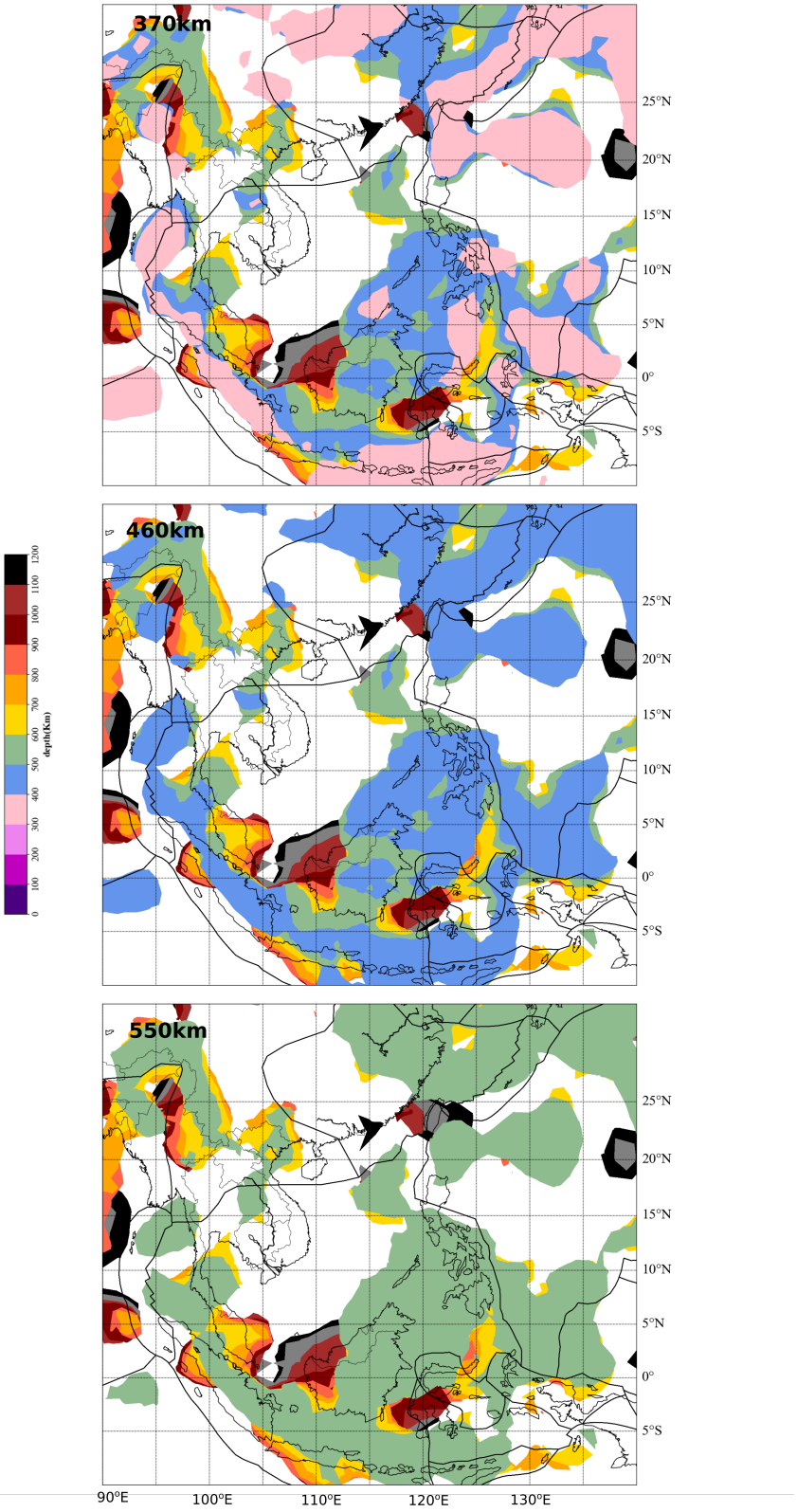

Figure 3.51: Contoured fast velocity anomalies for the JEABOX model, inset south of Taiwan at 370km, 460km and 550km. At each given depth , anomalies are contoured for values greater than +0.375%. a) 370km and above b) 460km and above c) 550km and above.

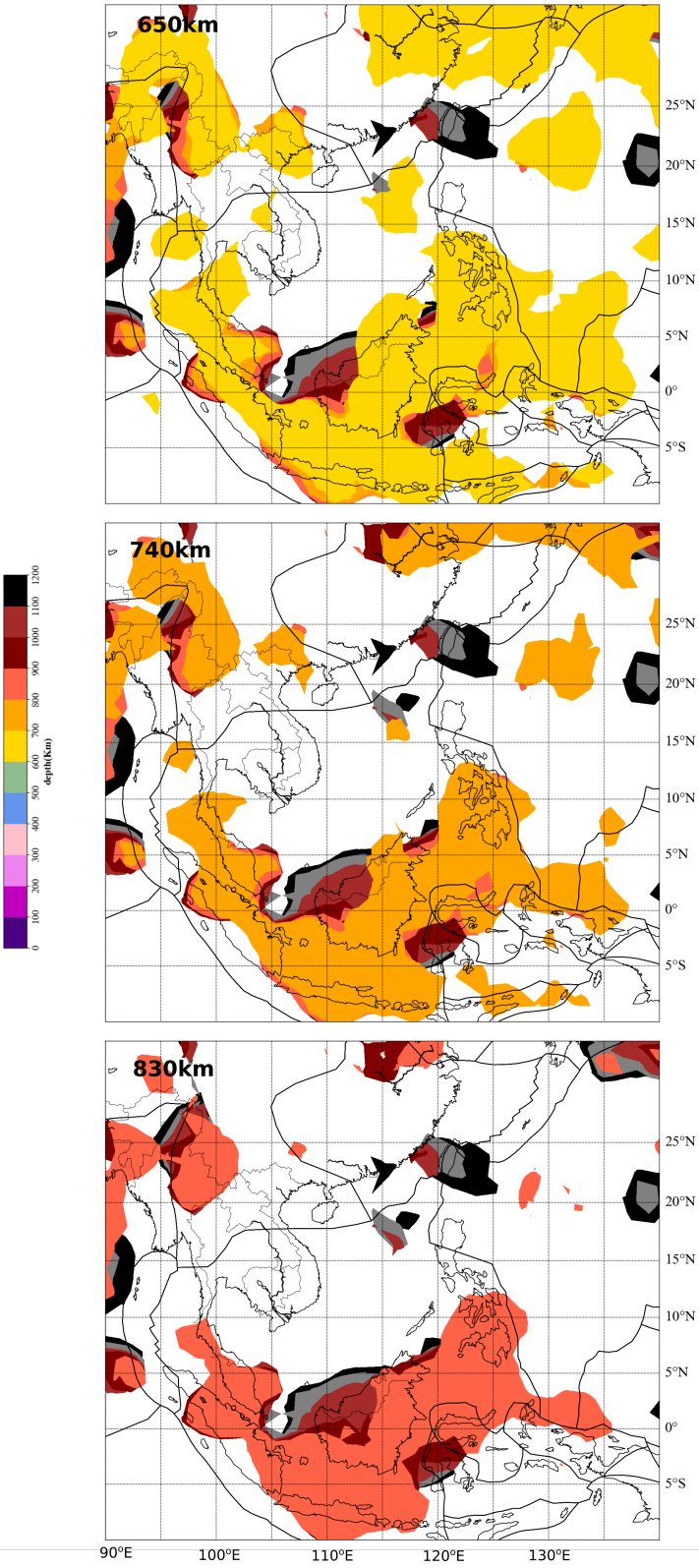

Figure 3.52: Contoured fast velocity anomalies for the JEABOX model, inset south of Taiwan at 650km, 740km and 830km. At each given depth , anomalies are contoured for values greater than +0.375%. a) 650km and above b) 740km and above c) 830km and above.

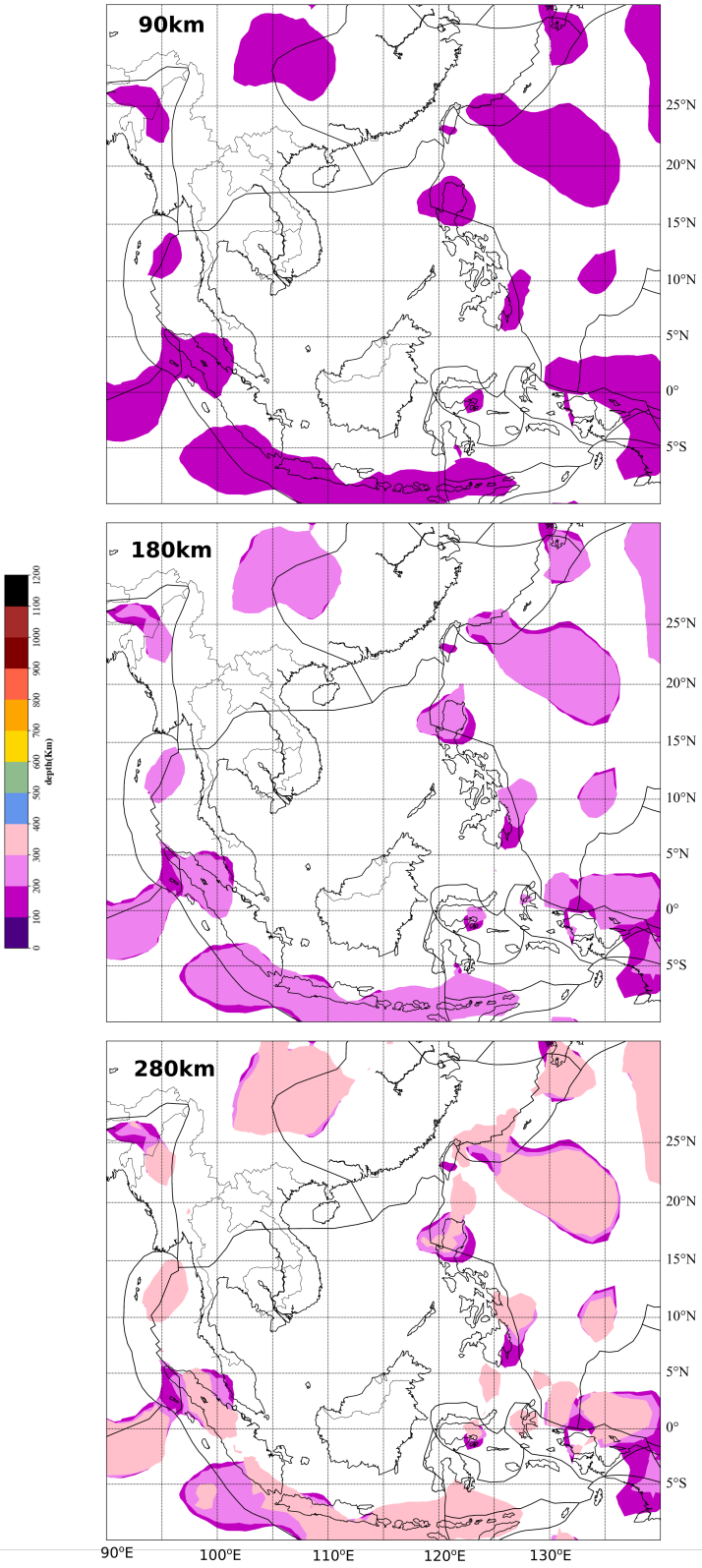

Figure 3.53: An inverted view of contoured fast velocity anomalies for the JEABOX model, inset south of Taiwan at 90km, 180km and 280km. At each given depth , anomalies are contoured for values greater than +0.375%. a) 90km and above b) 180km and above c) 280km and above.

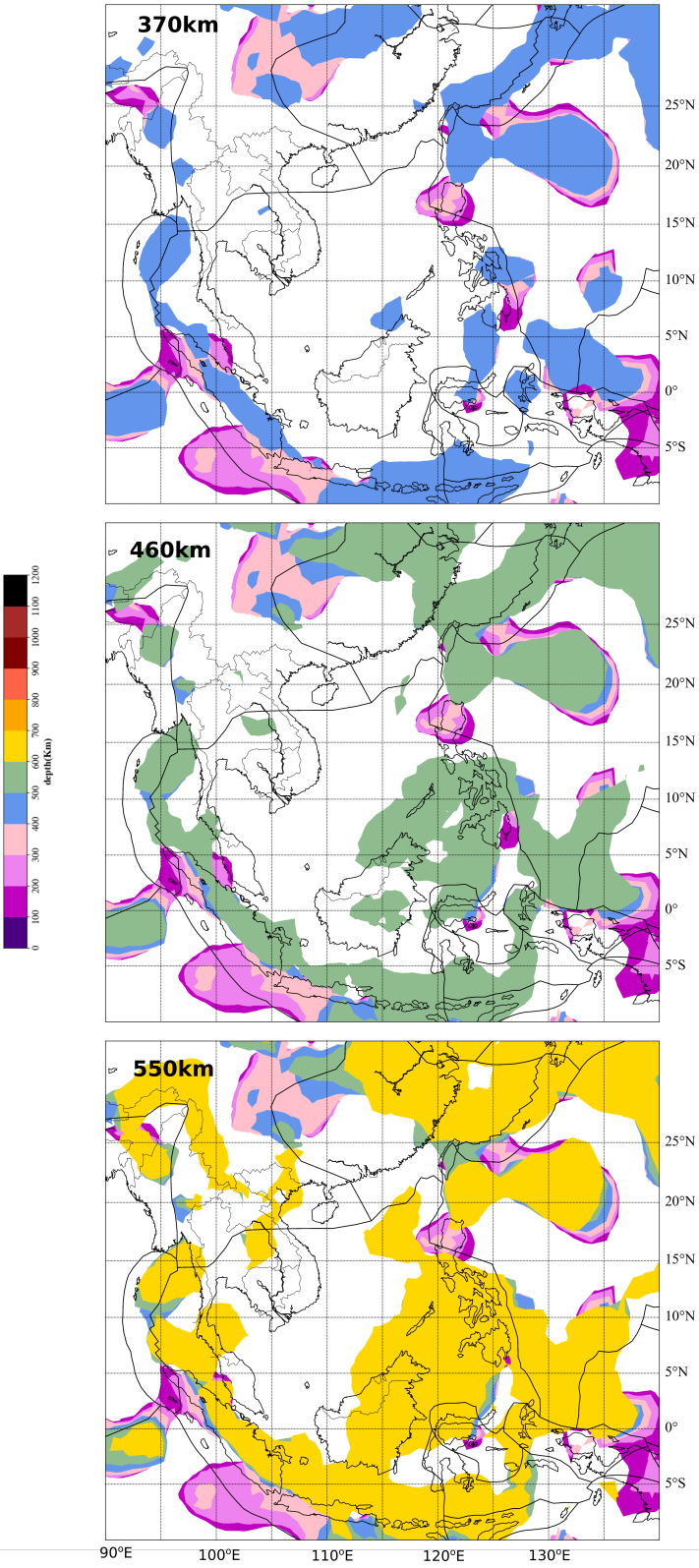

Figure 3.54: An inverted view of contoured fast velocity anomalies for the JEABOX model, inset south of Taiwan at 370km, 460km and 550km. At each given depth , anomalies are contoured for values greater than +0.375%. a) 370km and above b) 460km and above c) 550km and above.

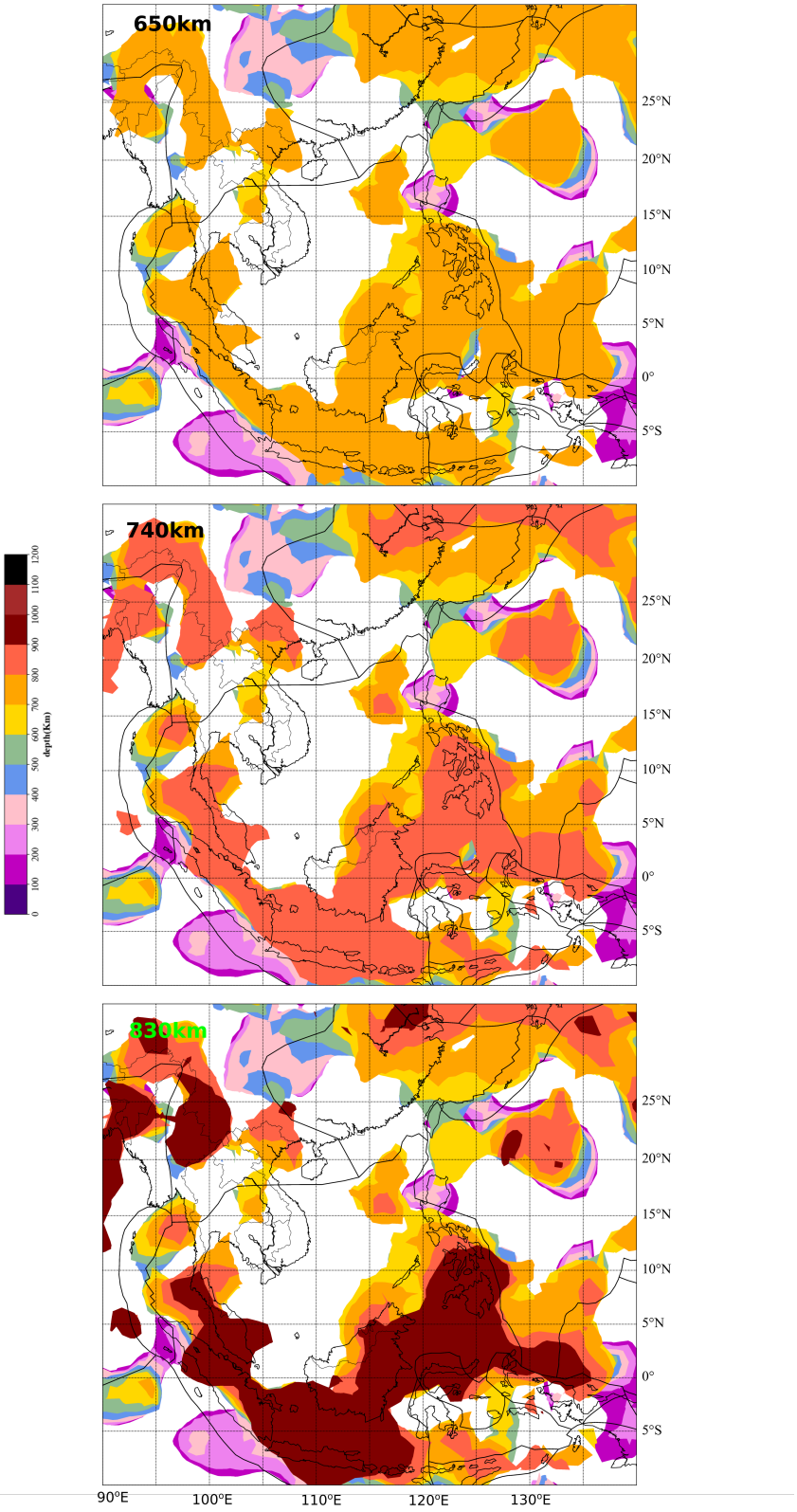

Figure 3.55: An inverted view of contoured fast velocity anomalies for the JEABOX model, inset south of Taiwan at 650km, 740km and 830km. At each given depth , anomalies are contoured for values greater than +0.375%. a) 650km and above b) 740km and above c) 830km and above.

...once I survived the fall landing in a trench scooped and jigsawed out/ of the earth hello earth nice to see you amazed to be alive.

— Stephen Sexton's *'Donut Plains 4' from 'If All the World and Love Were Young'*

4 Discussions and Conclusions

Contents

4.1 Discussion **145**
4.1.1 Japan and Izu-Bonin Slabs 145
4.1.2 Southeast Asia-Australia 150
4.1.3 Linking upper and lower mantle anomalies beneath east Asia 154
4.2 Summary **158**
4.3 Future work **161**

4.1 Discussion

4.1.1 Japan and Izu-Bonin Slabs

One key scientific motivation for creating the JEABOX tomography model is to attempt to improve our understanding of the morphology of subducted oceanic lithosphere, which appears to have stagnated in the mantle transition zone. Such subducted oceanic lithosphere, attributed to the Japan Arc, has been studied extensively. While there has been general consensus that slab is stagnated in the MTZ in this region (e.g. Fukao & Obayashi, 2013; Tao et al., 2018), its small-scale morphology is insufficiently imaged and is yet to be fully understood. JEABOX only resolves isotropic P-wave velocity: however, there are other models available that resolve for anisotropy, the directional dependence of seismic wavespeed. A case

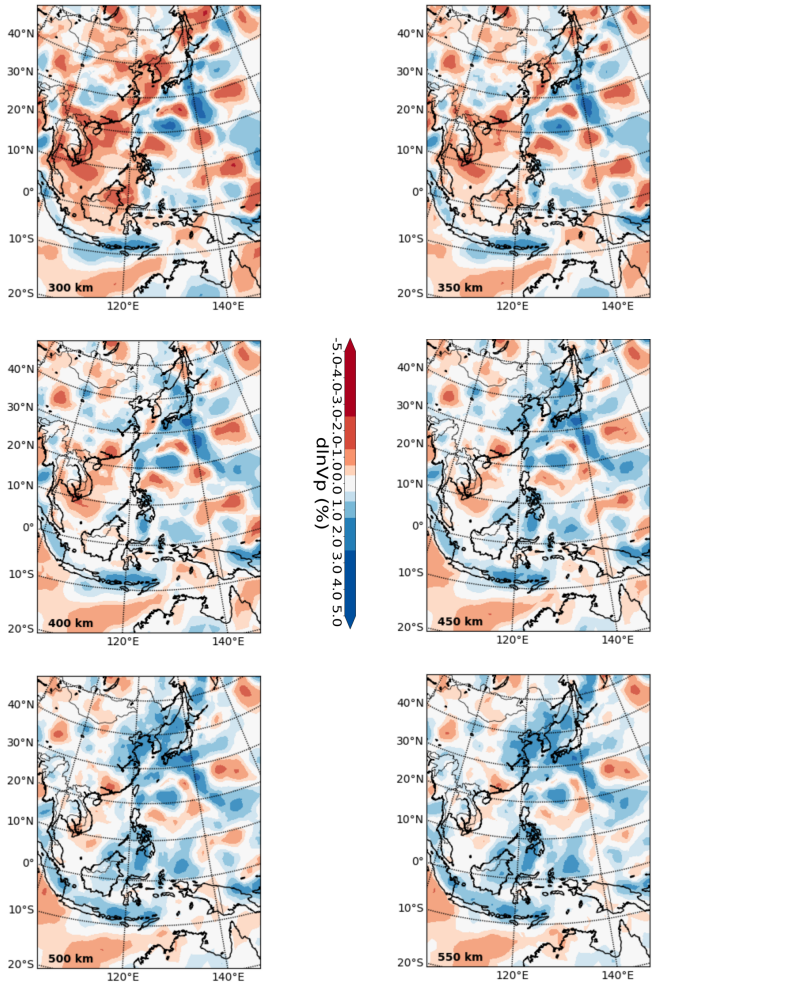

Figure 4.1: Plane view slices of JEABOX down to 550km.

study in point is Ma et al. (2019), who present a 3D P-wave model with azimuthal anisotropy. An important observation in their study is a sudden change from subduction parallel fast direction anisotropy above 400km depth, to subduction-perpendicular fast direction anisotropy. While this anisotropy could be attributed to sub-slab mantle flow uncorrelated to the subducted oceanic lithosphere itself, it is also possible that the anisotropy observed pertains to anisotropy within stagnant slab. Ma et al. noted that non-flat slab stagnation is a likely scenario: given that the stagnant slab appears to extend up to 2,000km to the west, they posit that resistance forces encountered by the front end of the slab could cause significant intra-slab deformation. Tomography slices form the JEABOX model matter because

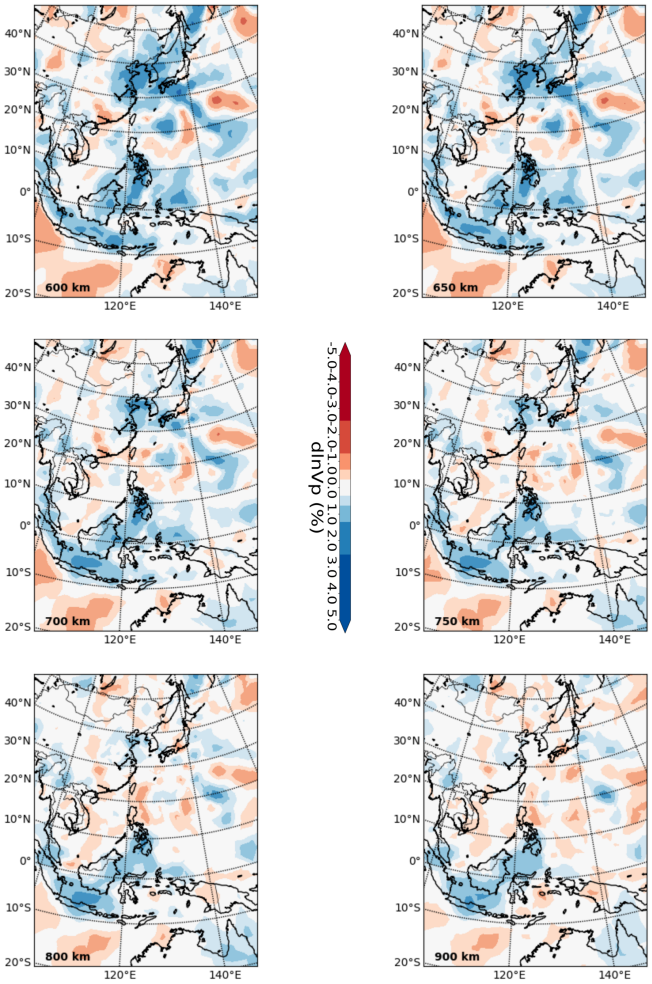

Figure 4.2: Plane view slices of JEABOX down to 900km.

they appear to exhibit sinuosity across several cross-sections in the Japan trench. The full waveform method presented in this study, predicated on regional waveforms, delivers an additional isotropic P-wave velocity model that evidences the non-flat deformation in stagnant slab hypothesized by Ma et al. (2019), in addition to confirming the lateral extent of slab stagnation related to the Japan trench.

As discussed previously, the JEABOX model appears to show a steeply diving seismically fast velocity anomaly related to the Izu-Bonin trench, and that its development takes place over a relatively short length scale (on the order of 100-200km) at the boundary of the Izu-Bonin trench : however, beyond this, further resolution tests are required to distinguish the smallest scale features

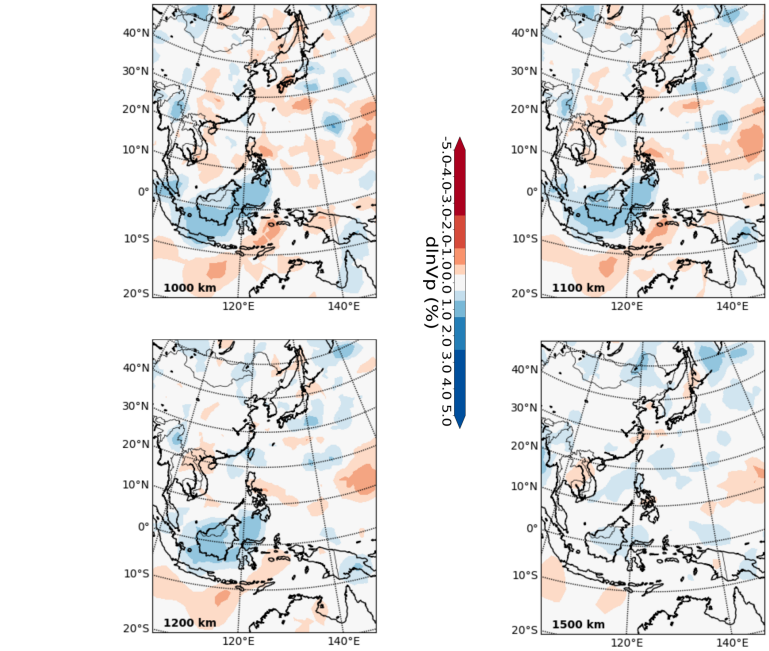

Figure 4.3: Plane view slices of JEABOX down to 1500km.

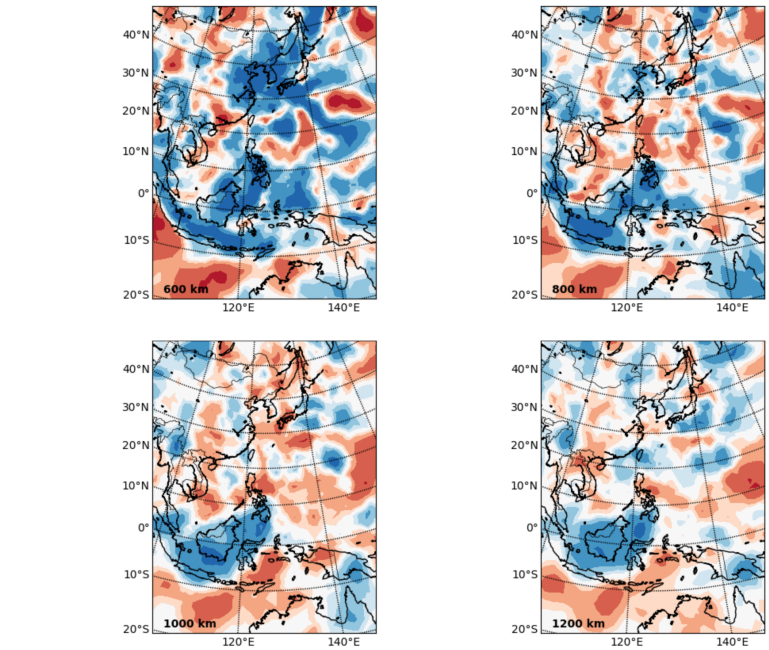

Figure 4.4: Plane view slices of JEABOX clipped at anomaly magnitudes of 1%.

interpretable in the JEABOX model proximal to these features. Tao et al. (2018) note poor resolution in their model near the Izu-Bonin slab, citing a relative paucity of seismic station coverage. It is worth noting that Ma et. al (2019) use an anti-clockwise toroidal trend in fast anisotropy directions, in tandem with their isotropic velocity model, to identify a slab tear at this boundary, relating the anisotropy to complex related corner flow through the slab tear. Without further resolution testing, JEABOX cannot evidence such a slab tear: however, the sharp change in slab subduction angle gives geometrical credence to the hypothesis of a slab tear.

While there is broad consensus on the two features detected in the JEABOX model discussed above, debate still centres around a seismically fast body in the mantle transition zone beneath eastern China (figures 4.1 and 4.2). Tao et al. deduce this feature to be a product of subduction of the relatively young Philippine Sea plate beneath Eurasia; however, Ma et al. (2019) contend that the size of the fast anomaly body implies that it is more likely to be attributed to the older, larger subduction of the Pacific plate. They argue that the stagnant slab in this region is an extension of the stagnant slab imaged northward of it, attributed to the Japan subduction. Here, the stagnant slab is a function of slab tearing at the junction between the Japan and Izu-Bonin slabs. In addition, they reconcile this hypothesis with the observed subduction angles of the Japan and Izu-Bonin (both Pacific) slabs and their posited separation depth. Further research is needed because this feature may hold the key to understanding the former tectonic behavior of the Philippine sea plate along its northwestern convergent plate margin. Cross-sections from the JEABOX model are important because I observe that, along east-west striking transects, the stagnant slab in the mantle transition zone emerges at roughly 25° north and remains a consistent feature progressively northward, along like-for-like longitudes. Figures A.48-A.51 and 4.1-4.2 show that, while the feature appears to connect to the seismically fast anomaly (which is attributed to the subducting Philippine Sea plate along the Ryukyu and northernmost southern Ryukyu trench) at upper mantle depths (410km), it is not possible to make a definite distinction between Philippine and Pacific slab in the MTZ at this location. Further resolution

tests will query whether the Philippine sea slab, from the surface to the top of the mantle transition zone, is a distinct seismically fast body from the stagnant slab in the MTZ, or whether there is connectivity. At this point in time, I would contend that this feature contains an amalgam of both Pacific and Philippine sea plate, that is predominantly Pacific plate, given the first-order strike of the feature and the pervasive extent of Pacific plate subduction.

4.1.2 Southeast Asia-Australia

As already discussed, the southern extent of the JEABOX model contains seismically fast anomalies that indicate the presence of protracted subduction throughout the entire upper mantle. Further tomography models are needed to be able to understand the subduction behavior along a convergent plate margin that extends from Sumatra through to the Banda arc. In addition to the subduction of the Indo-Australian plate from the south, there are also a suite of interfacing microplates near Sulawesi, as well as the Caroline plate north of Papua New Guinea, and the Philippine Sea plate to the north. Many of these trenches are oblique to one another: accounting for and comparing the seismologically observed slab-like features across tomography studies can help decouple the complex plate tectonic history of this region. JEABOX is an important addition due to its inclusion of regional waveform measurements, which can allow for interpretation of tomography, at MTZ depths, with confidence. Here I compare tomography slices with the joint P and S wave fast marching tomography study of Zenonos et al. (2019), alongside other tomography models. This study used an ISC travel-time dataset containing roughly 450,000 picks, to report a resolution of 130km in width for P-waves, and 220km for S-waves. Here I compare features resolved in their model with features recovered in JEABOX.

Along a north-south transect along roughly 105° longitude, Zenonos et al. (2019) identify subduction of the Australian plate under northern Sumatra down to at least 300km depth in their P-wave model. Fast velocity features are also seen at 600km depth, although they do not appear to be connected; however, along a similar transect in the S-wave model, the slab appears to marginally thicken

at the top of the transition zone and down to 500km depth. The fast velocity features in the uppermost lower mantle are also present. In the JEABOX model, the subducting Australian plate is also detected as moderately dipping toward the north and down to the top of the mantle transition zone (figures A.4 - A.6). The fast velocity body appears to thicken in the transition zone, and continues right down to 1,000km. The JEABOX P-wave model feature bears more resemblance to the S-wave slice of Zenonos et al. (2019) than it does to the P-wave model slice. While the JEABOX model honours regional P-wave measurements in a full waveform sense, the earthquake catalogue used by Zenonos et al. (2019) is much larger. In conclusion, JEABOX agrees strongly in first order Australian slab structure above the mantle transition zone, but presents with thickened slab material in the MTZ, along this transect.

Repeating the process, JEABOX helps provide insight into the debate centred around a slab gap in the subducting Australian plate beneath Java through to Sumbawa, to the east of Sumatra. Zenonos et al. (2019) report what appears to be more-or-less continuous slab subduction throughout the entire upper mantle, for a north-south P-wave transect along 118° longitude. which is not present in their S-wave model. There is evidence for a small hole in the slab at the top of the mantle transition zone, based on their model. The JEABOX model presents slightly differently to their findings along this transect, exhibiting a north-dipping fast velocity body, perceived as Australian slab, right down to the base of the MTZ. In addition, a much larger, fast velocity body is visible between roughly 660km and 1,000km depth just northward of the slab. This in turn blends into what appears to be infilled fast velocity in the mantle transition zone; although, I note that some of this infilled fast velocity (figures A.7-A.12) may be attributed to additional westward subduction of another slab, which will be discussed in the coming paragraphs. Based on observations in the JEABOX slice, there may be a slab gap due to dislocation between flat lying slab in the mantle transition zone and rollback of upper mantle Australian slab.

Beneath Java, which is between Sumbawa and Sumatra, JEABOX presents with what could be interpreted as either significant thinning or a slab gap in the subducting Australian slab at mantle transition zone depths, along a north-south 110° longitudinal transect, which is also seen in the P-wave model of Zenonos et al. (2019). This feature confirms several previous studies of the same transect. Zenonos et al. (2019) rightly point out that Fukao et al. (1992) argued that the subducting slab in the Java region dived steeply towards the mantle transition zone. Critically, Fukao et al. (1992) also advocated for the thickening and consequent buckling of subducted slab at mantle transition zone depths to form what they referred to as a high density megalith, which could penetrate into the lower mantle. I contend that such a megalith hypothesis agrees well with adjacent cross-sectional slices of the JEABOX model. Along similar transects right out to roughly 116°, the tomography slices present as a continuous subduction zone throughout the upper mantle and well into the lower mantle. In addition, a second limb can be seen to stagnate in the mantle transition zone. This overall slab geometry bears the hallmarks of a sinking, dense area of oceanic lithosphere, with ongoing slab stagnation at mantle transition zone depths. It is also in keeping with the idea of Zenonos et al. (2019) that, given the paucity of seismicity around 400km depth and tomographic evidence for slab thinning, the slab spreads orthogonal to the strike of the subduction zone. I note, however, that JEABOX shows continuous slab subduction throughout the upper mantle along 115° longitude, where they identify a hole in the slab at roughly 400km depth. Hall & Spakman (2015) similarly identify a slab gap between roughly 250-400km depth. One of the reasons why JEABOX does not detect this slab gap could be a relative lack of seismic coverage compared to other studies and knock-on effects for localised resolution. I have higher confidence in the model resolution of JEABOX at and below mantle transition depths.

Next, I compare east-to-west cross-sections of JEABOX with other state of the art tomography models of the southern Pacific in an effort to provide further insight into the subduction regimes of the region. Along a transect along roughly 2° latitude, Zenonos et al. (2019) identify what appear to be the westward-dipping Sangihe slab

and eastward-dipping Halmahera slabs beneath the Molucca Sea, a site of arc-arc collision. The former is believed to penetrate into the lower mantle whilst the latter is believed to only reach the top of the mantle transition zone. This is confirmed by Zenonos et al. (2019). JEABOX confirms further the westward dipping Sangihe slab which appears to penetrate into the lower mantle, with key differences. The slab appears to aggregate towards the west to a greater extent than other models in the mantle transition zone; however, other seismic fast velocity anomalies below the MTZ, much larger in size, blend into the trend of the Halmahera slab. Further resolution tests must be carried to clarify slab structure below the MTZ in this region. Regarding the Halmahera slab, JEABOX detects a seismically fast velocity body along the transects in question (figures A.35-A.37) that terminates in the transition zone, but the dip of this feature is variable and does not appear to be well resolved.

Further south, JEABOX corroborates to first order the identification of the westward subducting Banda slab (figure A.33). Its dip is steep in the upper mantle, then it appears to accumulate laterally in the mantle transition zone, before penetrating into the uppermost lower mantle. Zenonos et al. (2019) also detect the Banda slab, although in their model, the slab has a more or less moderate and continuous dip from 200km right through to 800km depth. This is apparent in both their P-wave and S-wave models. JEABOX presents with a new tomography method that uses full waveform based measurements of regional waveforms: the divergence in slab morphology with other models may be to do with the improved seismic illumination at mantle transition zone depths. I do, however, concede that data coverage is deficient with respect to other studies which use eathquakes with a low moment magnitude, due to the moment magnitude cap (Mw 5.8-6.9) used in this study. Similarly, in plane view, JEABOX exhibits a curved geometry to the seismically fast anomaly beneath the Banda arc and is most visible between 300km and 550km depth: this is a slight contrast to other studies, which resolve this curved geometry from as shallow as 200km depth.

4.1.3 Linking upper and lower mantle anomalies beneath east Asia

It is worth noting at this point that the JEABOX model is slightly biased towards fitting regional P-wave data, which make up a small subset of the overall dataset used in inversion i.e. the model has been tuned to fit data that samples from the mantle transition zone down to roughly 1,000km depth. It is therefore of interest that JEABOX confirms, to first order, a number of the extant seismically fast velocity bodies detected by prior global tomographies. This is particularly evident in plane view slices of the JEABOX model. Figure 4.5-4.6 shows comparisons of plane view slices of the JEABOX model with votemaps at different depth slices, created by Parsons and Hosseini (pers. comm, 2022), which were created in SubMachine, a quantitative tomography comparison tool (Hosseini et al., 2018). The votemaps represent agreement between the DETOX P2 (Hosseini et al., 2019), GAP P4 (Obayashi et al., 2013), LLNLG3DV3 (Simmons et al., 2012), MITP08 (Li et al., 2008) and UUP07 (Amaru, 2007) P-wave models. Votemaps are constructed for common features between one or more velocity models, with fast structure perturbations to the background model greater than 0.5% dVp. One of the main common features of interest between JEABOX and the votemaps of the other models is the first order continuity of the Indo-Australian slab, stretching from Sumatra right through to Java, throughout the transition zone and uppermost lower mantle. As mentioned previously, more resolution tests are needed beneath southeast Asia before any significant tomotectonic interpretation of the model is carried out.

Another feature of interest is the consistent evidence of subduction in both the votemaps and JEABOX along the Izu-Bonin and Marianas trenches. The arcuate geometry of the Marianas slab is particularly apparent in JEABOX, across the MTZ and into the uppermost lower mantle. Also apparent is the seismically fast anomaly beneath Korea, the Yellow Sea and eastern China. Here I discuss these two features and how they evolve in depth, in context of the Pacific plate's recent subduction history, at and below the mantle transition zone. This is important in order to understand the history of the Philippine Sea plate as well, where

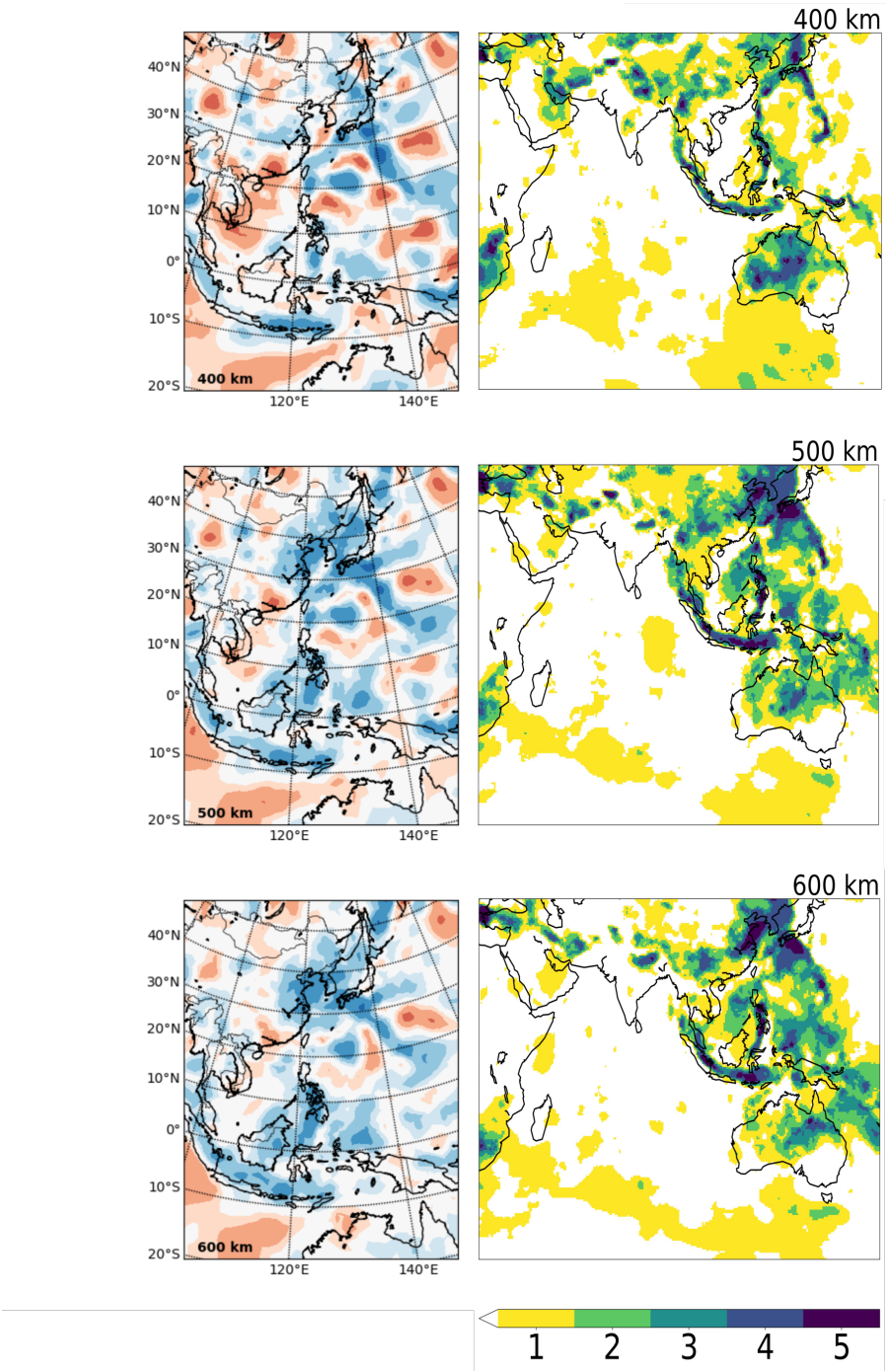

Figure 4.5: Votemap depth slices (Parsons & Hosseini, pers. comm.) of high velocity structures in the western Pacific, compared with JEABOX, to 600km depth. Votemaps were created using the DETOX-P2, GAP P4, LLNLG3DV3, MITP08 and UUP07 models. The JEABOX colour scale is bounded between -5% and 5% as per the figures shown previously.

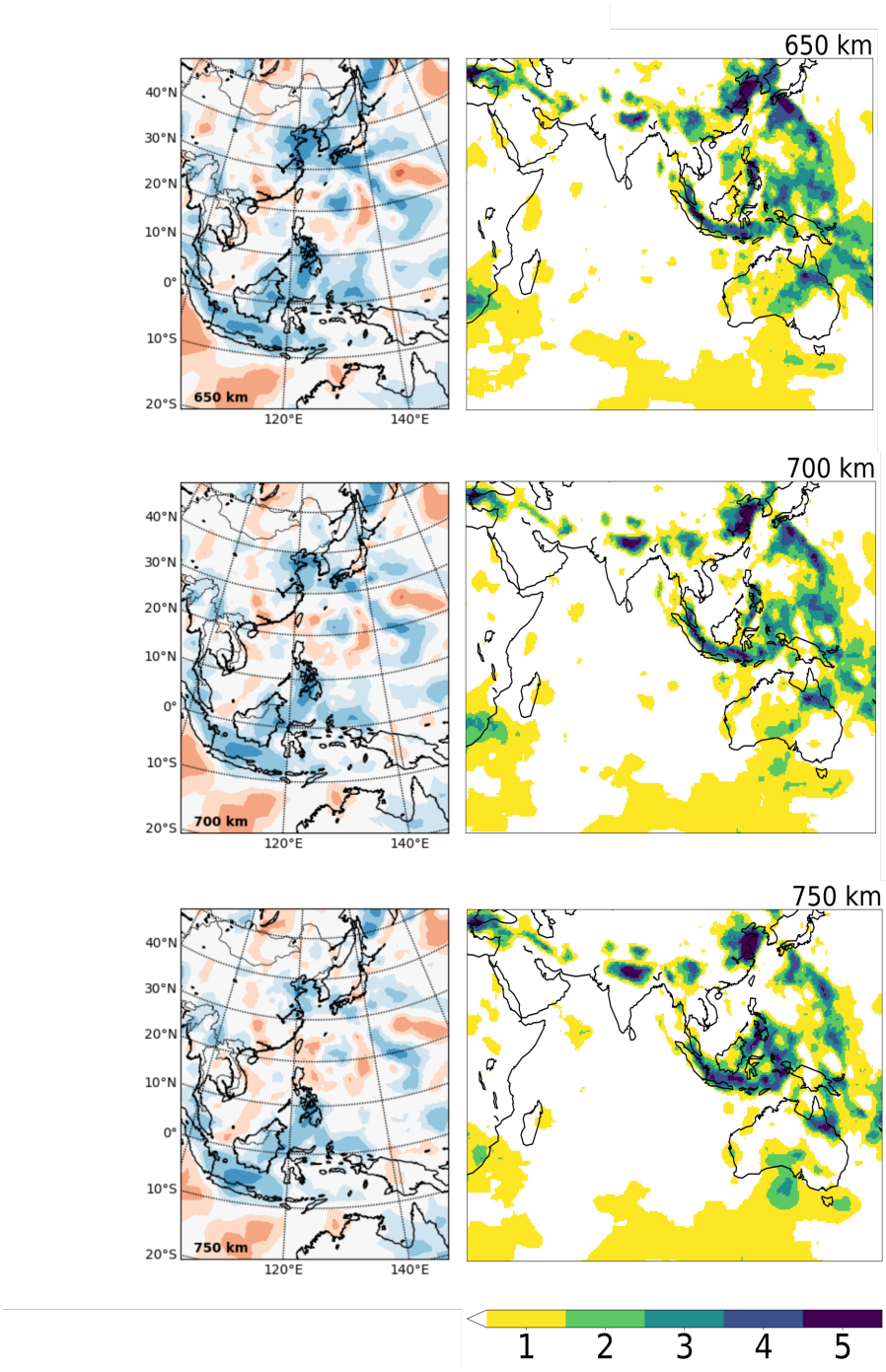

Figure 4.6: Votemap depth slices (Parsons & Hosseini, pers. comm.) of high velocity structures in the western Pacific, compared with JEABOX, to 750km depth. Votemaps were created using the DETOX-P2, GAP P4, LLNLG3DV3, MITP08 and UUP07 models. The JEABOX colour scale is bounded between -5% and 5% as per the figures shown previously.

seismic resolution is poor, by considering the related plate tectonic history, in regions with sufficient resolution.

The most recent plate tectonic model of the east Asian margin was carried out by Wu et al. (pers comm.; 2022). By creating a fully kinematic plate model of the region, by adding to the global plate model of Matthews et al. (2016), they reconciled the main tomography features in the MITP-08 P-wave model (Li et al., 2008) and FWEA-18 full waveform inversion of Tao et al. (2018) with the interaction of the Pacific plate and historical Izanagi sea plate, believed to be the conjugate margin of the Pacific plate before its ~60-50Ma subduction beneath Eurasia. Wu et al. (2022) correct for tomographic smearing in MITP-08 to identify roughly 2300-5000km of stagnant Pacific slab beneath the Japan trench, and roughly 3,500-5,200km from the FWEA-18 model, along-strike. JEABOX is in broad agreement with these measurements. A critical finding of their study is a roughly 200km (in depth) slow velocity anomaly, relative to ambient fast velocity anomalies, stretching from The Yellow Sea to Sakhalin in eastern Russia. They identify this as the seismological signature of the ~55Ma subducted Izanagi-Pacific plate boundary, evidenced to be a palaeo-spreading ridge, visible in the MITP-08 model (Li et al., 2008). This relatively low velocity anomaly is not immediately apparent in depth sections of the JEABOX model (figure 4.3) when plotted within a velocity perturbation range best representative of the overall model (from -5% to +5% dVp); however, figure 4.3 compared with figure 4.4 shows that evidence for this slab gap is in fact present in JEABOX when plotted between -1% to +1%, and appears to correlate spatially well with the MITP-08 model of Li et. al (2008). Furthermore, cross-sections taken by Wu et al. (2022) through the MITP-08 model (Li et al., 2008), as evidence of Izanagi plate detachment from the Pacific plate corroborate (figure A.57) similar cross-sections in JEABOX. I also note that, for example, the slab morphology in figure A.57 agrees well with the 'top-down' mantle flow model of Seton et. al (2015) proposed for the region: this is also collocated in time with the detachment of the Izanagi plate form the Pacific plate between 60-50Ma.

Future work will quantify the volume of subducted slab in the JEABOX model in this region: this is important because subducted slab volumes can test and corroborate hypotheses for former plate tectonic paradigms. In this case: quantifying the respective volume of subducted Pacific and Izanagi slabs can shed more insight on the location and time, extent of and mechanism for slab detachment. As a full waveform based model, JEABOX, similar to the FWEA-18 model, is best positioned to quantify the volume of subducted slab at MTZ depths. This is of importance in relation to the study of Wu et al. (2022) because the proposed transform fault, known as the Qingdao line, marks the southwest terminus of the historical Izanagi and Pacific plate arrangement, and is integral to understanding the history of the Philippine Sea plate over the past 50 million years. Lallemand (2016) shows the evolution of a similarly demarcated transform fault at 60Myr into the early Izu-Bonin Marianas subduction zone by 50 Myr.

4.2 Summary

In this thesis I have attempted to present the component steps required to produce JEABOX, a P-wave tomography model of subduction zones in the western hemisphere, with regional-distance sensitivity kernels based on the full waveform spectral element solver, Axisem, in what is the first tomography of its kind. It is a computationally cheaper alternative to some of the full waveform based solvers used currently for global and regional tomography. In addition, sensitivity kernels are calculated for every measurement rather than kernels representative of an entire earthquake. These sensitivity kernels allow triplicated P-waves, observed between approximately 1500km-3000km source-receiver distance, to improve body wave tomography resolution at mantle transition zone depths. Specifically:

- I have presented a finite-frequency, cross-correlation based travel-time measurement workflow, used to previous good effect for teleseismic scale tomography datasets, and applied it to regional body waves.

- This dataset of multifrequency travel-times was measured against an Axisem-based Green's function database in Instaseis, which takes into account explicit source time function estimations from broadband-based earthquake data for a given event, to maximize the fidelity of the synthetic seismogram against which a given travel-time is measured.

- This process yielded approximately **50,000** travel-time measurements for regional and near-teleseismic P-waves across the western Pacific, with east Asia and Japan as a targeted area focus. These measurements were accumulated across six overlapping frequency passbands, from 30s down to 5s dominant period.

- I have discussed future means by which the frequency-dependent content of triplicated body waves might be better harnessed in future incarnations of cross-correlation processes for tomography using orthogonal Slepian data tapers and provided a working example. I have also shown an example of coherence-based stacking of waveforms as applied to regional body wave codas, created in collaboration.

- Next, I addressed the accumulation of sensitivity measurements required to accompany the regional P-wave multifrequency measurement dataset above. I have presented the batch calculation of a source depth bank of Axisem wavefields and their complementary (MC) kernels on high performance computing resources, in addition to their post-processing and data warehousing.

- I have outlined the common corrections applied to the multifrequency measurement travel-time dataset, and outlined the amalgamation of this dataset with approximately **1 million** similar, teleseismic multifrequency travel-times created for the DETOX-P1 global P-wave tomography model by Hosseini et al. (2020). I have used a western Pacific subset of the DETOX-P1 data to supplement the regional P-wave data coverage for this study and projected both onto the discrete inversion grid used in this study. Both of these have

been combined with travel-time picks from the ISC catalogue. I solved for P-wave velocity using this dataset with an existing, explicit matrix inversion scheme. Multiple iterations of the inversion, in order to converge on the final JEABOX model, were affordable and only took approximately one day to run on an 80 CPU local cluster.

- Next, the regularisation process has been outlined, including the logic behind the resultant model solution of choice, which finds an acceptable tradeoff between overall model misfit and the model norm. I also presented the resolution tests carried out in this study. These are relatively computationally cheap and accessible.

From here I have presented a gallery of cross-sections and depth sections of the JEABOX model, which provides tomography resolution in the upper mantle, transition zone and down to mid-mantle depths at roughly 1200km, extending from the Kuril arc in the north, through the Japanese Islands and Izu-Bonin arc. From here coverage continues through southern Ryukyu and the Philippine subduction zones, extending through Malaysia and Indonesia in the southern hemisphere, through to the Sunda-Java trench and beneath Borneo. Figure A.102 is included to reconcile observed waveform delays in the multifrequency measurement process with results from tomography. Shown are waveforms recorded across the western Pacific for an event in the Komandorsky Islands Region. Travel-time delays of up to 5 seconds are observed. Taking into account the likely trajectory of those waveforms, in context of the resolved velocity structure by JEABOX, one can link the observed travel-times to accumulated subducted lithosphere in the mantle transition zone. For a source-receiver path with earth arc distance in the region of 3,000km, one expects an intra-earth path on the order of 4,000-5,000km. If, to first order, the predicted travel time is on the order of 400s, a 5% velocity perturbation to this model amounts to 20s. If one assumes that this 5% perturbation is encountered for up to 1,000km of the entire propagation path (dependent on the specific path through the mantle transition zone), it is possible to account for 4s of travel-time

delay: this is borne out in figure A.102, where at 25 degrees 3-4s of travel-time delay is recorded.
Targeted resolution tests have confirmed that the model can be recovered well beneath the Japan and Kuril trenches, in addition to acceptable recovery of first order structures underneath Izu-Bonin. These resolution tests provide seismic evidence for what appears to be flat slab subduction beneath Japan (east-west) and Kuril (southeast to northwest) and steep subduction under Izu-Bonin. Resolution is poor in the middle of the Philippine Sea plate.

4.3 Future work

Future work will complete a catalogue of resolution tests for each and every seismically fast feature which may be representative of subduction zones, throughout the rest of the JEABOX model, with a particular emphasis on the Philippines, Vietnam and the South China Sea, Malaysia, Indonesia, Borneo and Papua New Guinea. I have discussed possible tectonic avenues of inquiry, including scrutiny of the large subduction-like seismically fast bodies observed under Borneo, where previous studies have indicated interaction between several subducted slabs, in both a north-south and west-east manner.

I close by concluding that the next iteration of the JEABOX model, now that the prototype workflow for embedding full-waveform based regional P-waves in the existing finite-frequency tomography workflow is in place, will have the capability to incorporate more data, and at higher frequencies.

Appendices

The craziness is receding but no clarity is taking its place. I look for resolution and find...

— Joan Didion's 'The Year of Magical Thinking'

A

Appendix

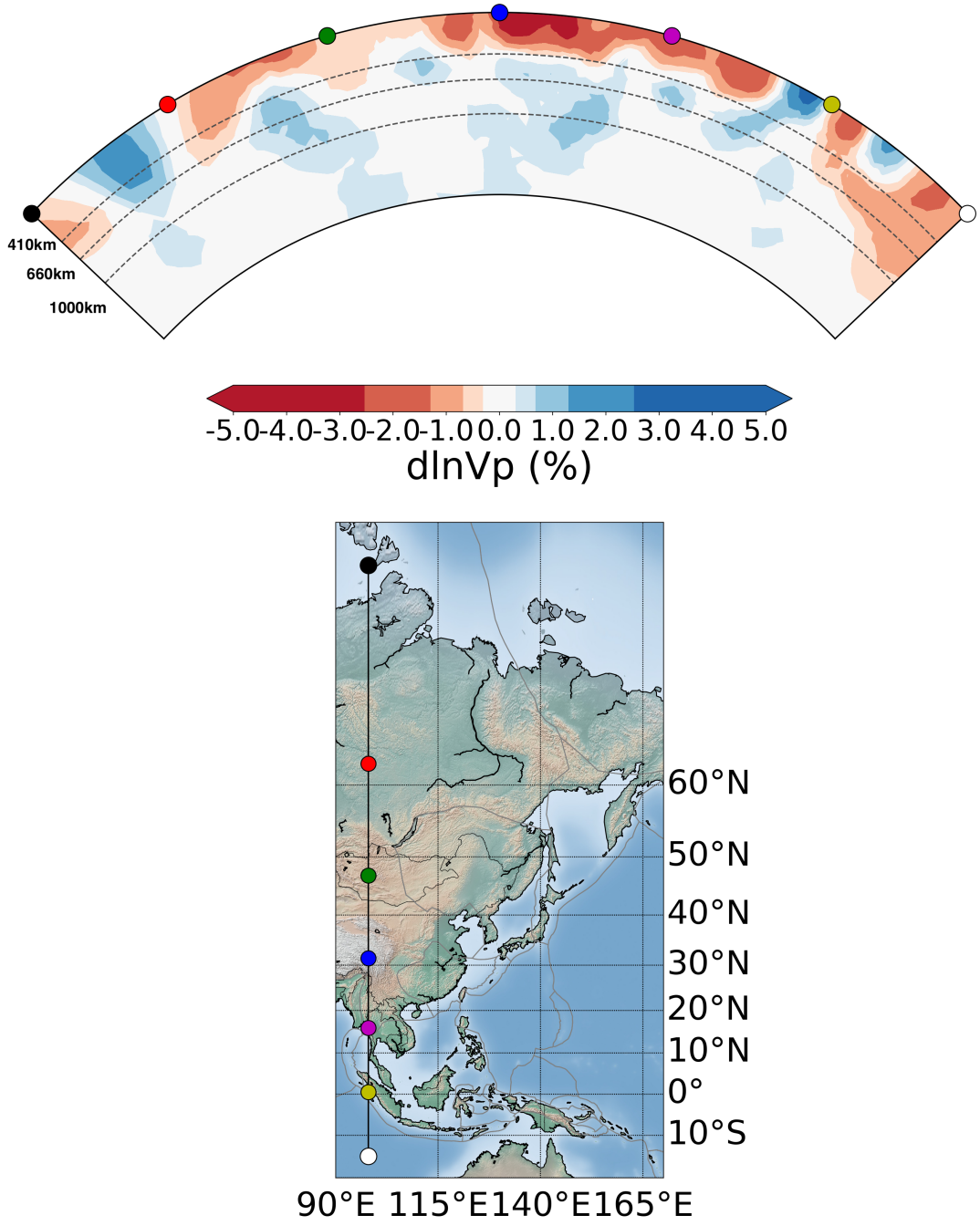

Figure A.1: (Top) P-wave cross-section of seismic velocity for the JEABOX tomography model, which is comprised of teleseismic P-wave multifrequency cross-correlation measurements and Dahlen sensitivity kernels, ray theory based P-wave travel-time picks from the ISC catalogue and targeted regional P-wave cross-correlation measurements and full waveform sensitivity measurements based on Axisem. The logarithmic colour scheme is bounded between +5% and -5%. Cross-section trends from south to north, along a longitude of 98° and between 15°S and 20°N in latitude. (Bottom) Regional map view of the study region, which highlights the location of the cross-section shown above. The colour of the nodes on the bottom transect correspond to the coloured nodes in the cross-section above.

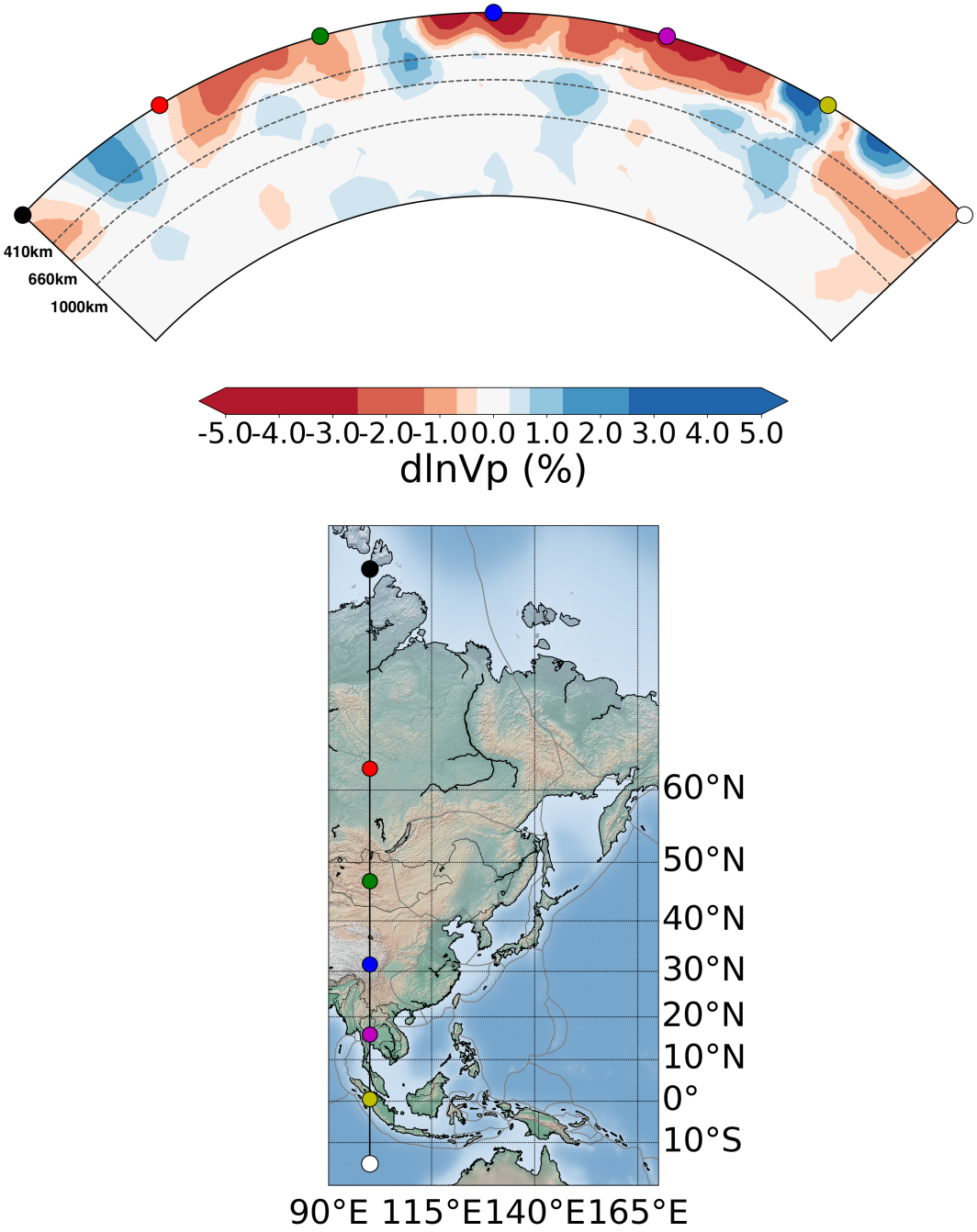

Figure A.2: (Top) Same type of cross-section as figure A1 but for a transect from south to north, along a longitude of 100° and between 15°S and 20°N in latitude . (Bottom) Regional map view of the study region, which highlights the location of the cross-section shown above. The colour of the nodes on the bottom transect correspond to the coloured nodes in the cross-section above.

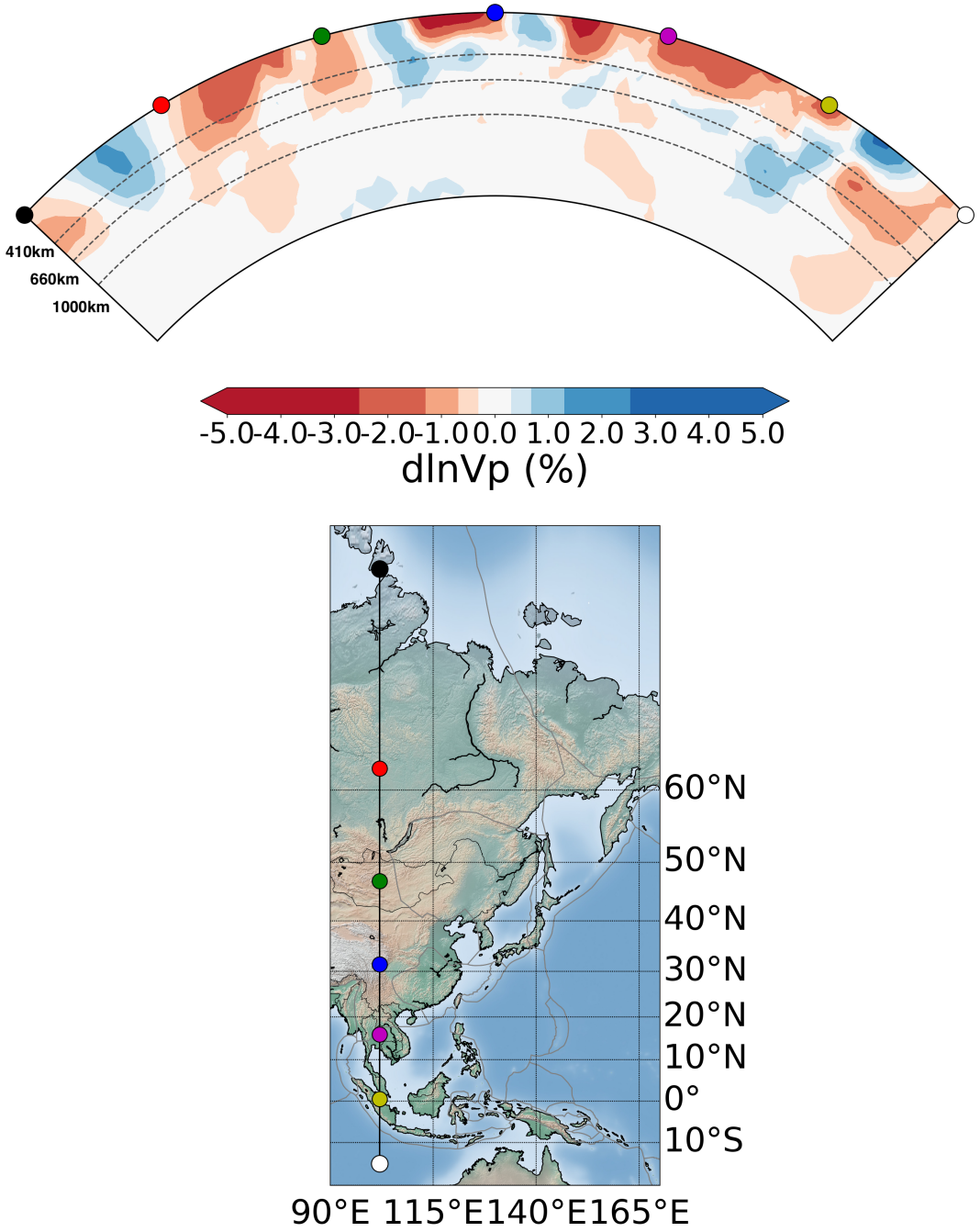

Figure A.3: (Top) Same type of cross-section as figure A1 but for a transect from south to north, along a longitude of 102° and between 15°S and 20°N in latitude . (Bottom) Regional map view of the study region, which highlights the location of the cross-section shown above. The colour of the nodes on the bottom transect correspond to the coloured nodes in the cross-section above.

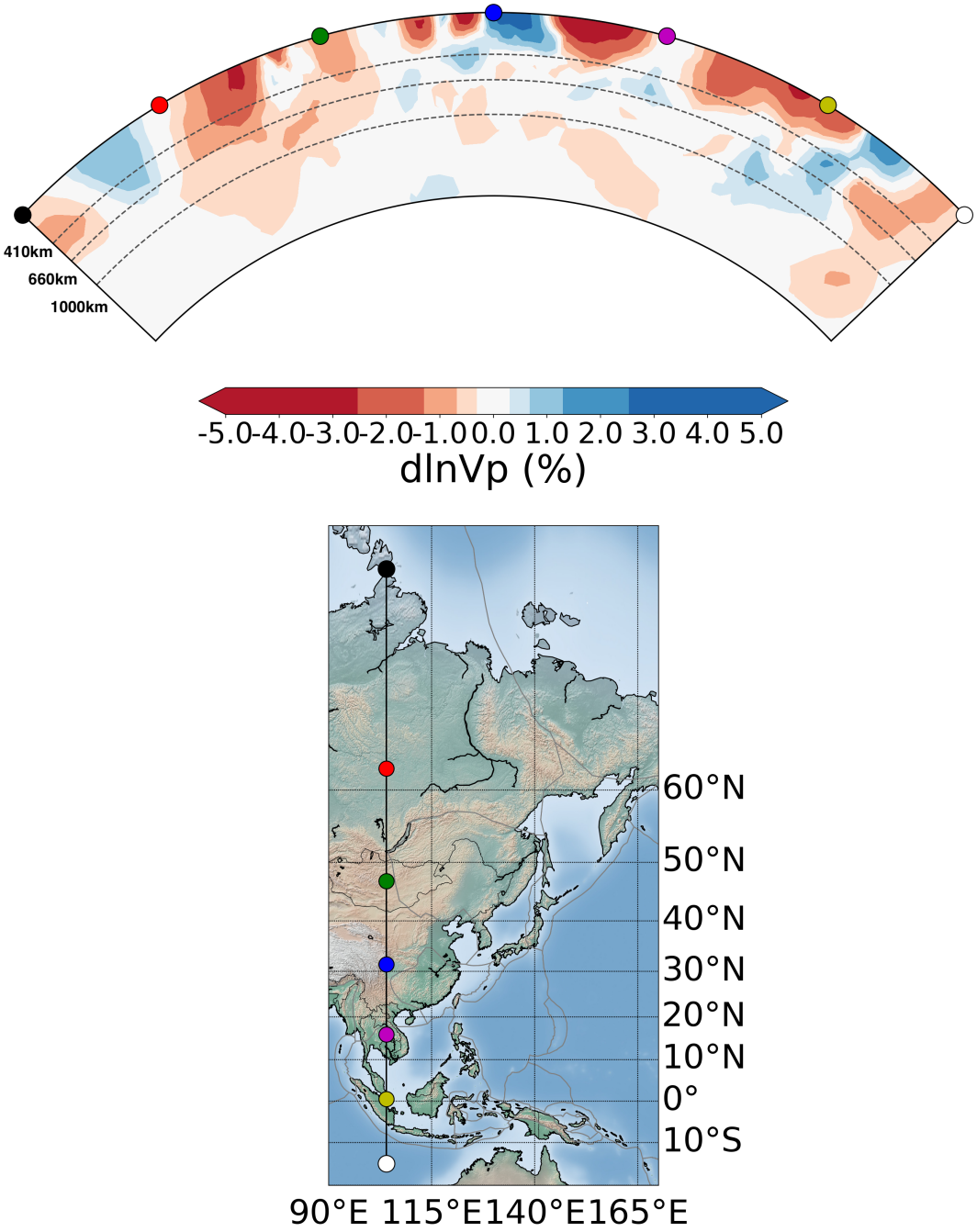

Figure A.4: (Top) Same type of cross-section as figure A1 but for a transect from south to north, along a longitude of 104° and between 15°S and 20°N in latitude . (Bottom) Regional map view of the study region, which highlights the location of the cross-section shown above. The colour of the nodes on the bottom transect correspond to the coloured nodes in the cross-section above.

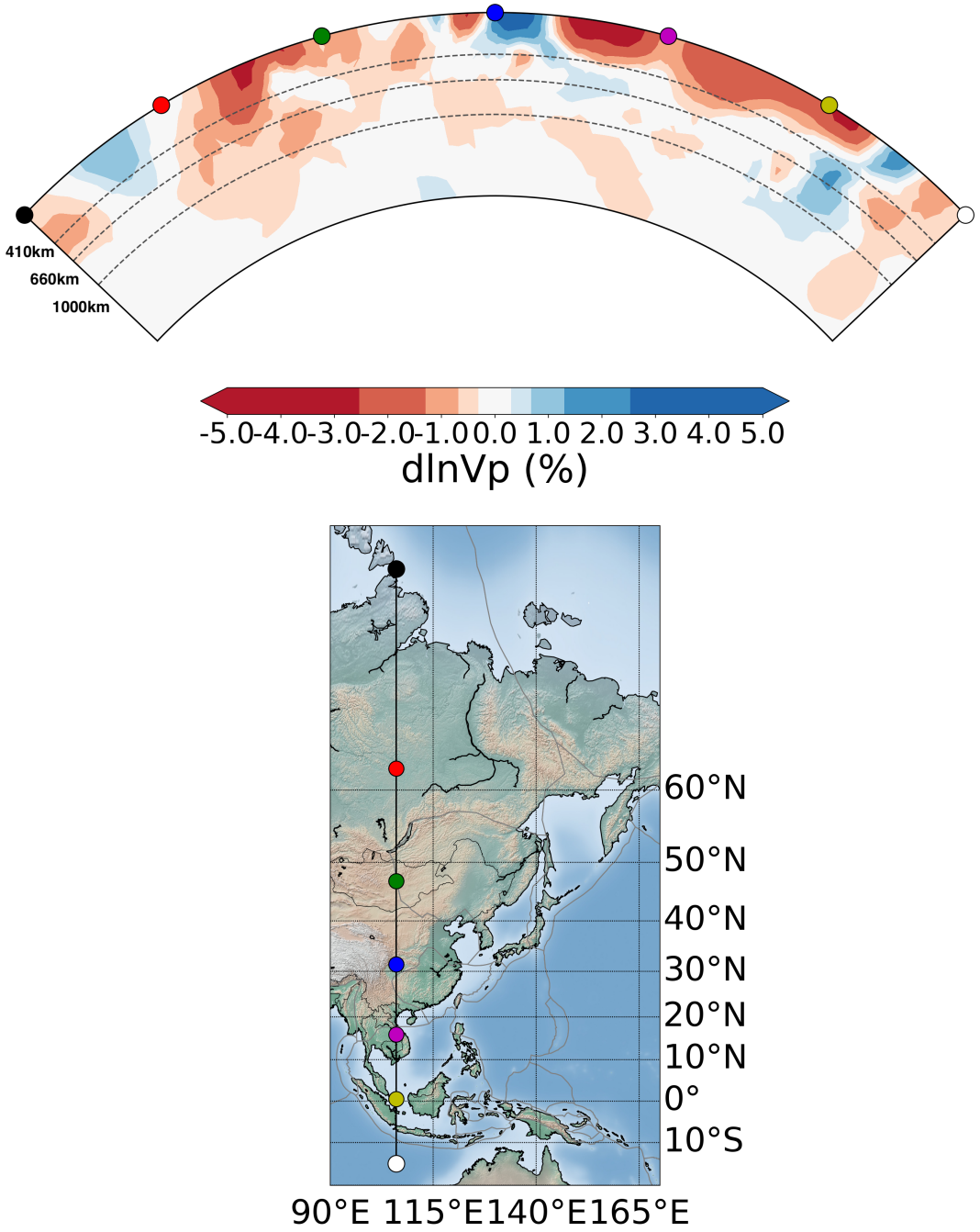

Figure A.5: (Top) Same type of cross-section as figure A1 but for a transect from south to north, along a longitude of 106° and between 15°S and 20°N in latitude . (Bottom) Regional map view of the study region, which highlights the location of the cross-section shown above. The colour of the nodes on the bottom transect correspond to the coloured nodes in the cross-section above.

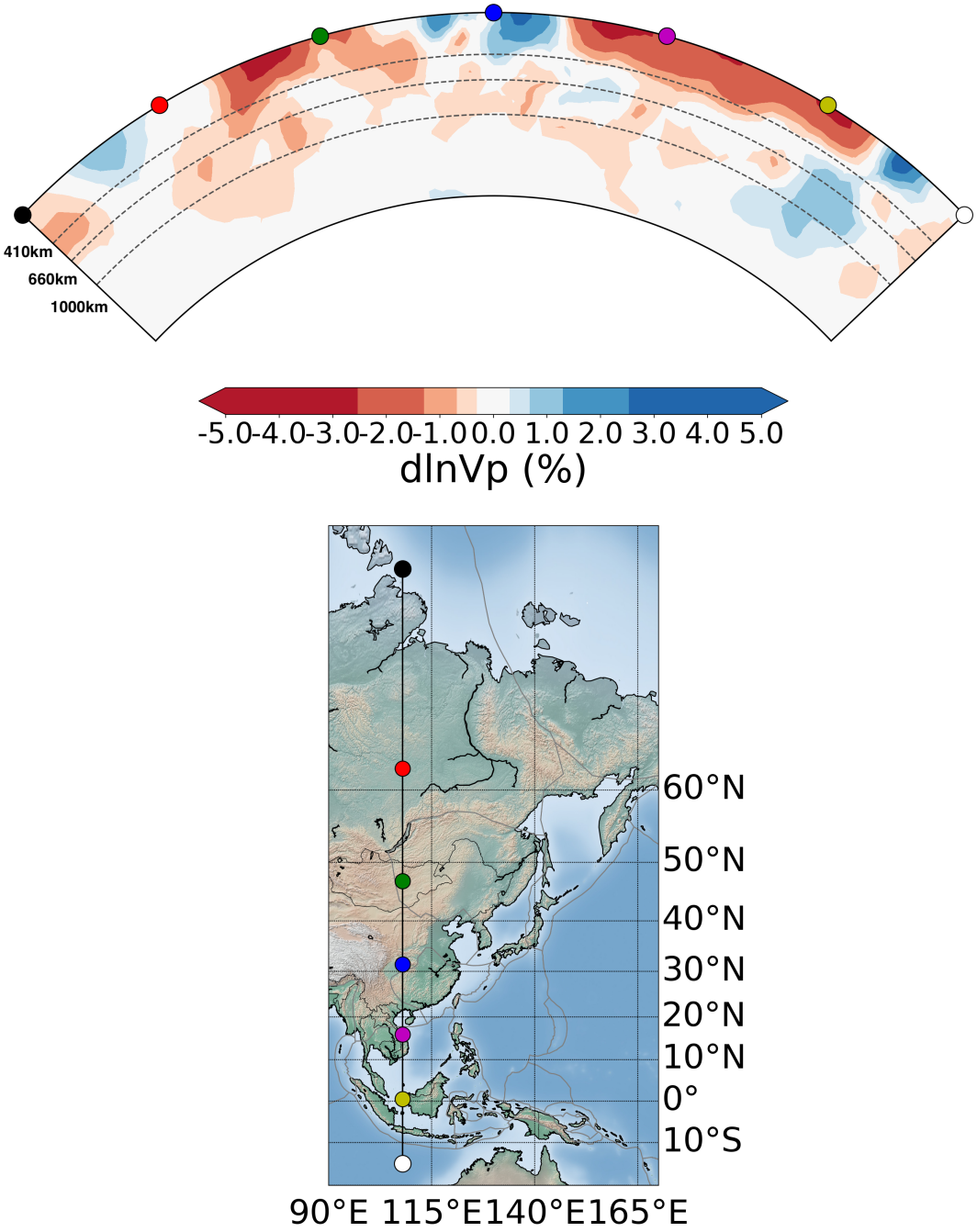

Figure A.6: (Top) Same type of cross-section as figure A1 but for a transect from south to north, along a longitude of 108° and between 15°S and 20°N in latitude . (Bottom) Regional map view of the study region, which highlights the location of the cross-section shown above. The colour of the nodes on the bottom transect correspond to the coloured nodes in the cross-section above.

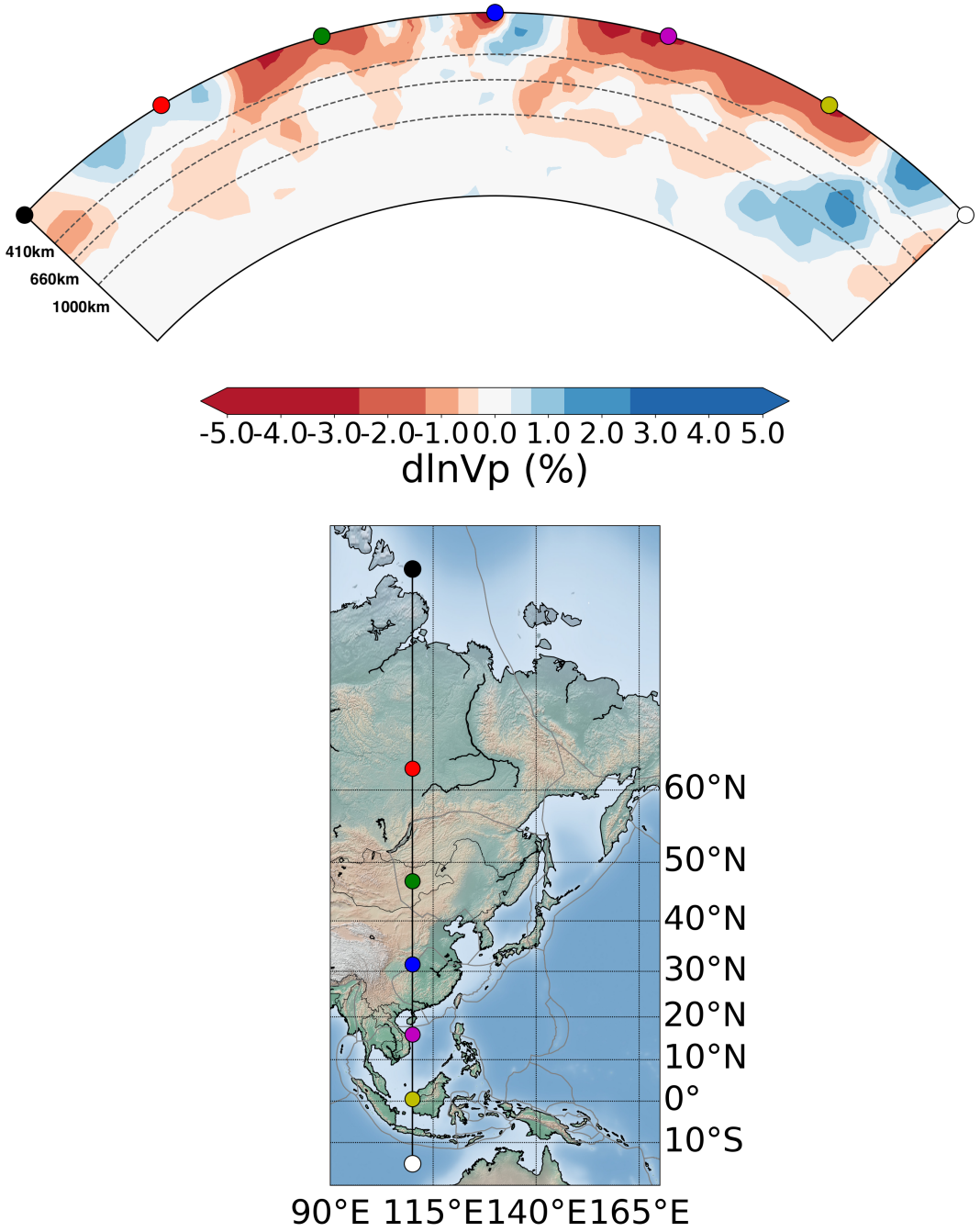

Figure A.7: (Top) Same type of cross-section as figure A1 but for a transect from south to north, along a longitude of 110° and between 15°S and 20°N in latitude . (Bottom) Regional map view of the study region, which highlights the location of the cross-section shown above. The colour of the nodes on the bottom transect correspond to the coloured nodes in the cross-section above.

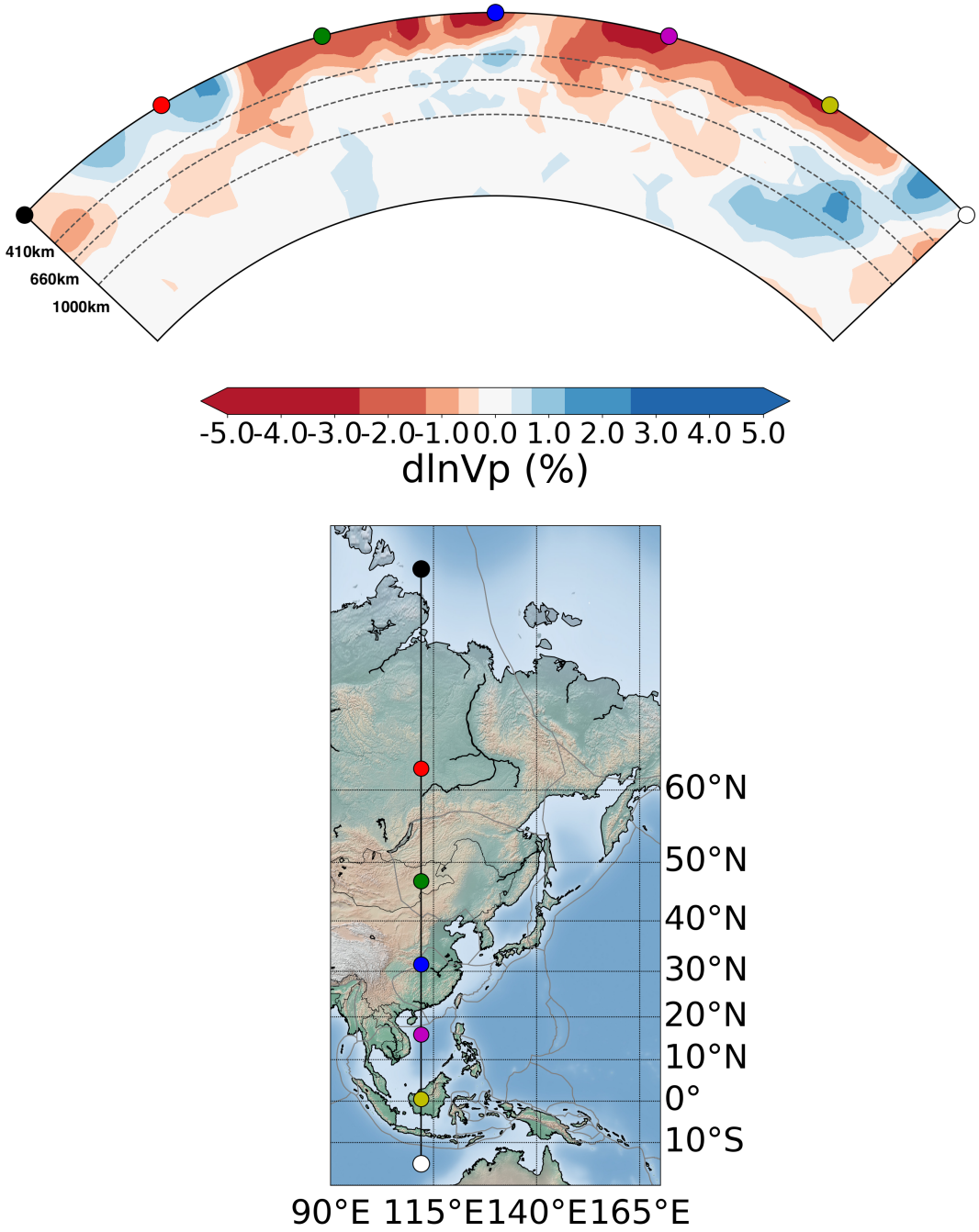

Figure A.8: (Top) Same type of cross-section as figure A1 but for a transect from south to north, along a longitude of 112° and between 15°S and 20°N in latitude . (Bottom) Regional map view of the study region, which highlights the location of the cross-section shown above. The colour of the nodes on the bottom transect correspond to the coloured nodes in the cross-section above.

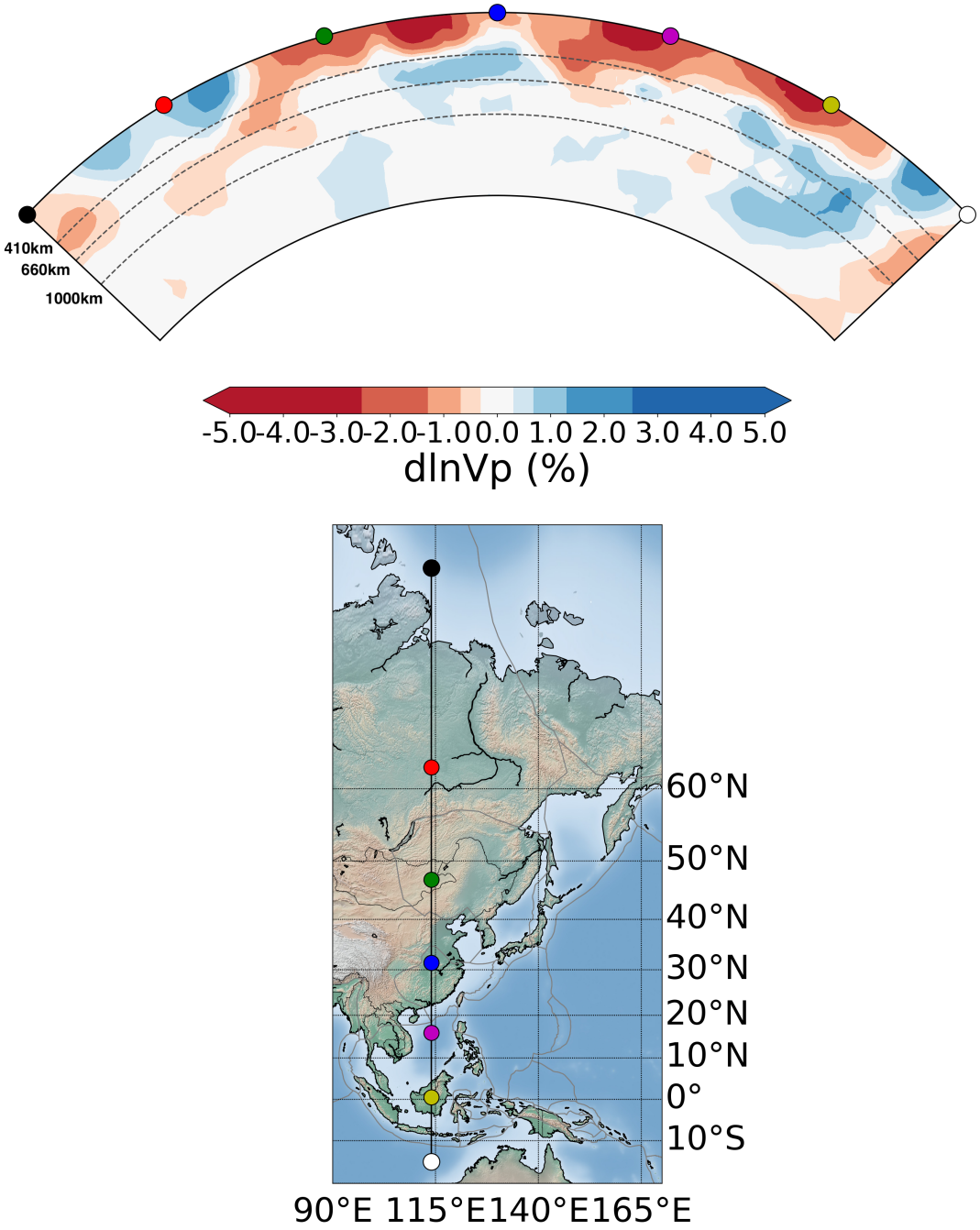

Figure A.9: (Top) Same type of cross-section as figure A1 but for a transect from south to north, along a longitude of 114° and between 15°S and 20°N in latitude . (Bottom) Regional map view of the study region, which highlights the location of the cross-section shown above. The colour of the nodes on the bottom transect correspond to the coloured nodes in the cross-section above.

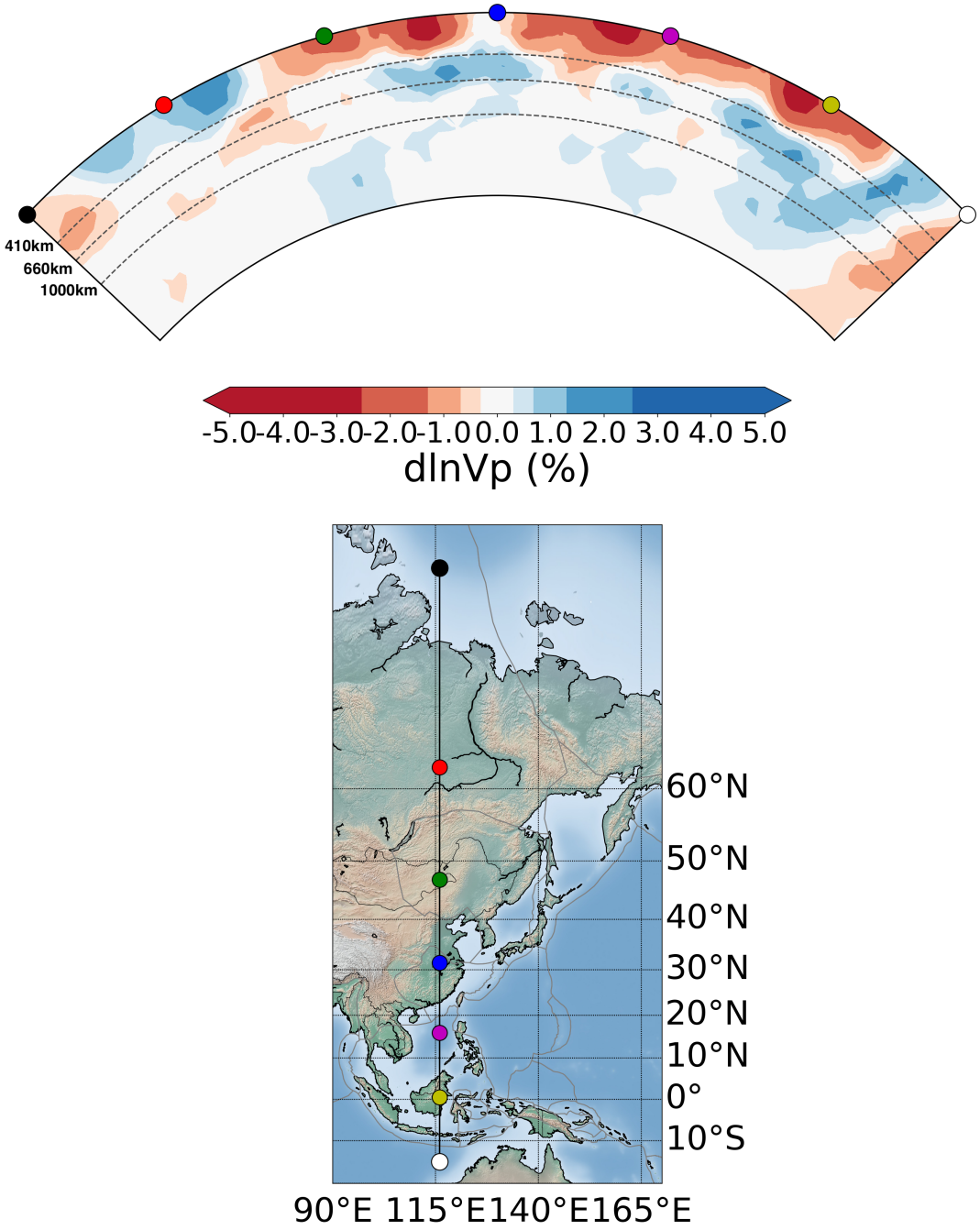

Figure A.10: (Top) Same type of cross-section as figure A1 but for a transect from south to north, along a longitude of 116° and between 15°S and 20°N in latitude . (Bottom) Regional map view of the study region, which highlights the location of the cross-section shown above. The colour of the nodes on the bottom transect correspond to the coloured nodes in the cross-section above.

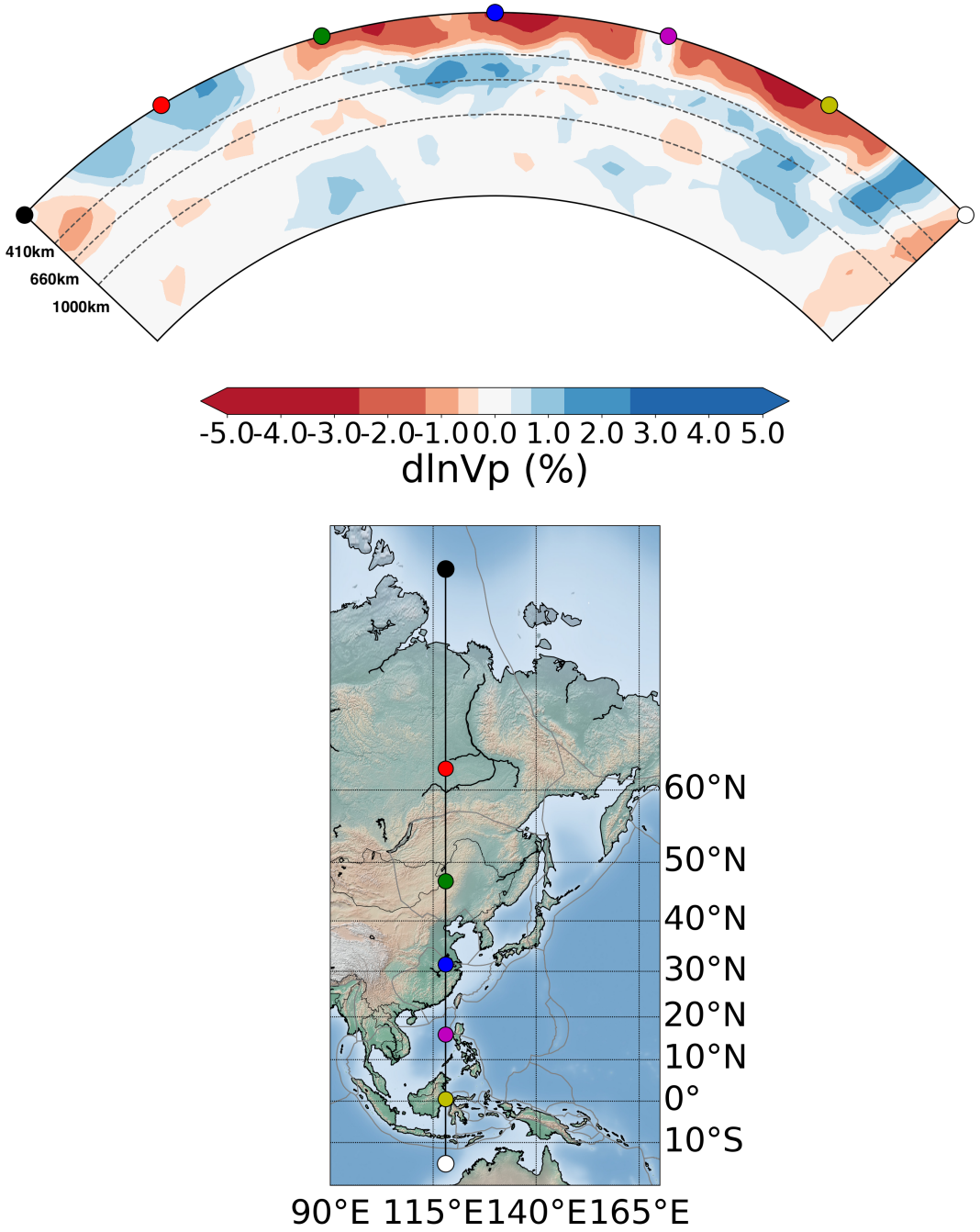

Figure A.11: (Top) Same type of cross-section as figure A1 but for a transect from south to north, along a longitude of 118° and between 15°S and 20°N in latitude . (Bottom) Regional map view of the study region, which highlights the location of the cross-section shown above. The colour of the nodes on the bottom transect correspond to the coloured nodes in the cross-section above.

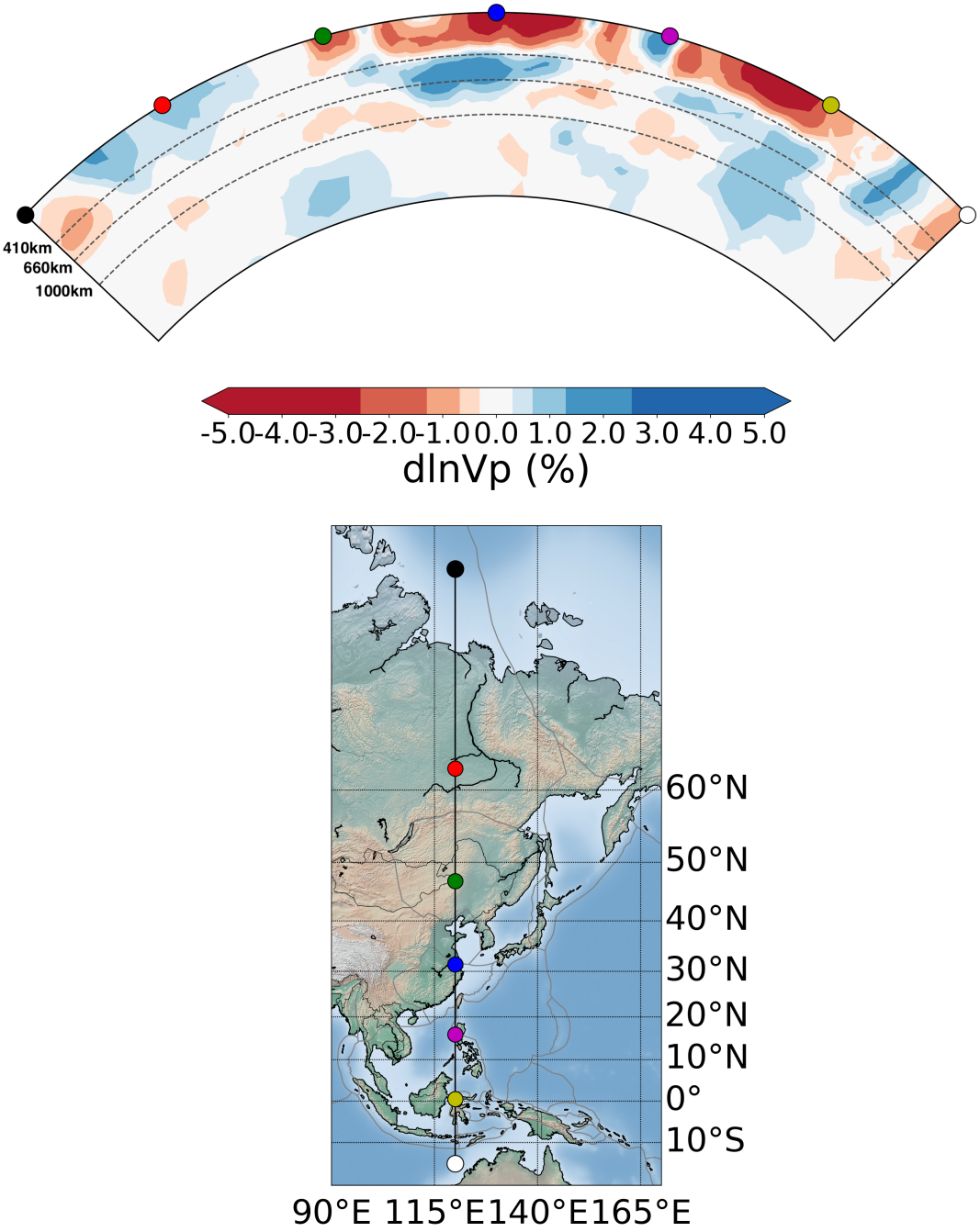

Figure A.12: (Top) Same type of cross-section as figure A1 but for a transect from south to north, along a longitude of 120° and between 15°S and 20°N in latitude . (Bottom) Regional map view of the study region, which highlights the location of the cross-section shown above. The colour of the nodes on the bottom transect correspond to the coloured nodes in the cross-section above.

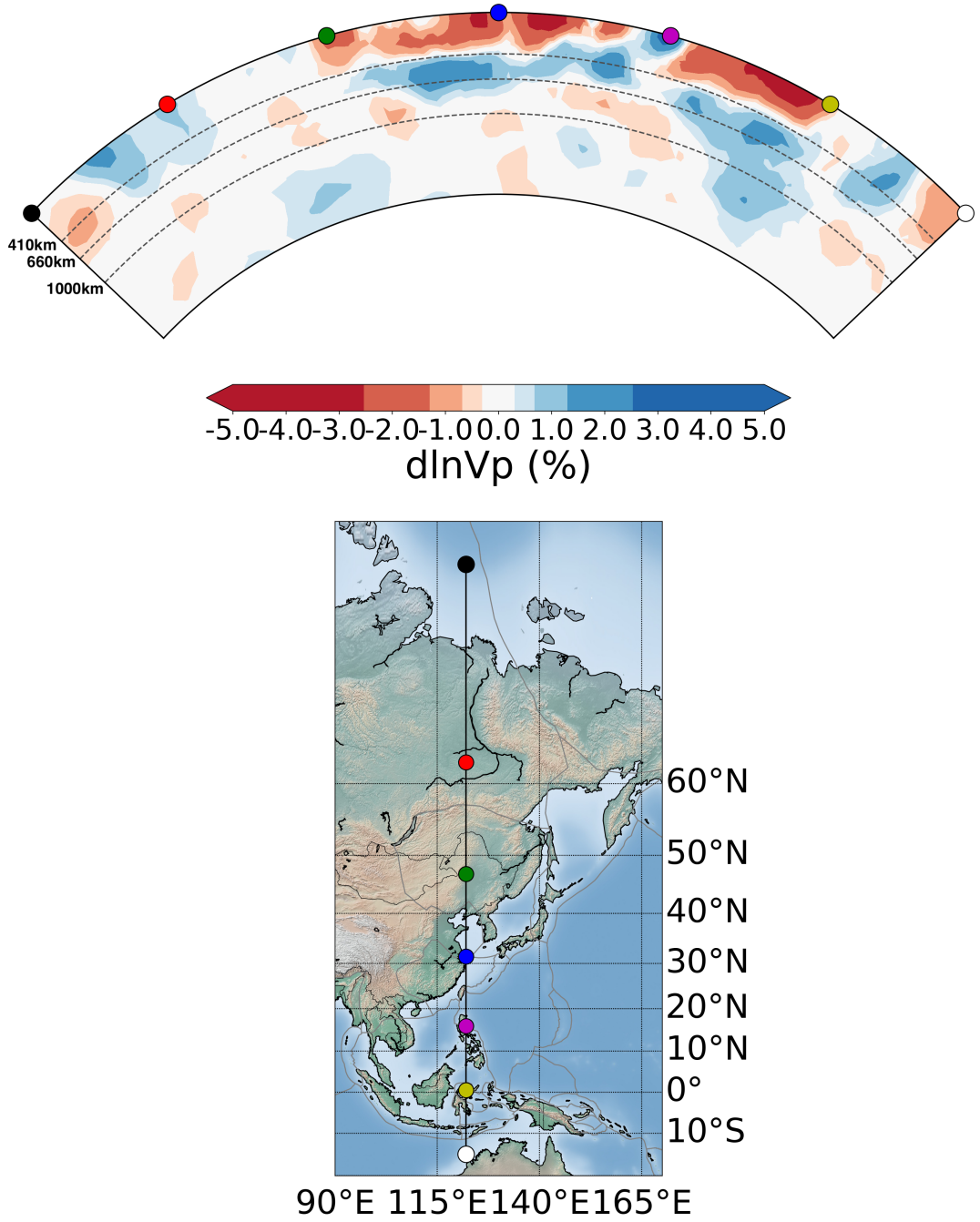

Figure A.13: (Top) Same type of cross-section as figure A1 but for a transect from south to north, along a longitude of 122° and between 15°S and 20°N in latitude . (Bottom) Regional map view of the study region, which highlights the location of the cross-section shown above. The colour of the nodes on the bottom transect correspond to the coloured nodes in the cross-section above.

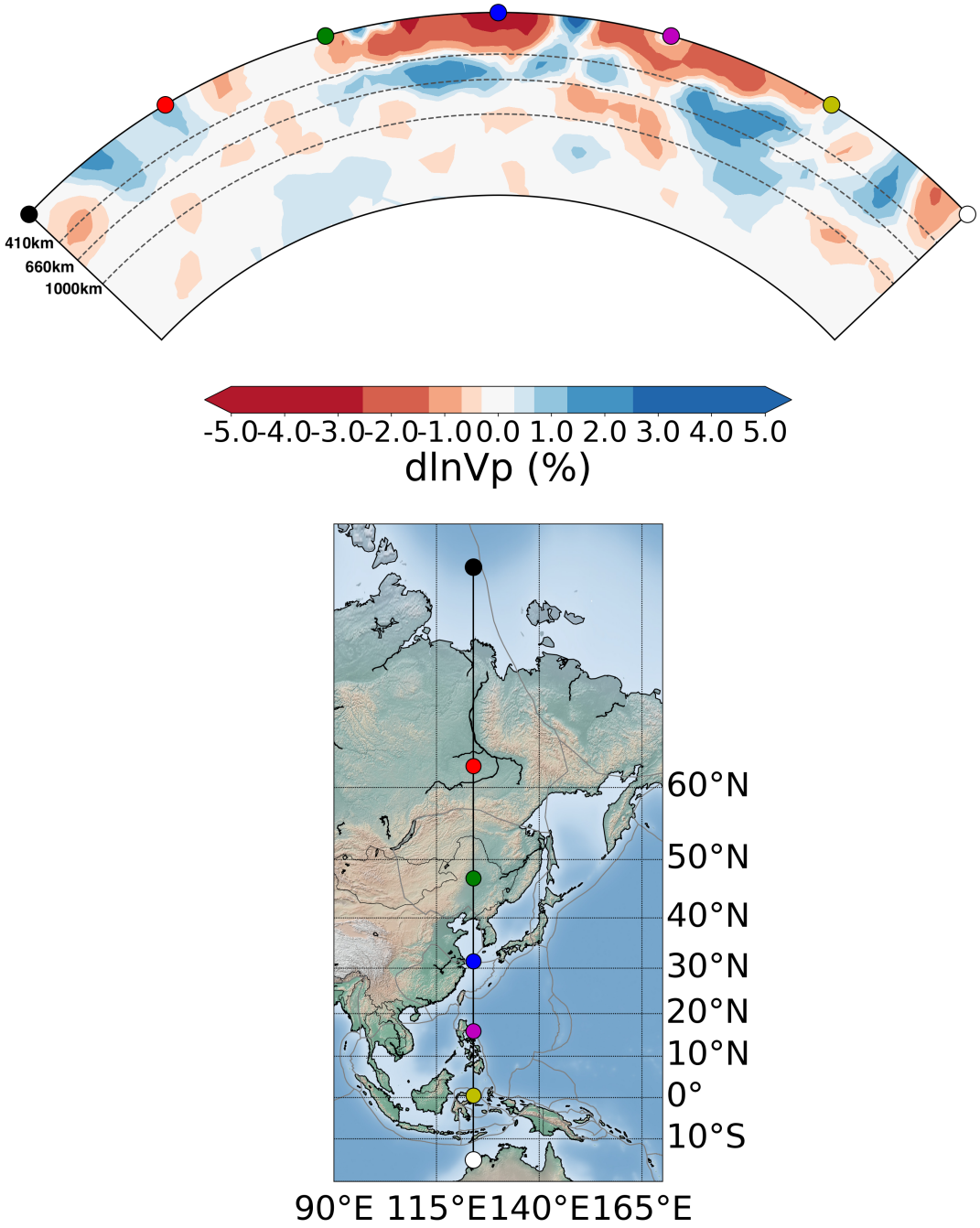

Figure A.14: (Top) Same type of cross-section as figure A1 but for a transect from south to north, along a longitude of 124° and between 15°S and 20°N in latitude . (Bottom) Regional map view of the study region, which highlights the location of the cross-section shown above. The colour of the nodes on the bottom transect correspond to the coloured nodes in the cross-section above.

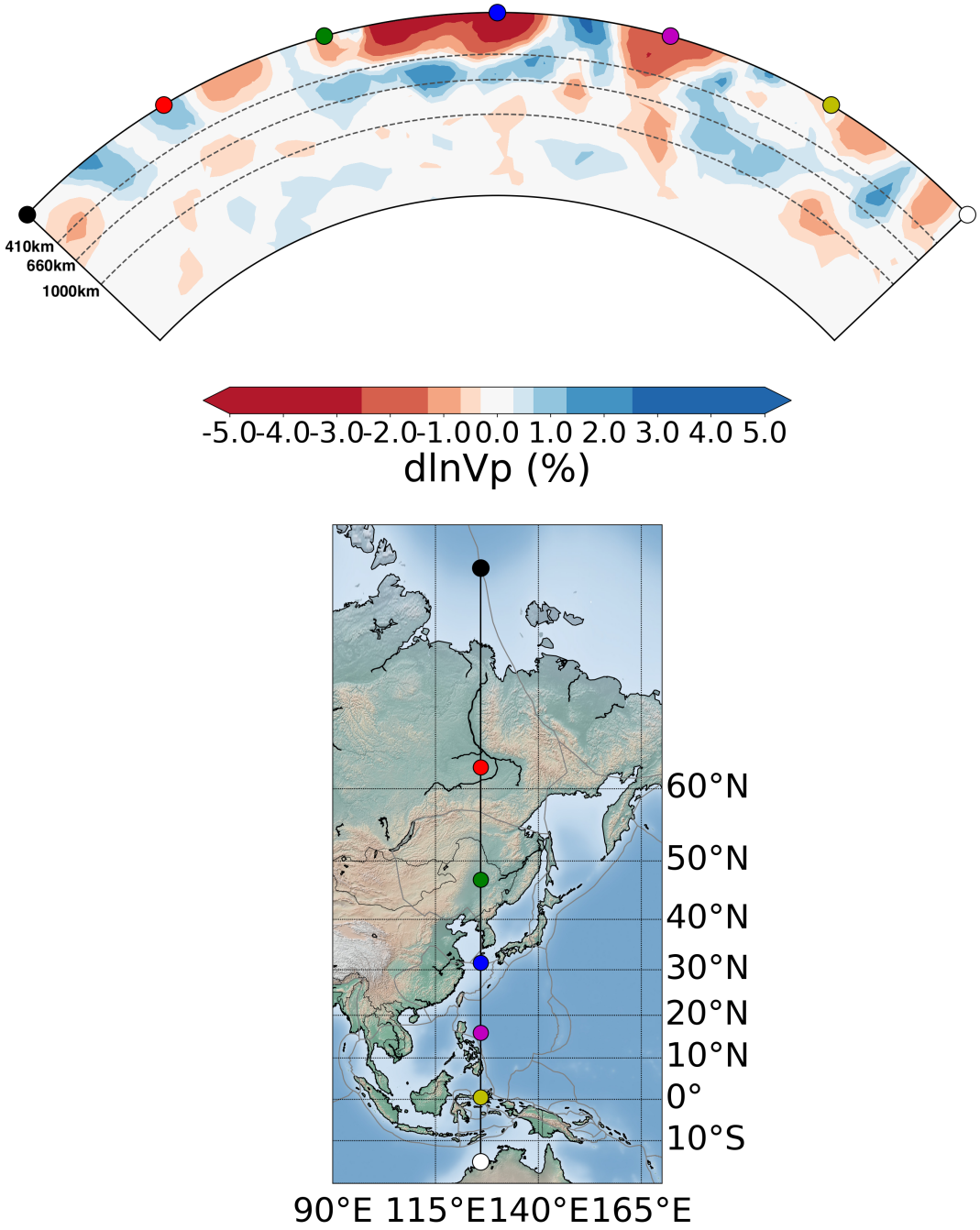

Figure A.15: (Top) Same type of cross-section as figure A1 but for a transect from south to north, along a longitude of 126° and between 15°S and 20°N in latitude . (Bottom) Regional map view of the study region, which highlights the location of the cross-section shown above. The colour of the nodes on the bottom transect correspond to the coloured nodes in the cross-section above.

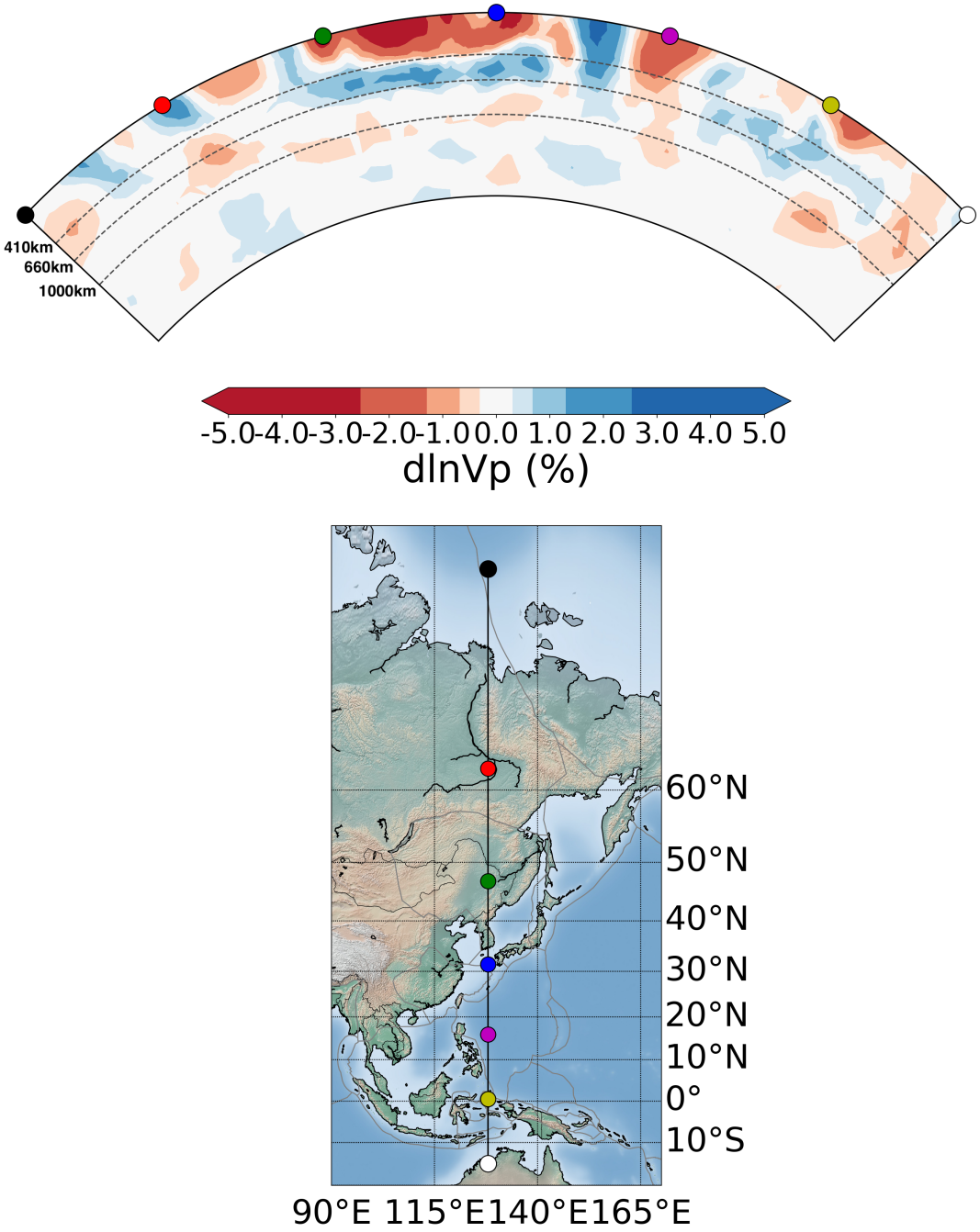

Figure A.16: (Top) Same type of cross-section as figure A1 but for a transect from south to north, along a longitude of 128° and between 15°S and 20°N in latitude . (Bottom) Regional map view of the study region, which highlights the location of the cross-section shown above. The colour of the nodes on the bottom transect correspond to the coloured nodes in the cross-section above.

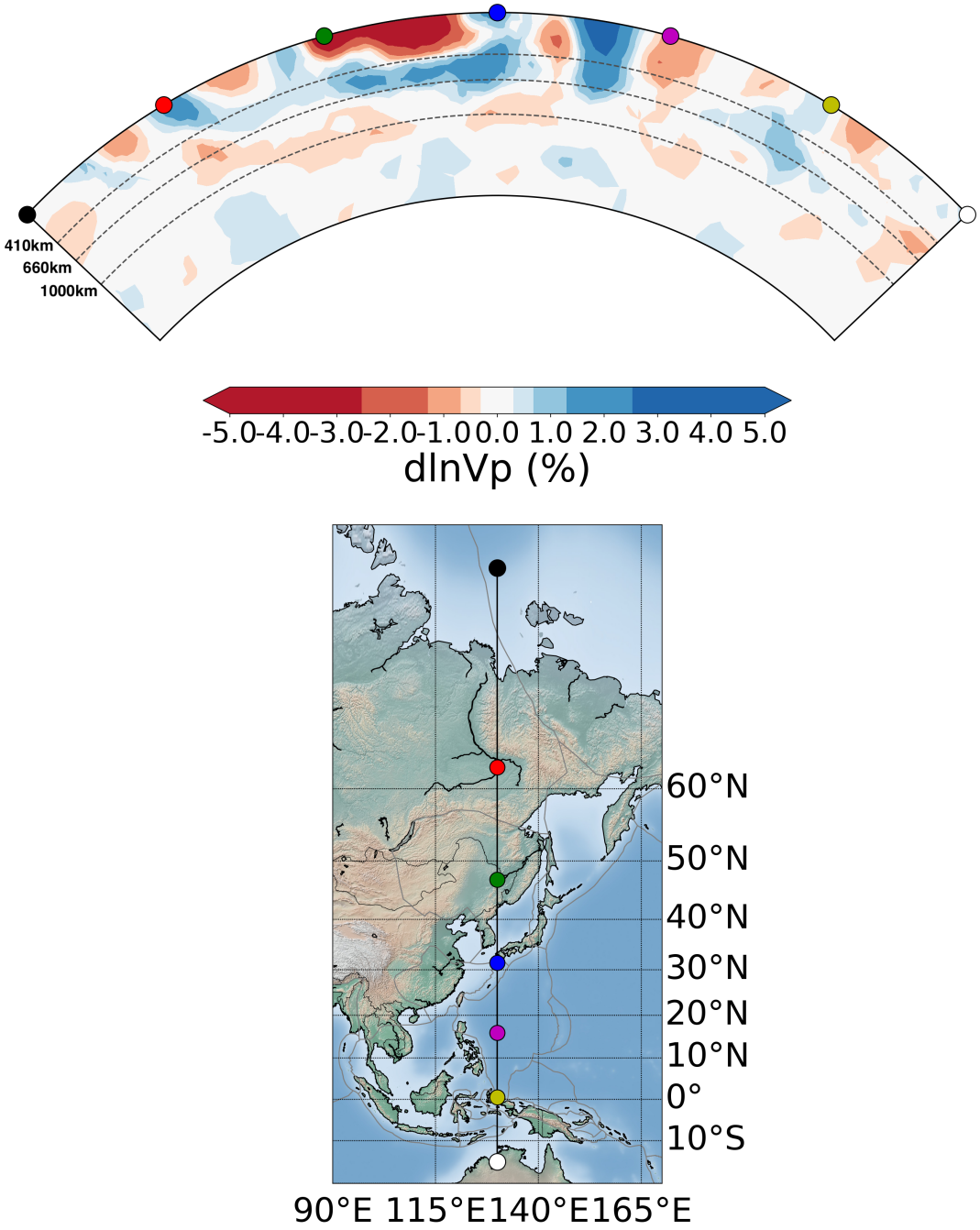

Figure A.17: (Top) Same type of cross-section as figure A1 but for a transect from south to north, along a longitude of 130° and between 15°S and 20°N in latitude . (Bottom) Regional map view of the study region, which highlights the location of the cross-section shown above. The colour of the nodes on the bottom transect correspond to the coloured nodes in the cross-section above.

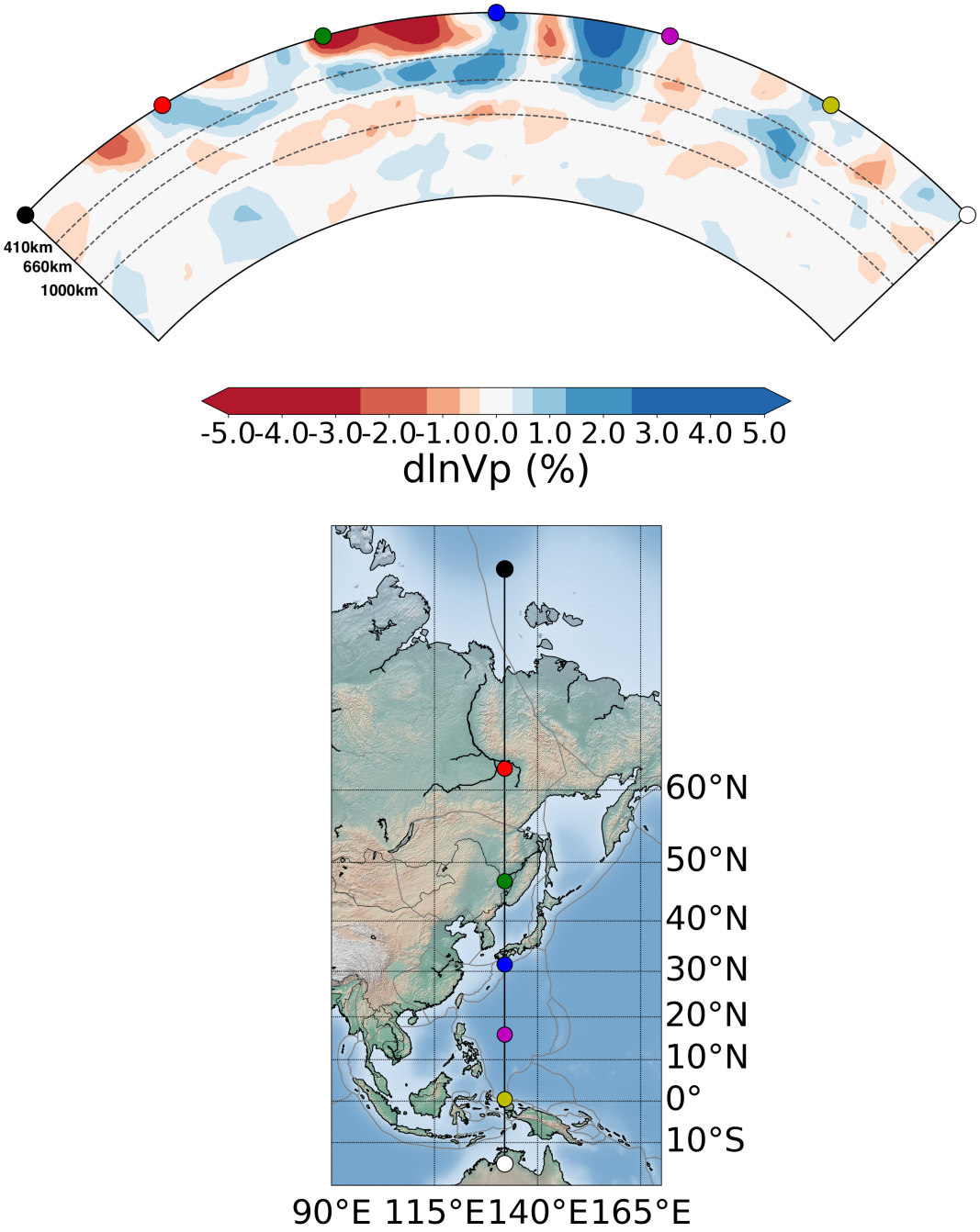

Figure A.18: (Top) Same type of cross-section as figure A1 but for a transect from south to north, along a longitude of 132° and between 15°S and 20°N in latitude . (Bottom) Regional map view of the study region, which highlights the location of the cross-section shown above. The colour of the nodes on the bottom transect correspond to the coloured nodes in the cross-section above.

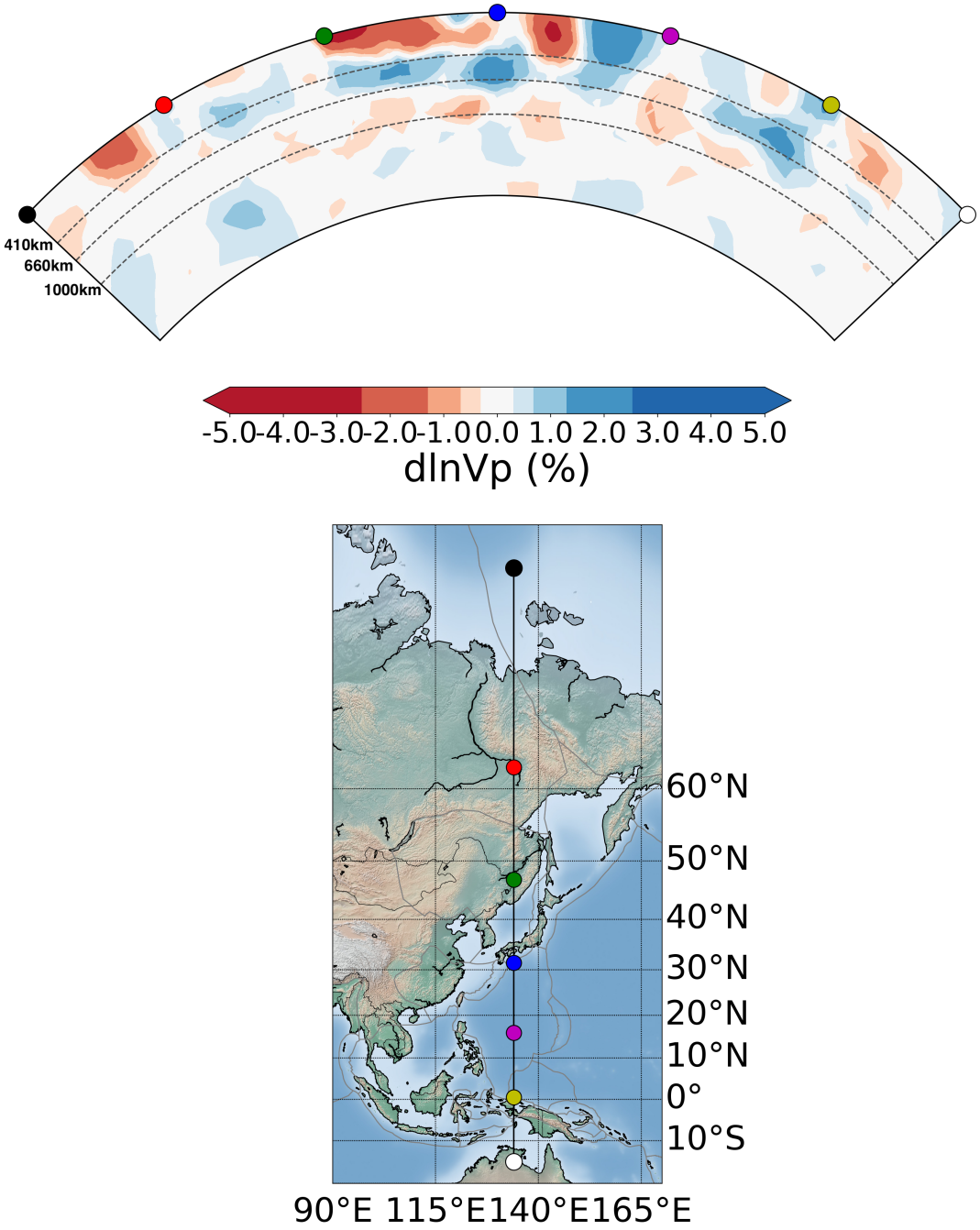

Figure A.19: (Top) Same type of cross-section as figure A1 but for a transect from south to north, along a longitude of 134° and between 15°S and 20°N in latitude . (Bottom) Regional map view of the study region, which highlights the location of the cross-section shown above. The colour of the nodes on the bottom transect correspond to the coloured nodes in the cross-section above.

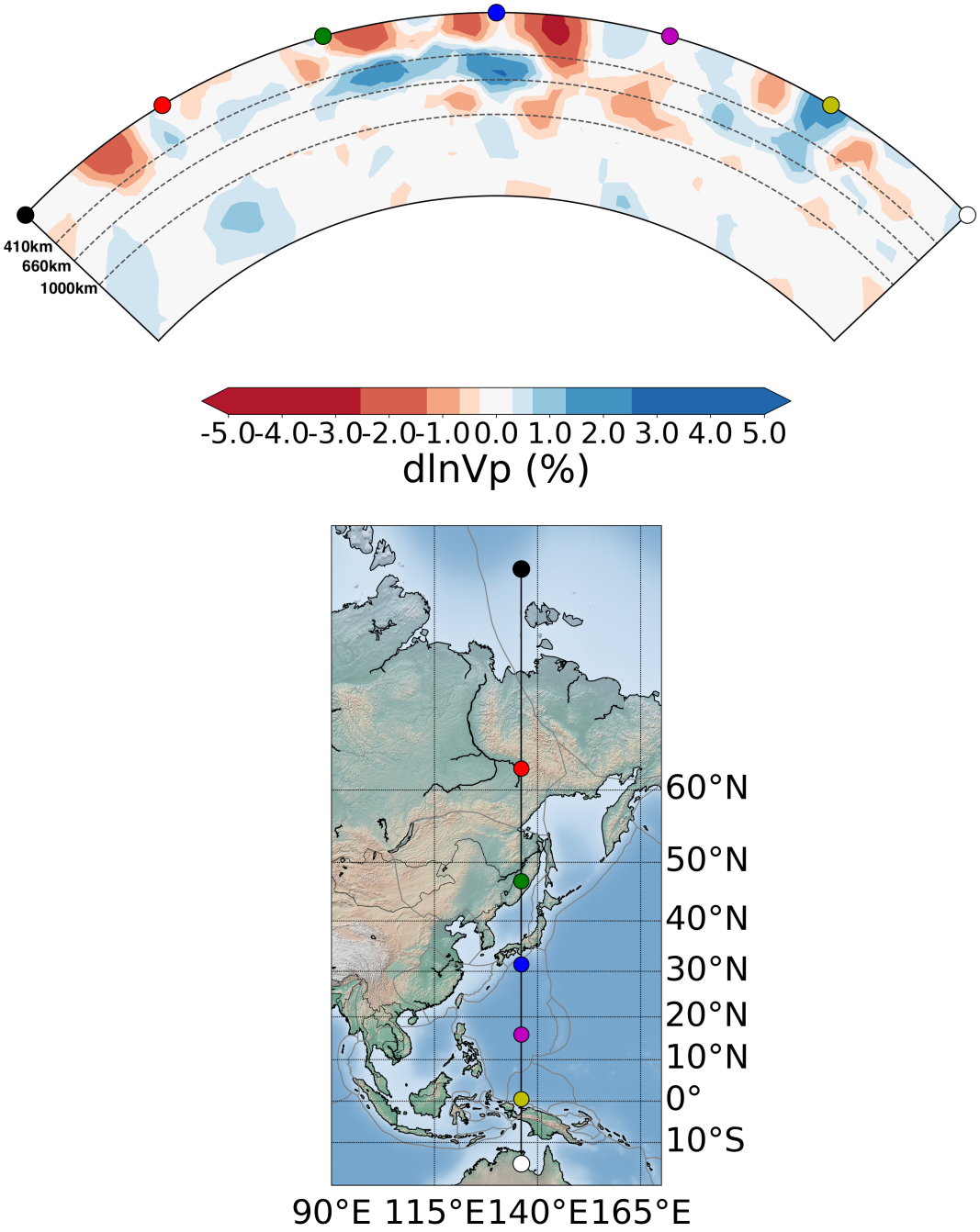

Figure A.20: (Top) Same type of cross-section as figure A1 but for a transect from south to north, along a longitude of 136° and between 15°S and 20°N in latitude . (Bottom) Regional map view of the study region, which highlights the location of the cross-section shown above. The colour of the nodes on the bottom transect correspond to the coloured nodes in the cross-section above.

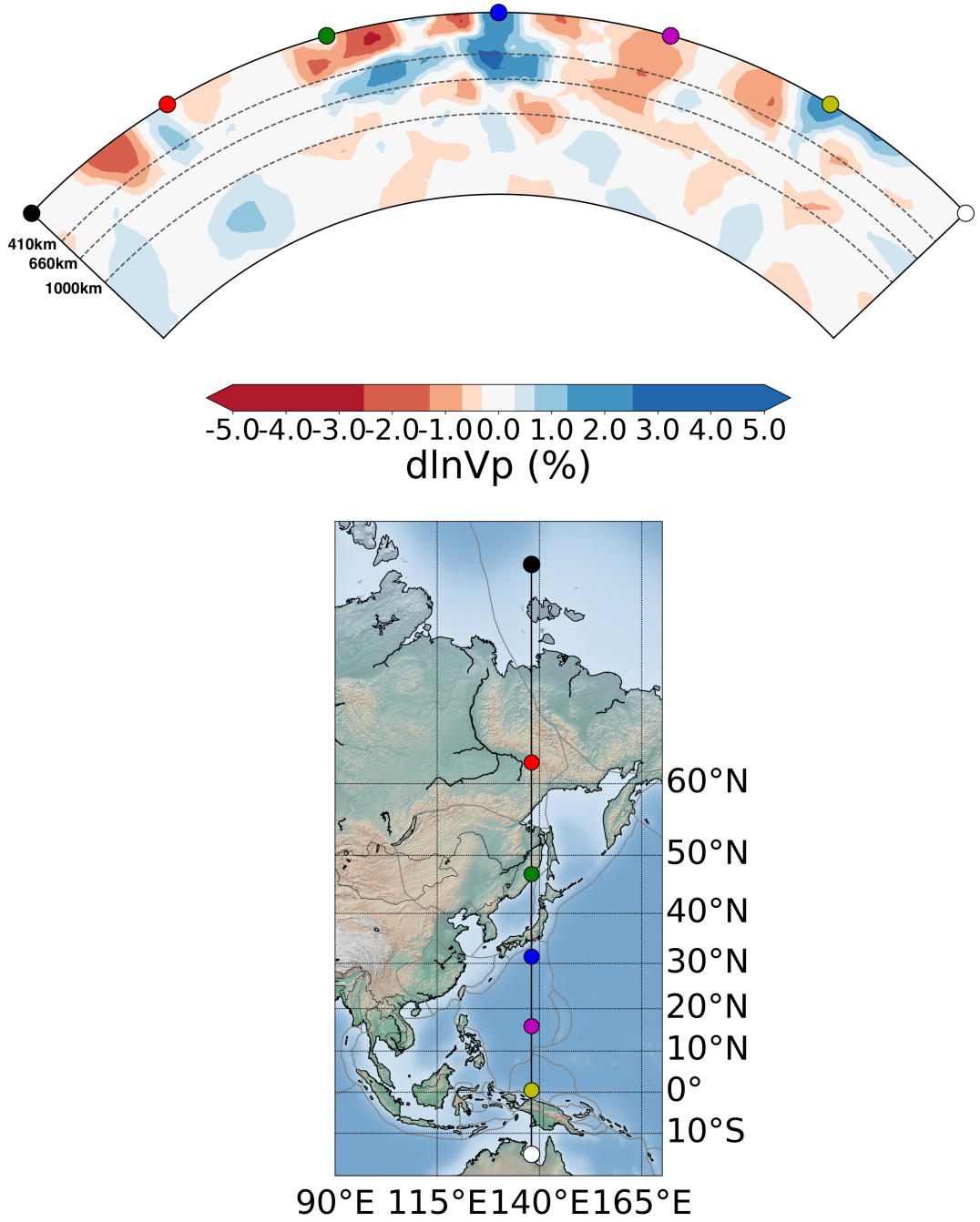

Figure A.21: (Top) Same type of cross-section as figure A1 but for a transect from south to north, along a longitude of 138° and between 15°S and 20°N in latitude . (Bottom) Regional map view of the study region, which highlights the location of the cross-section shown above. The colour of the nodes on the bottom transect correspond to the coloured nodes in the cross-section above.

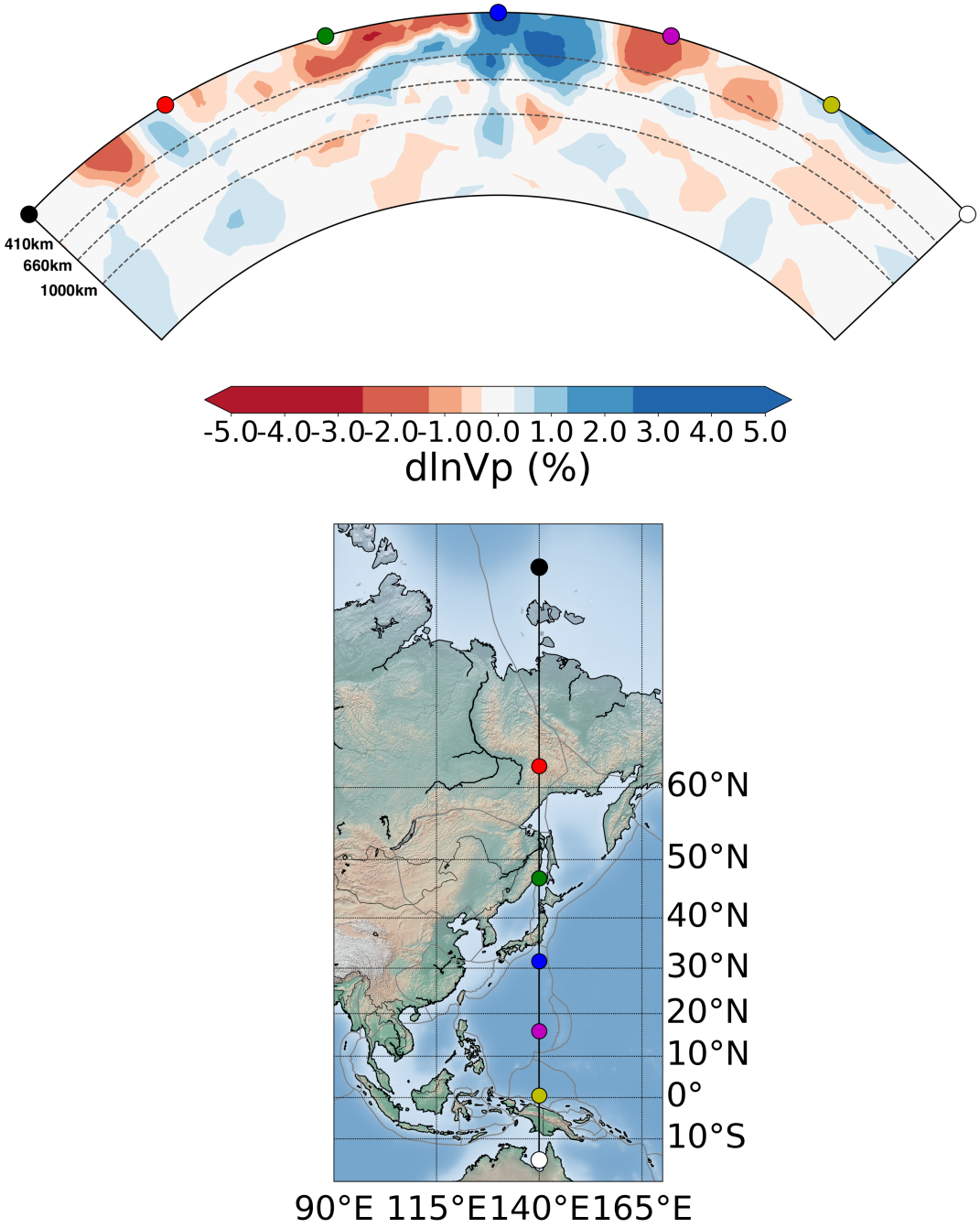

Figure A.22: (Top) Same type of cross-section as figure A1 but for a transect from south to north, along a longitude of 140° and between 15°S and 20°N in latitude . (Bottom) Regional map view of the study region, which highlights the location of the cross-section shown above. The colour of the nodes on the bottom transect correspond to the coloured nodes in the cross-section above.

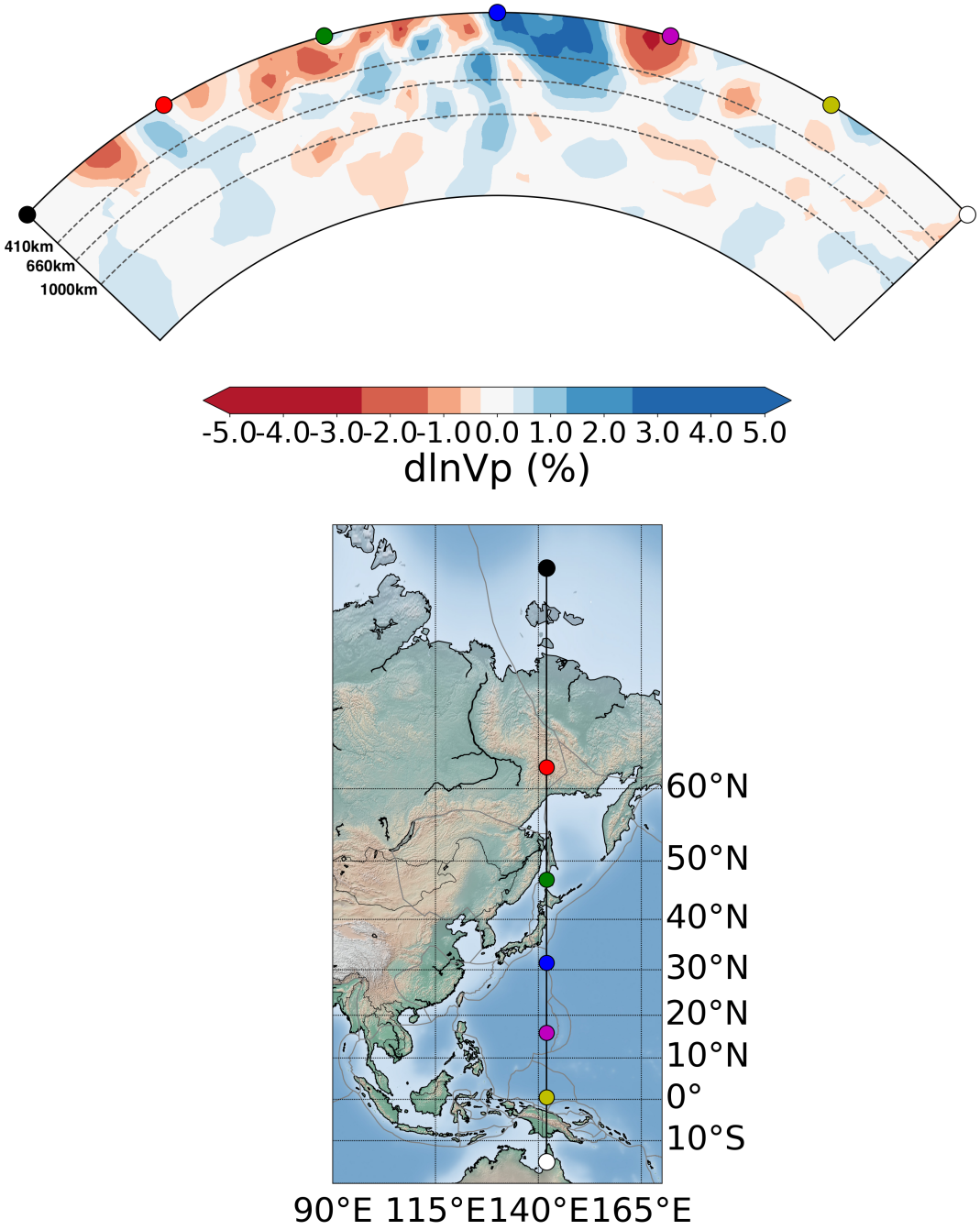

Figure A.23: (Top) Same type of cross-section as figure A1 but for a transect from south to north, along a longitude of 142° and between 15°S and 20°N in latitude . (Bottom) Regional map view of the study region, which highlights the location of the cross-section shown above. The colour of the nodes on the bottom transect correspond to the coloured nodes in the cross-section above.

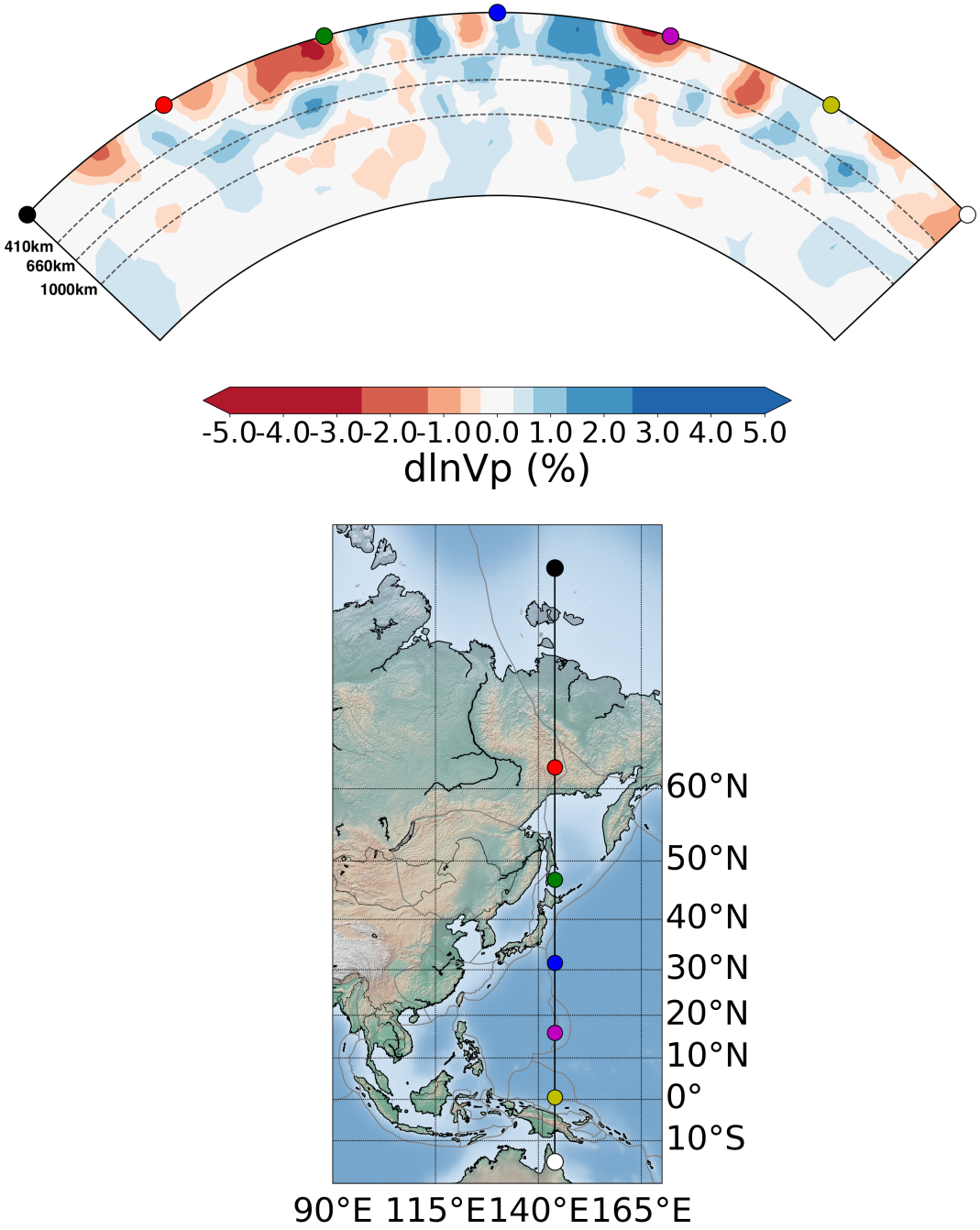

Figure A.24: (Top) Same type of cross-section as figure A1 but for a transect from south to north, along a longitude of 144° and between 15°S and 20°N in latitude . (Bottom) Regional map view of the study region, which highlights the location of the cross-section shown above. The colour of the nodes on the bottom transect correspond to the coloured nodes in the cross-section above.

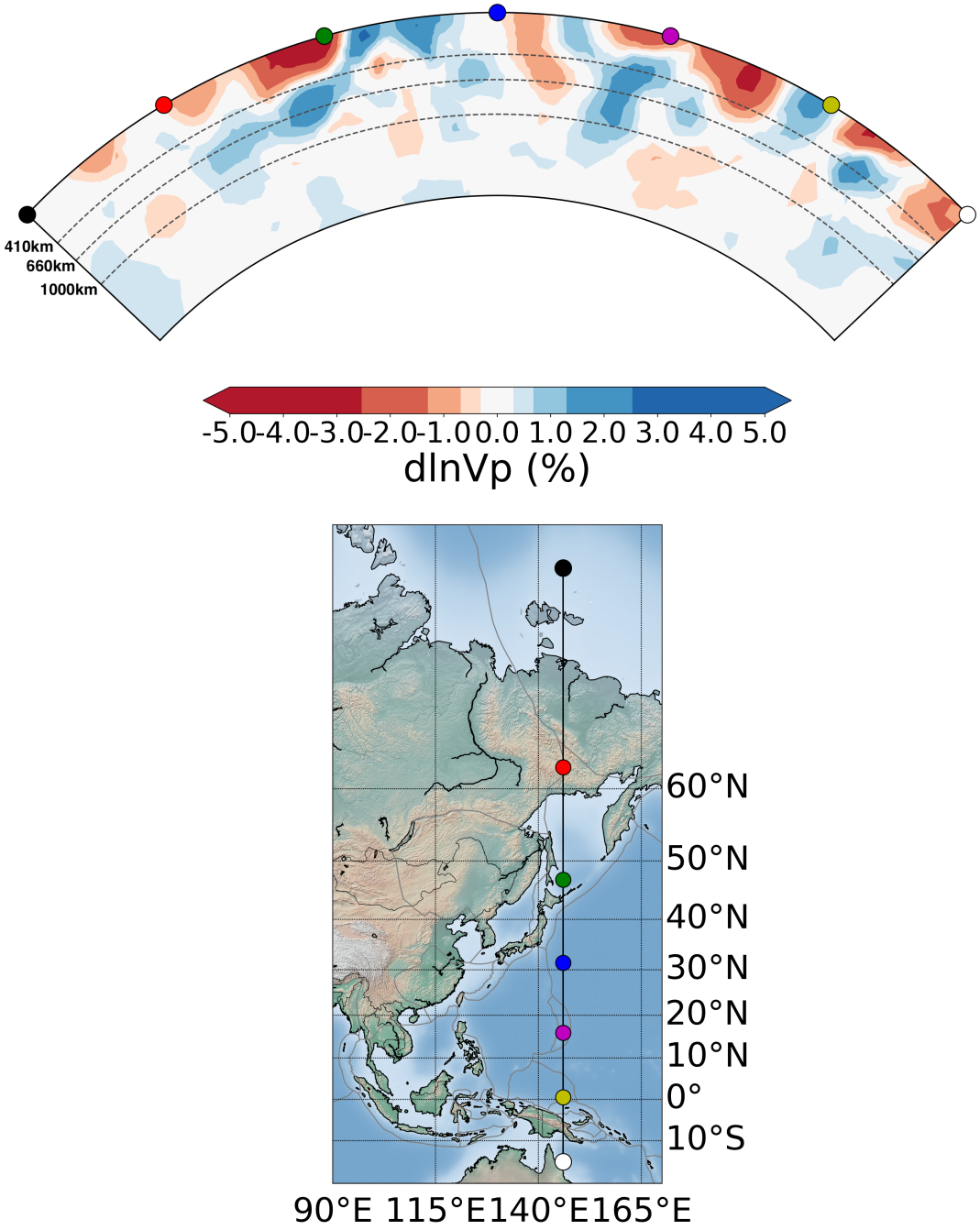

Figure A.25: (Top) Same type of cross-section as figure A1 but for a transect from south to north, along a longitude of 146° and between 15°S and 20°N in latitude . (Bottom) Regional map view of the study region, which highlights the location of the cross-section shown above. The colour of the nodes on the bottom transect correspond to the coloured nodes in the cross-section above.

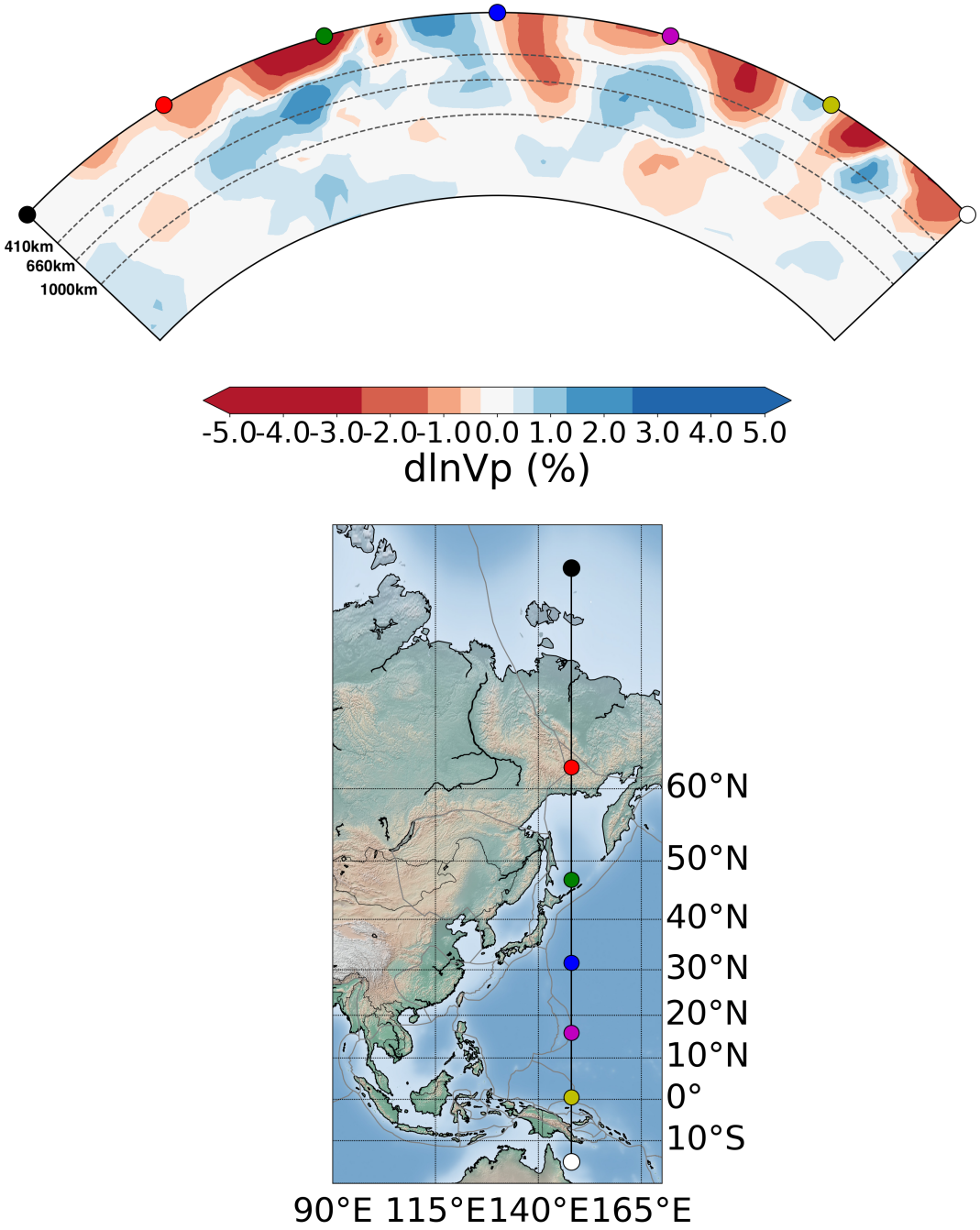

Figure A.26: (Top) Same type of cross-section as figure A1 but for a transect from south to north, along a longitude of 148° and between 15°S and 20°N in latitude . (Bottom) Regional map view of the study region, which highlights the location of the cross-section shown above. The colour of the nodes on the bottom transect correspond to the coloured nodes in the cross-section above.

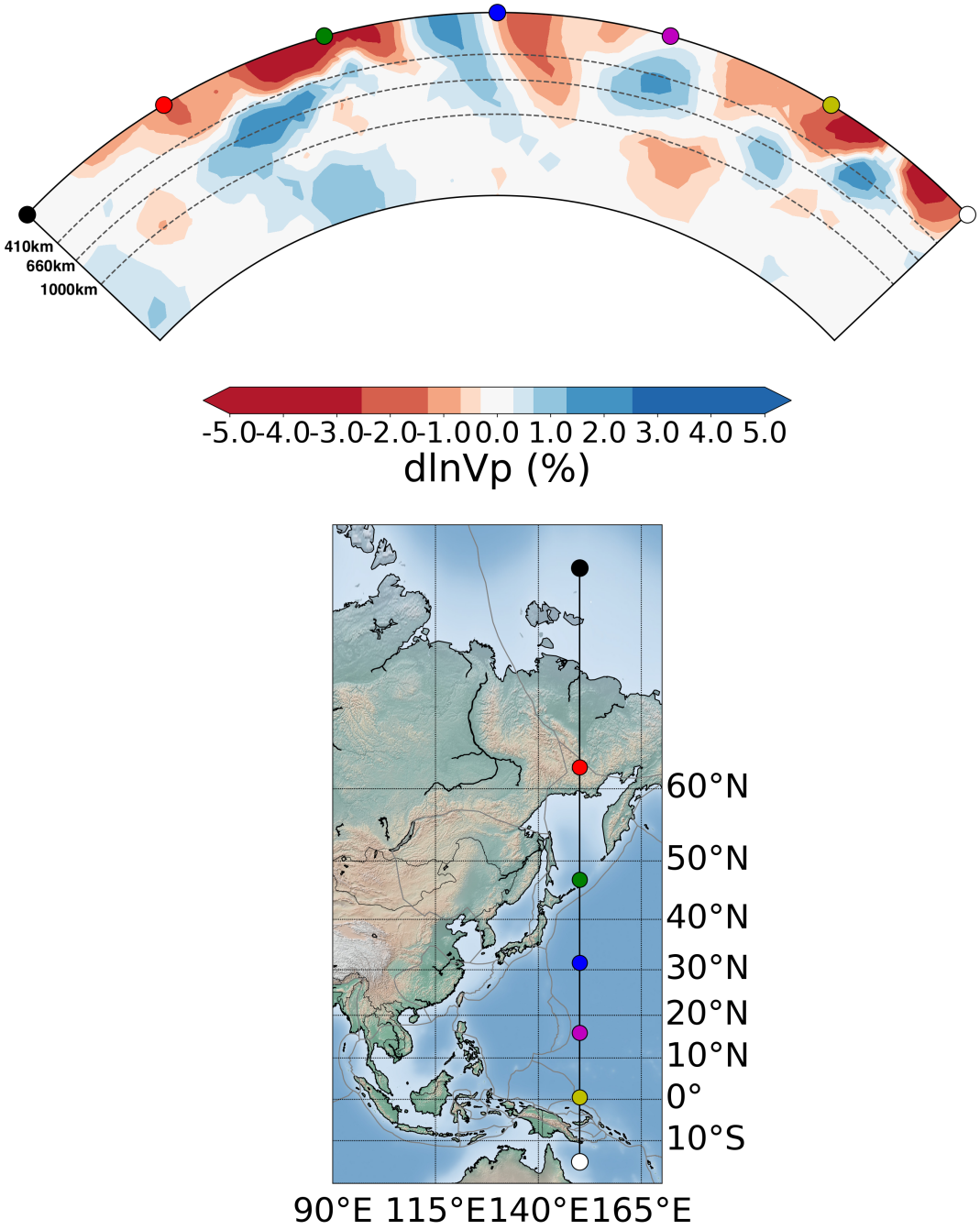

Figure A.27: (Top) Same type of cross-section as figure A1 but for a transect from south to north, along a longitude of 150° and between 15°S and 20°N in latitude . (Bottom) Regional map view of the study region, which highlights the location of the cross-section shown above. The colour of the nodes on the bottom transect correspond to the coloured nodes in the cross-section above.

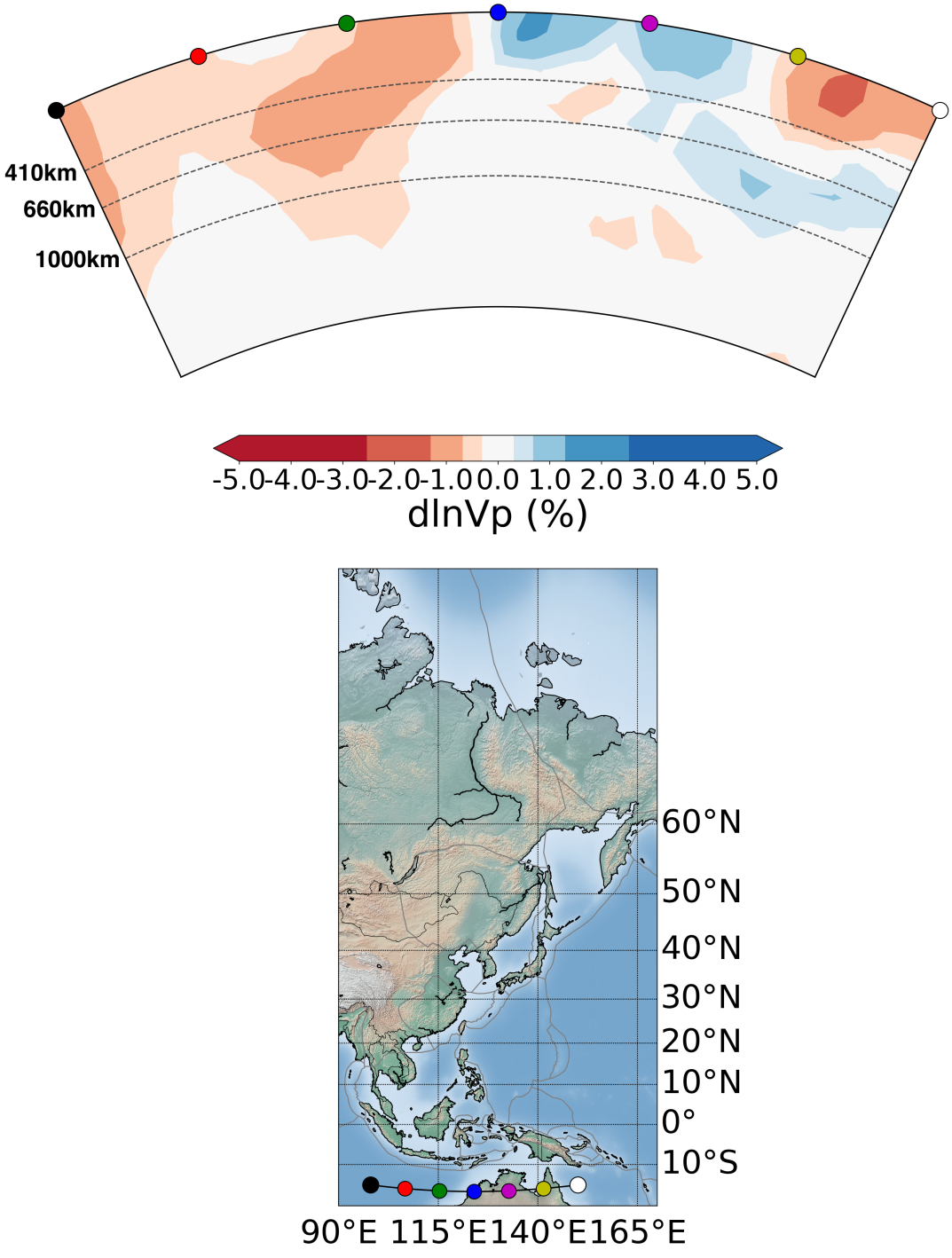

Figure A.28: (Top) Same type of cross-section as figure A1 but for a transect from east to west, along a latitude of -15° and between 98°E and 150°E in latitude . (Bottom) Regional map view of the study region, which highlights the location of the cross-section shown above. The colour of the nodes on the bottom transect correspond to the coloured nodes in the cross-section above.

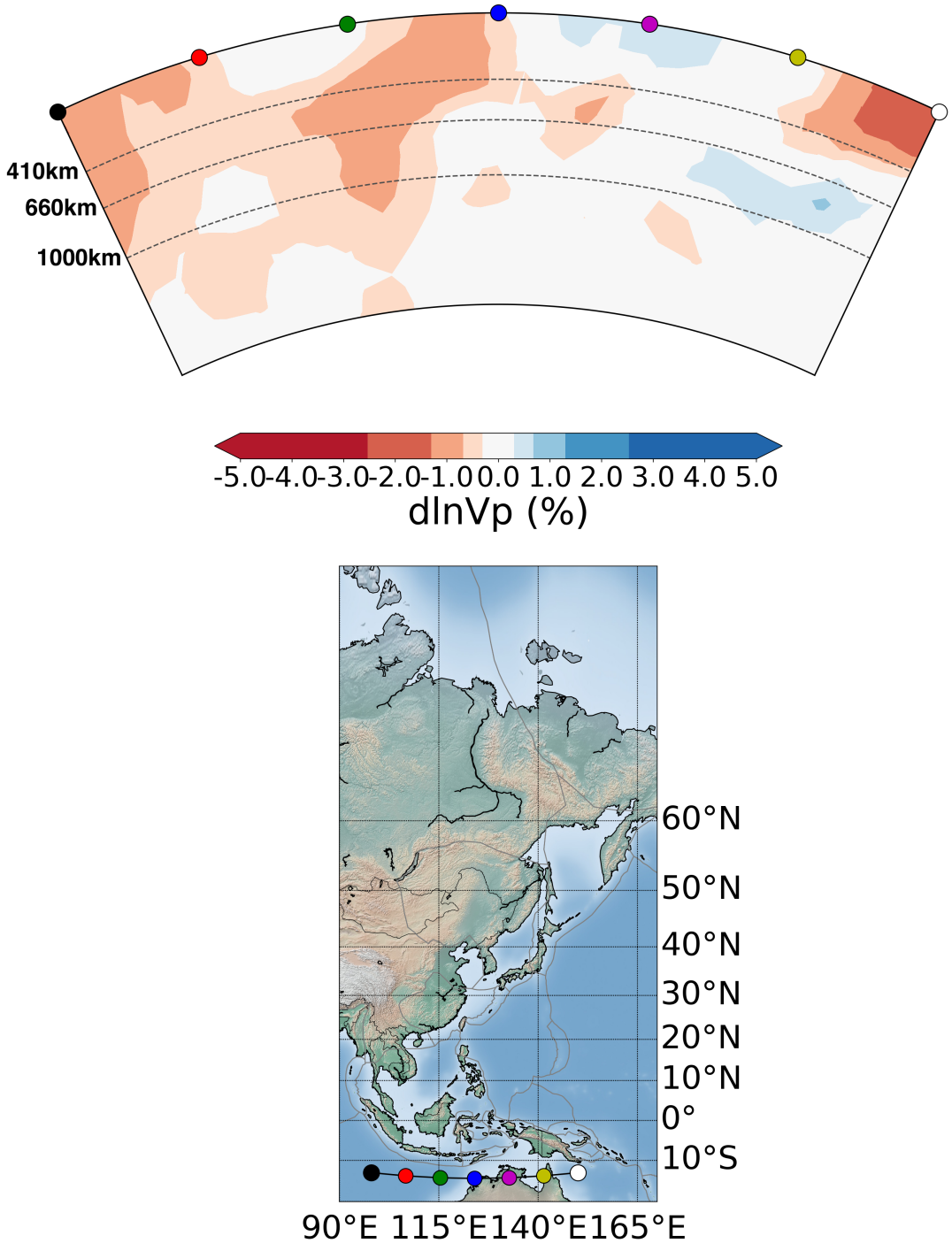

Figure A.29: (Top) Same type of cross-section as figure A1 but for a transect from east to west, along a latitude of -13° and between 98°E and 150°E in latitude . (Bottom) Regional map view of the study region, which highlights the location of the cross-section shown above. The colour of the nodes on the bottom transect correspond to the coloured nodes in the cross-section above.

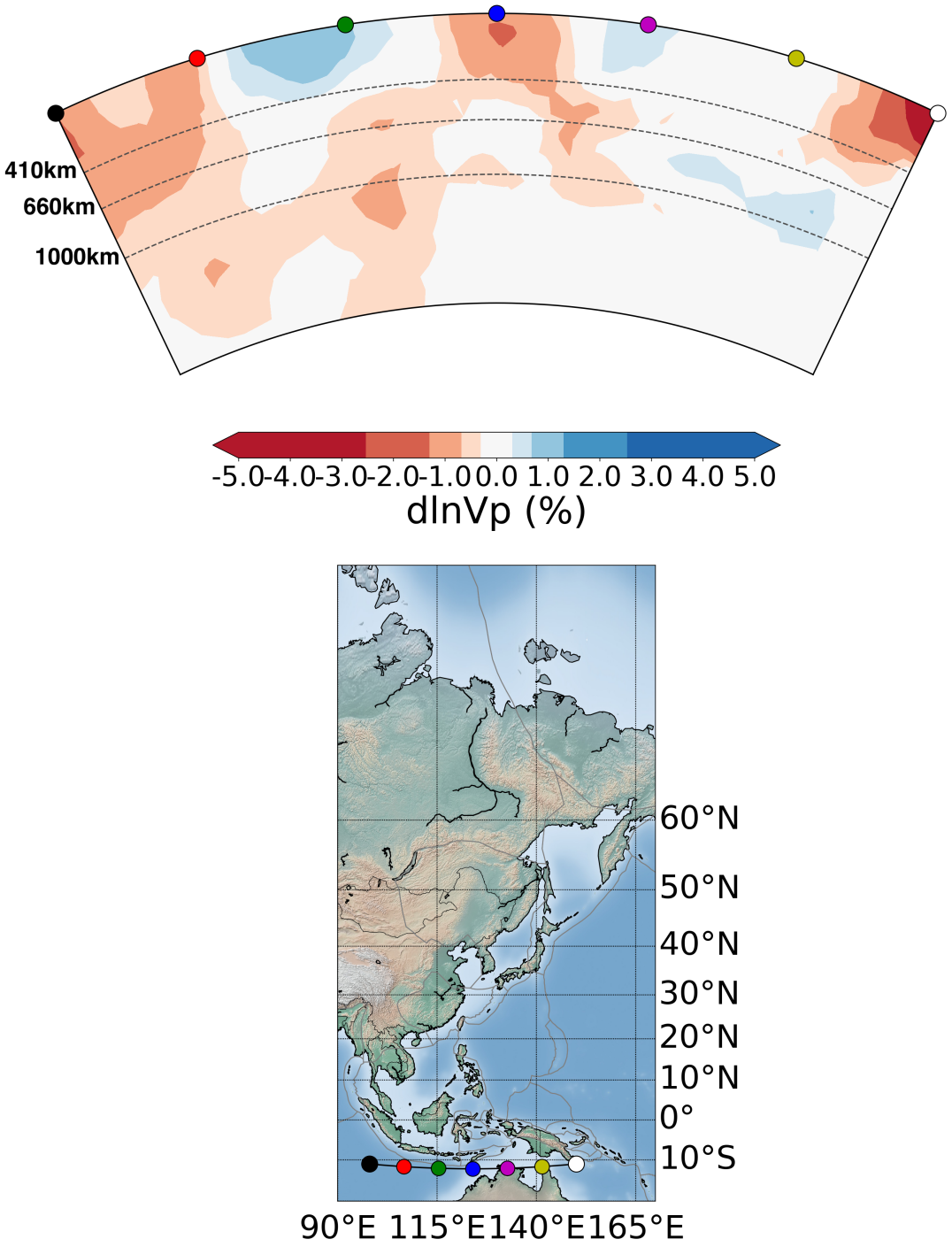

Figure A.30: (Top) Same type of cross-section as figure A1 but for a transect from east to west, along a latitude of -11° and between 98°E and 150°E in latitude . (Bottom) Regional map view of the study region, which highlights the location of the cross-section shown above. The colour of the nodes on the bottom transect correspond to the coloured nodes in the cross-section above.

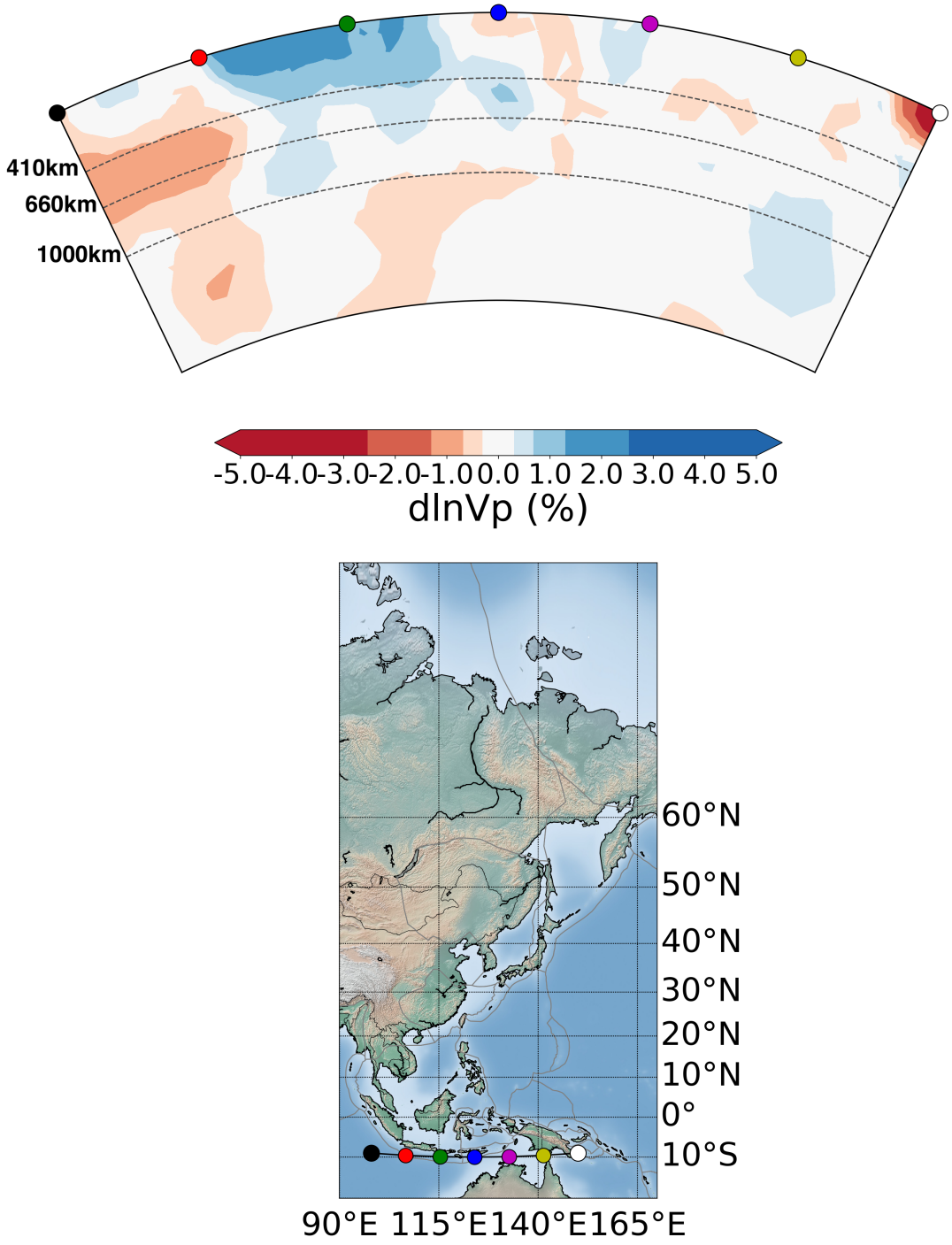

Figure A.31: (Top) Same type of cross-section as figure A1 but for a transect from east to west, along a latitude of -9° and between 98°E and 150°E in latitude . (Bottom) Regional map view of the study region, which highlights the location of the cross-section shown above. The colour of the nodes on the bottom transect correspond to the coloured nodes in the cross-section above.

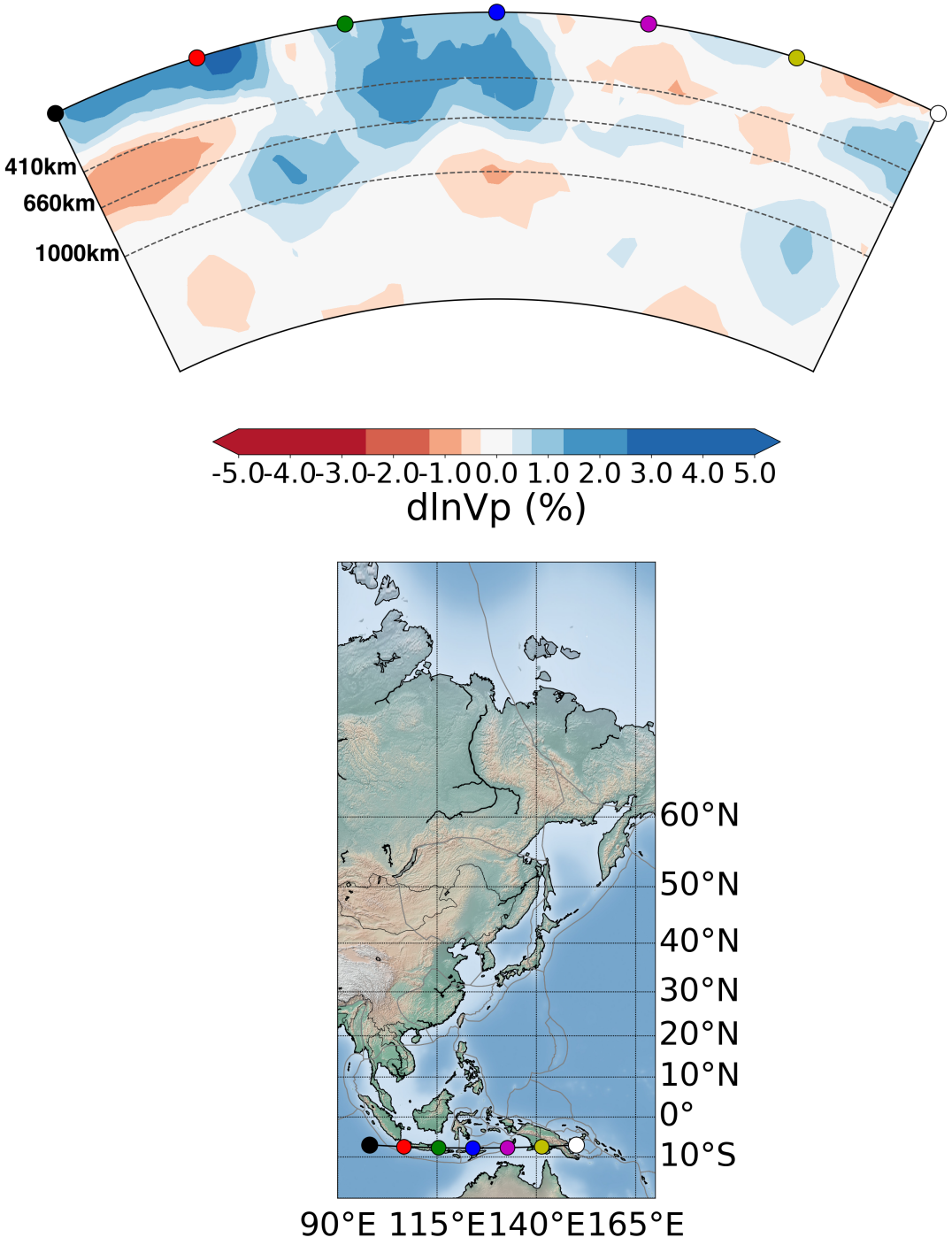

Figure A.32: (Top) Same type of cross-section as figure A1 but for a transect from east to west, along a latitude of -7° and between 98°E and 150°E in latitude . (Bottom) Regional map view of the study region, which highlights the location of the cross-section shown above. The colour of the nodes on the bottom transect correspond to the coloured nodes in the cross-section above.

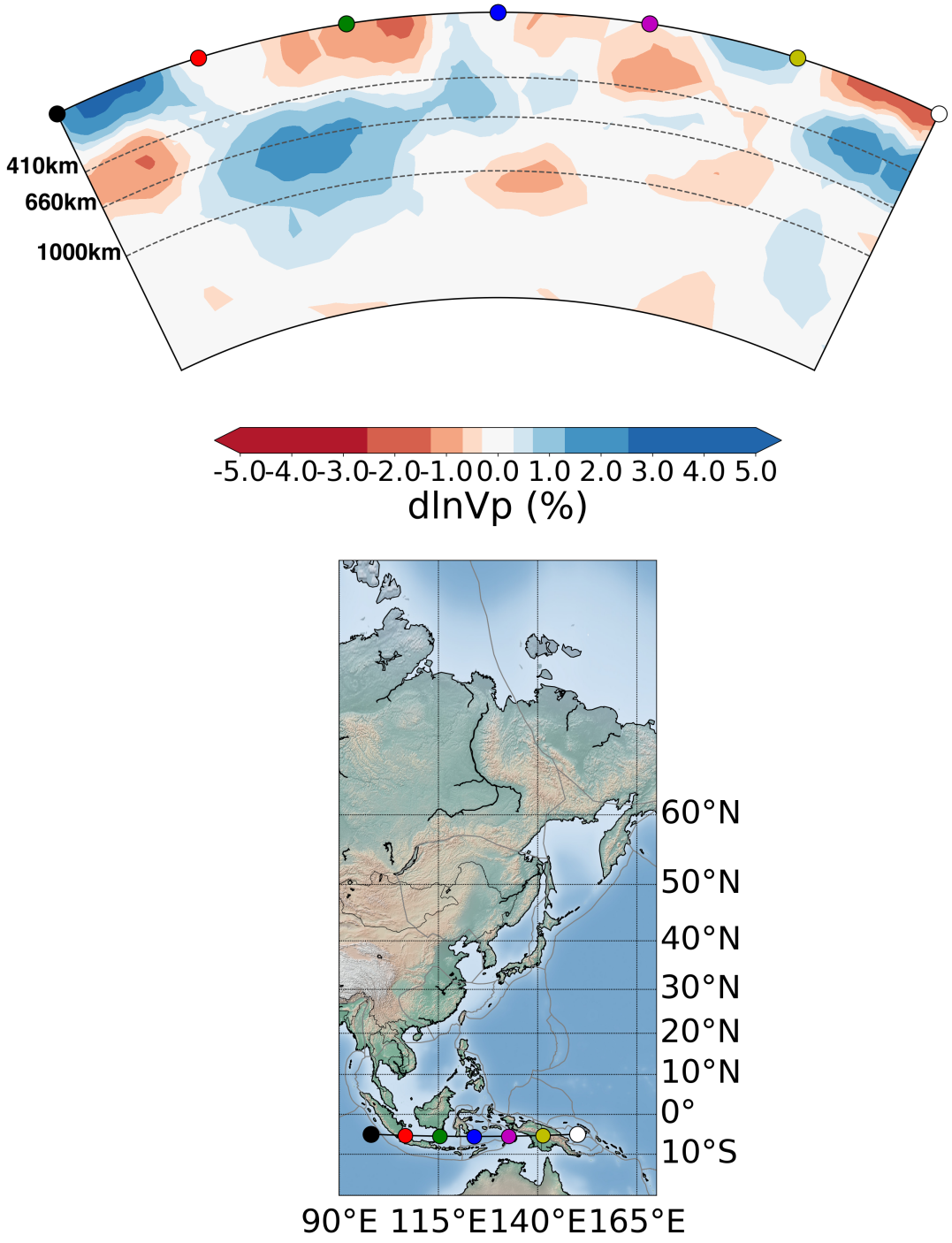

Figure A.33: (Top) Same type of cross-section as figure A1 but for a transect from east to west, along a latitude of -5° and between 98°E and 150°E in latitude . (Bottom) Regional map view of the study region, which highlights the location of the cross-section shown above. The colour of the nodes on the bottom transect correspond to the coloured nodes in the cross-section above.

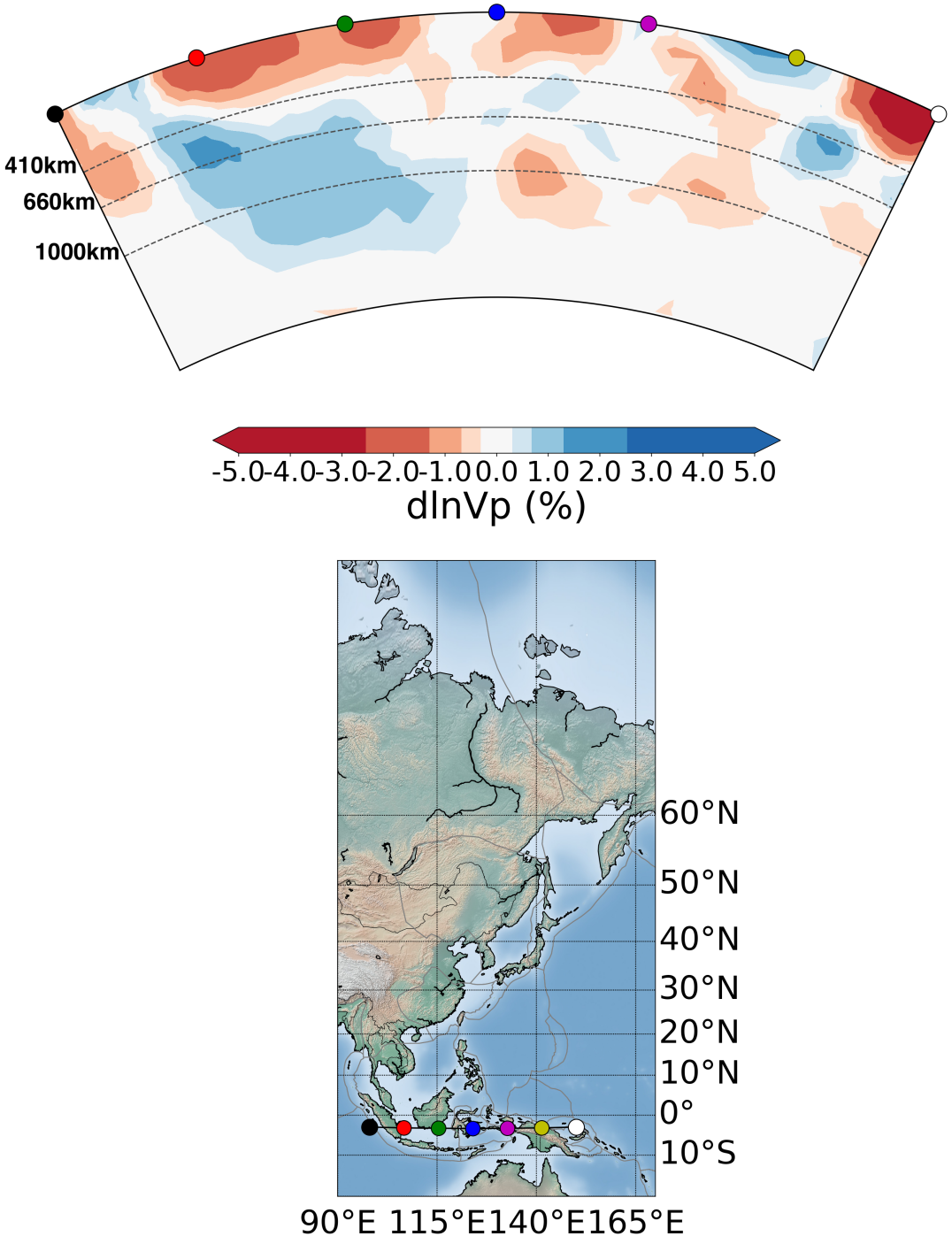

Figure A.34: (Top) Same type of cross-section as figure A1 but for a transect from east to west, along a latitude of -3° and between 98°E and 150°E in latitude . (Bottom) Regional map view of the study region, which highlights the location of the cross-section shown above. The colour of the nodes on the bottom transect correspond to the coloured nodes in the cross-section above.

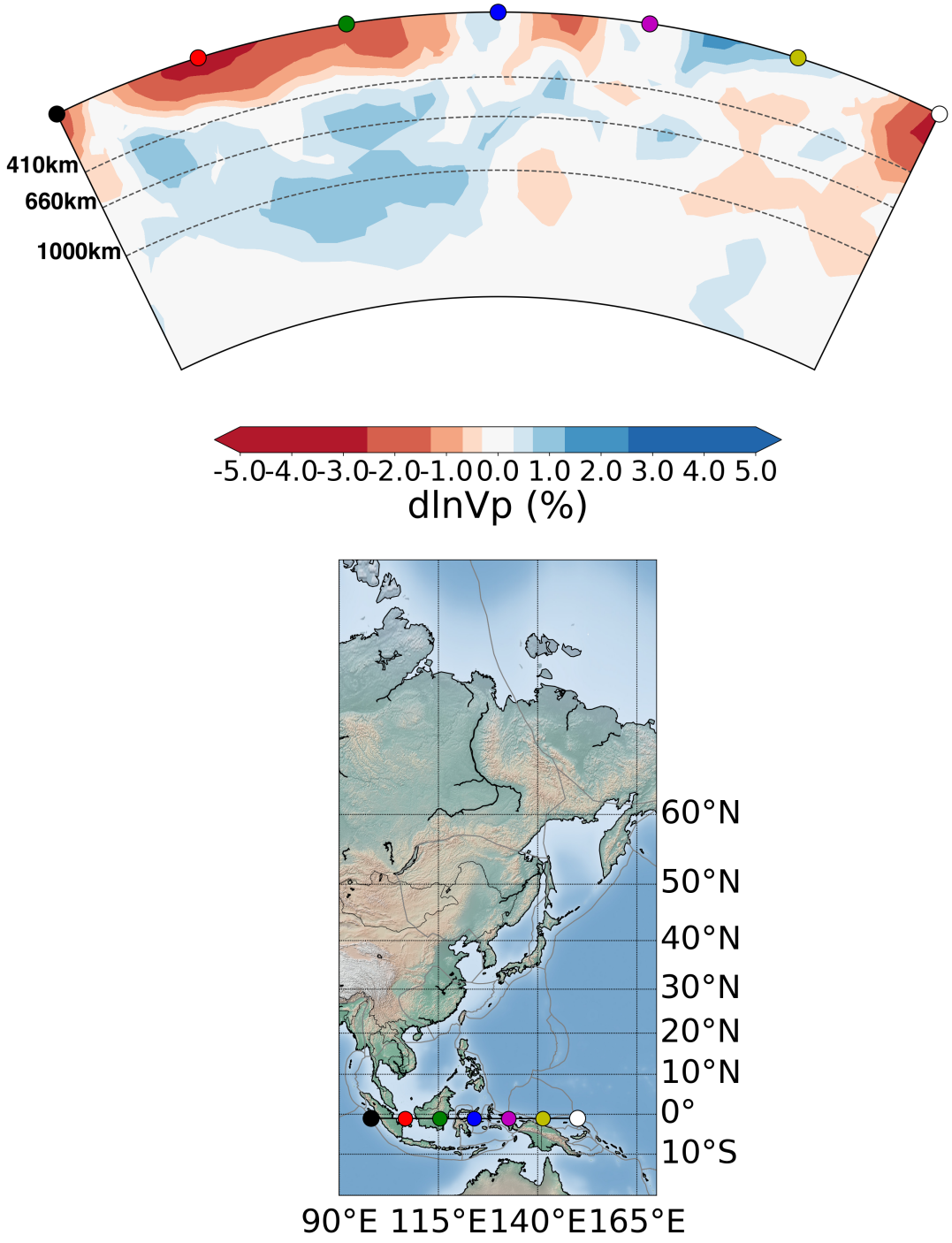

Figure A.35: (Top) Same type of cross-section as figure A1 but for a transect from east to west, along a latitude of -1° and between 98°E and 150°E in latitude . (Bottom) Regional map view of the study region, which highlights the location of the cross-section shown above. The colour of the nodes on the bottom transect correspond to the coloured nodes in the cross-section above.

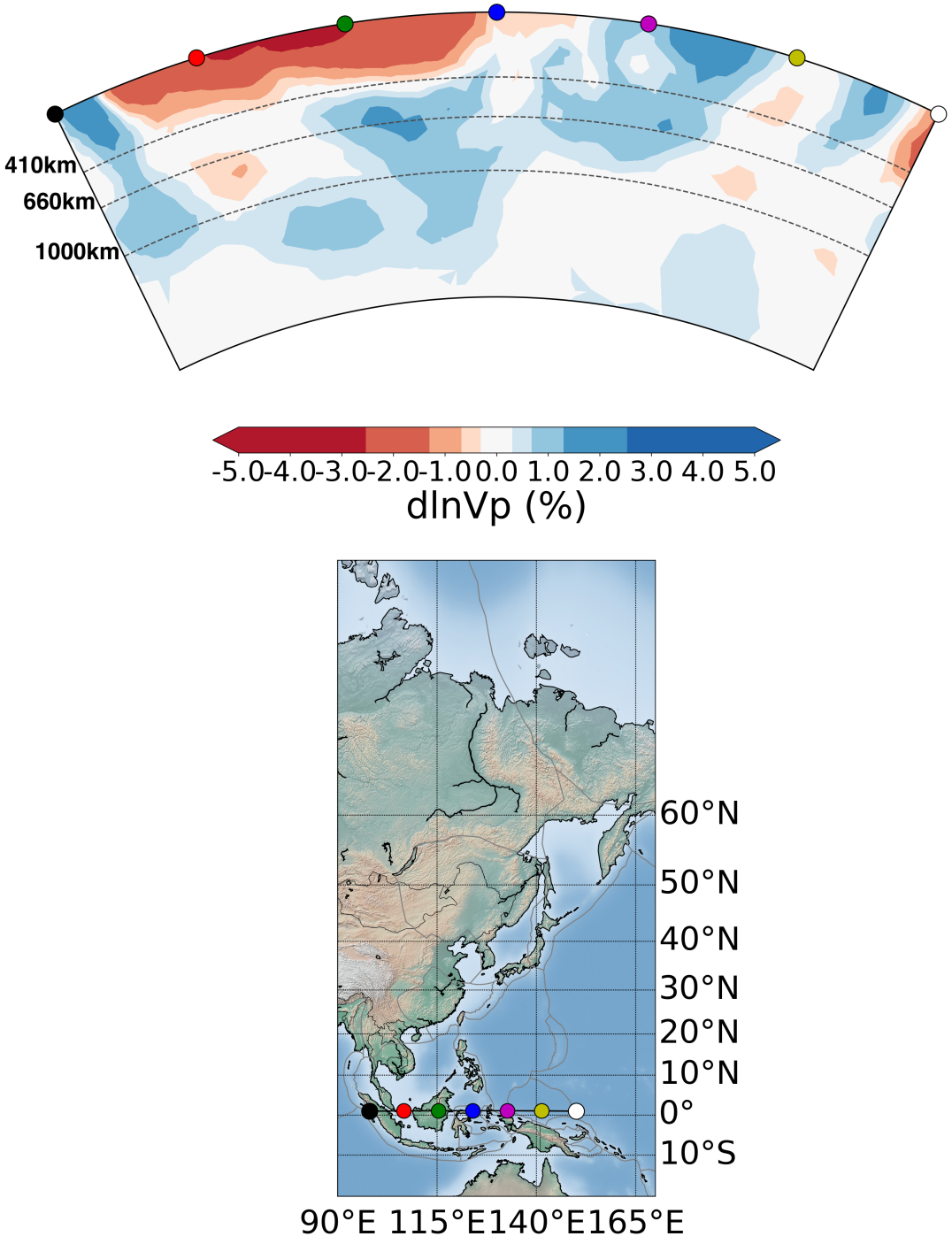

Figure A.36: (Top) Same type of cross-section as figure A1 but for a transect from east to west, along a latitude of 1°N and between 98°E and 150°E in latitude . (Bottom) Regional map view of the study region, which highlights the location of the cross-section shown above. The colour of the nodes on the bottom transect correspond to the coloured nodes in the cross-section above.

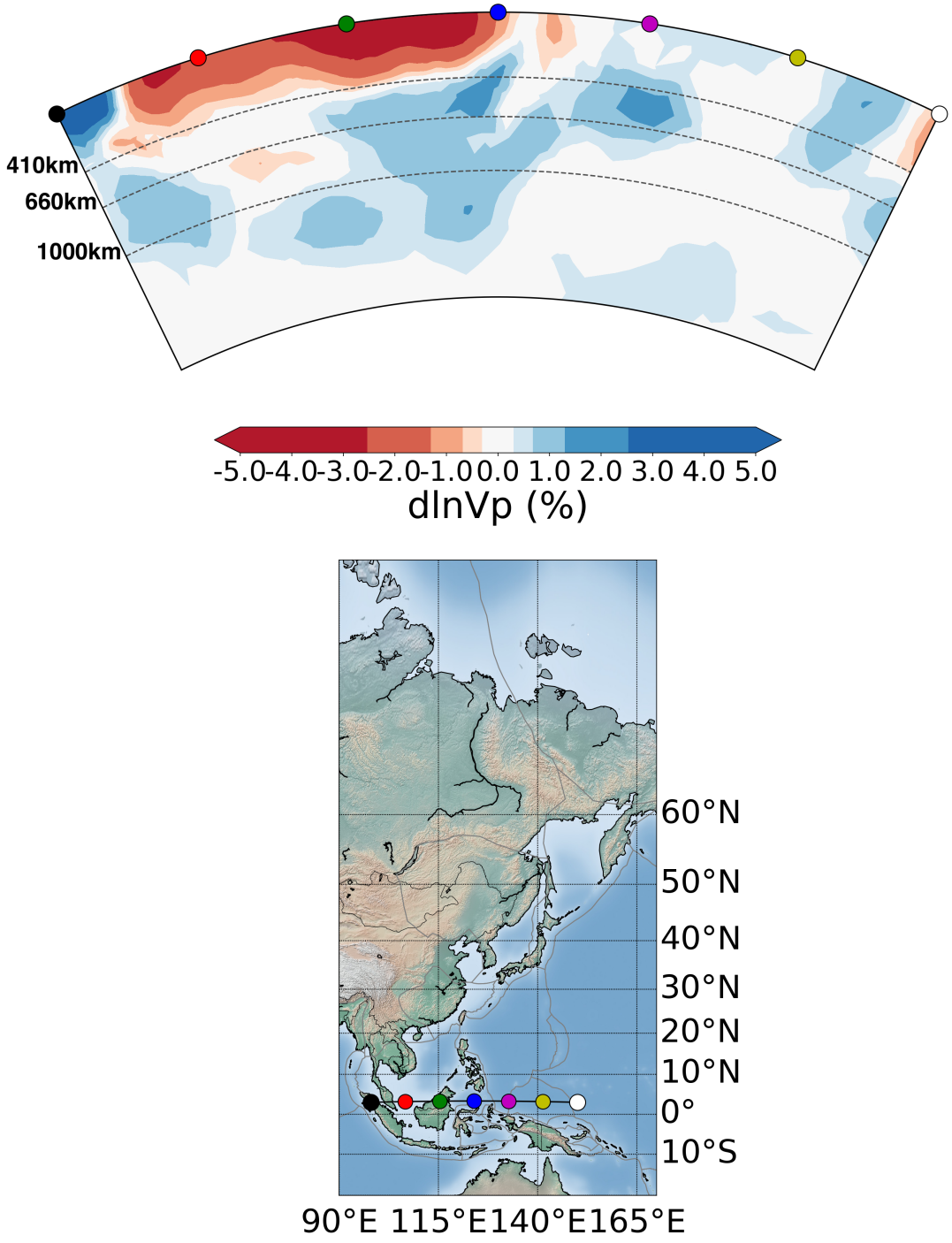

Figure A.37: (Top) Same type of cross-section as figure A1 but for a transect from east to west, along a latitude of 3ºN and between 98ºE and 150ºE in latitude . (Bottom) Regional map view of the study region, which highlights the location of the cross-section shown above. The colour of the nodes on the bottom transect correspond to the coloured nodes in the cross-section above.

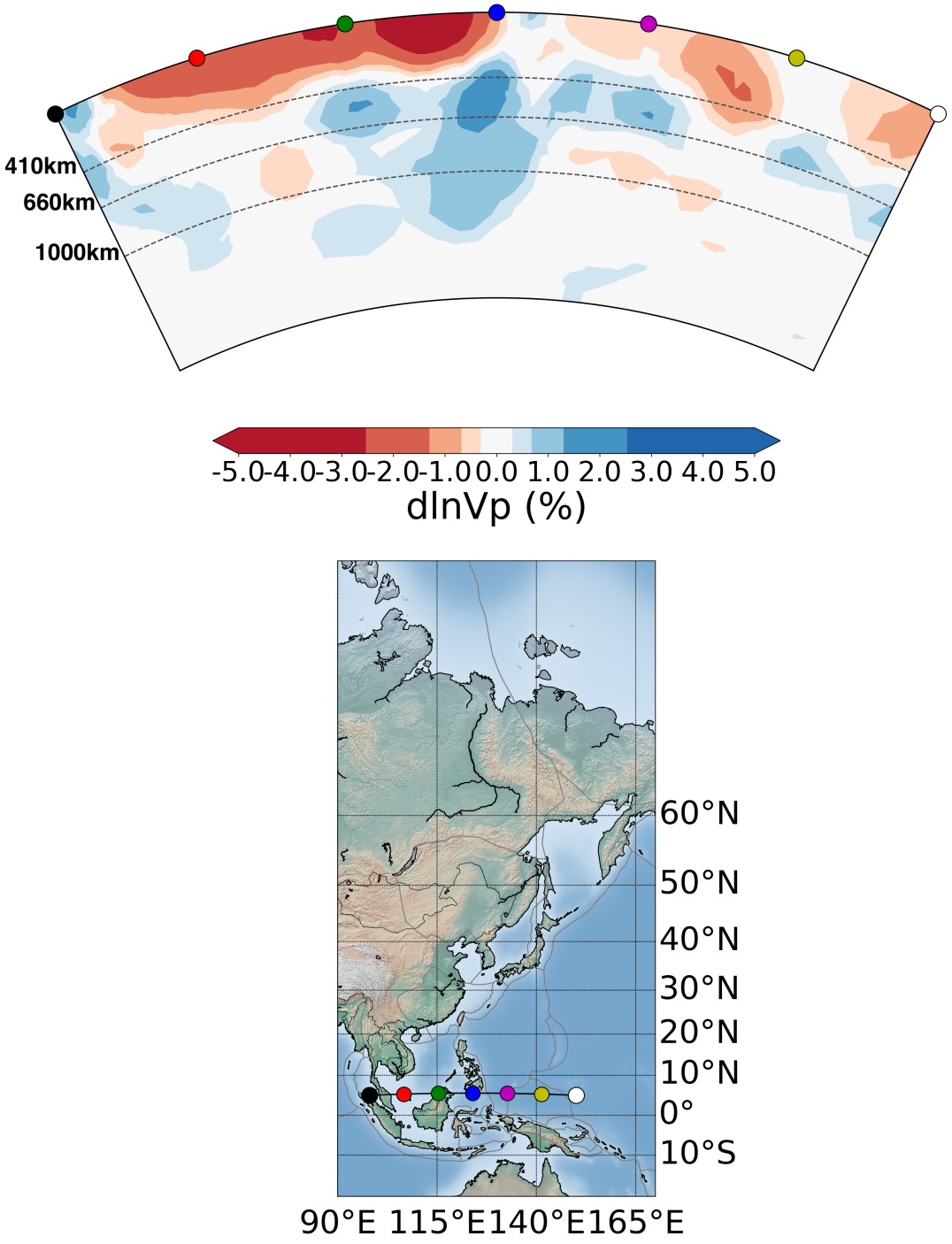

Figure A.38: (Top) Same type of cross-section as figure A1 but for a transect from east to west, along a latitude of 5°N and between 98°E and 150°E in latitude . (Bottom) Regional map view of the study region, which highlights the location of the cross-section shown above. The colour of the nodes on the bottom transect correspond to the coloured nodes in the cross-section above.

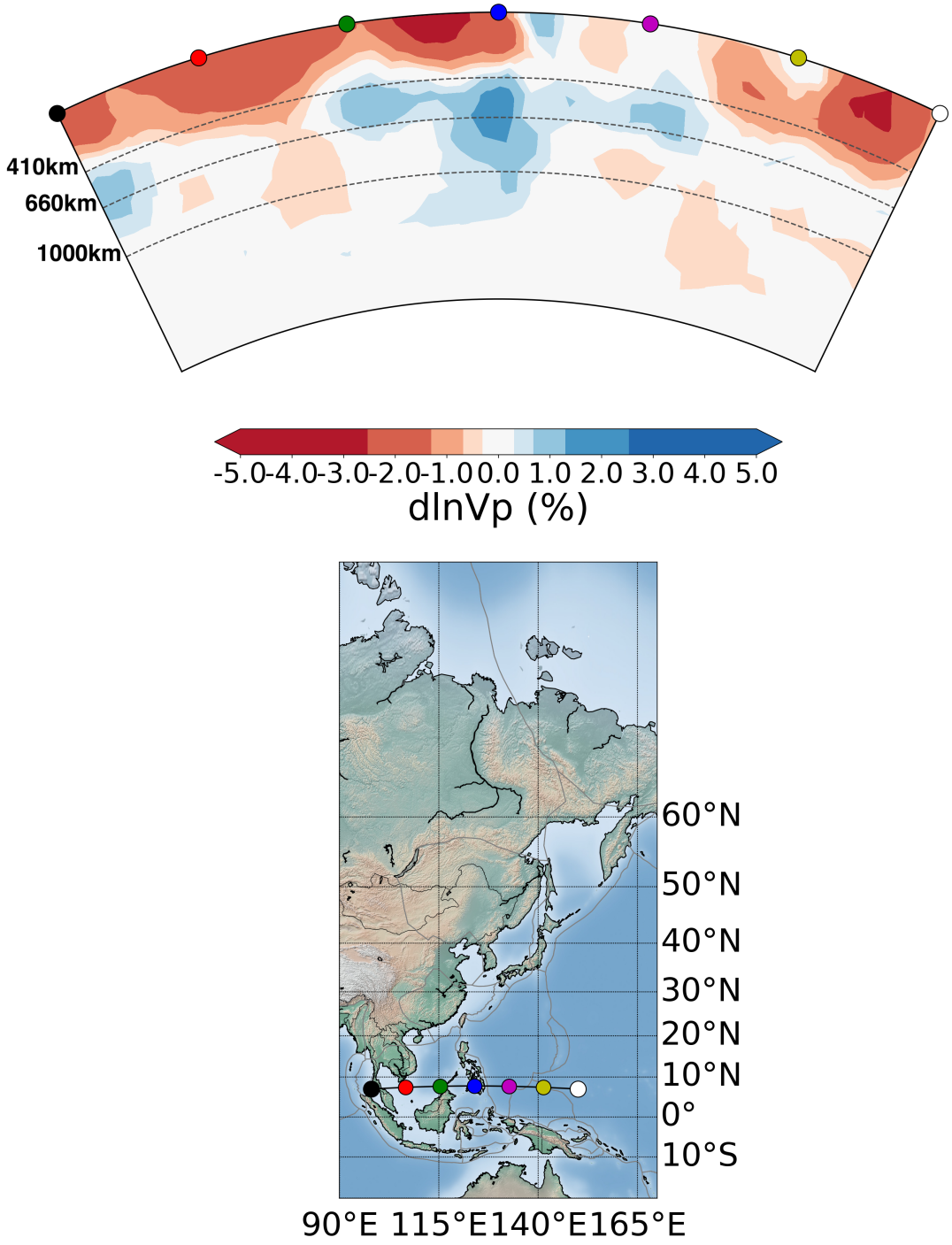

Figure A.39: (Top) Same type of cross-section as figure A1 but for a transect from east to west, along a latitude of 7°N and between 98°E and 150°E in latitude . (Bottom) Regional map view of the study region, which highlights the location of the cross-section shown above. The colour of the nodes on the bottom transect correspond to the coloured nodes in the cross-section above.

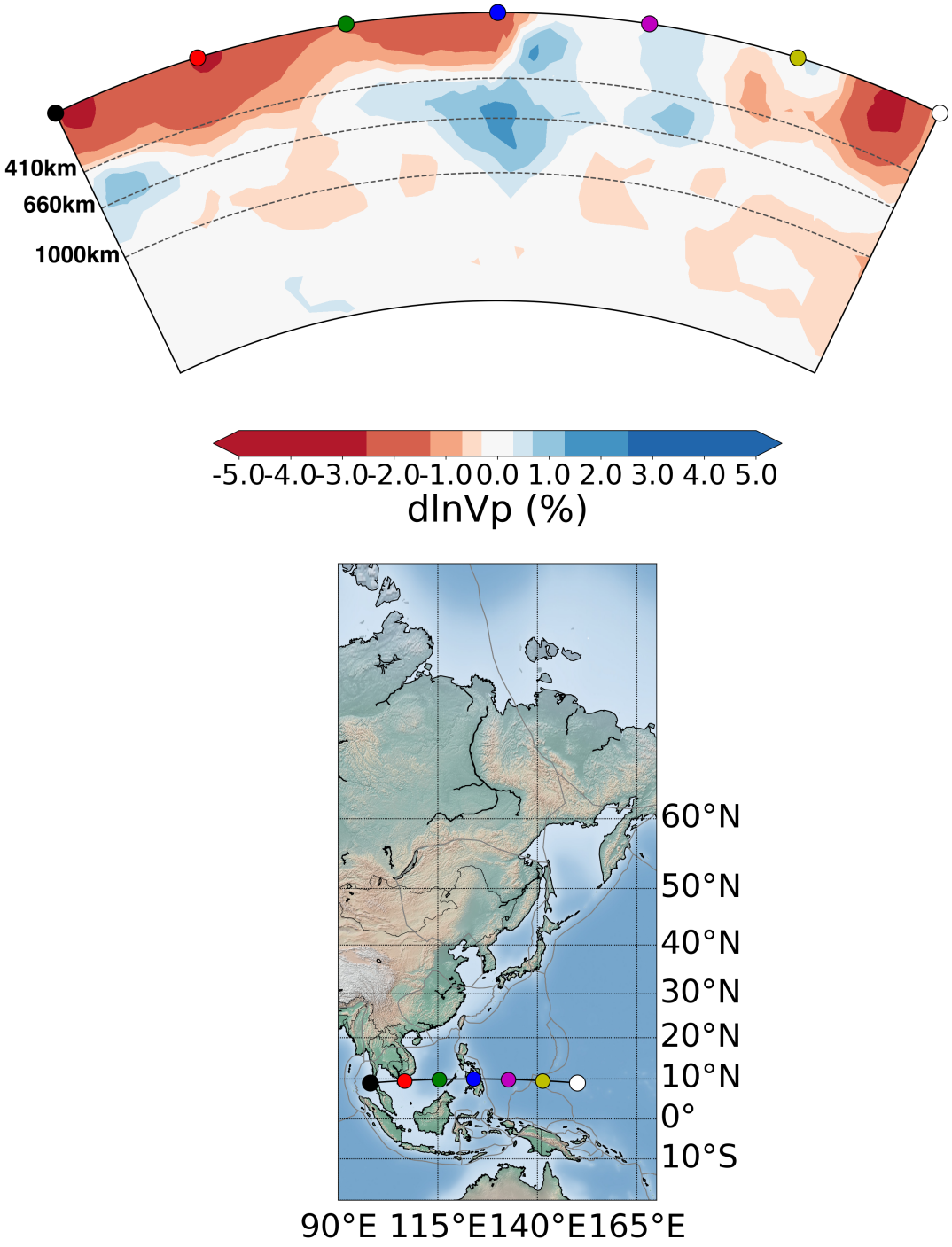

Figure A.40: (Top) Same type of cross-section as figure A1 but for a transect from east to west, along a latitude of 9°N and between 98°E and 150°E in latitude . (Bottom) Regional map view of the study region, which highlights the location of the cross-section shown above. The colour of the nodes on the bottom transect correspond to the coloured nodes in the cross-section above.

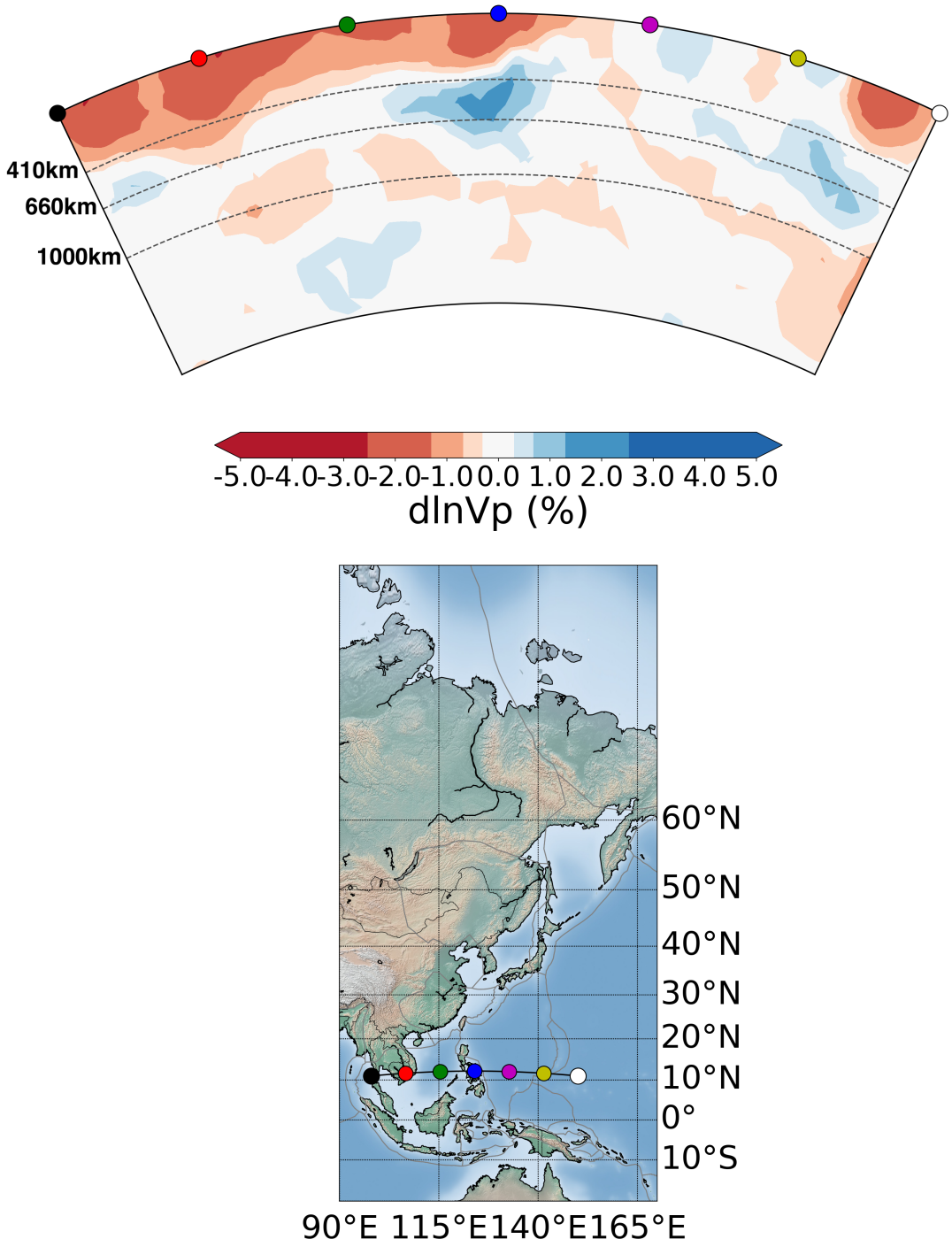

Figure A.41: (Top) Same type of cross-section as figure A1 but for a transect from east to west, along a latitude of 11°N and between 98°E and 150°E in latitude . (Bottom) Regional map view of the study region, which highlights the location of the cross-section shown above. The colour of the nodes on the bottom transect correspond to the coloured nodes in the cross-section above.

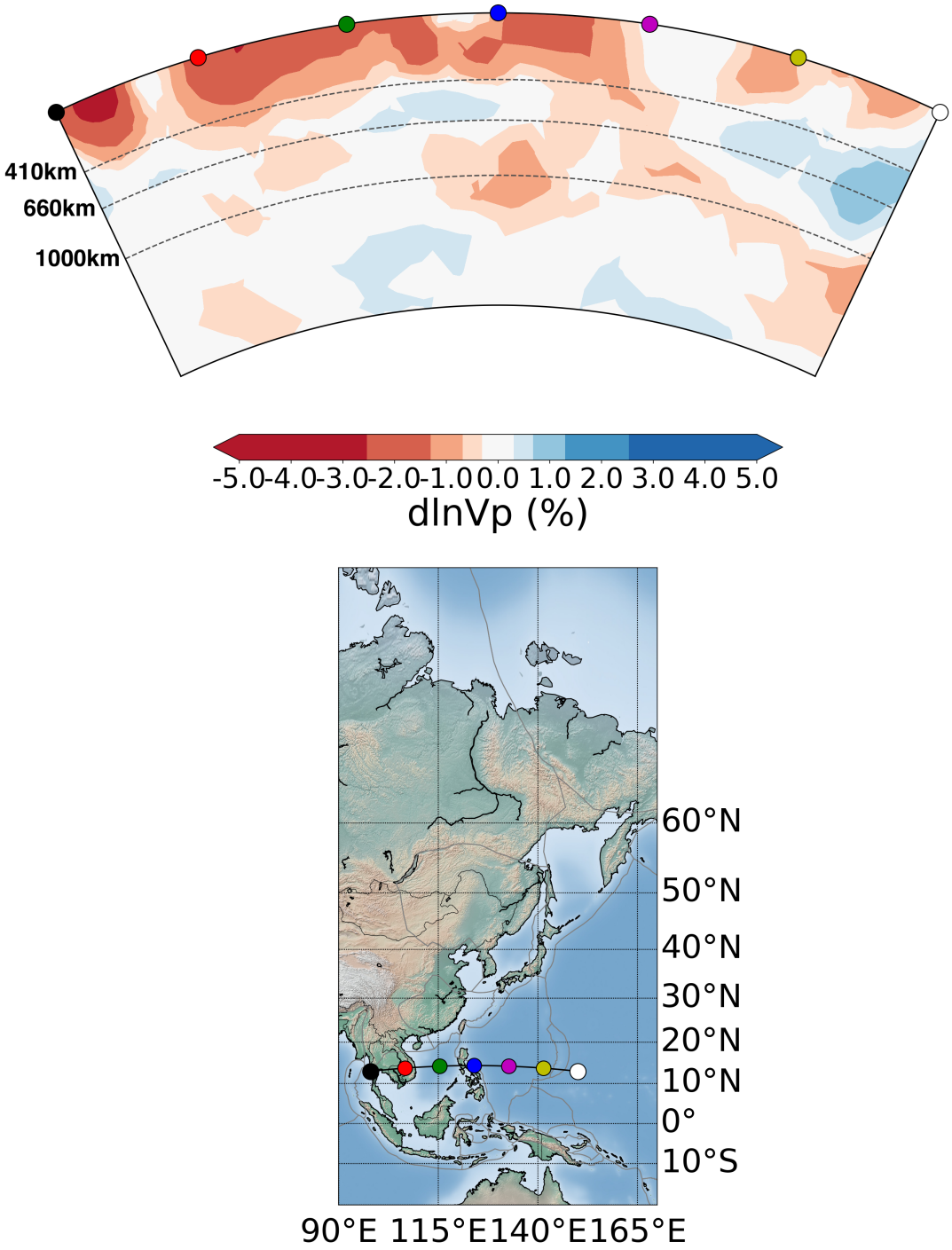

Figure A.42: (Top) Same type of cross-section as figure A1 but for a transect from east to west, along a latitude of 13°N and between 98°E and 150°E in latitude . (Bottom) Regional map view of the study region, which highlights the location of the cross-section shown above. The colour of the nodes on the bottom transect correspond to the coloured nodes in the cross-section above.

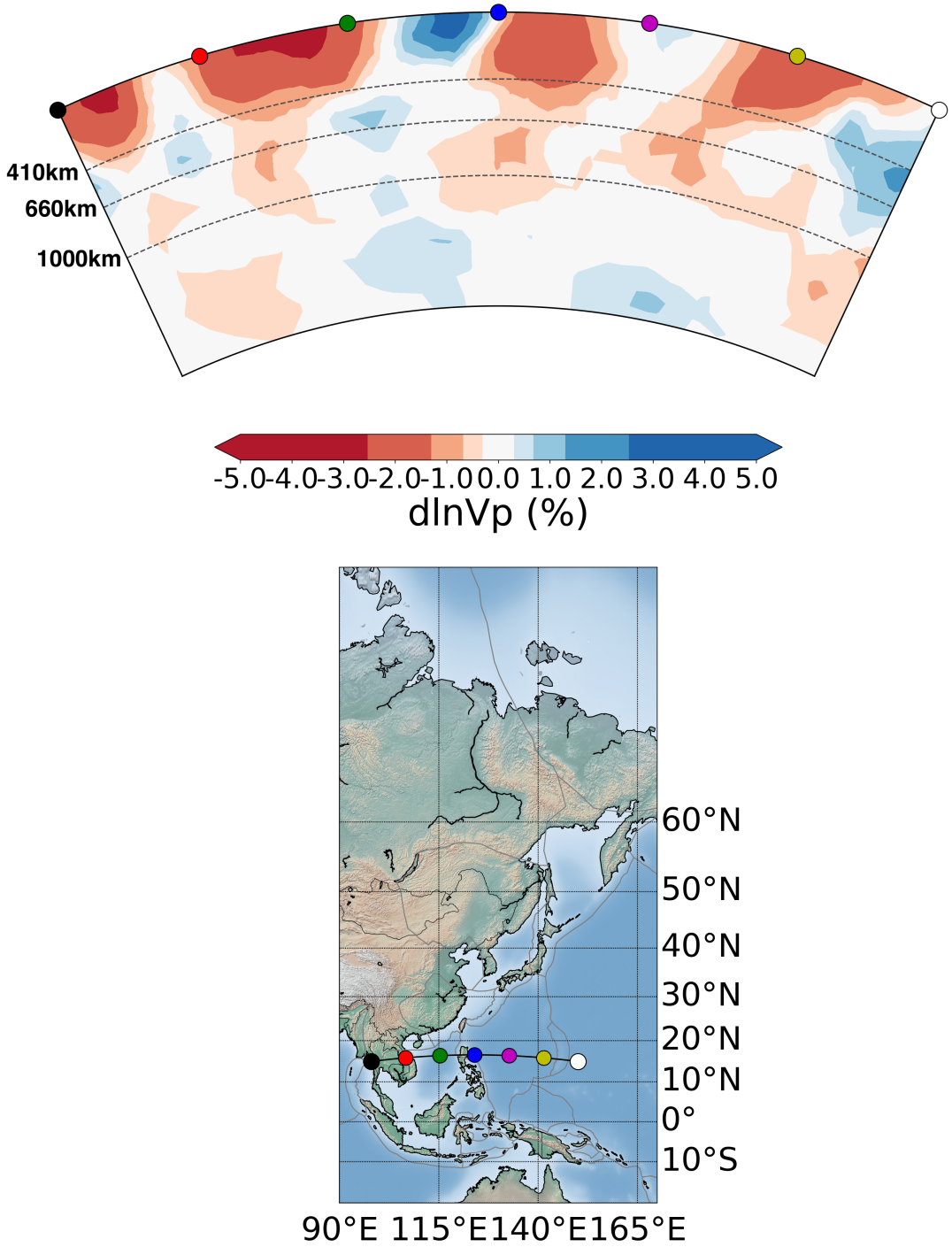

Figure A.43: (Top) Same type of cross-section as figure A1 but for a transect from east to west, along a latitude of 15°N and between 98°E and 150°E in latitude . (Bottom) Regional map view of the study region, which highlights the location of the cross-section shown above. The colour of the nodes on the bottom transect correspond to the coloured nodes in the cross-section above.

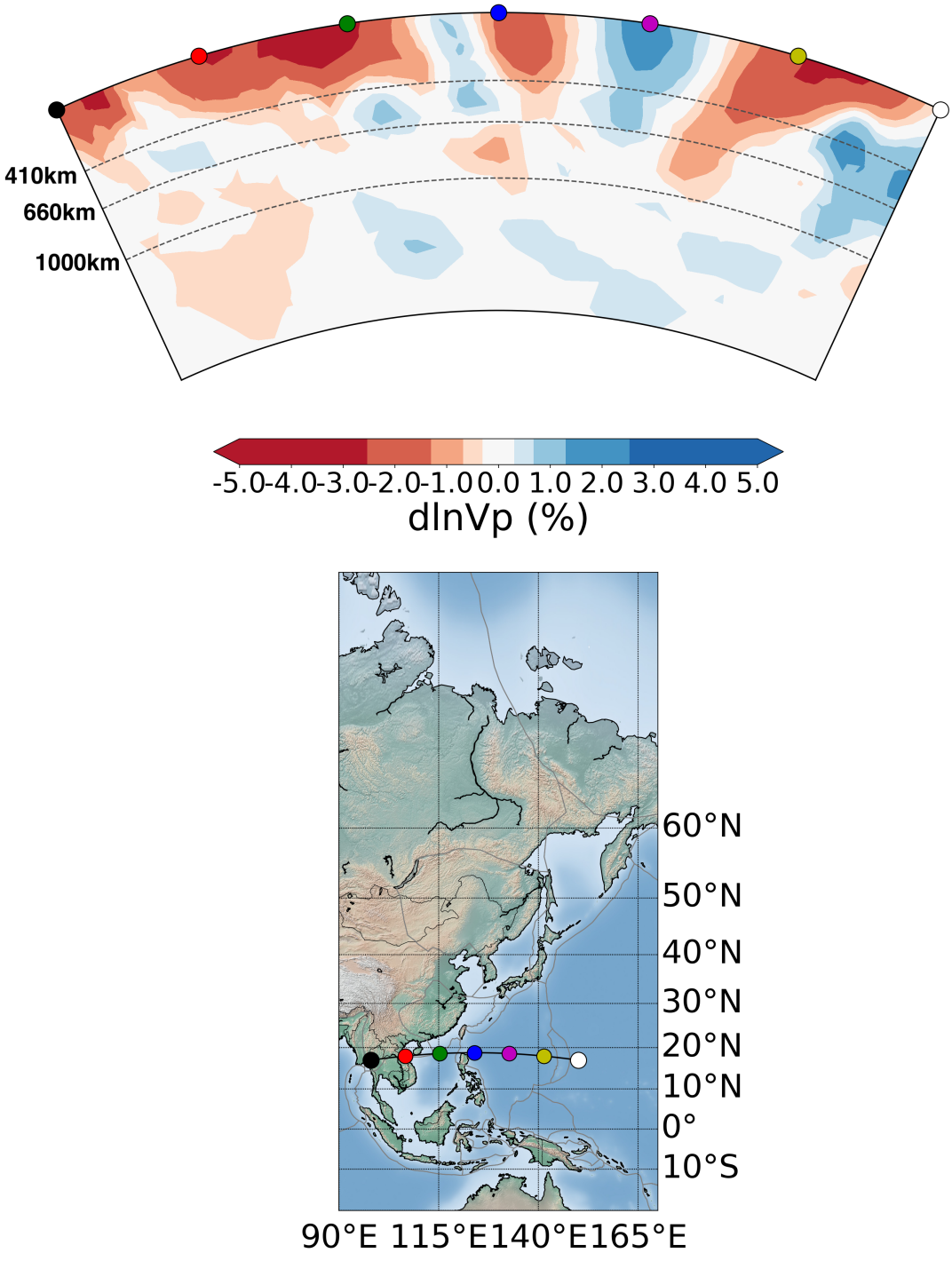

Figure A.44: (Top) Same type of cross-section as figure A1 but for a transect from east to west, along a latitude of 17°N and between 98°E and 150°E in latitude . (Bottom) Regional map view of the study region, which highlights the location of the cross-section shown above. The colour of the nodes on the bottom transect correspond to the coloured nodes in the cross-section above.

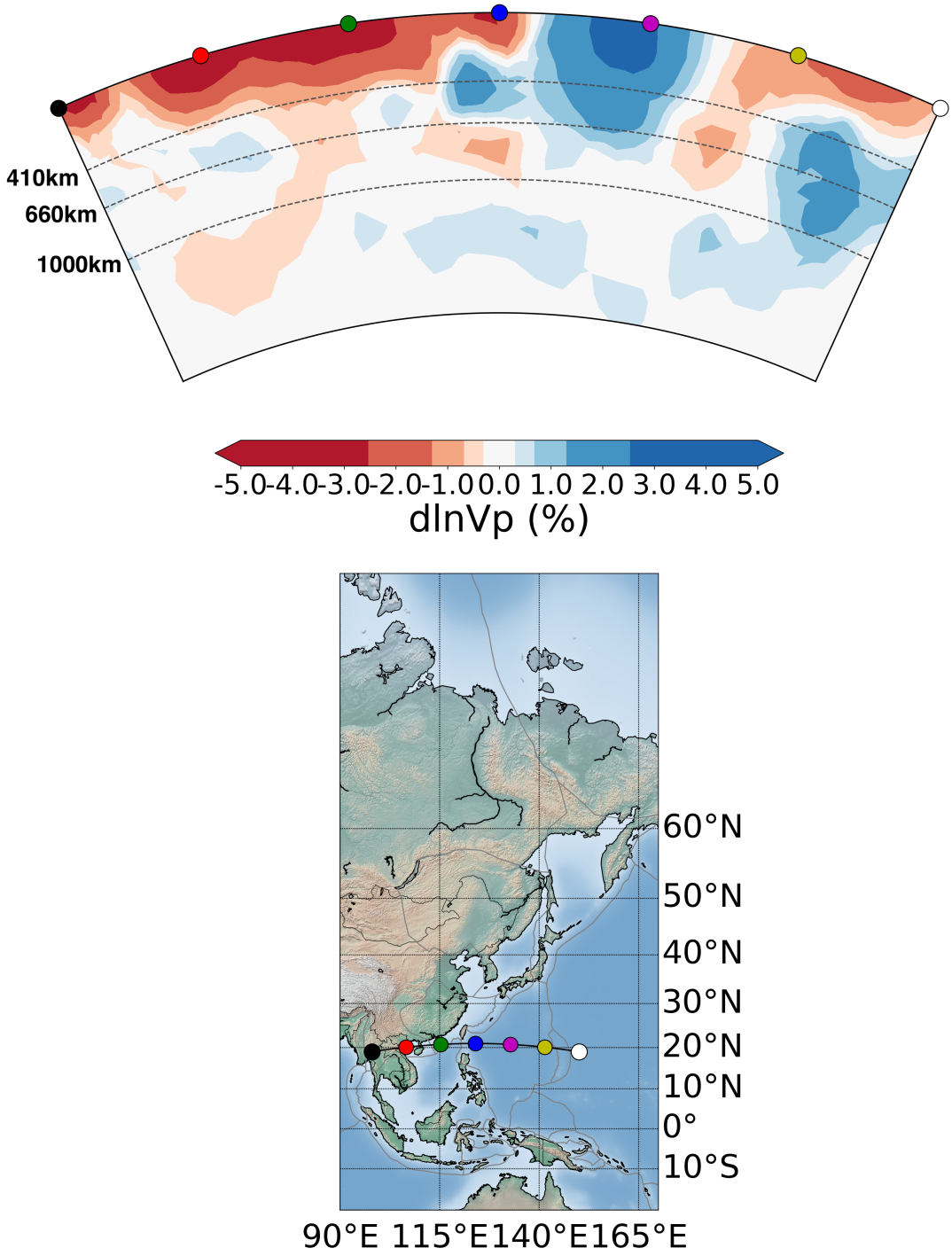

Figure A.45: (Top) Same type of cross-section as figure A1 but for a transect from east to west, along a latitude of 19°N and between 98°E and 150°E in latitude . (Bottom) Regional map view of the study region, which highlights the location of the cross-section shown above. The colour of the nodes on the bottom transect correspond to the coloured nodes in the cross-section above.

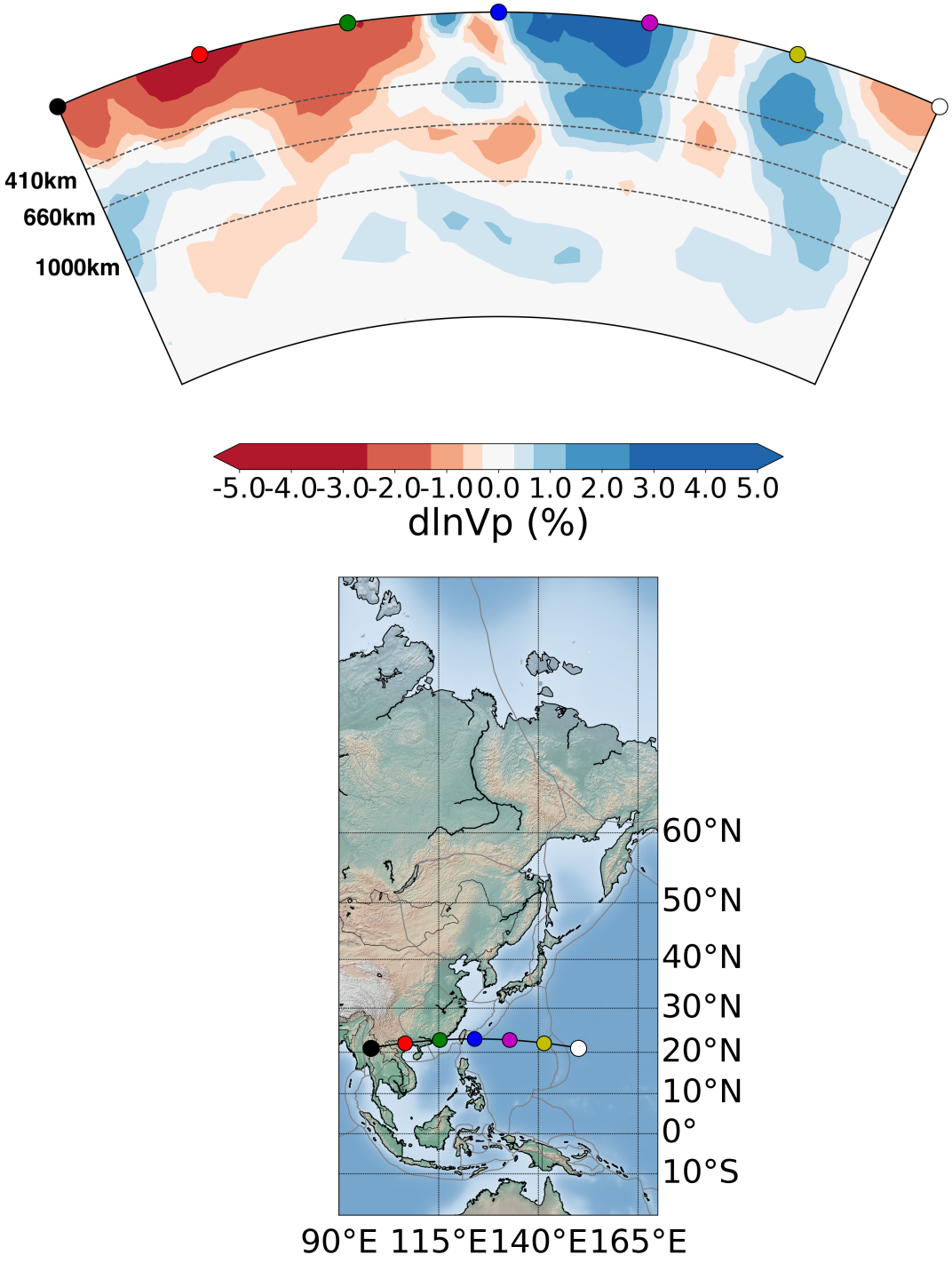

Figure A.46: (Top) Same type of cross-section as figure A1 but for a transect from east to west, along a latitude of 21°N and between 98°E and 150°E in latitude . (Bottom) Regional map view of the study region, which highlights the location of the cross-section shown above. The colour of the nodes on the bottom transect correspond to the coloured nodes in the cross-section above.

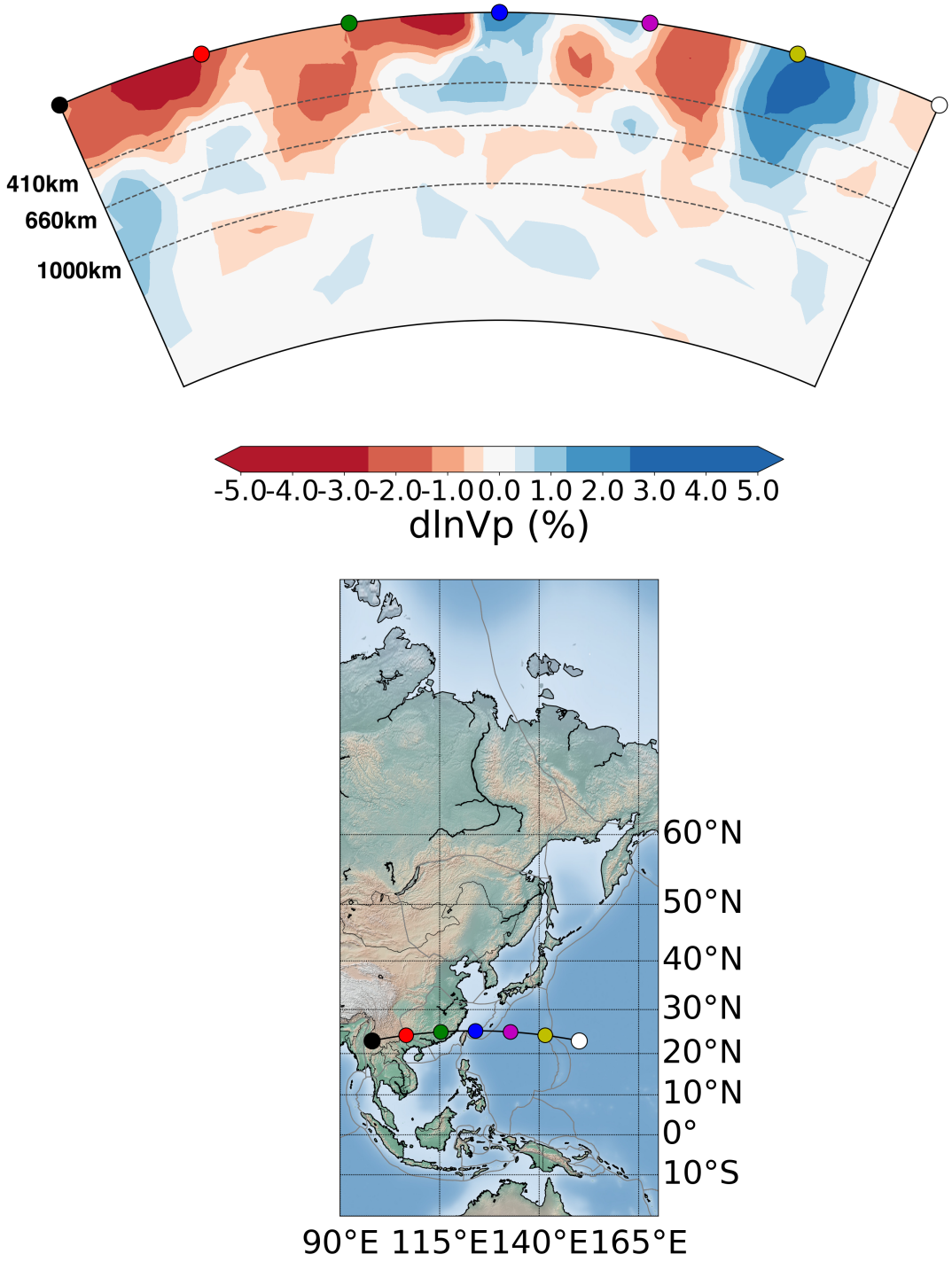

Figure A.47: (Top) Same type of cross-section as figure A1 but for a transect from east to west, along a latitude of 23°N and between 98°E and 150°E in latitude . (Bottom) Regional map view of the study region, which highlights the location of the cross-section shown above. The colour of the nodes on the bottom transect correspond to the coloured nodes in the cross-section above.

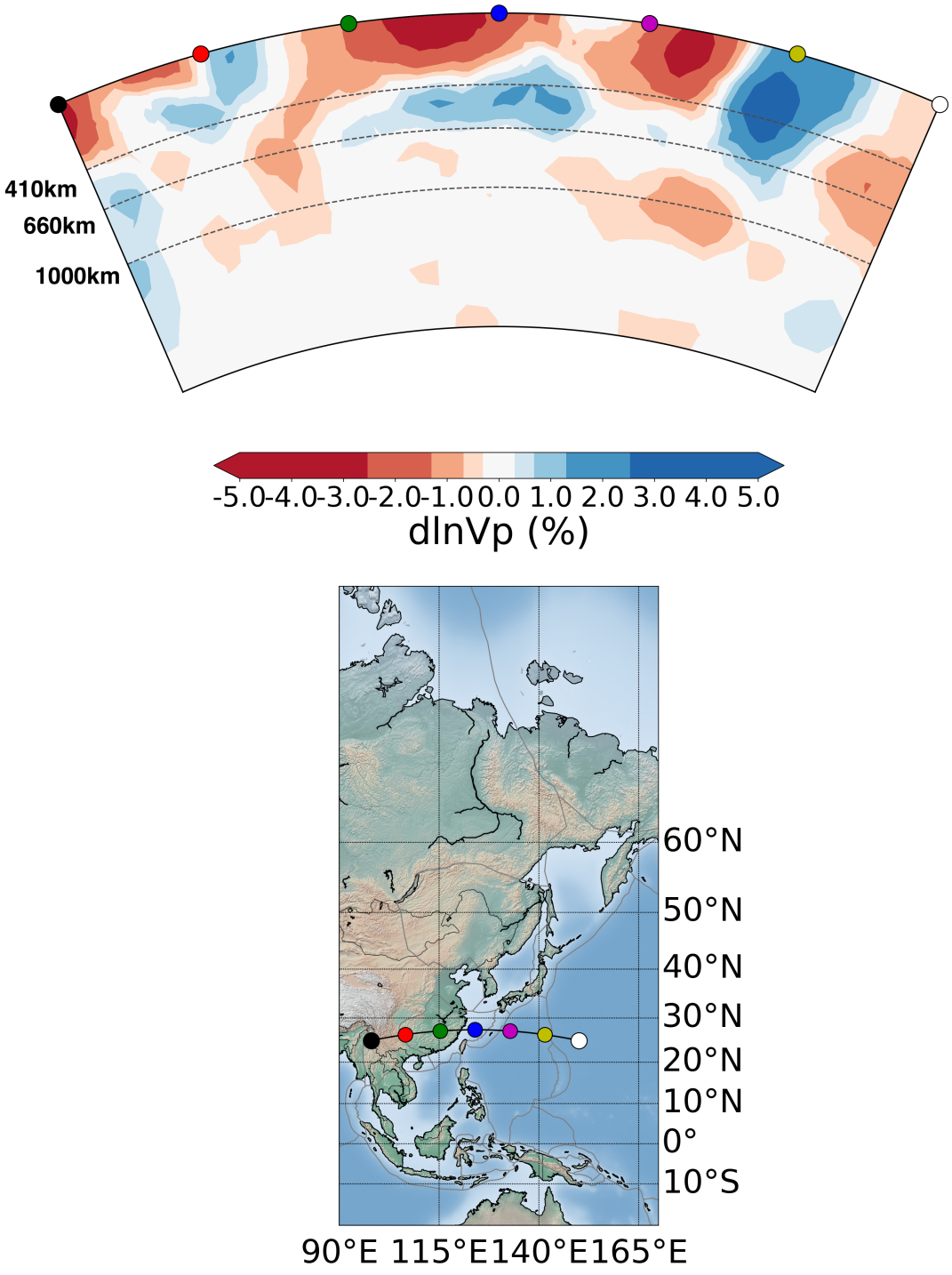

Figure A.48: (Top) Same type of cross-section as figure A1 but for a transect from east to west, along a latitude of 25°N and between 98°E and 150°E in latitude . (Bottom) Regional map view of the study region, which highlights the location of the cross-section shown above. The colour of the nodes on the bottom transect correspond to the coloured nodes in the cross-section above.

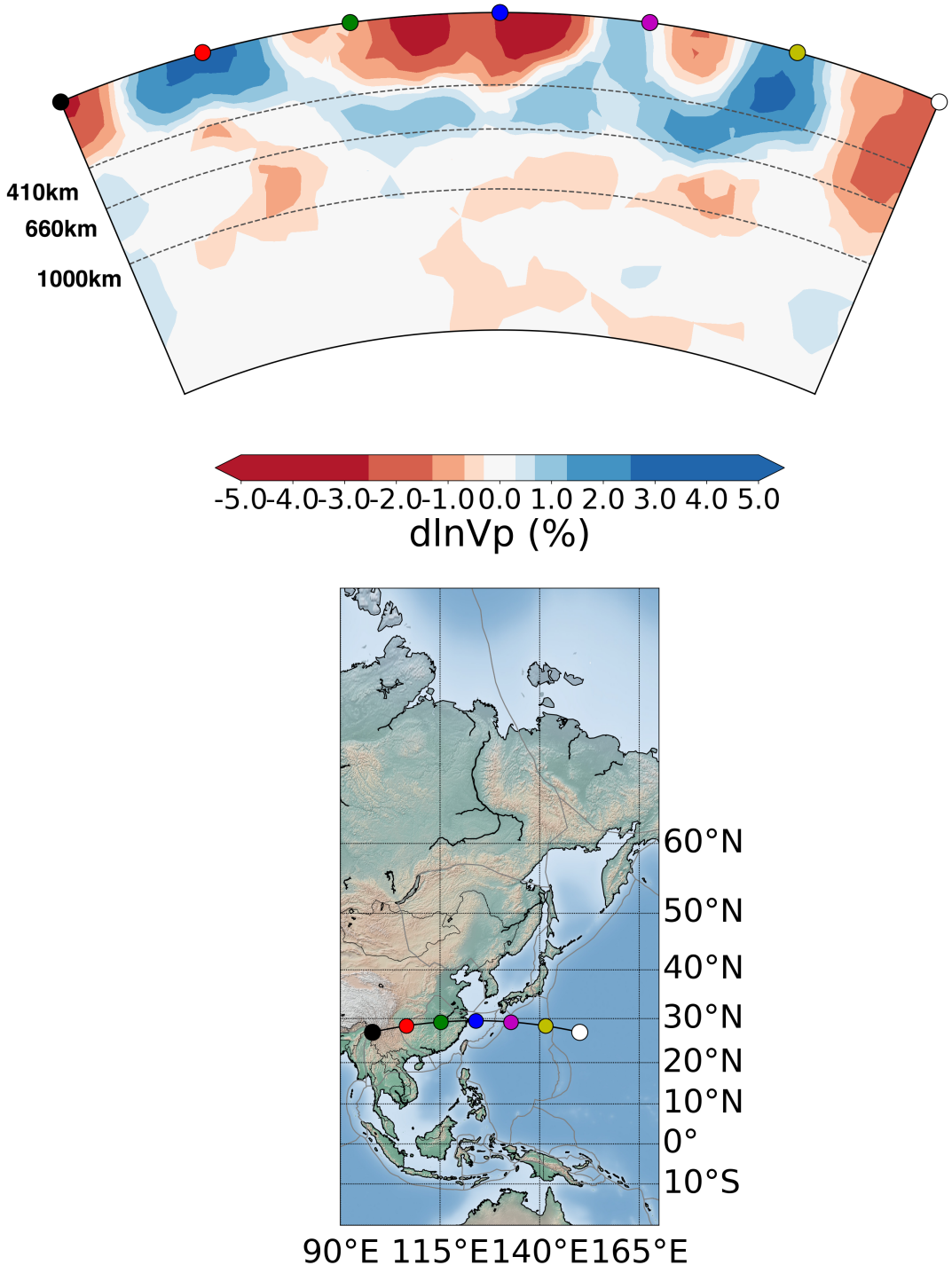

Figure A.49: (Top) Same type of cross-section as figure A1 but for a transect from east to west, along a latitude of 27°N and between 98°E and 150°E in latitude . (Bottom) Regional map view of the study region, which highlights the location of the cross-section shown above. The colour of the nodes on the bottom transect correspond to the coloured nodes in the cross-section above.

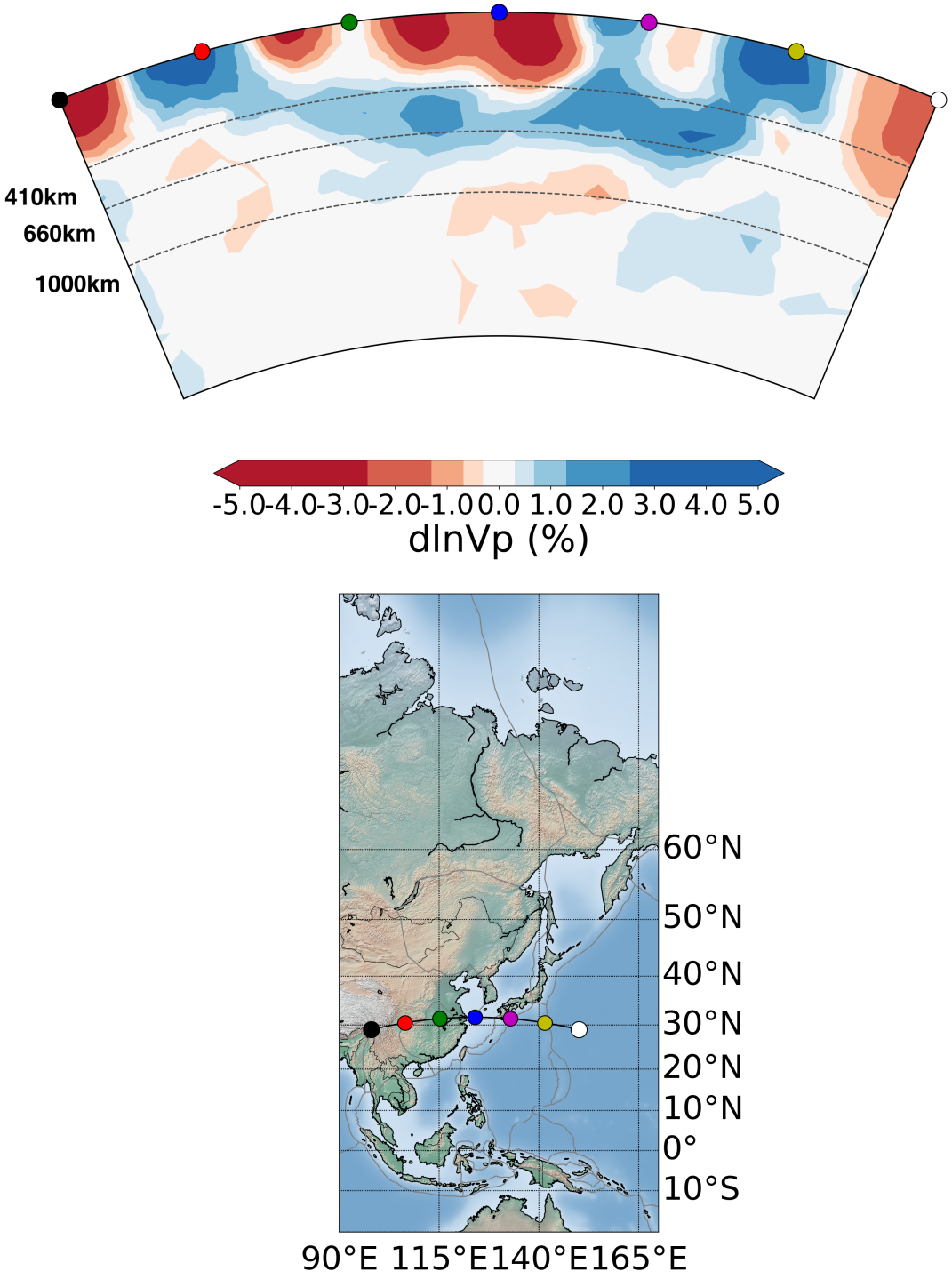

Figure A.50: (Top) Same type of cross-section as figure A1 but for a transect from east to west, along a latitude of 29°N and between 98°E and 150°E in latitude . (Bottom) Regional map view of the study region, which highlights the location of the cross-section shown above. The colour of the nodes on the bottom transect correspond to the coloured nodes in the cross-section above.

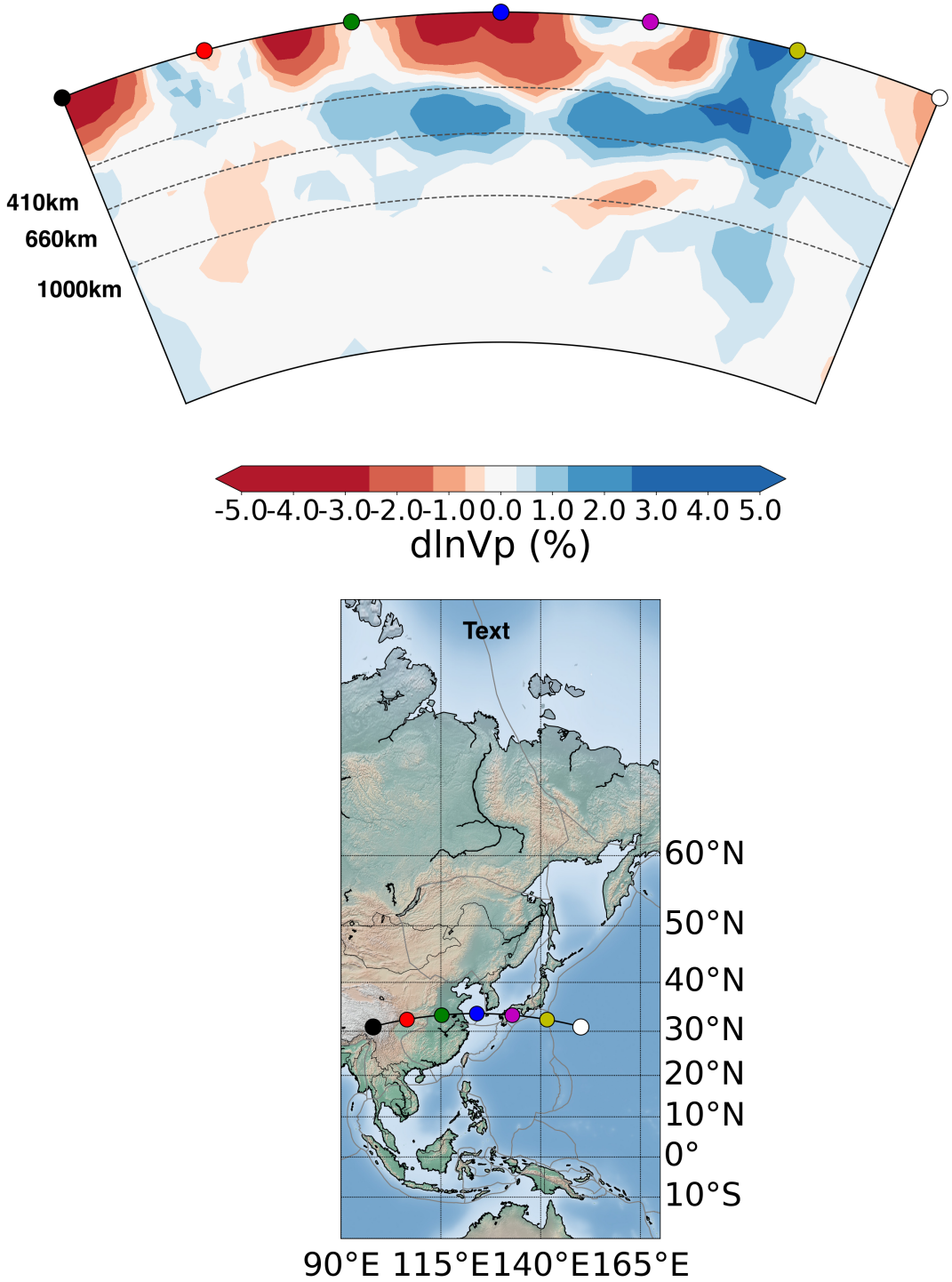

Figure A.51: (Top) Same type of cross-section as figure A1 but for a transect from east to west, along a latitude of 31°N and between 98°E and 150°E in latitude . (Bottom) Regional map view of the study region, which highlights the location of the cross-section shown above. The colour of the nodes on the bottom transect correspond to the coloured nodes in the cross-section above.

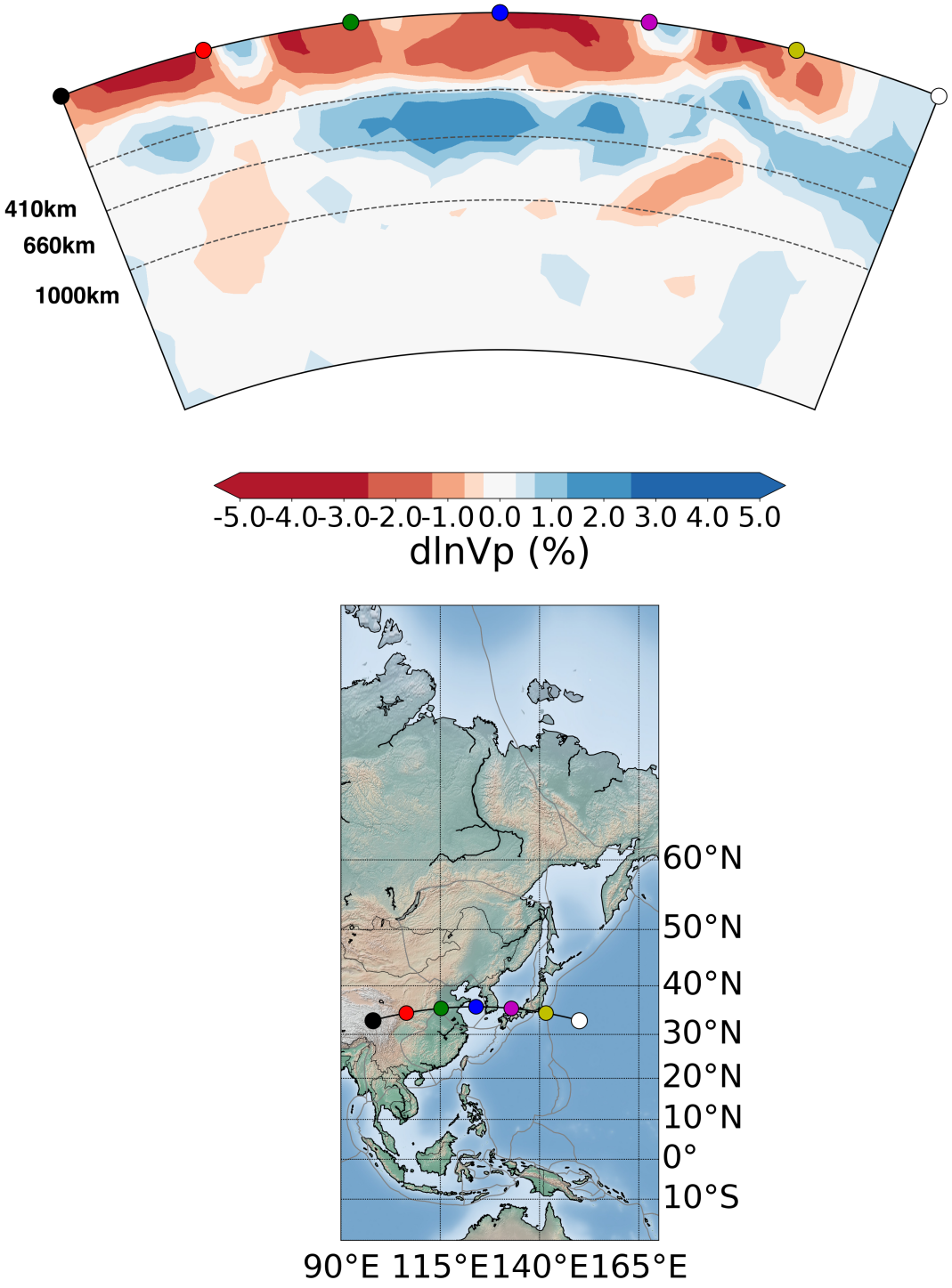

Figure A.52: (Top) Same type of cross-section as figure A1 but for a transect from east to west, along a latitude of 33°N and between 98°E and 150°E in latitude . (Bottom) Regional map view of the study region, which highlights the location of the cross-section shown above. The colour of the nodes on the bottom transect correspond to the coloured nodes in the cross-section above.

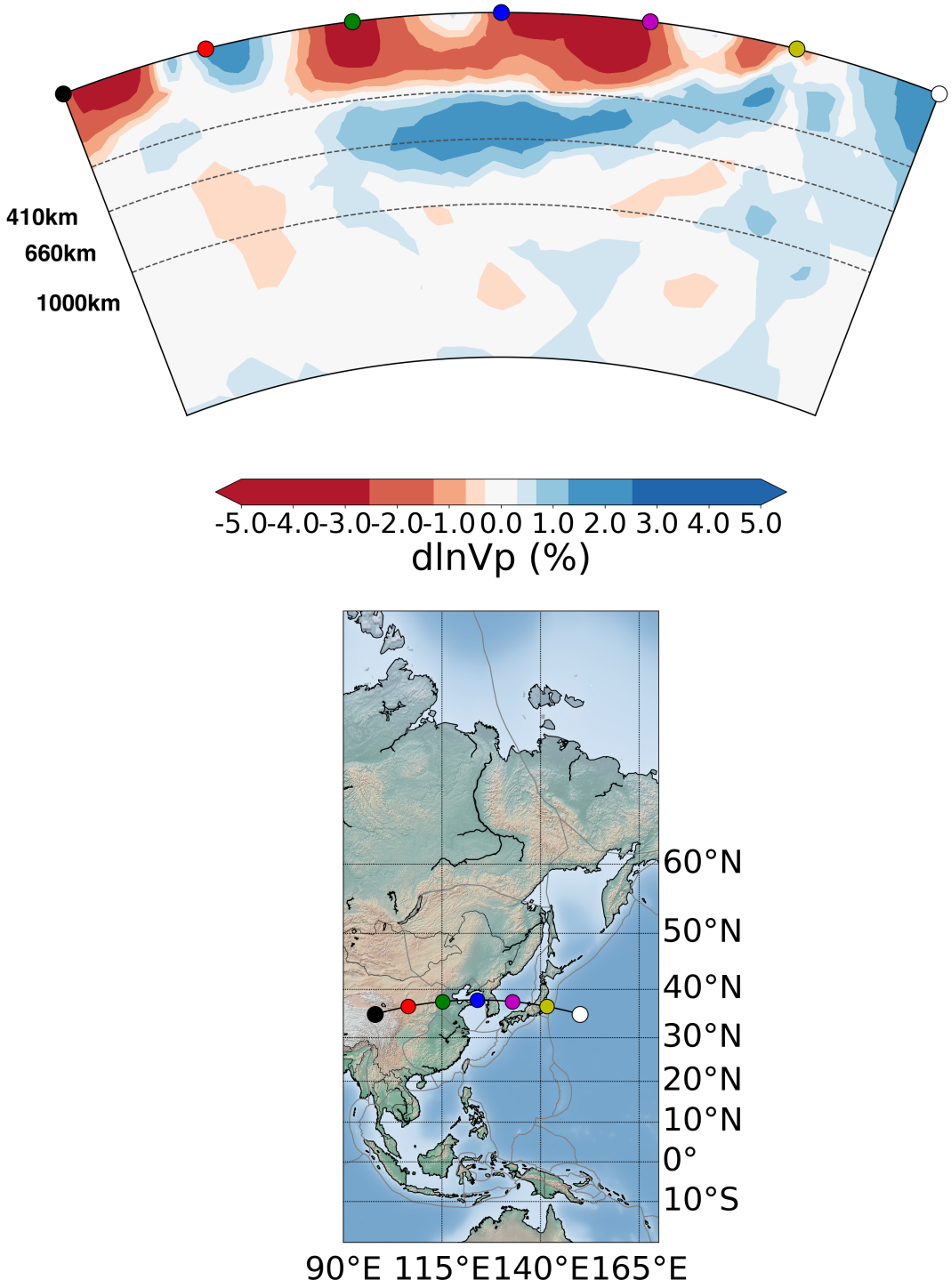

Figure A.53: (Top) Same type of cross-section as figure A1 but for a transect from east to west, along a latitude of 35°N and between 98°E and 150°E in latitude . (Bottom) Regional map view of the study region, which highlights the location of the cross-section shown above. The colour of the nodes on the bottom transect correspond to the coloured nodes in the cross-section above.

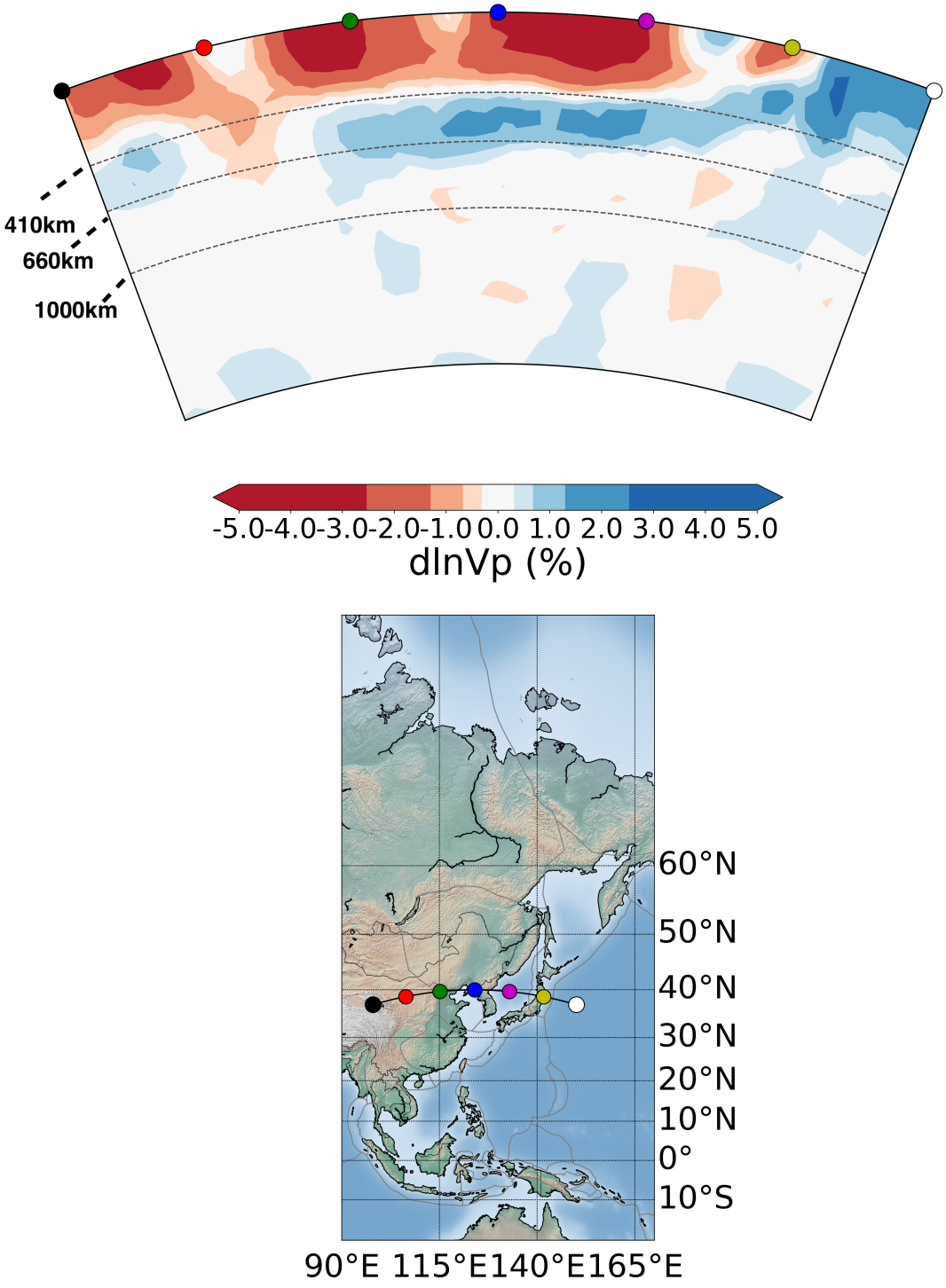

Figure A.54: (Top) Same type of cross-section as figure A1 but for a transect from east to west, along a latitude of 37°N and between 98°E and 150°E in latitude . (Bottom) Regional map view of the study region, which highlights the location of the cross-section shown above. The colour of the nodes on the bottom transect correspond to the coloured nodes in the cross-section above.

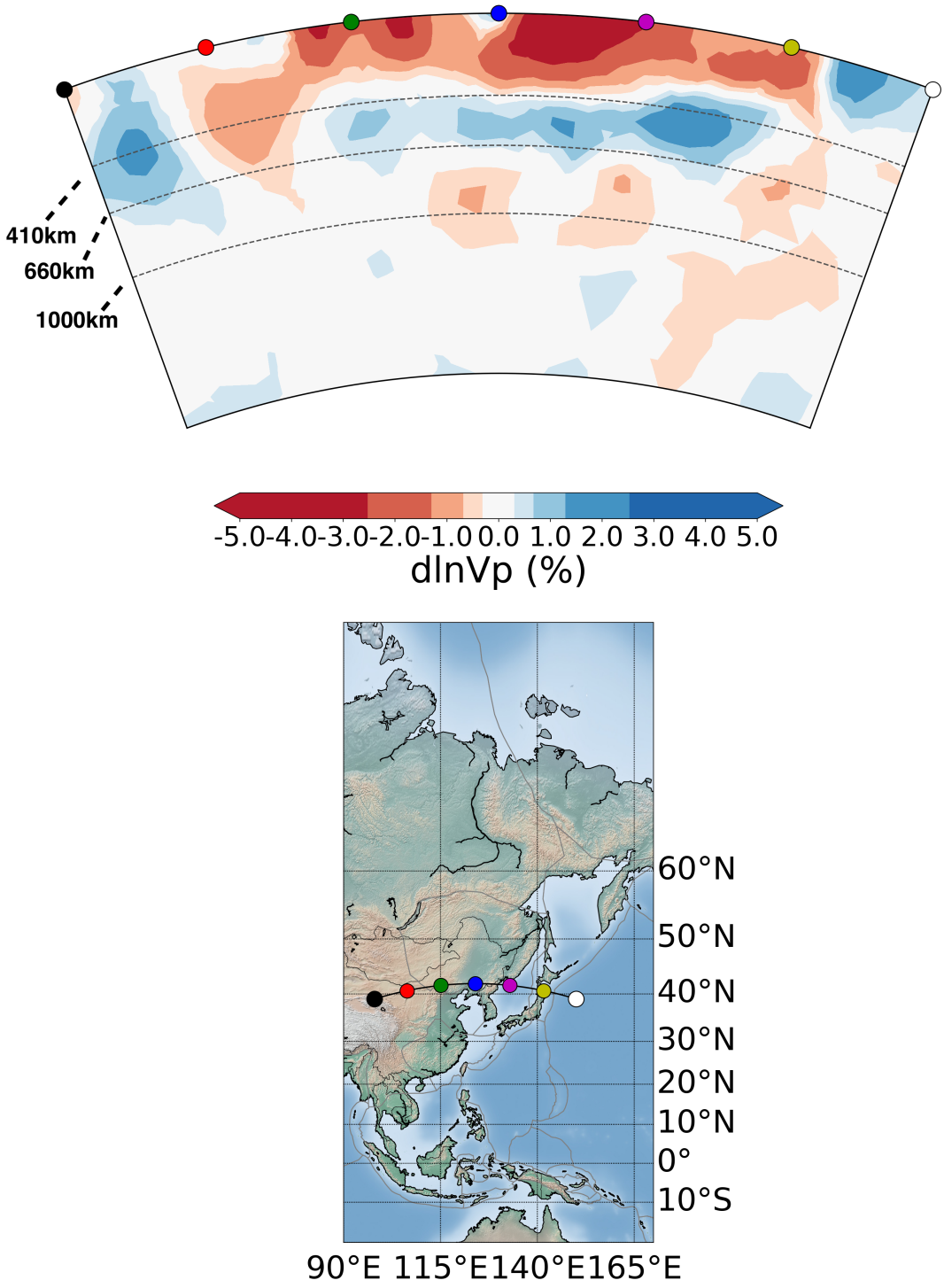

Figure A.55: (Top) Same type of cross-section as figure A1 but for a transect from east to west, along a latitude of 39°N and between 98°E and 150°E in latitude . (Bottom) Regional map view of the study region, which highlights the location of the cross-section shown above. The colour of the nodes on the bottom transect correspond to the coloured nodes in the cross-section above.

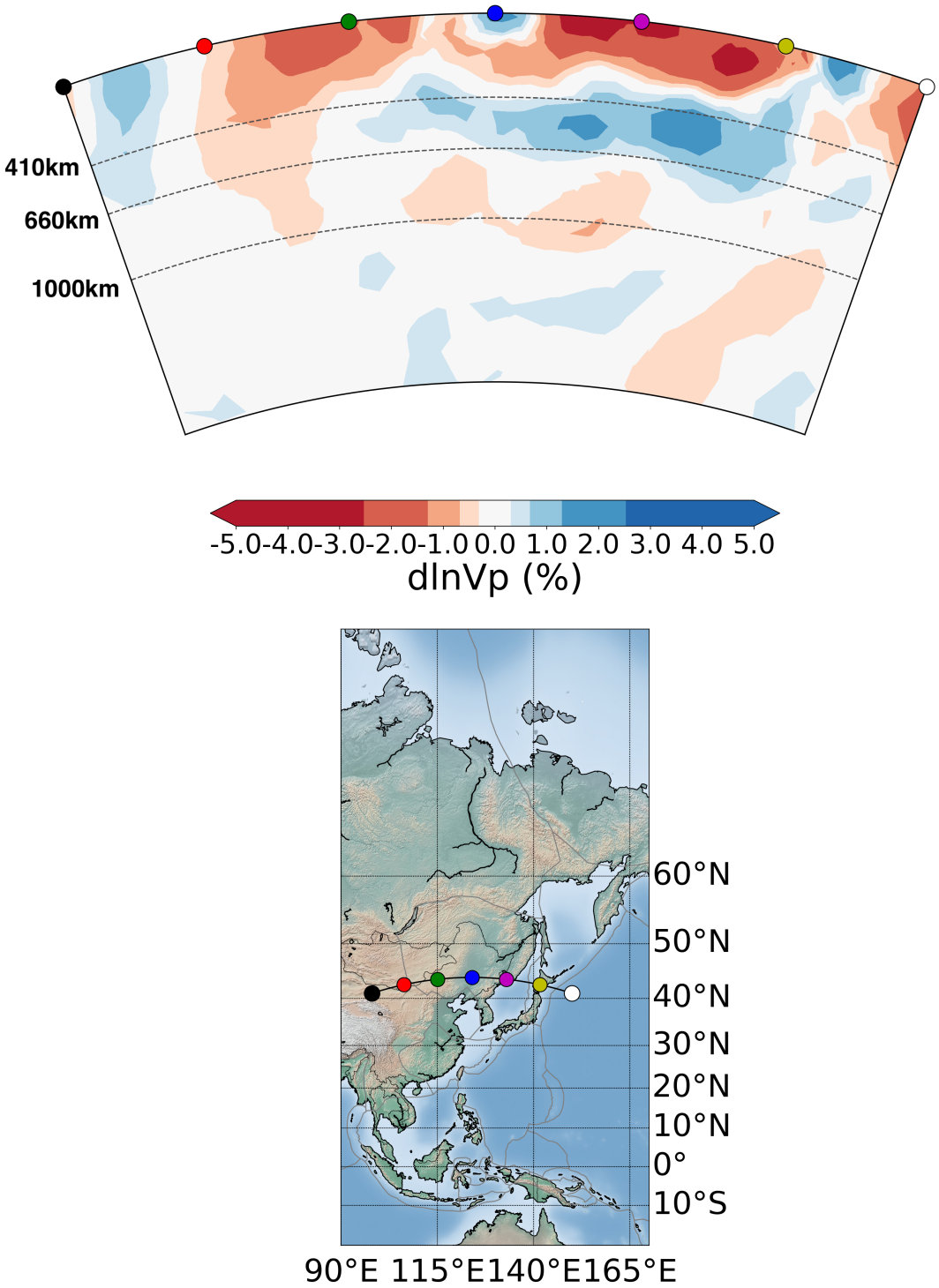

Figure A.56: (Top) Same type of cross-section as figure A1 but for a transect from east to west, along a latitude of 41°N and between 98°E and 150°E in latitude . (Bottom) Regional map view of the study region, which highlights the location of the cross-section shown above. The colour of the nodes on the bottom transect correspond to the coloured nodes in the cross-section above.

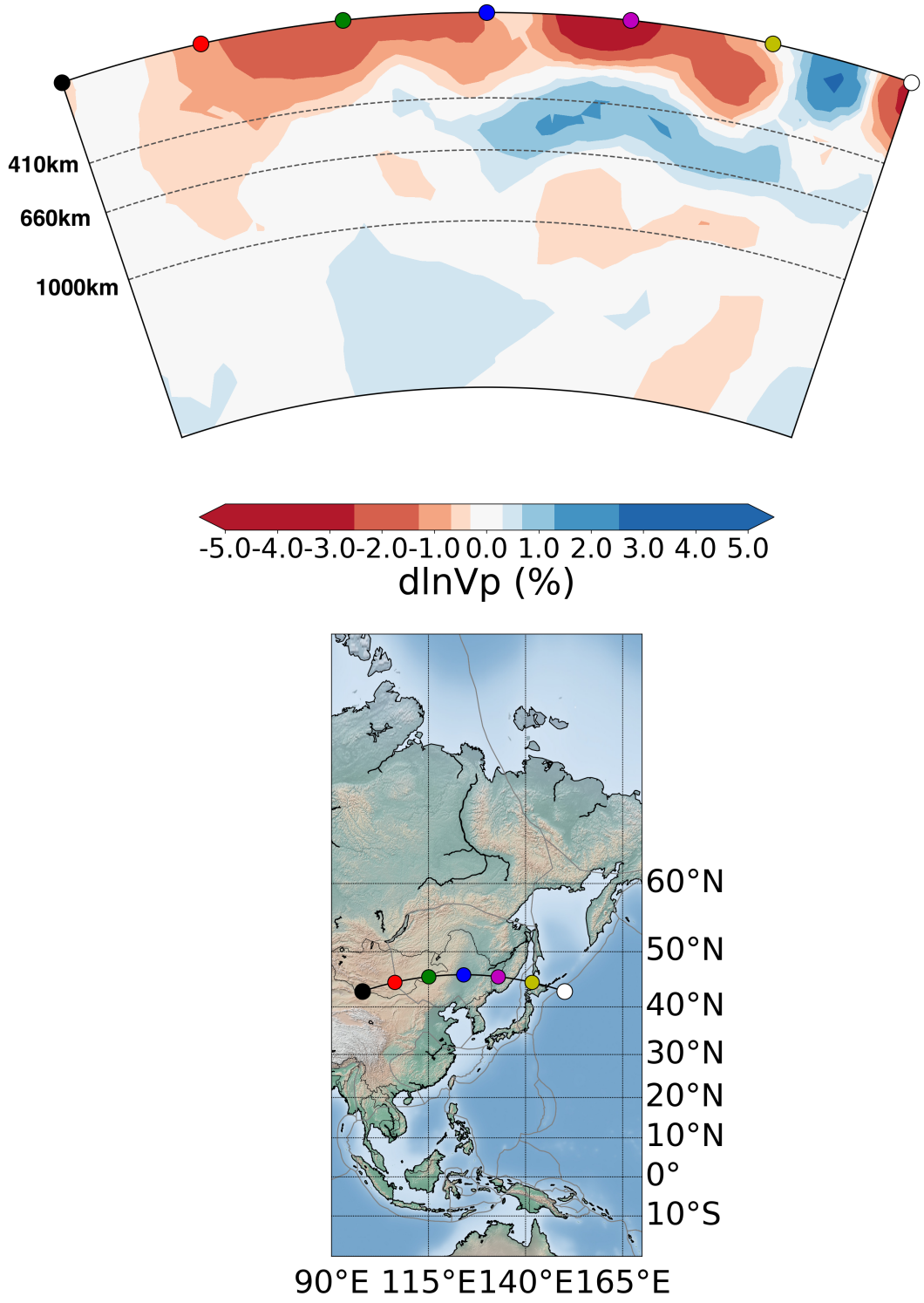

Figure A.57: (Top) Same type of cross-section as figure A1 but for a transect from east to west, along a latitude of 43°N and between 98°E and 150°E in latitude . (Bottom) Regional map view of the study region, which highlights the location of the cross-section shown above. The colour of the nodes on the bottom transect correspond to the coloured nodes in the cross-section above.

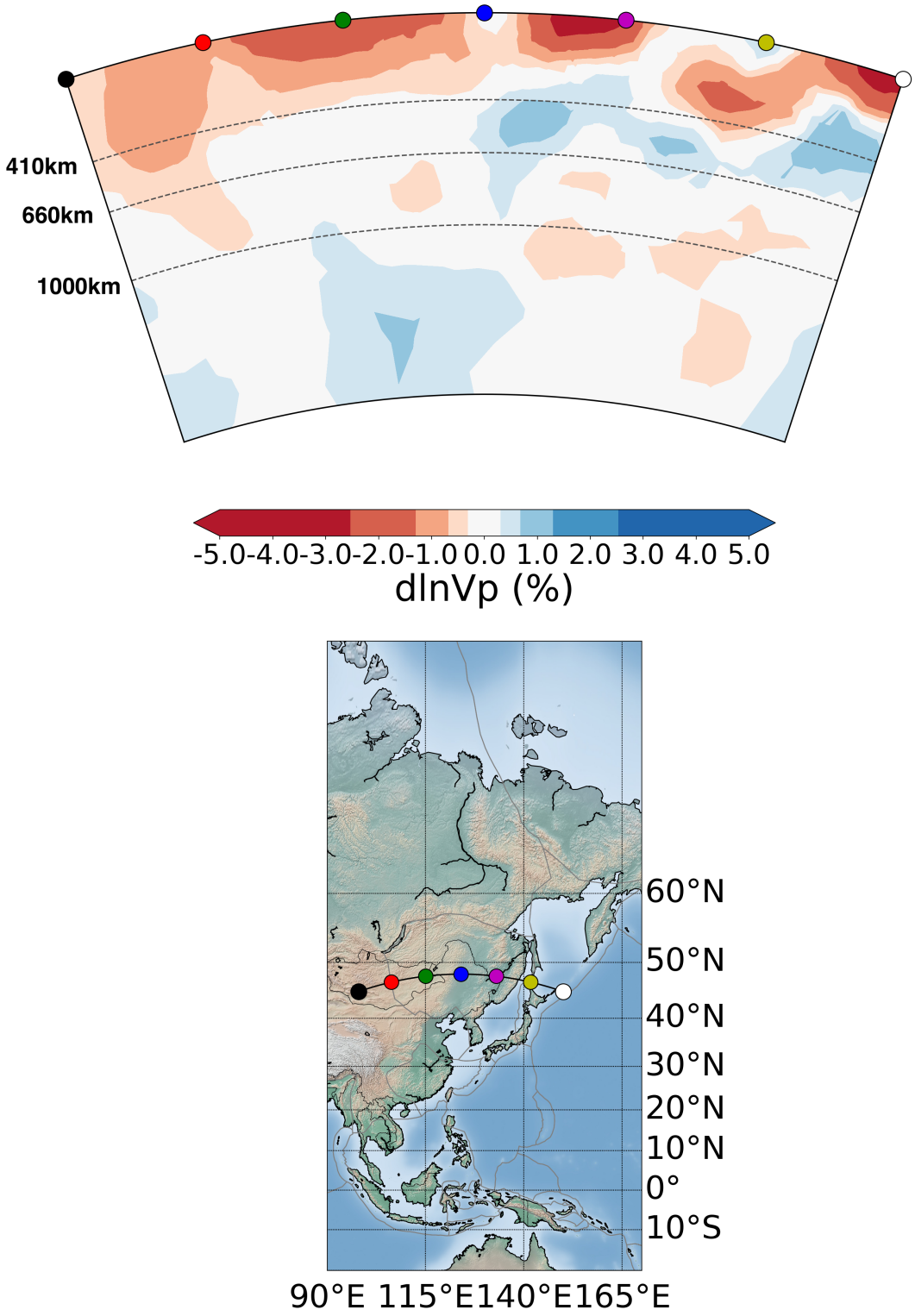

Figure A.58: (Top) Same type of cross-section as figure A1 but for a transect from east to west, along a latitude of 45°N and between 98°E and 150°E in latitude . (Bottom) Regional map view of the study region, which highlights the location of the cross-section shown above. The colour of the nodes on the bottom transect correspond to the coloured nodes in the cross-section above.

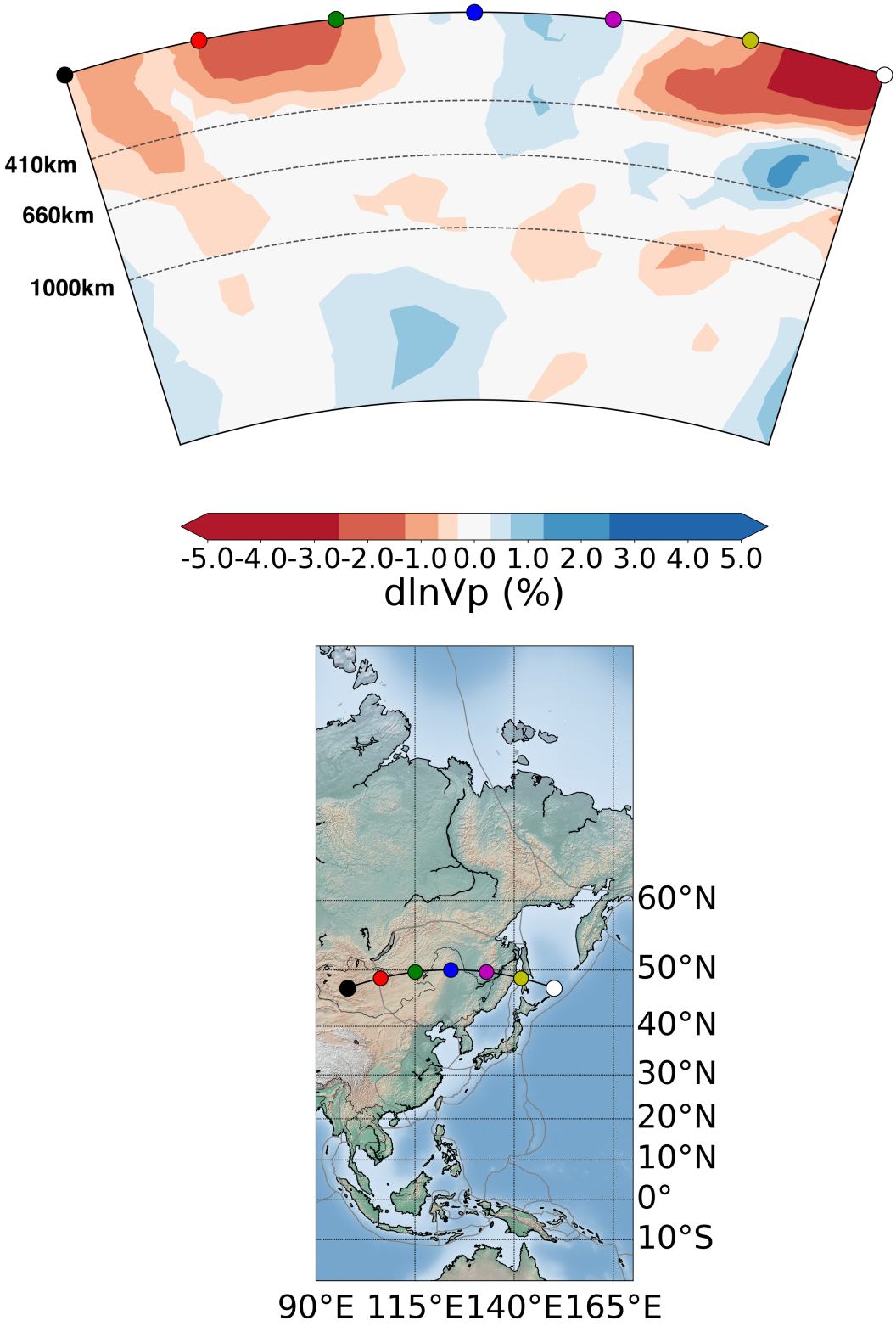

Figure A.59: (Top) Same type of cross-section as figure A1 but for a transect from east to west, along a latitude of 47°N and between 98°E and 150°E in latitude . (Bottom) Regional map view of the study region, which highlights the location of the cross-section shown above. The colour of the nodes on the bottom transect correspond to the coloured nodes in the cross-section above.

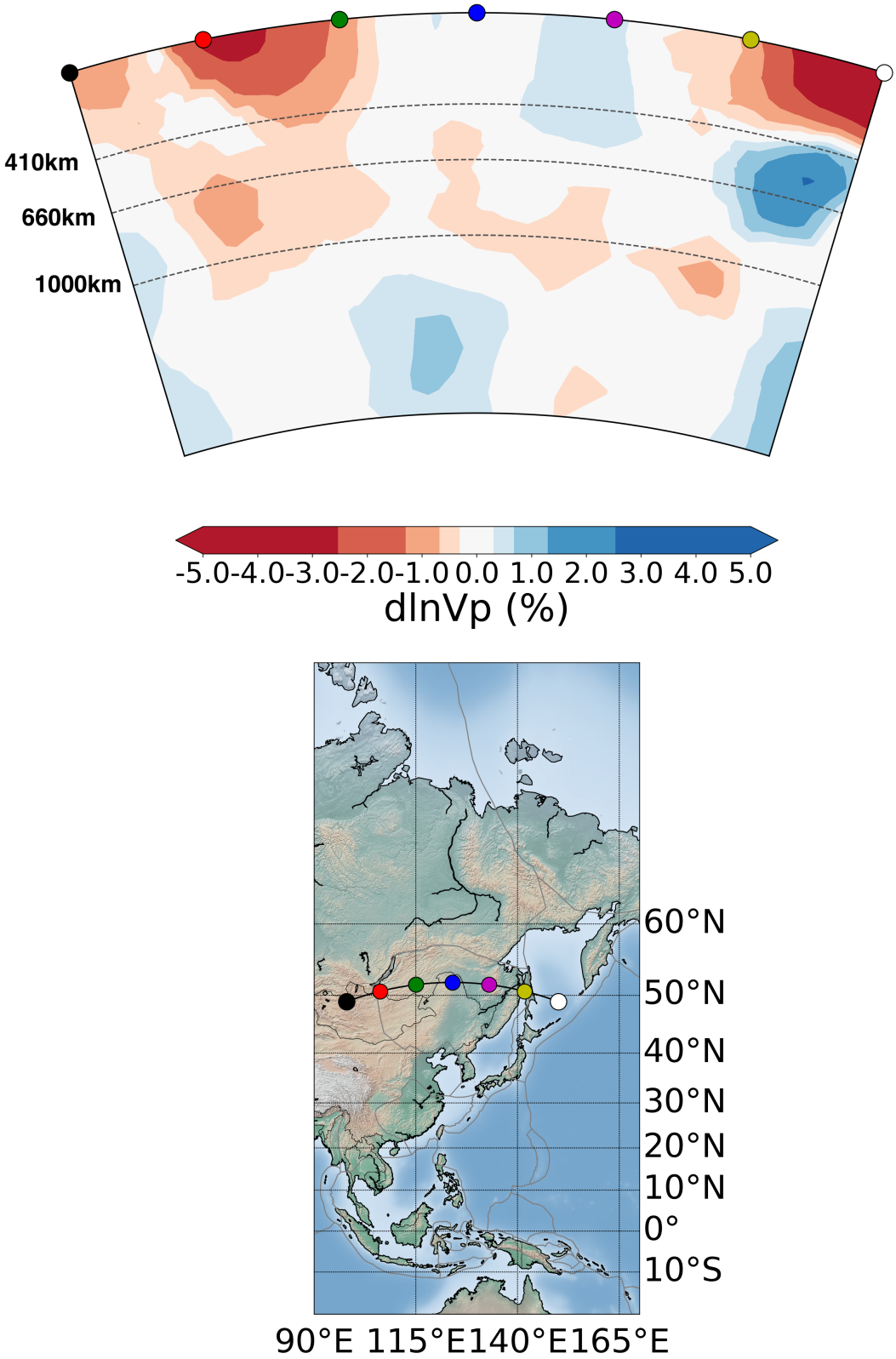

Figure A.60: (Top) Same type of cross-section as figure A1 but for a transect from east to west, along a latitude of 49°N and between 98°E and 150°E in latitude . (Bottom) Regional map view of the study region, which highlights the location of the cross-section shown above. The colour of the nodes on the bottom transect correspond to the coloured nodes in the cross-section above.

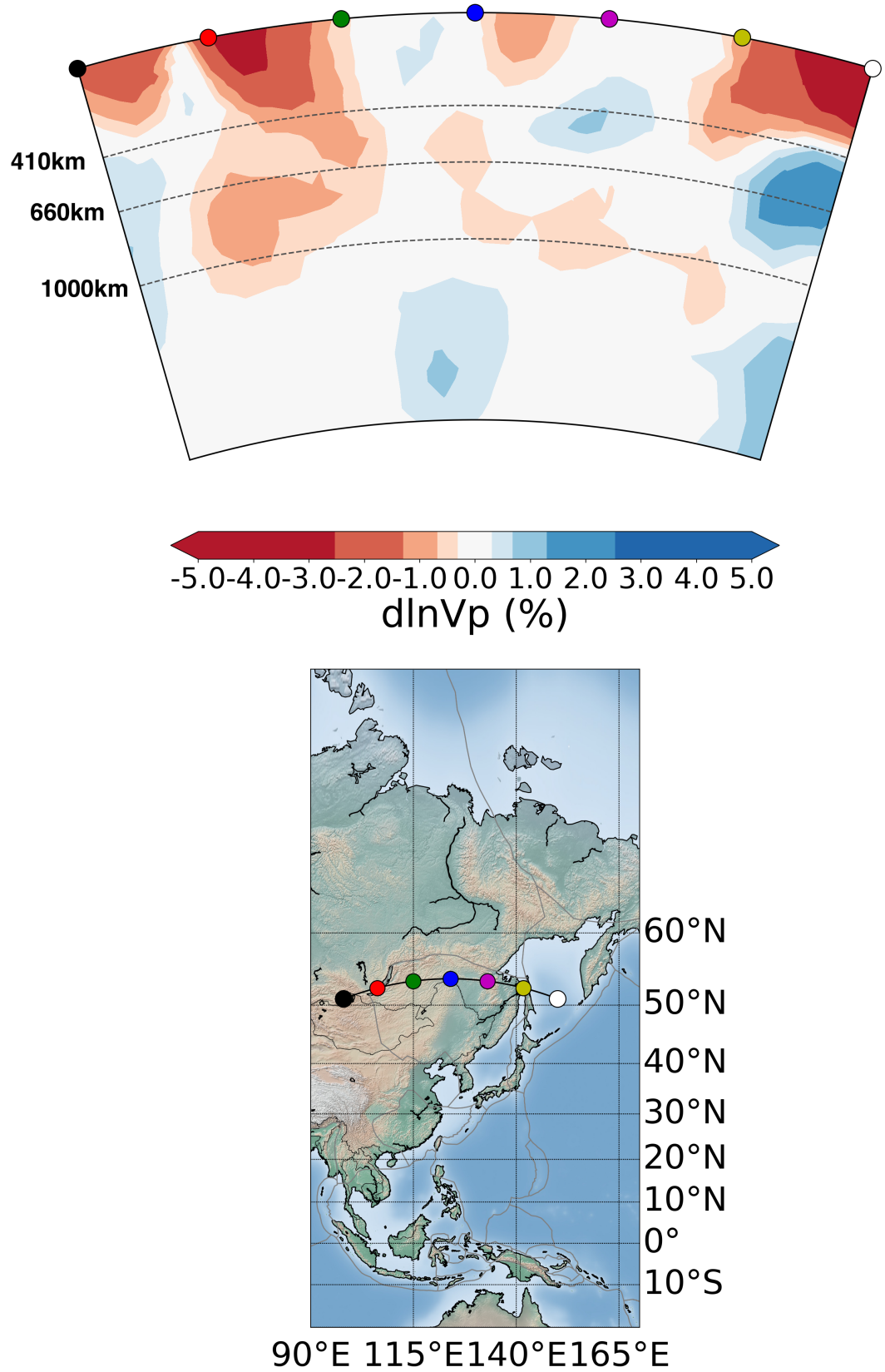

Figure A.61: (Top) Same type of cross-section as figure A1 but for a transect from east to west, along a latitude of 51°N and between 98°E and 150°E in latitude . (Bottom) Regional map view of the study region, which highlights the location of the cross-section shown above. The colour of the nodes on the bottom transect correspond to the coloured nodes in the cross-section above.

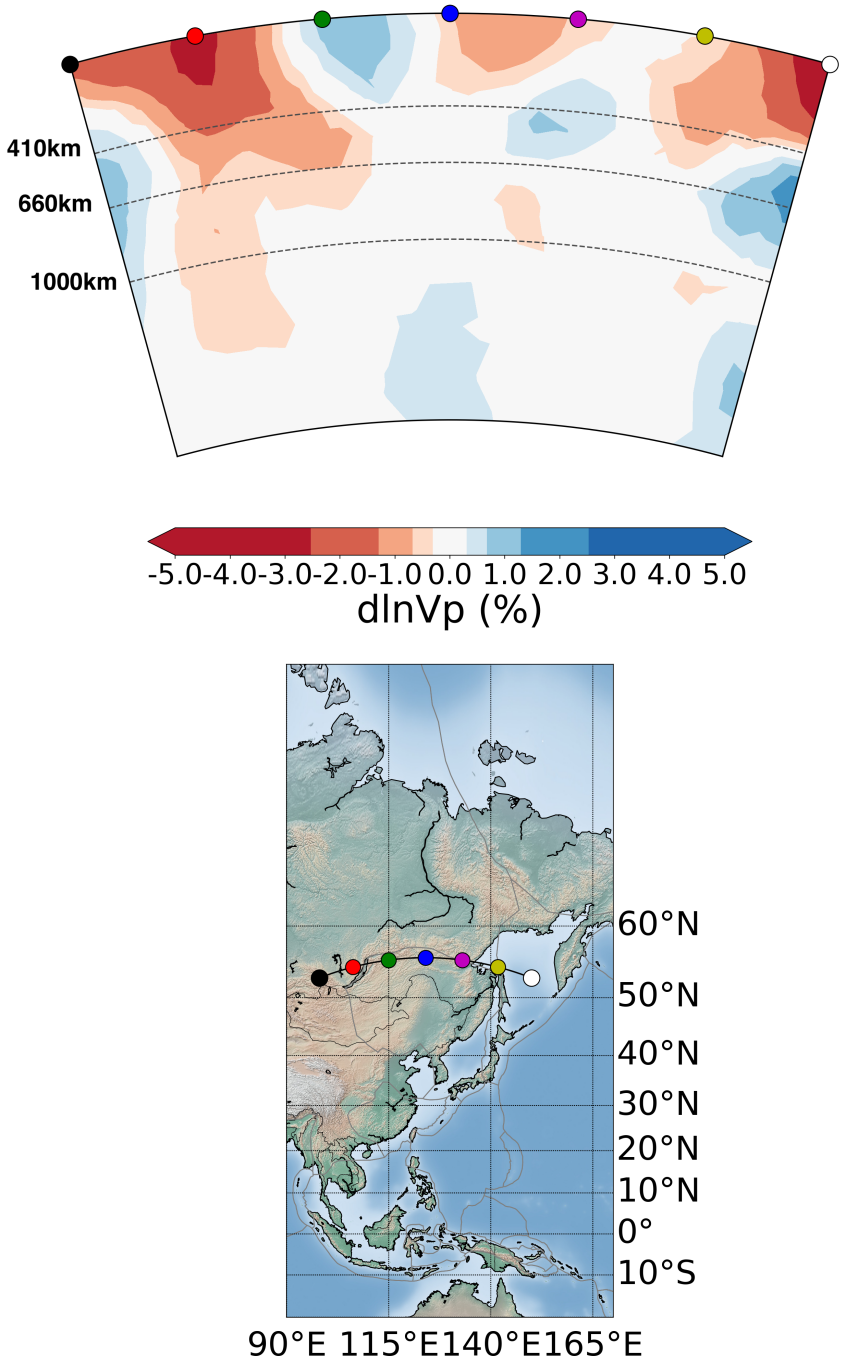

Figure A.62: (Top) Same type of cross-section as figure A1 but for a transect from east to west, along a latitude of 53°N and between 98°E and 150°E in latitude . (Bottom) Regional map view of the study region, which highlights the location of the cross-section shown above. The colour of the nodes on the bottom transect correspond to the coloured nodes in the cross-section above.

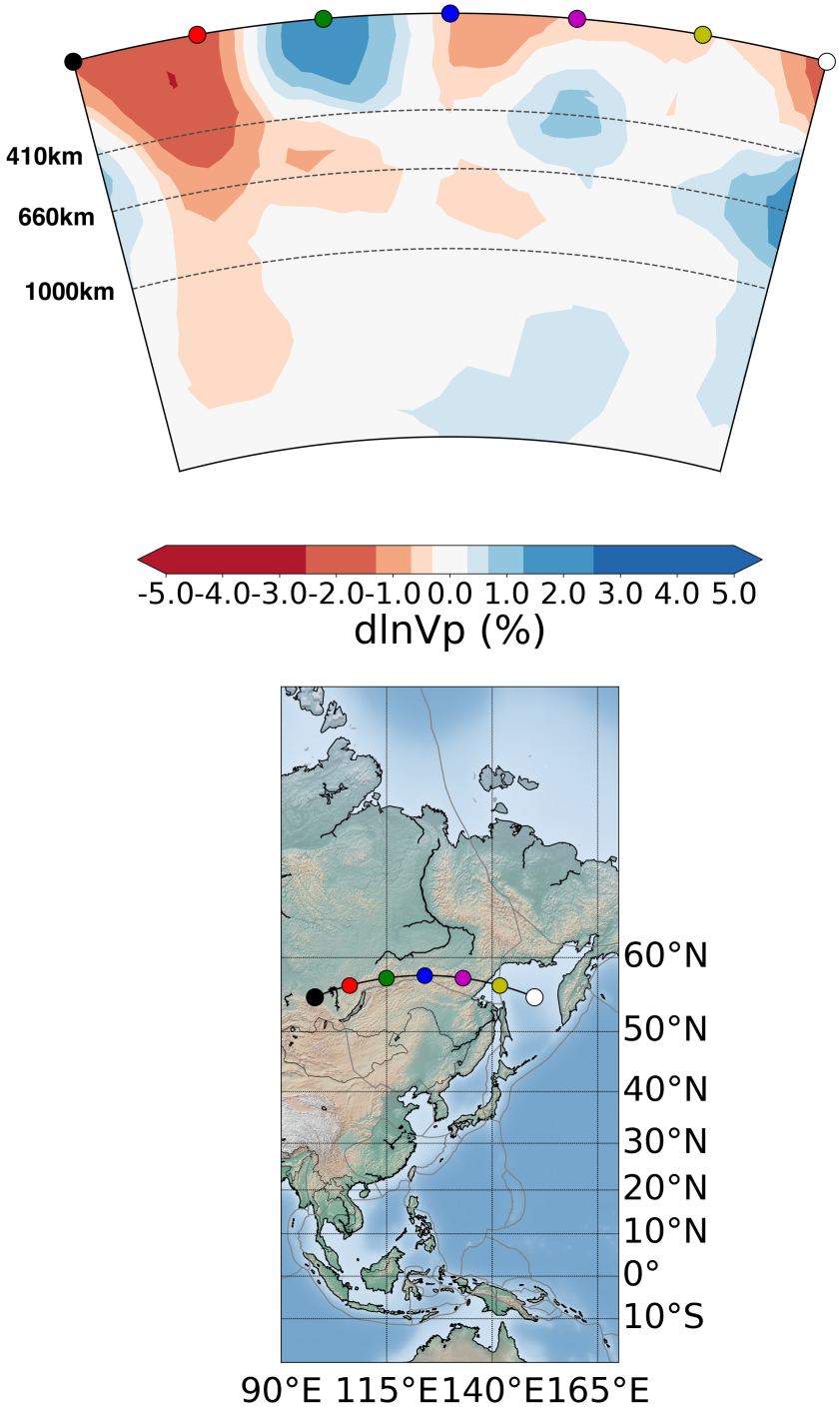

Figure A.63: (Top) Same type of cross-section as figure A1 but for a transect from east to west, along a latitude of 55°N and between 98°E and 150°E in latitude . (Bottom) Regional map view of the study region, which highlights the location of the cross-section shown above. The colour of the nodes on the bottom transect correspond to the coloured nodes in the cross-section above.

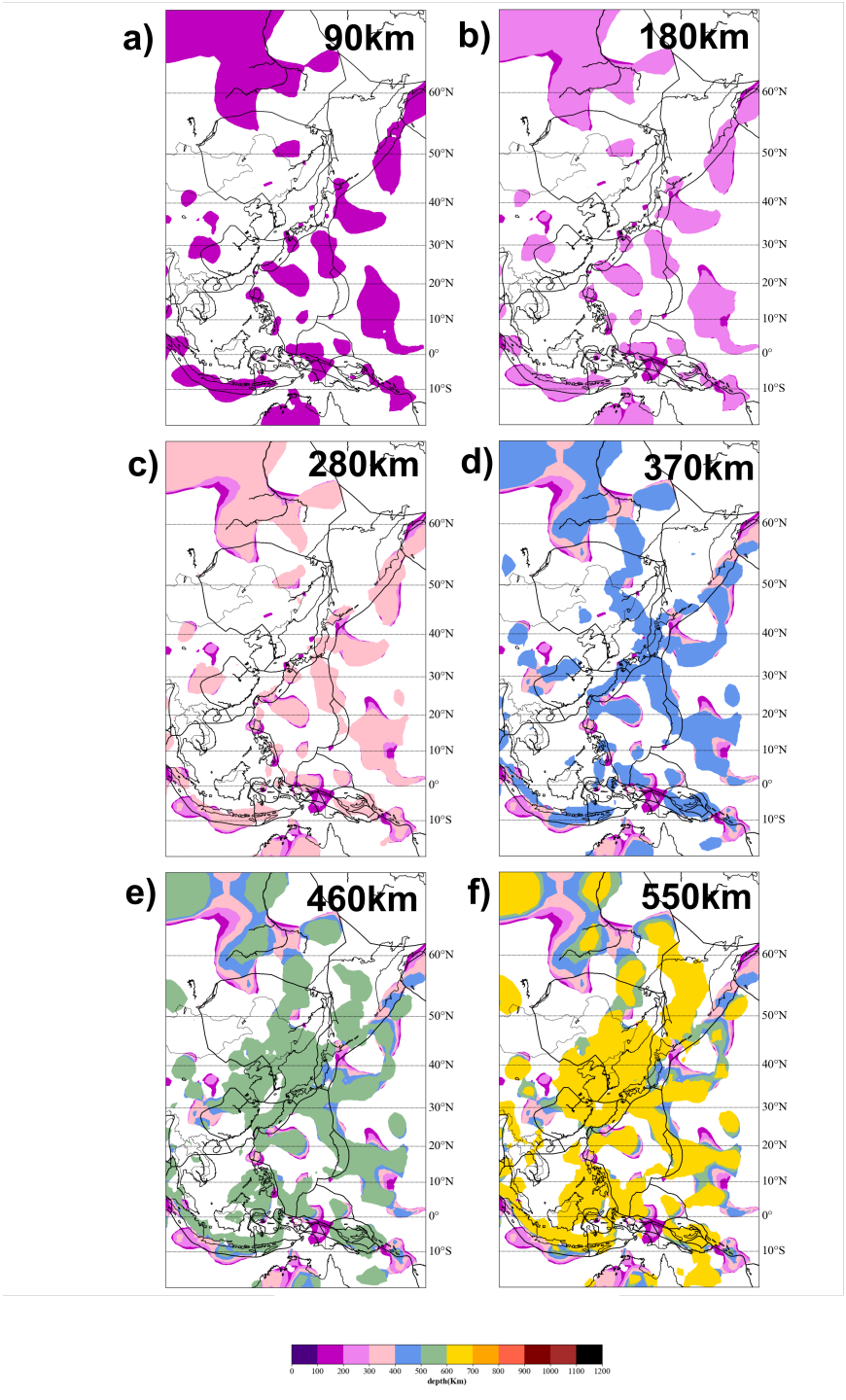

Figure A.64: Inverted view of contoured fast velocities of the JEABOX model, down to 550km depth.

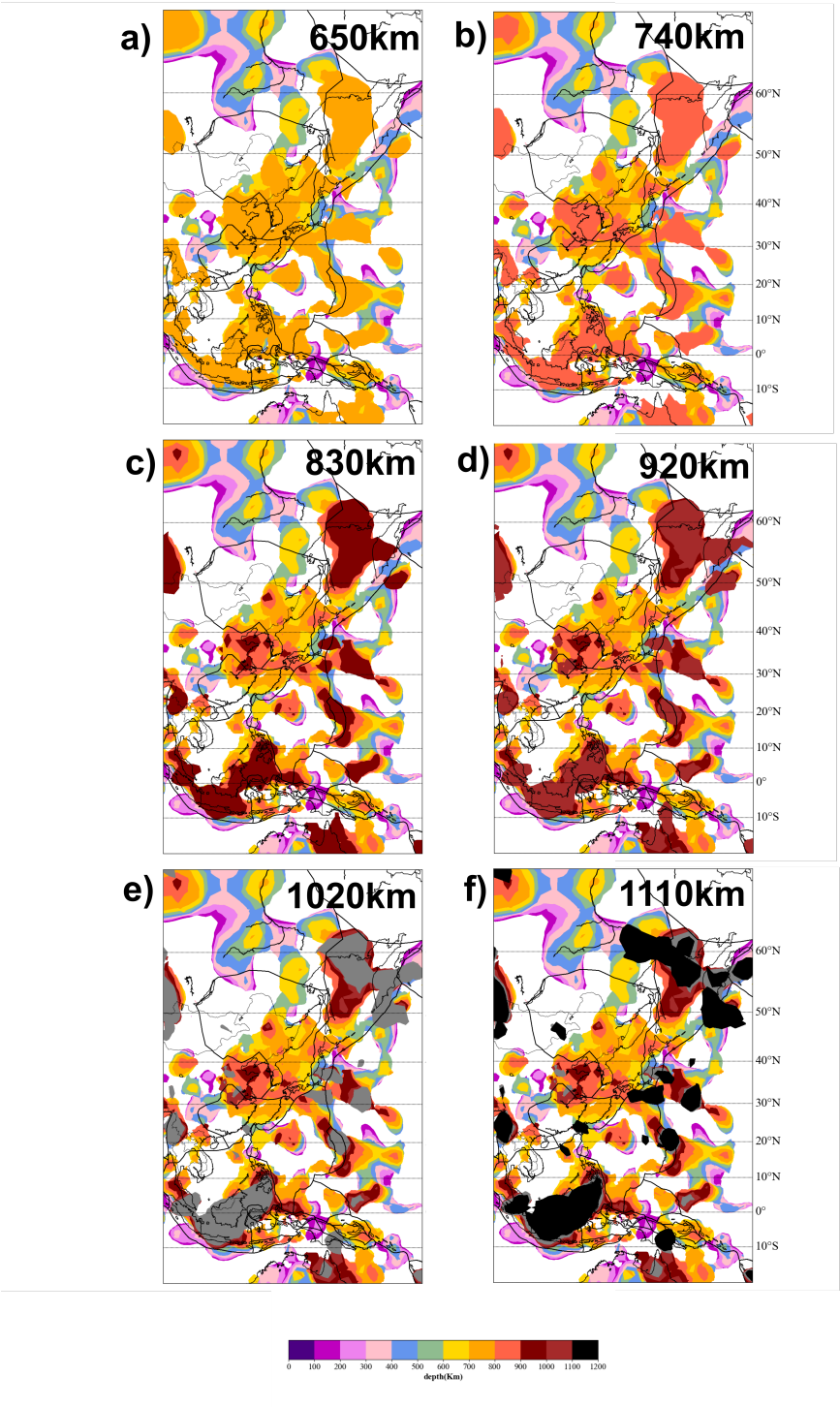

Figure A.65: Inverted view of contoured fast velocities of the JEABOX model, from 650km down to 1100km depth.

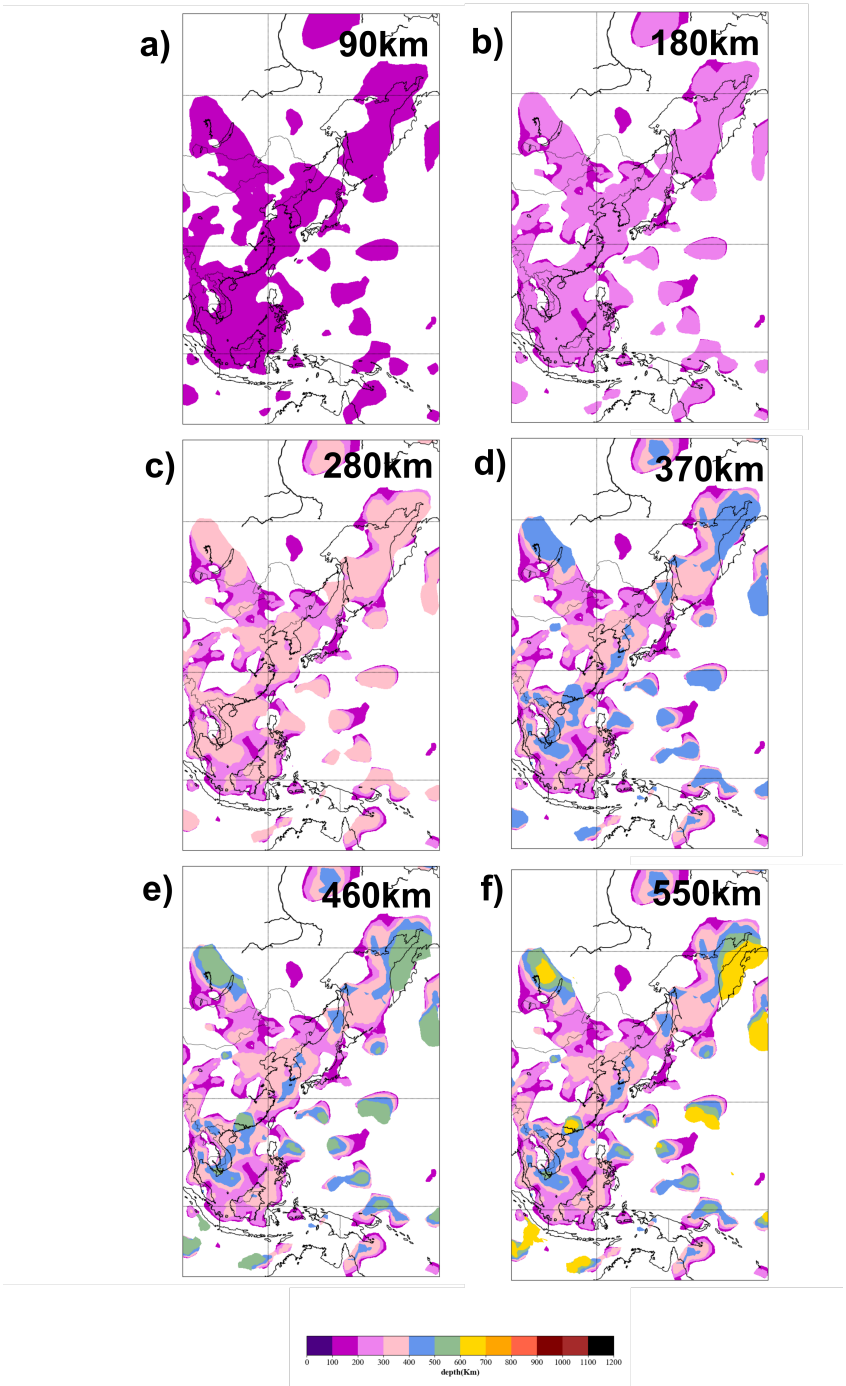

Figure A.66: Inverted view of contoured slow velocities of the JEABOX model, down to 550km depth.

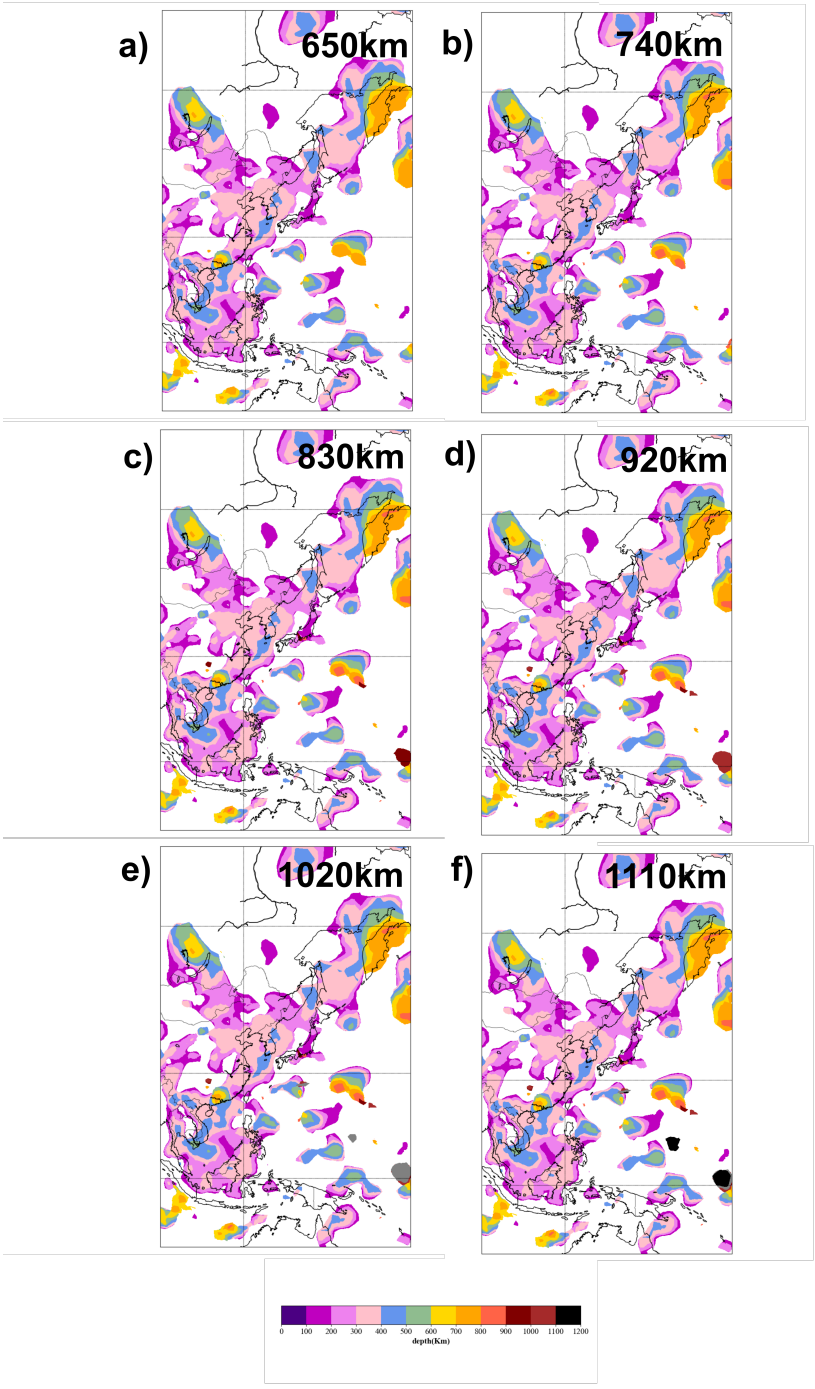

Figure A.67: Inverted view of contoured slow velocities of the JEABOX model, from 650km down to 1100km depth.

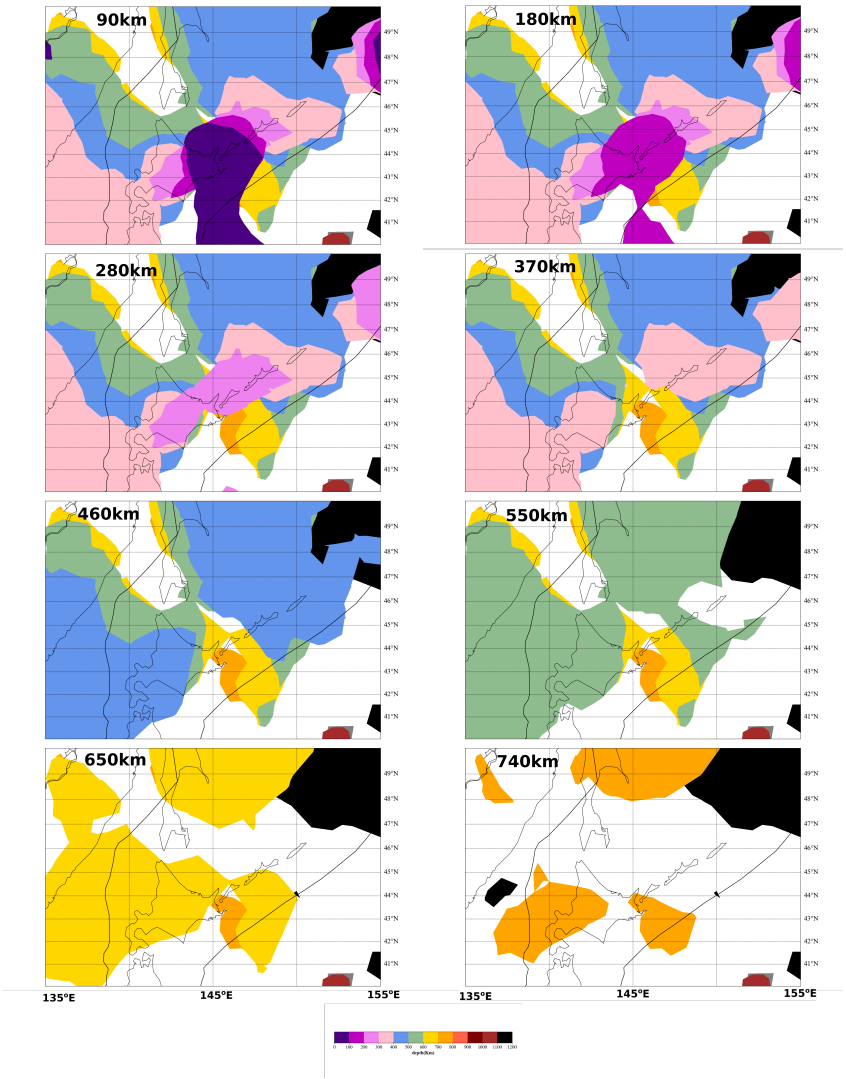

Figure A.68: Contoured fast velocities of the JEABOX model along the Kuril trench.

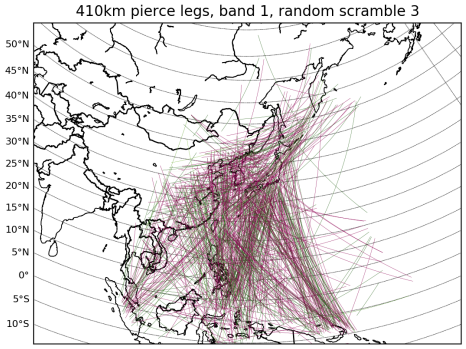

(a) image1

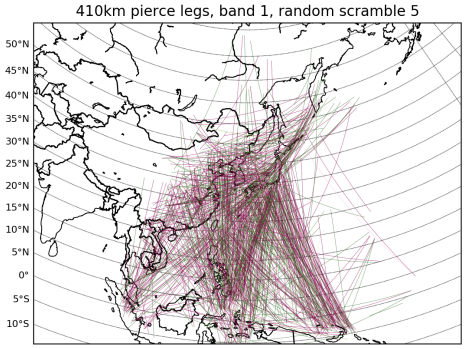

(b) image2

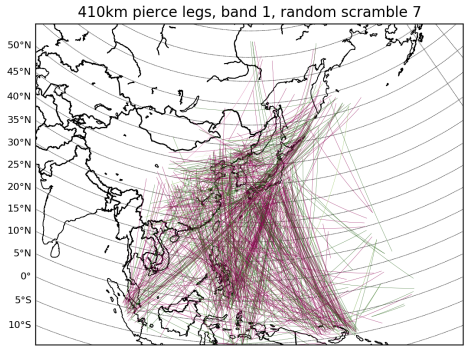

(c) image3

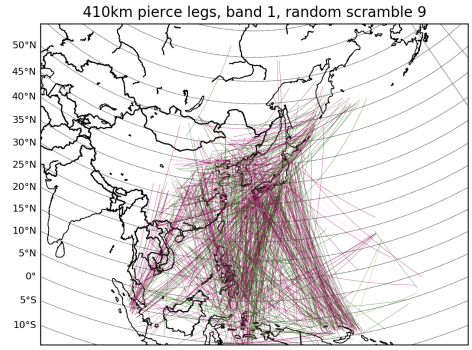

(d) image4

Figure A.69: Supplementary randomised coverage subsets of 410km grazing regional P-wave paths for band one (filtered with a 30s dominant period Gabor filter

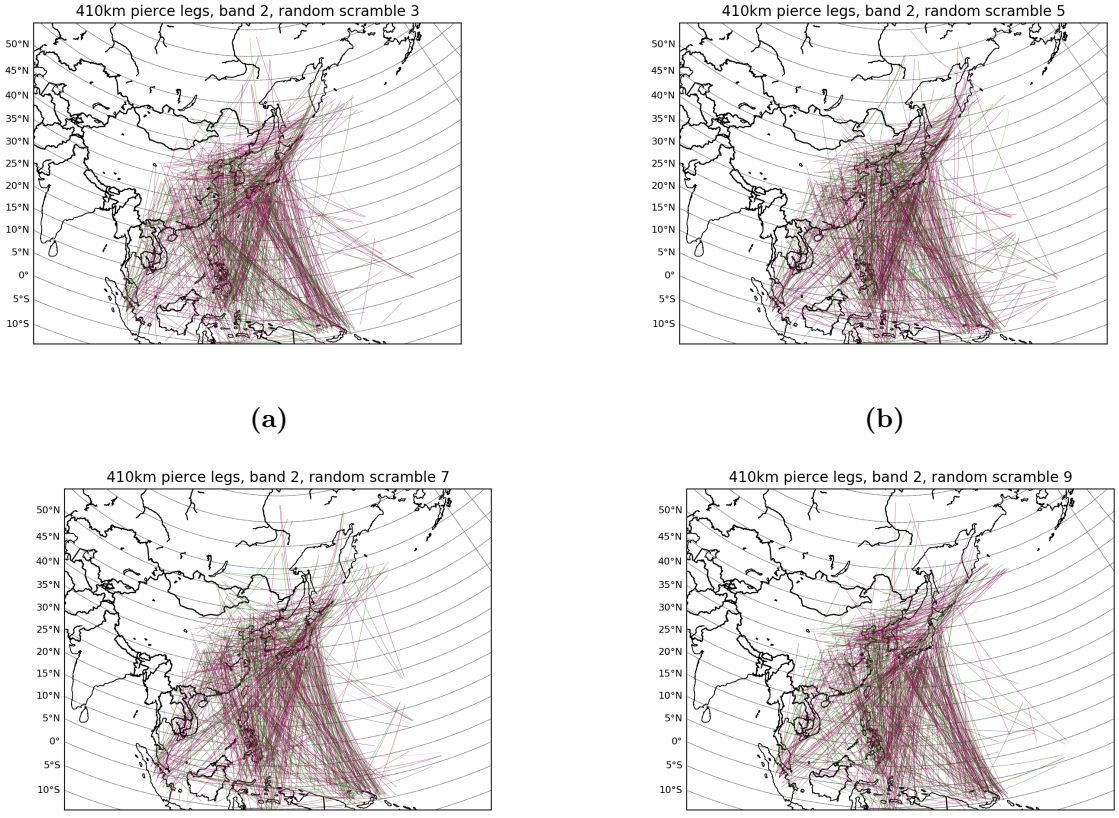

(a) **(b)**

(c) **(d)**

Figure A.70: Supplementary randomised coverage subsets of 410km grazing regional P-wave paths for band two (filtered with a 21s dominant period Gabor filter)

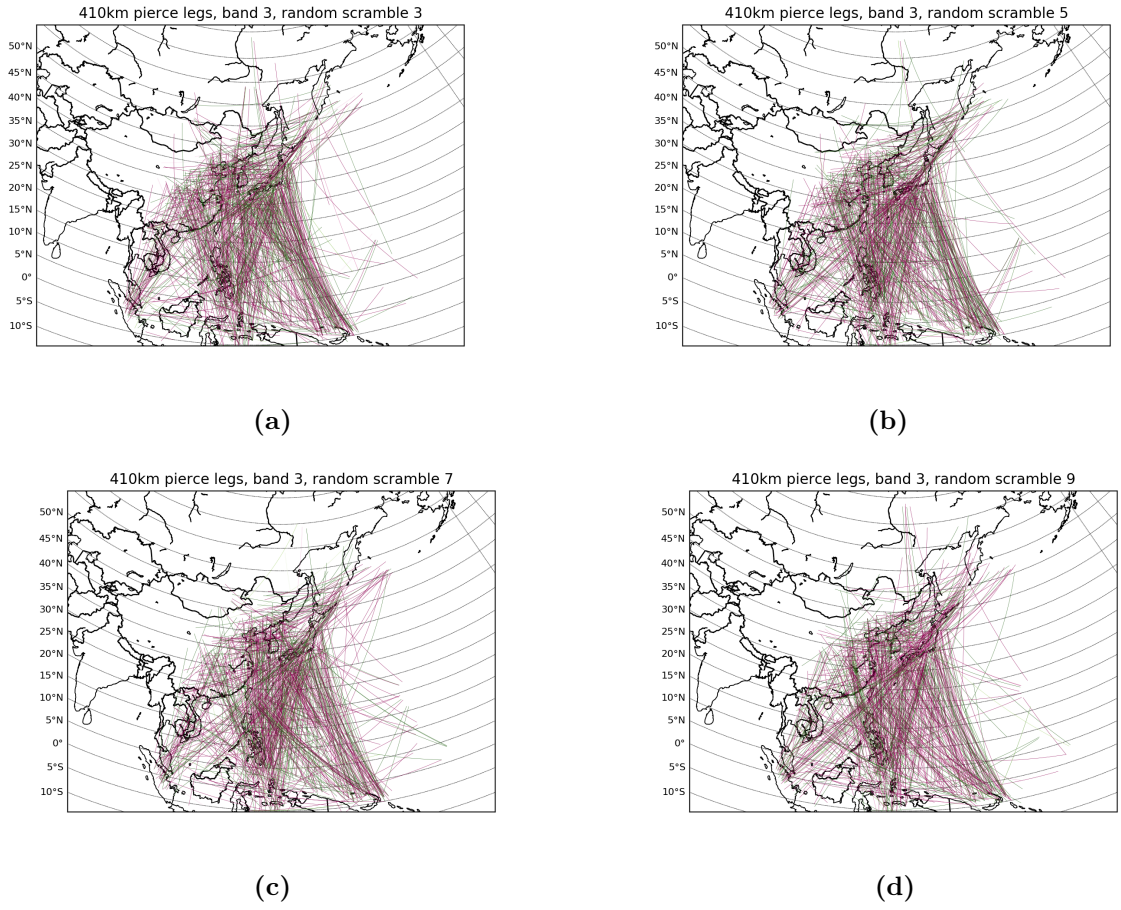

(a) **(b)**

(c) **(d)**

Figure A.71: Supplementary randomised coverage subsets of 410km grazing regional P-wave paths for band three (filtered with a 15s dominant period Gabor filter)

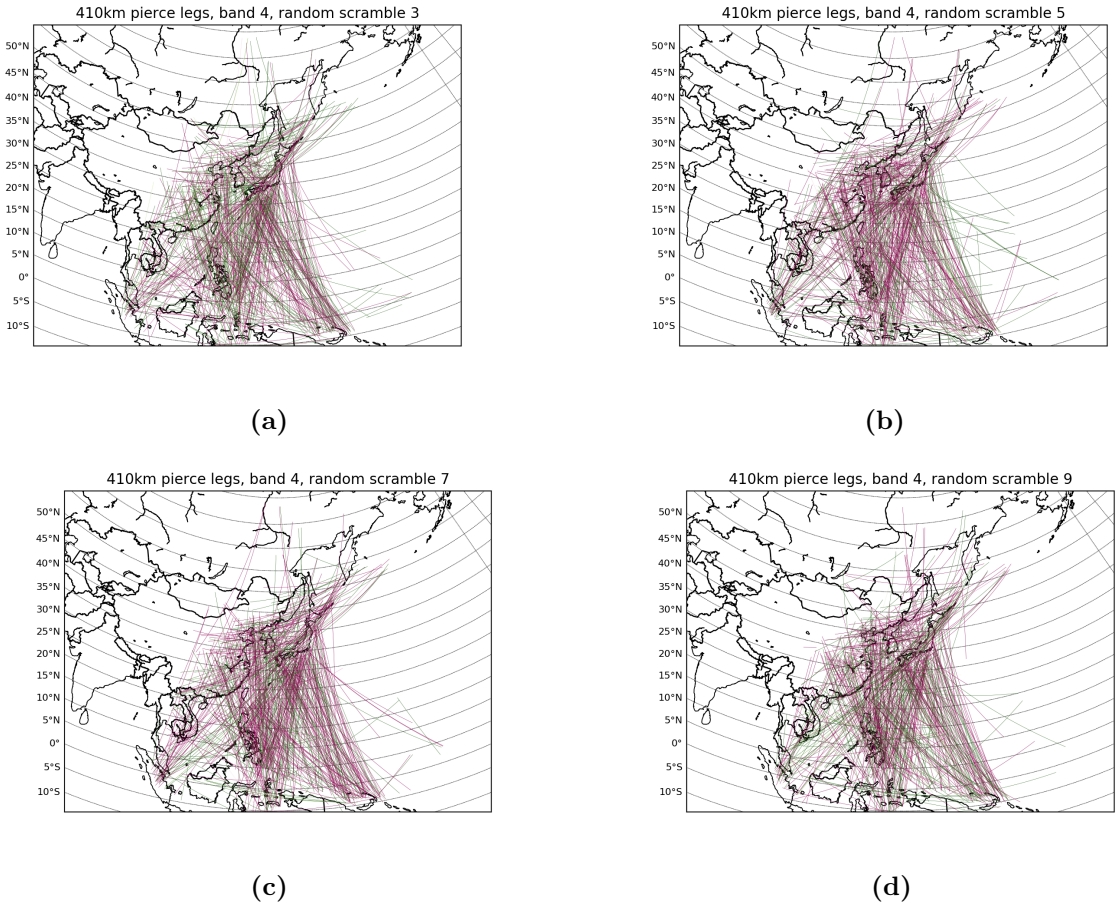

(a) **(b)**

(c) **(d)**

Figure A.72: Supplementary randomised coverage subsets of 410km grazing regional P-wave paths for band four (filtered with a 10s dominant period Gabor filter)

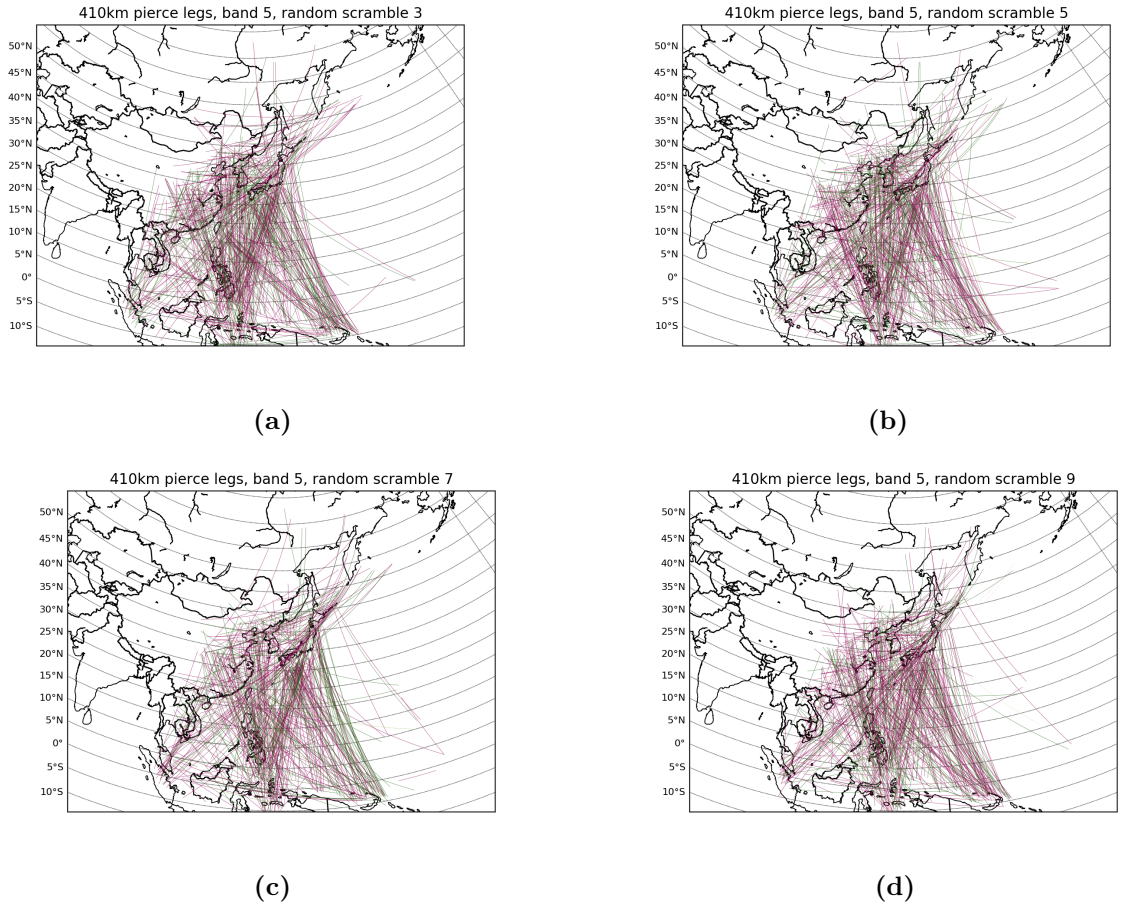

(a) **(b)**

(c) **(d)**

Figure A.73: Supplementary randomised coverage subsets of 410km grazing regional P-wave paths for band five (filtered with a 7.5s dominant period Gabor filter)

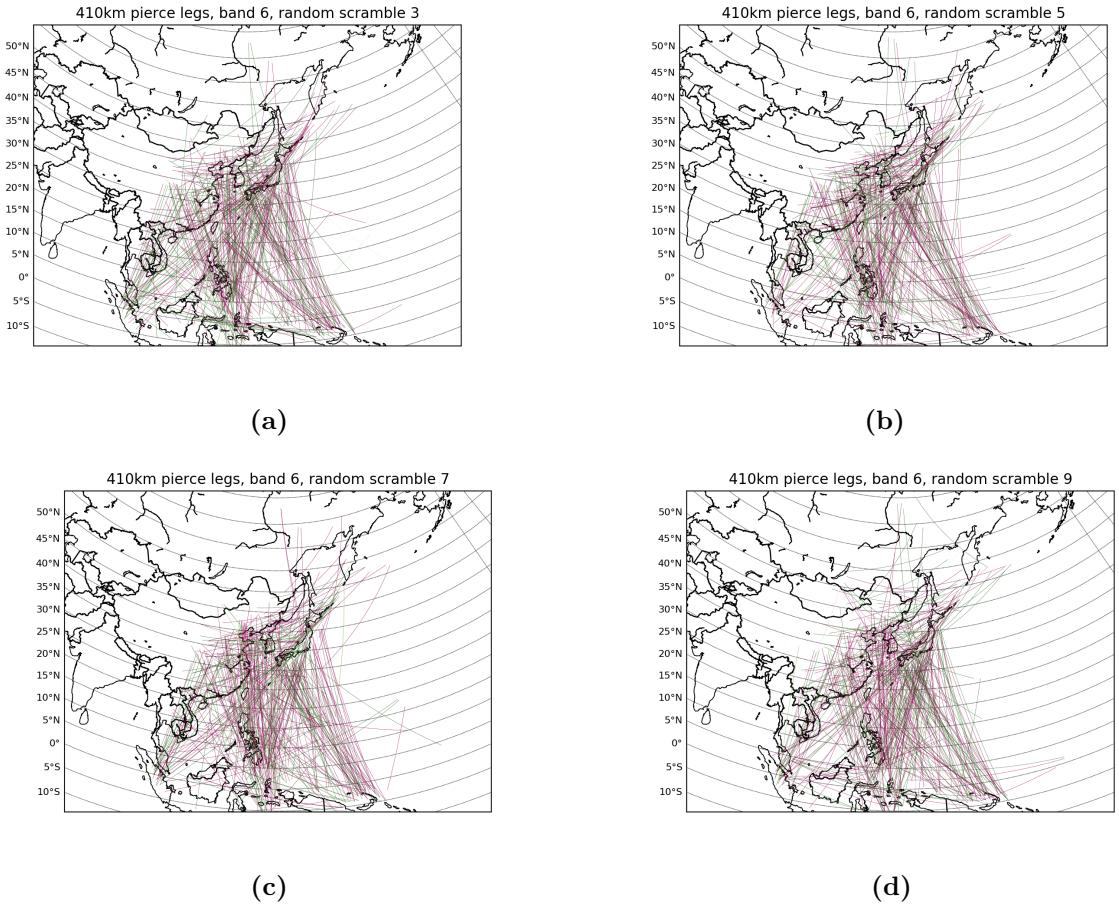

(a) **(b)**

(c) **(d)**

Figure A.74: Supplementary randomised coverage subsets of 410km grazing regional P-wave paths for band six (filtered with a 5s dominant period Gabor filter)

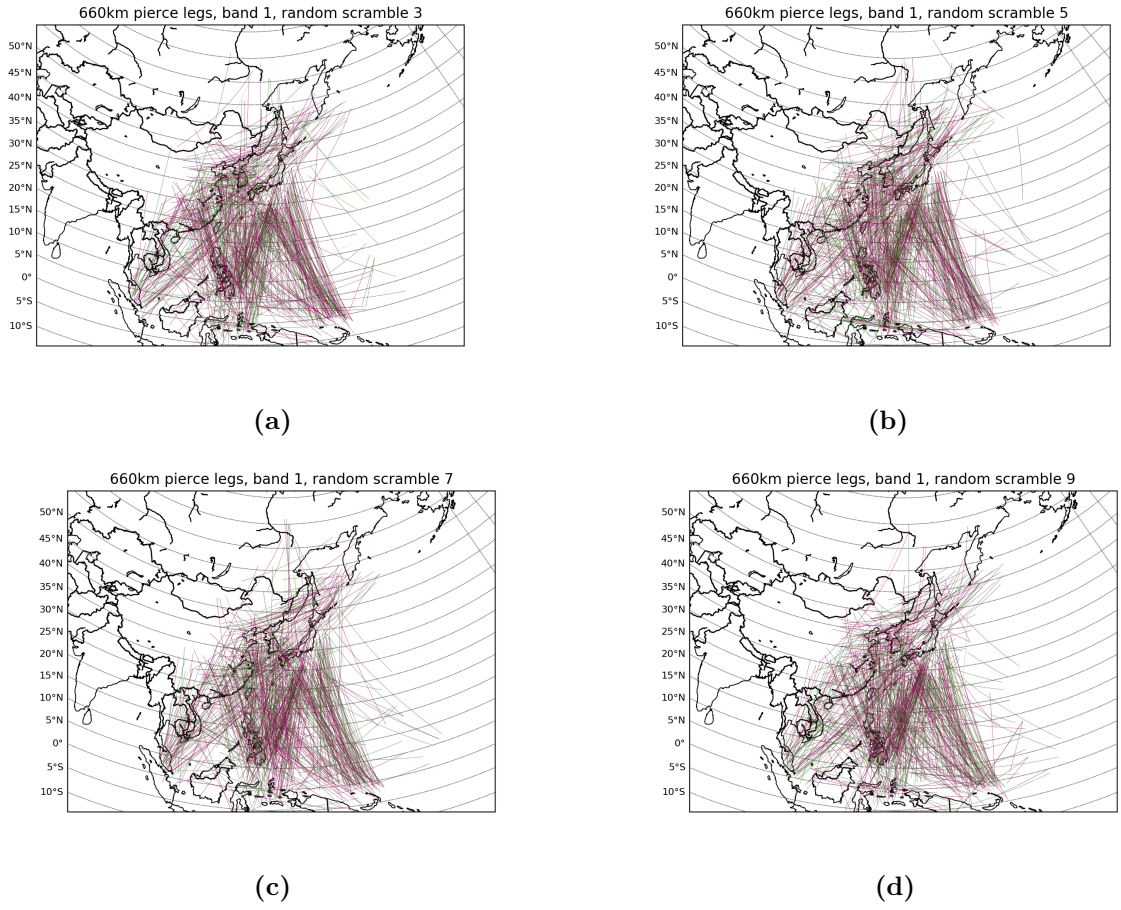

(a) **(b)**

(c) **(d)**

Figure A.75: Supplementary randomised coverage subsets of 660km grazing regional P-wave paths for band one (filtered with a 30s dominant period Gabor filter)

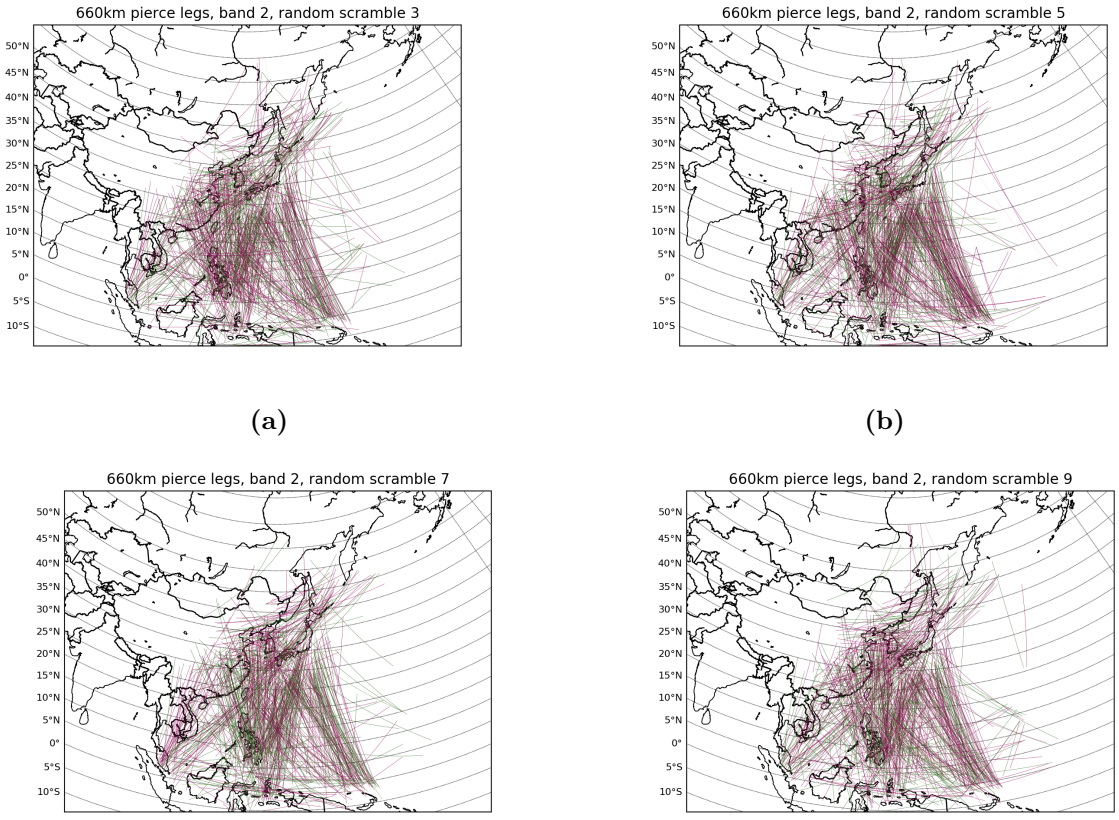

(a) **(b)**

(c) **(d)**

Figure A.76: Supplementary randomised coverage subsets of 660km grazing regional P-wave paths for band two (filtered with a 21s dominant period Gabor filter)

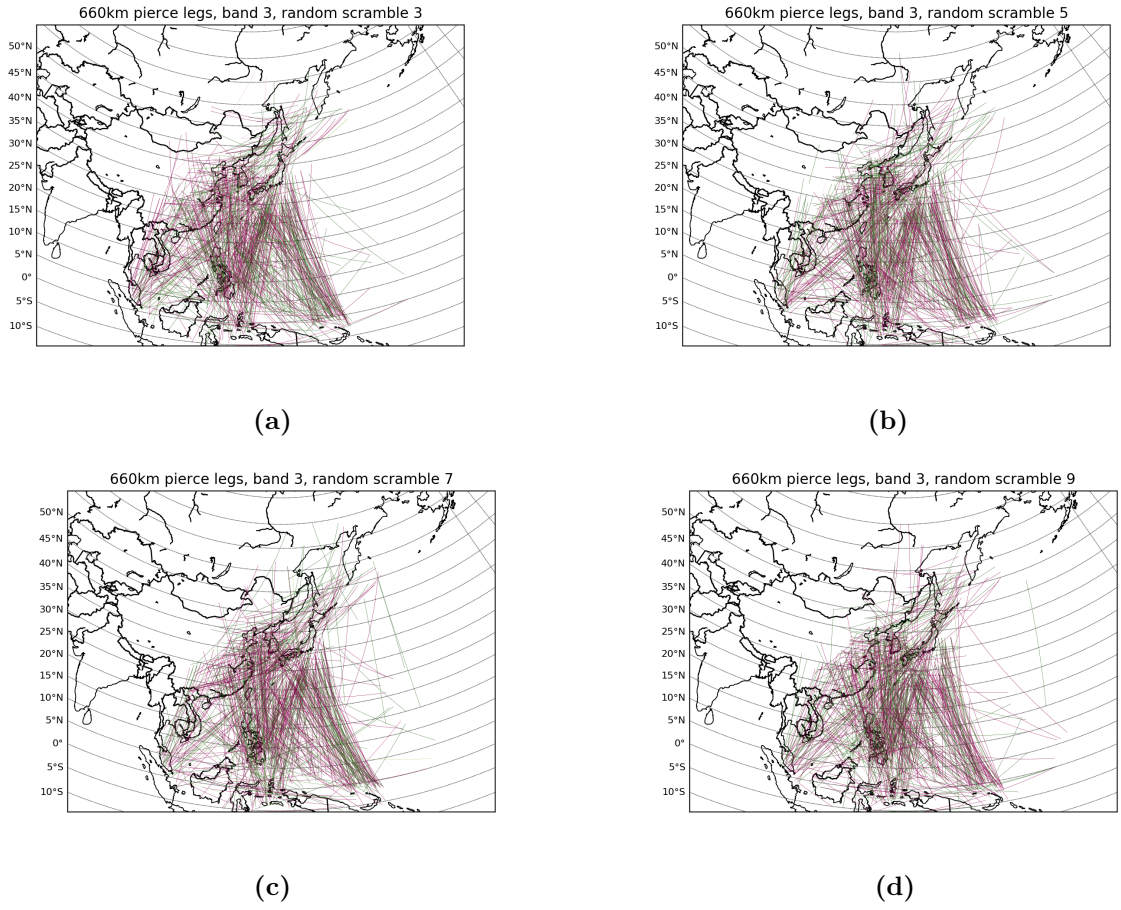

(a) **(b)**

(c) **(d)**

Figure A.77: Supplementary randomised coverage subsets of 660km grazing regional P-wave paths for band three (filtered with a 15s dominant period Gabor filter)

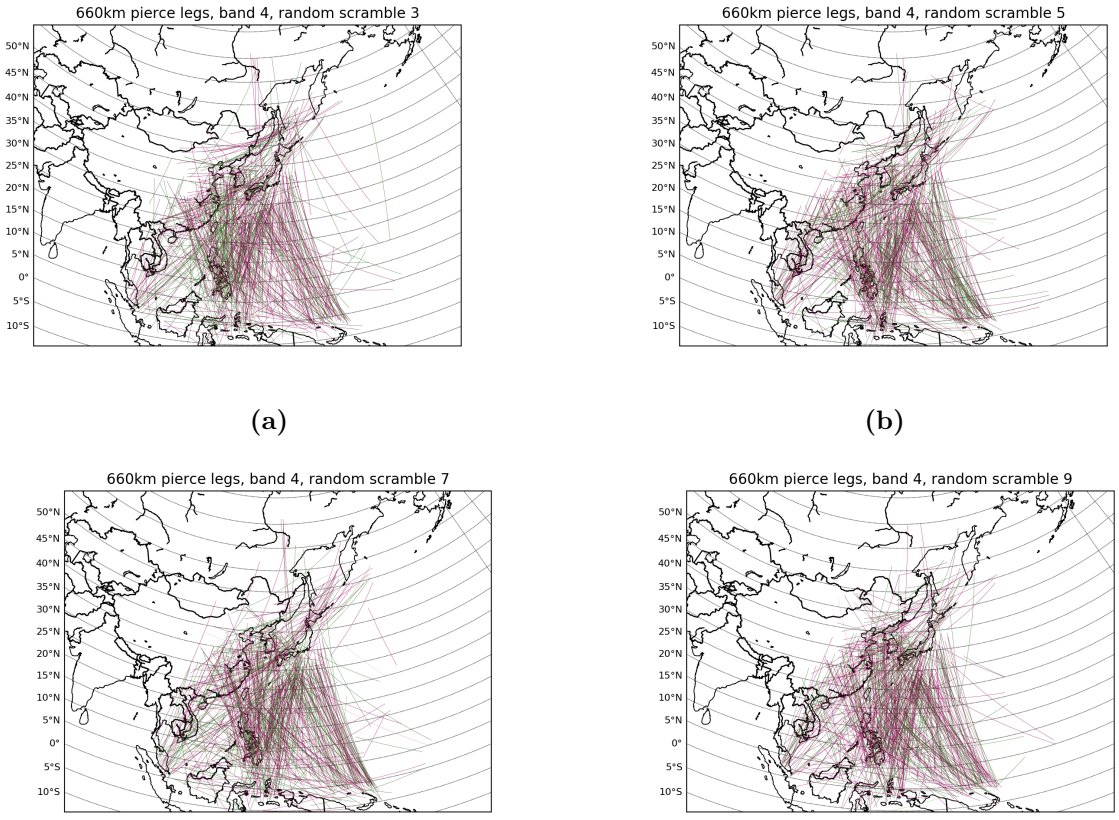

(a) **(b)**

(c) **(d)**

Figure A.78: Supplementary randomised coverage subsets of 660km grazing regional P-wave paths for band four (filtered with a 10s dominant period Gabor filter)

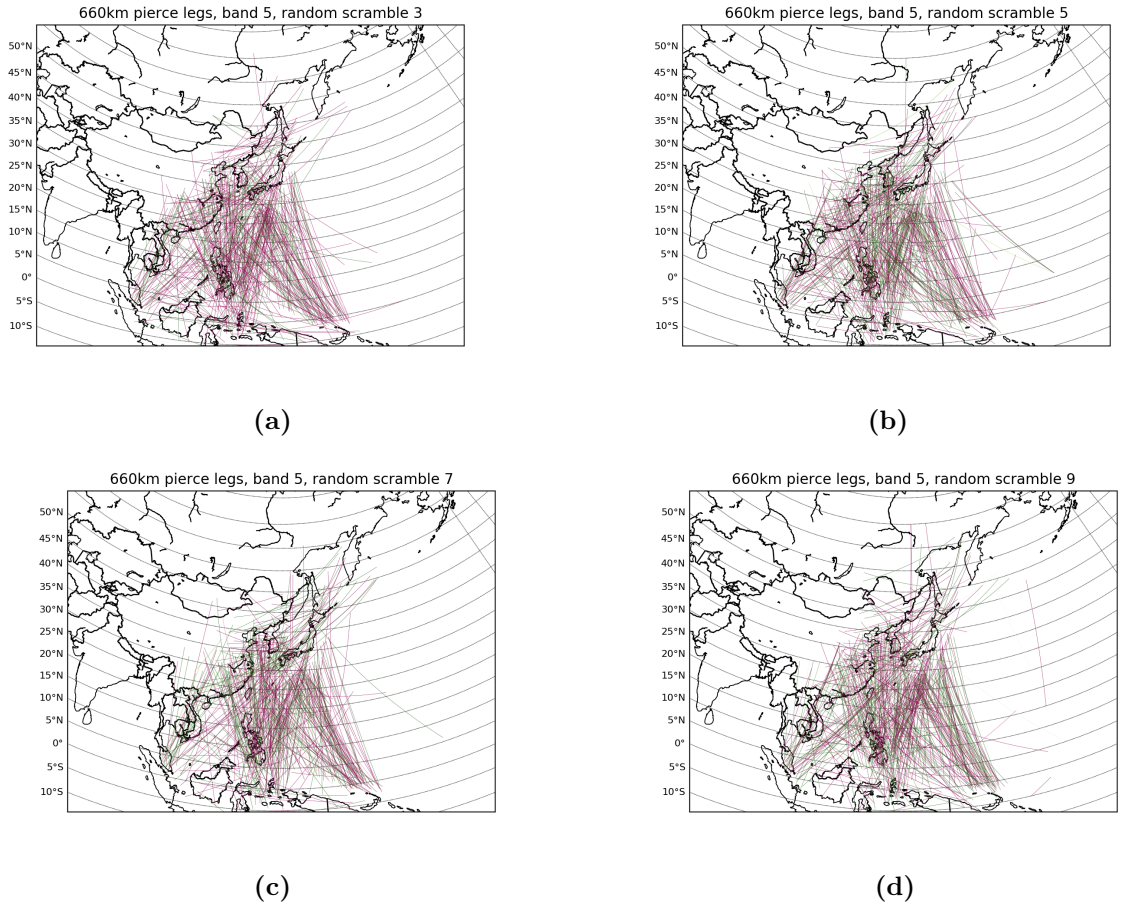

(a) **(b)**

(c) **(d)**

Figure A.79: Supplementary randomised coverage subsets of 660km grazing regional P-wave paths for band five (filtered with a 7.5s dominant period Gabor filter)

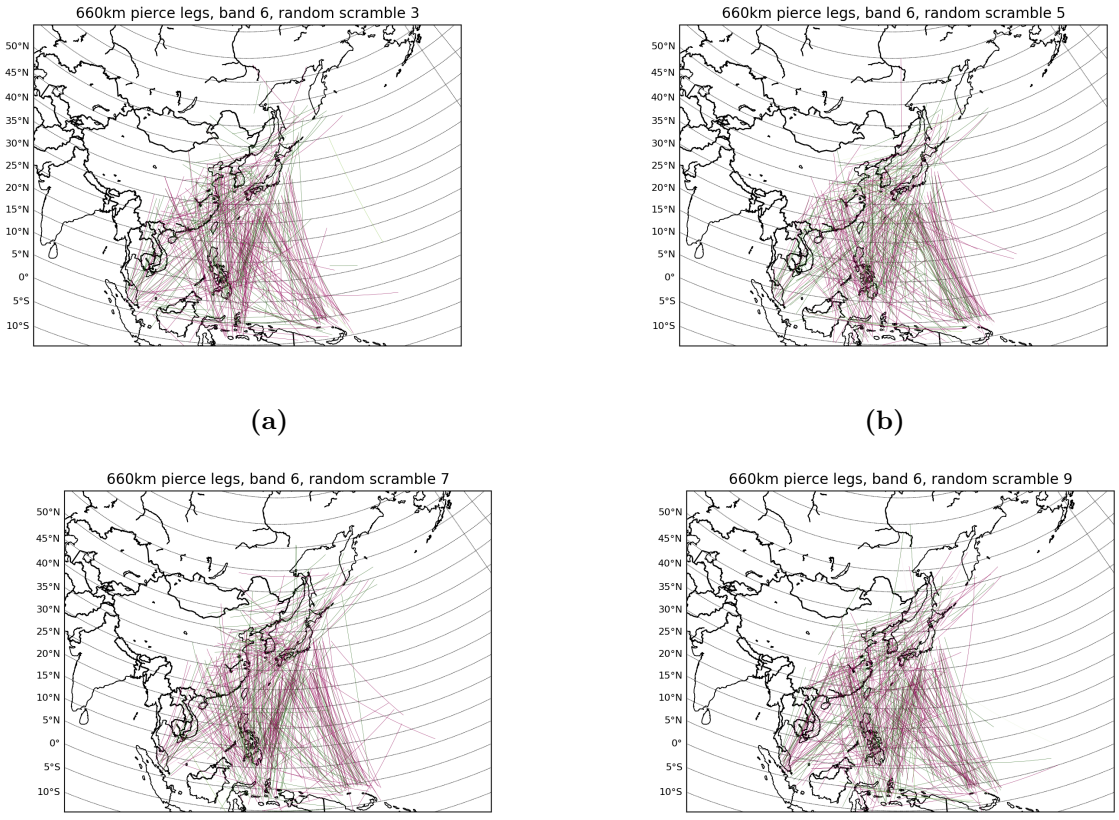

(a) **(b)**

(c) **(d)**

Figure A.80: Supplementary randomised coverage subsets of 660km grazing regional P-wave paths for band six (filtered with a 5s dominant period Gabor filter)

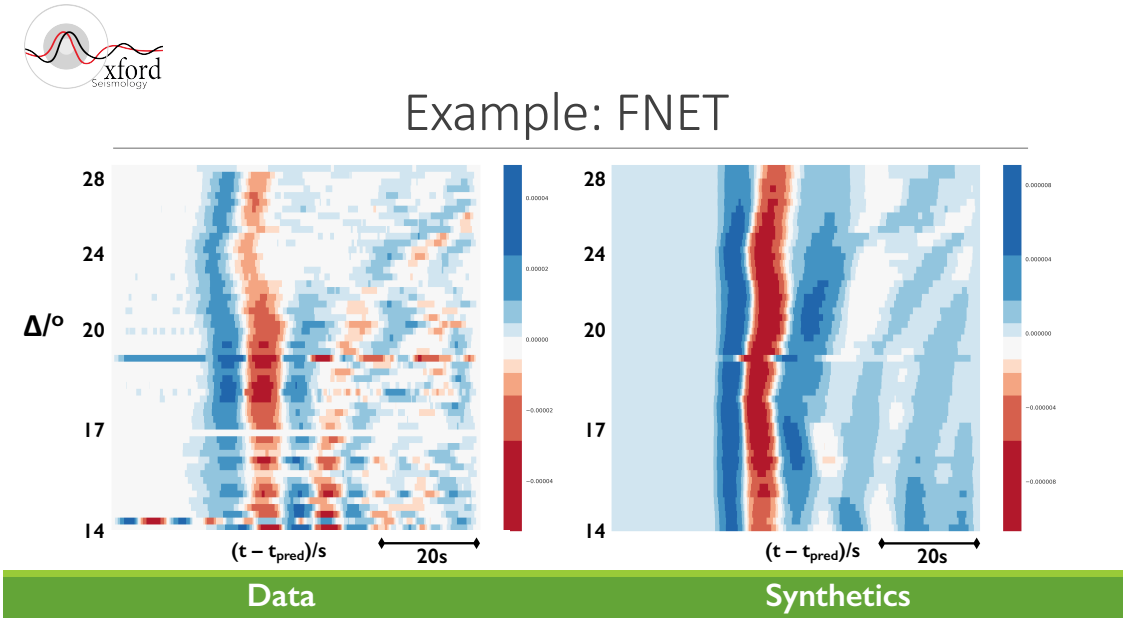

Figure A.81: Raw colour-coded record section of broadband data (left) and Instaseis synthetics. (right)

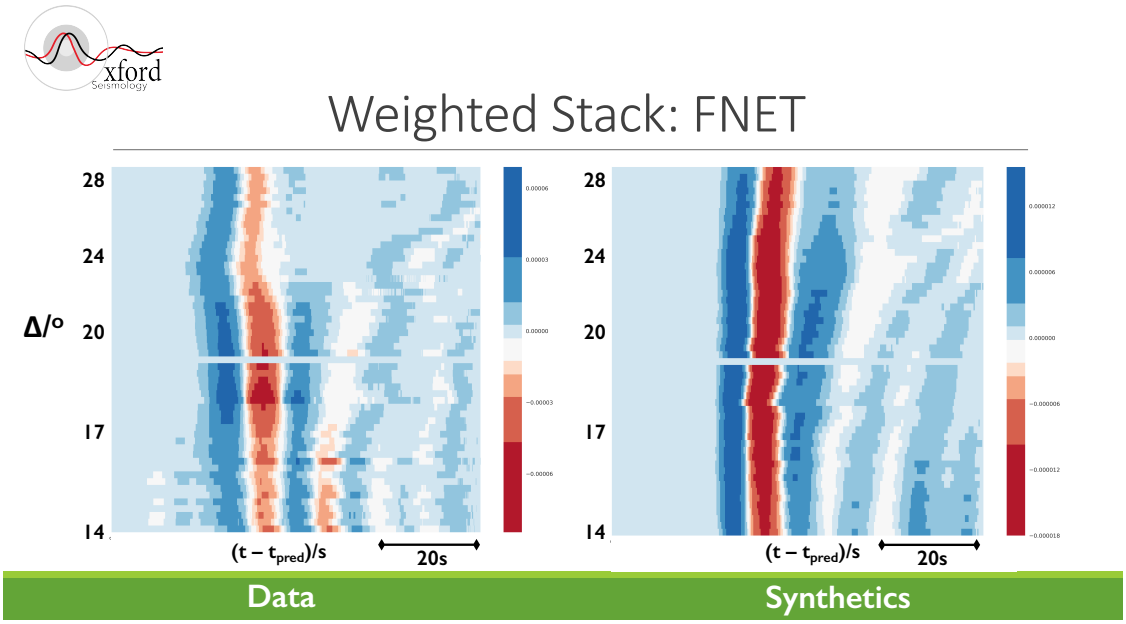

Figure A.82: Raw colour-coded record section of broadband data (left) and Instaseis synthetics. (right)

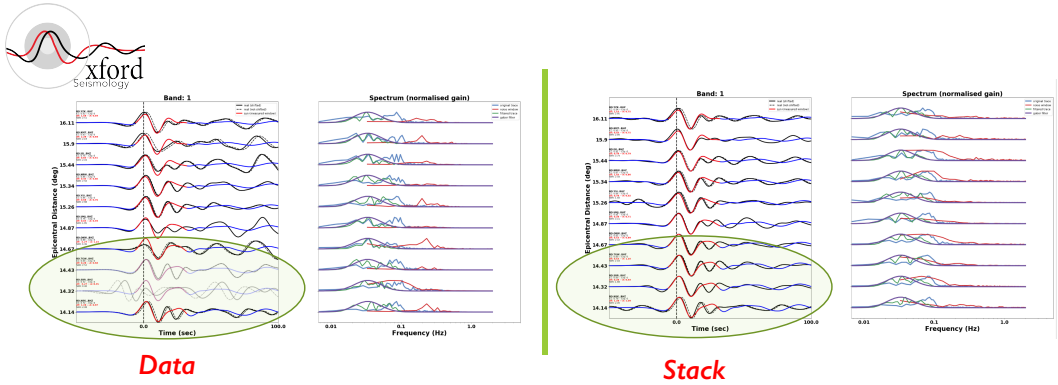

Figure A.83: Coherence-weighted stacks used during the finite-frequency measurement process. Visible is an improvement on the measurement success for this set of measurements using coherence-weighted stacking of neighbouring waveforms. Also shown on the plot are the frequency spectra for both waveforms and the Gabor filters applied.

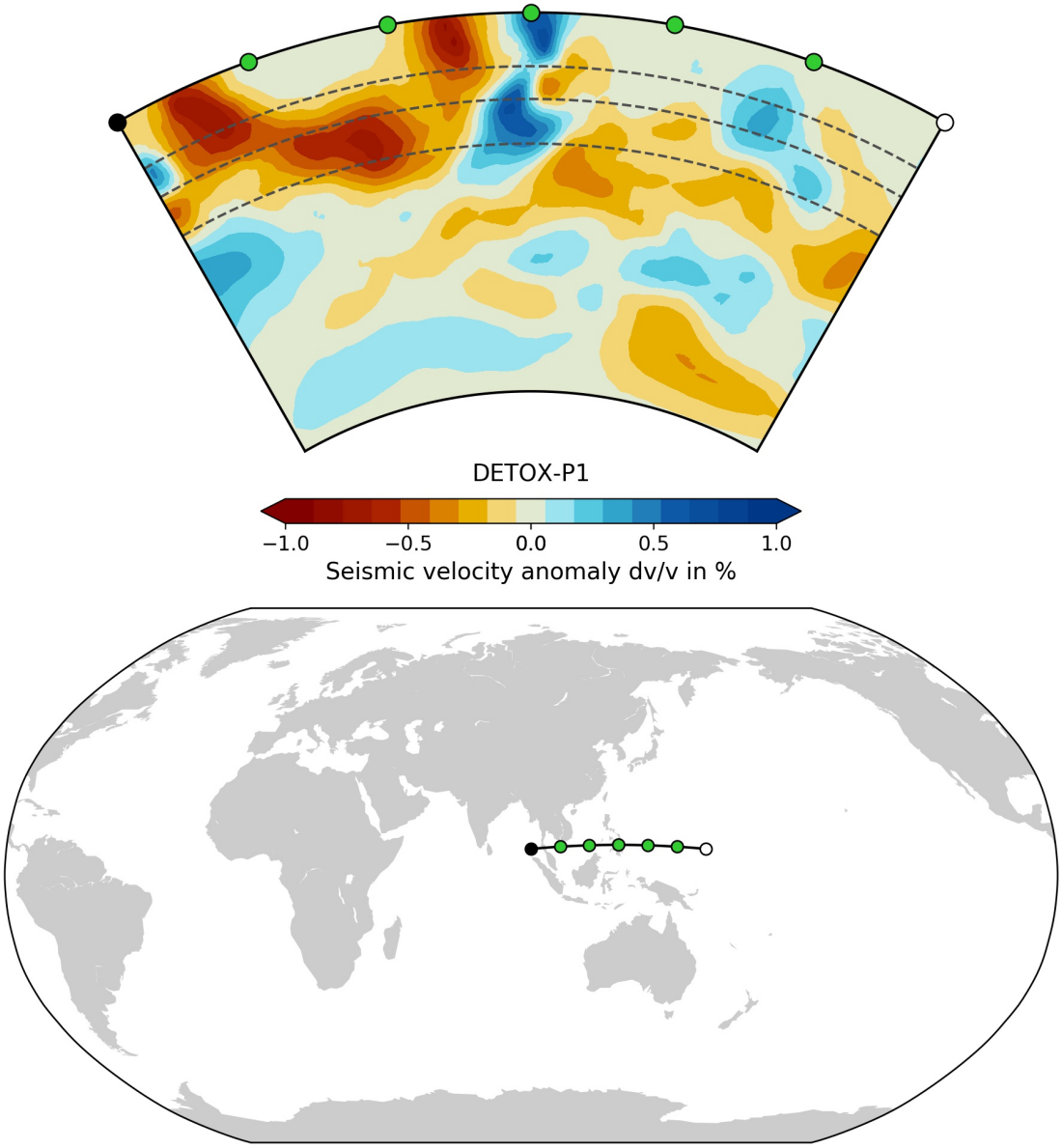

Figure A.84: East-West cross-section through DETOX P1 at 8°N, produced using SubMachine.

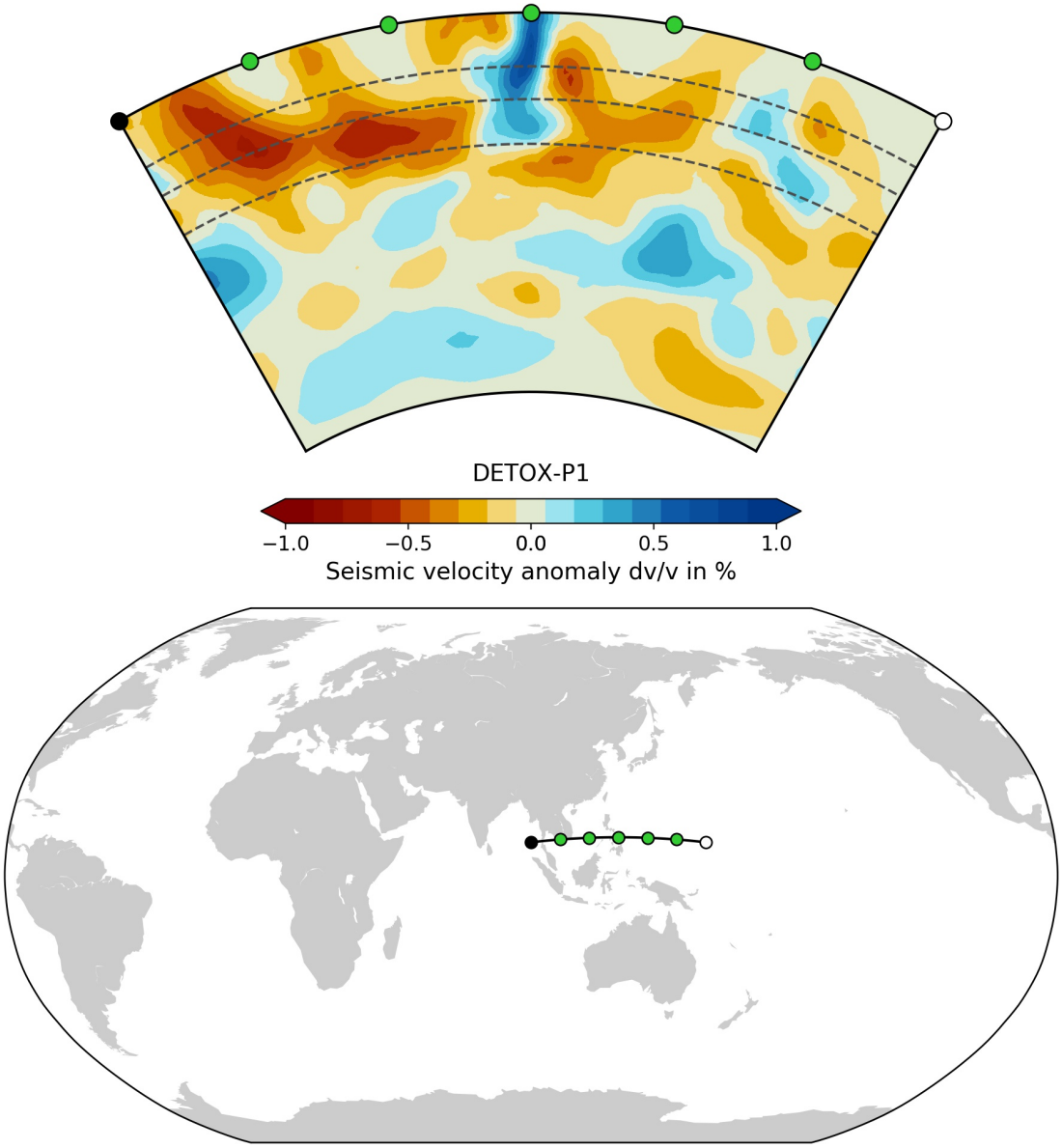

Figure A.85: East-West cross-section through DETOX P1 at 10°N, produced using SubMachine.

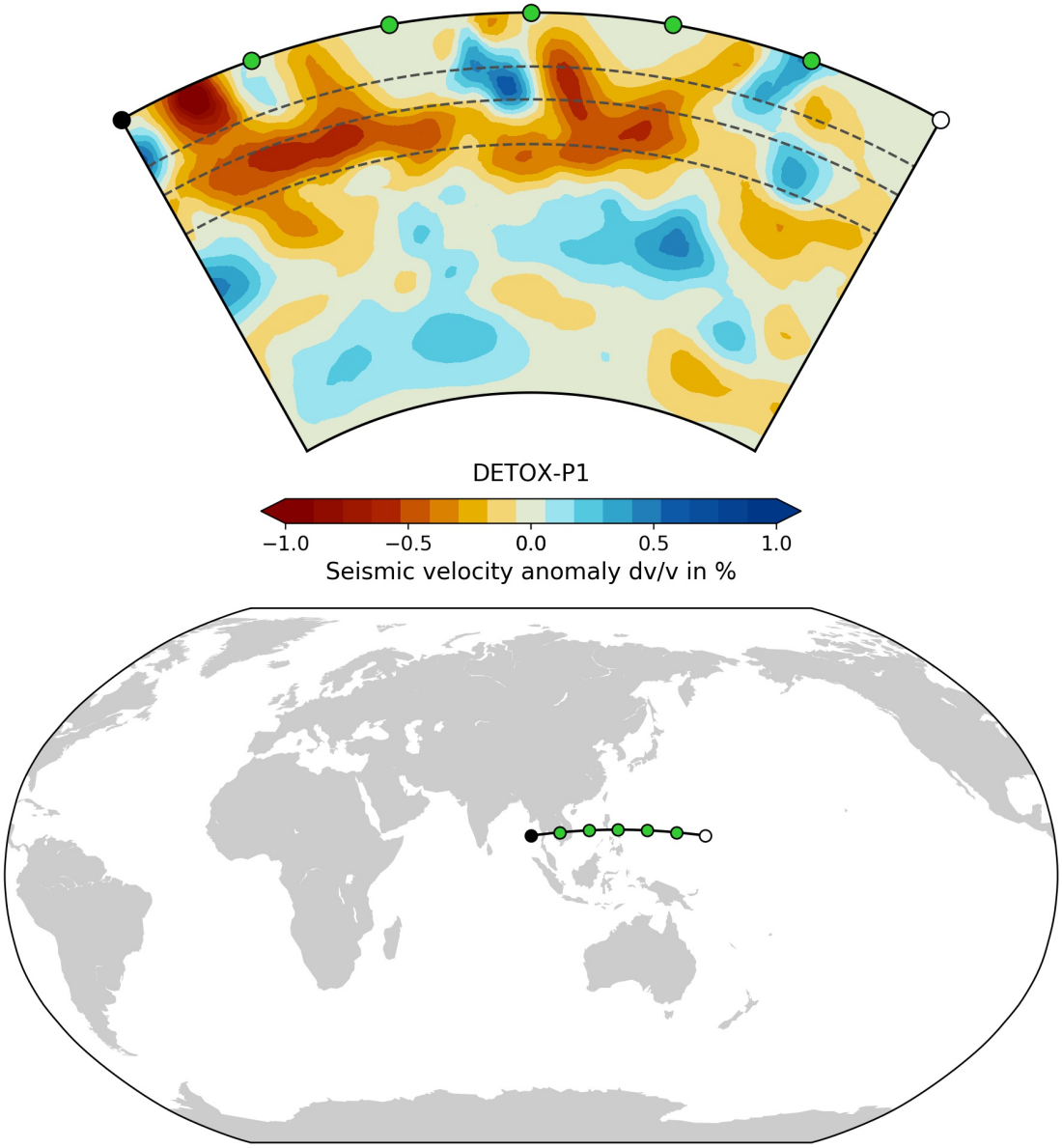

Figure A.86: East-West cross-section through DETOX P1 at 12°N, produced using SubMachine.

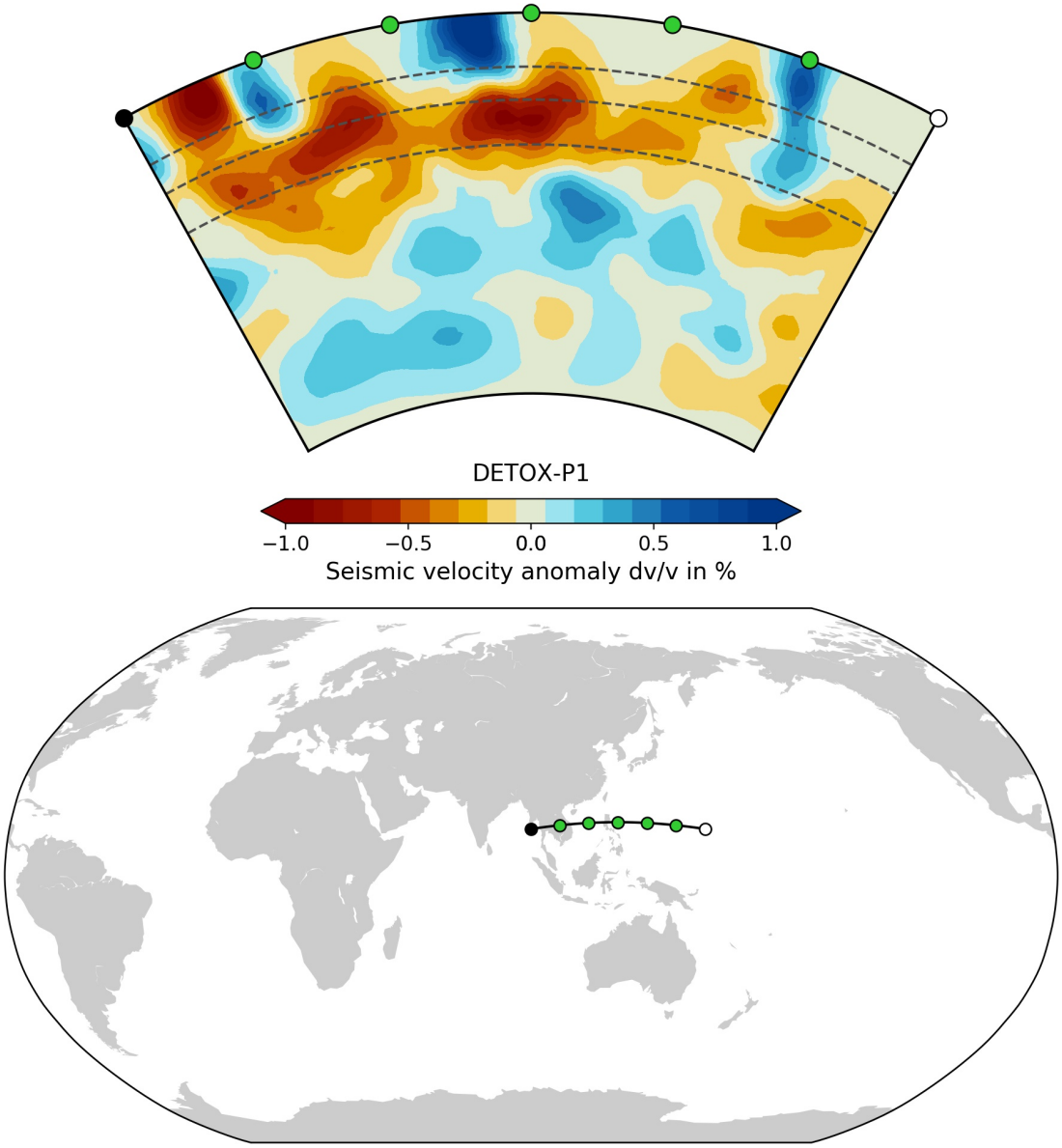

Figure A.87: East-West cross-section through DETOX P1 at 14°N, produced using SubMachine.

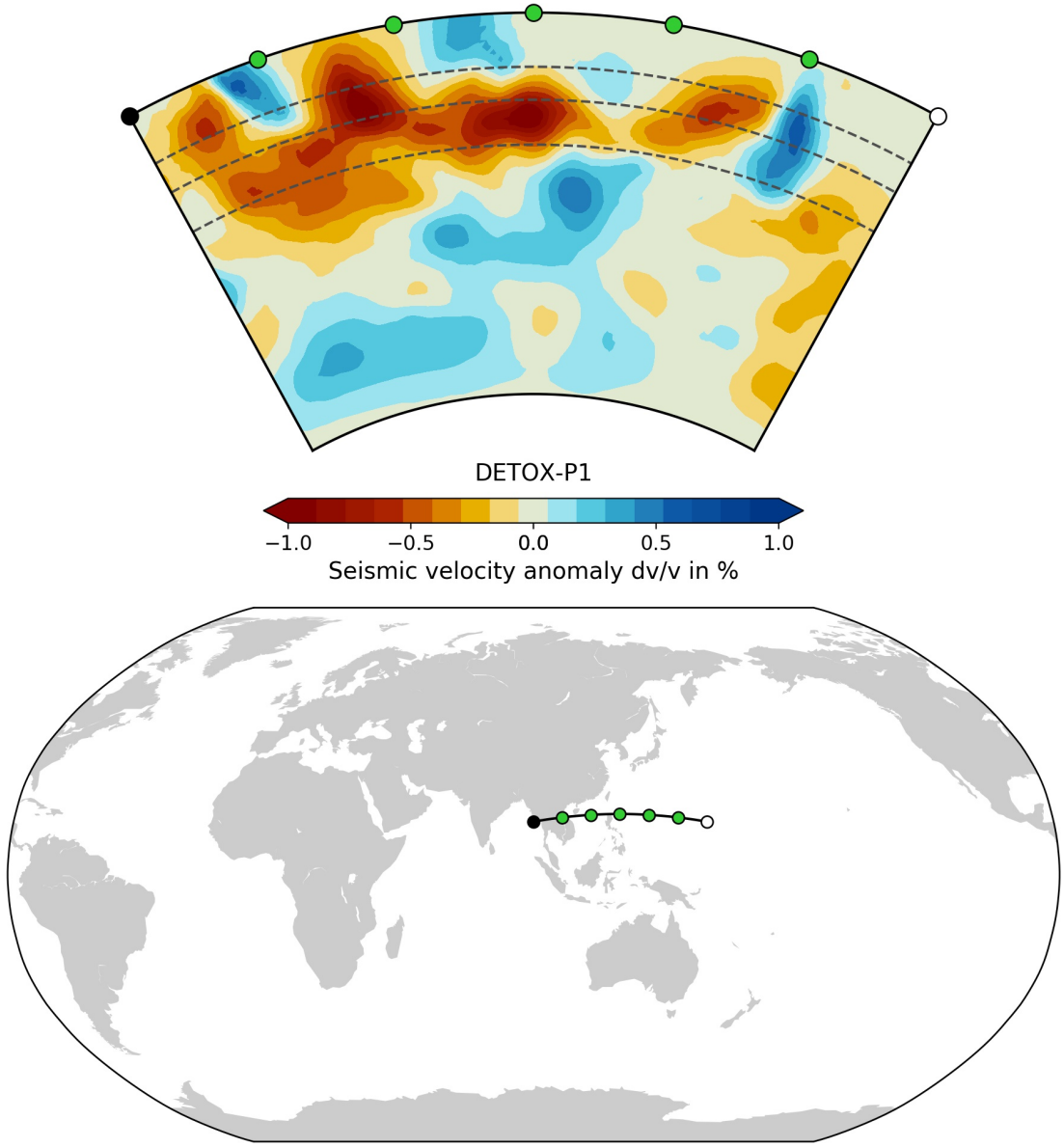

Figure A.88: East-West cross-section through DETOX P1 at 16°N, produced using SubMachine.

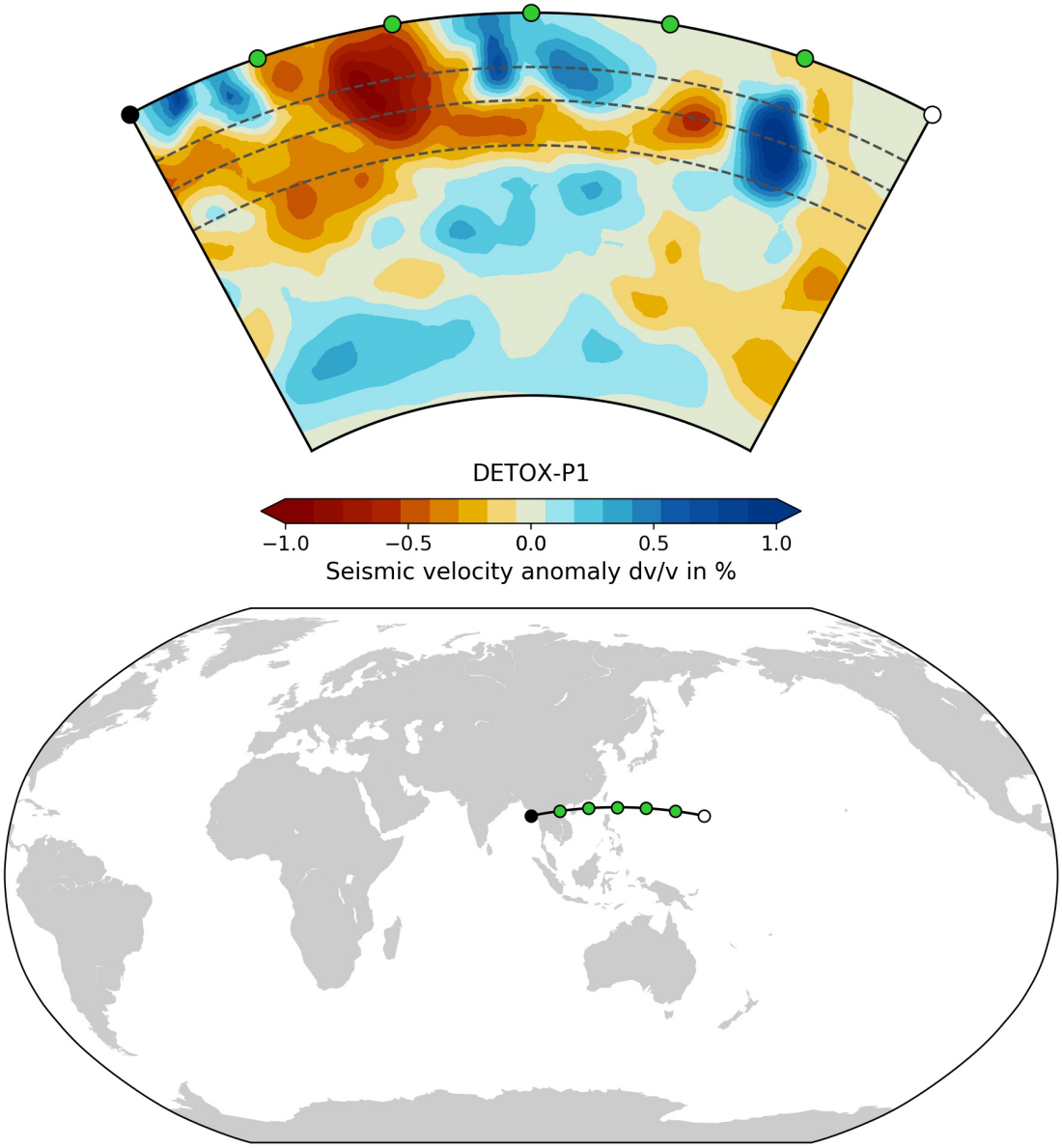

Figure A.89: East-West cross-section through DETOX P1 at 18°N, produced using SubMachine.

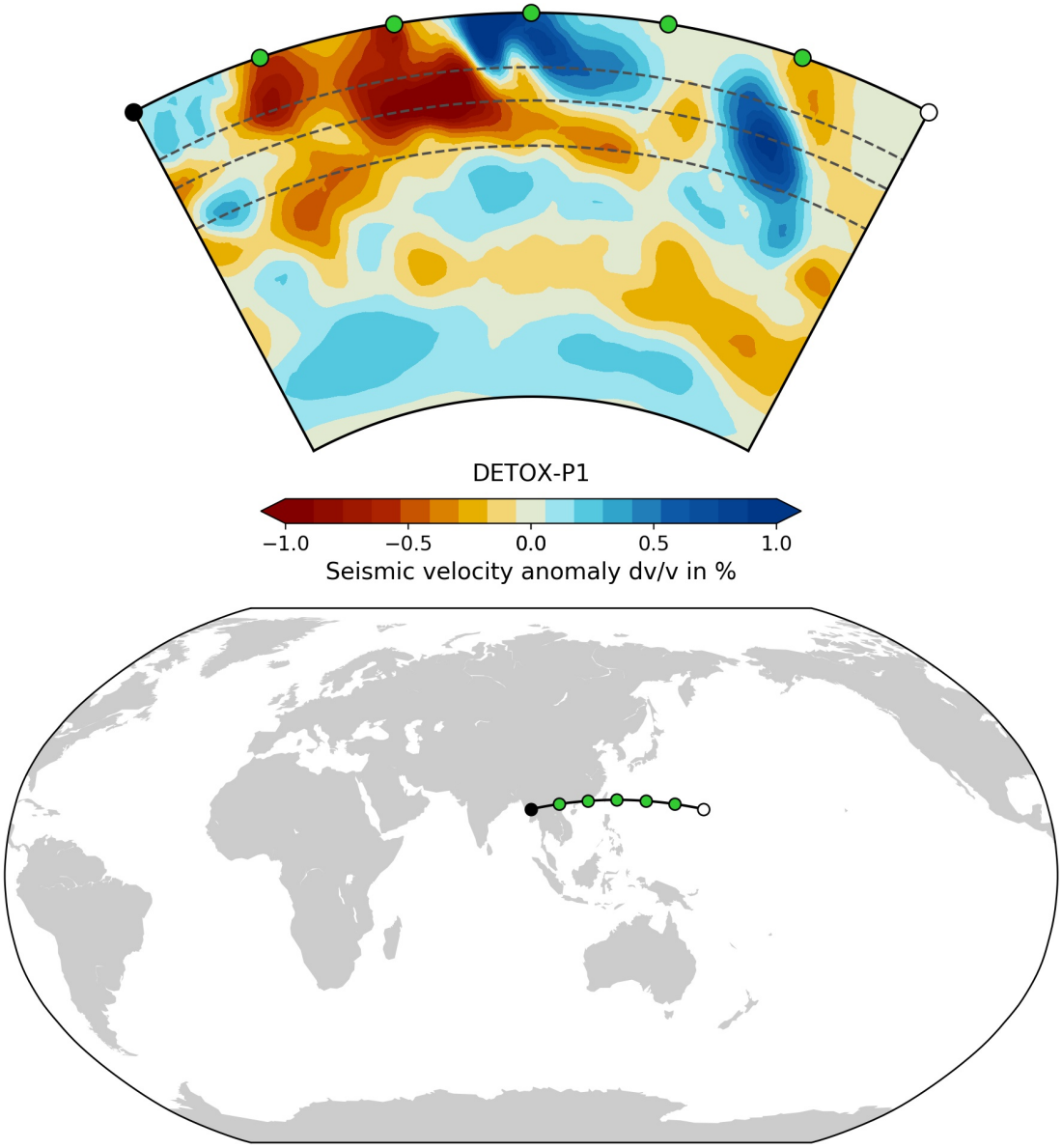

Figure A.90: East-West cross-section through DETOX P1 at 20°N, produced using SubMachine.

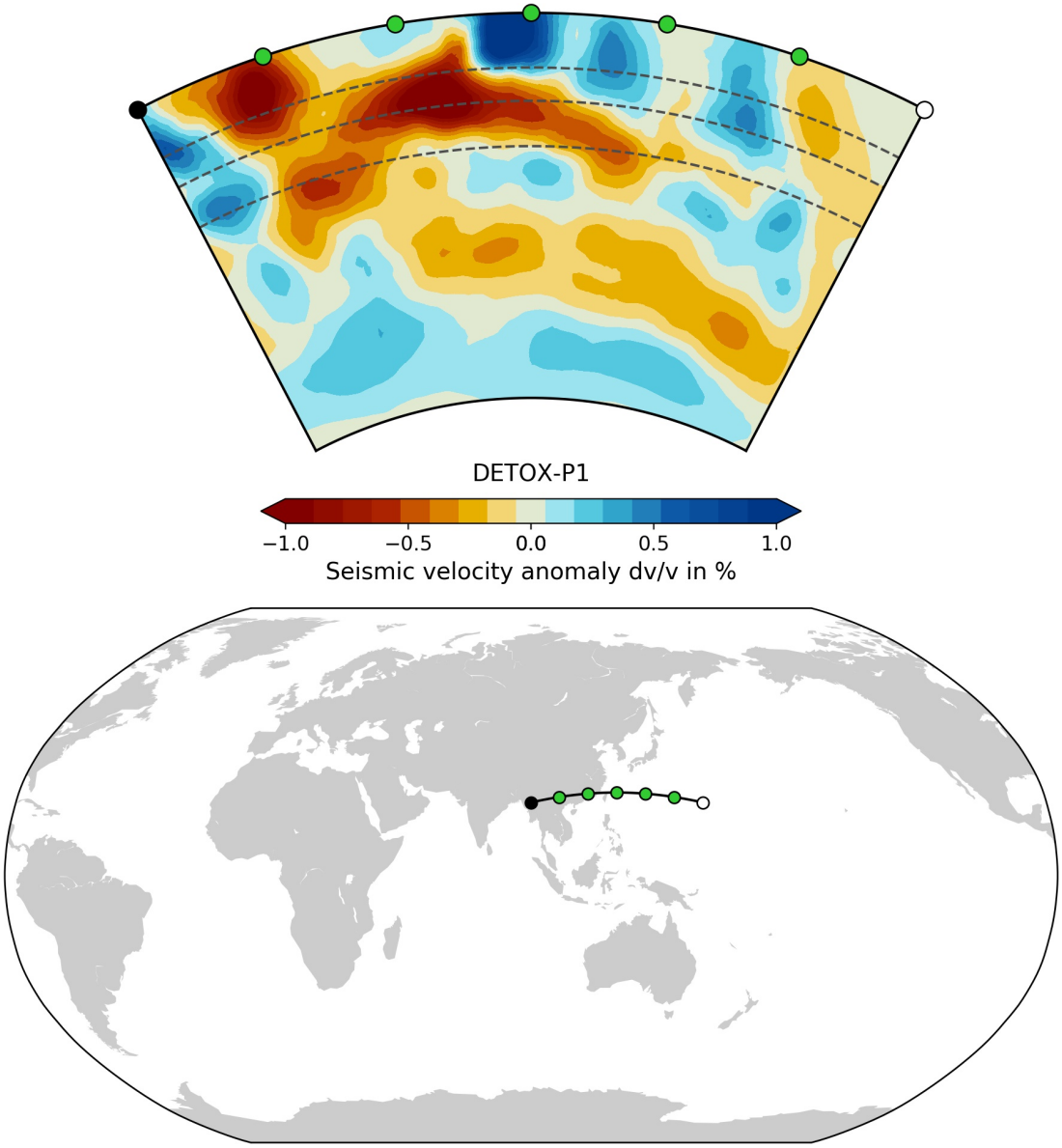

Figure A.91: East-West cross-section through DETOX P1 at 22°N, produced using SubMachine.

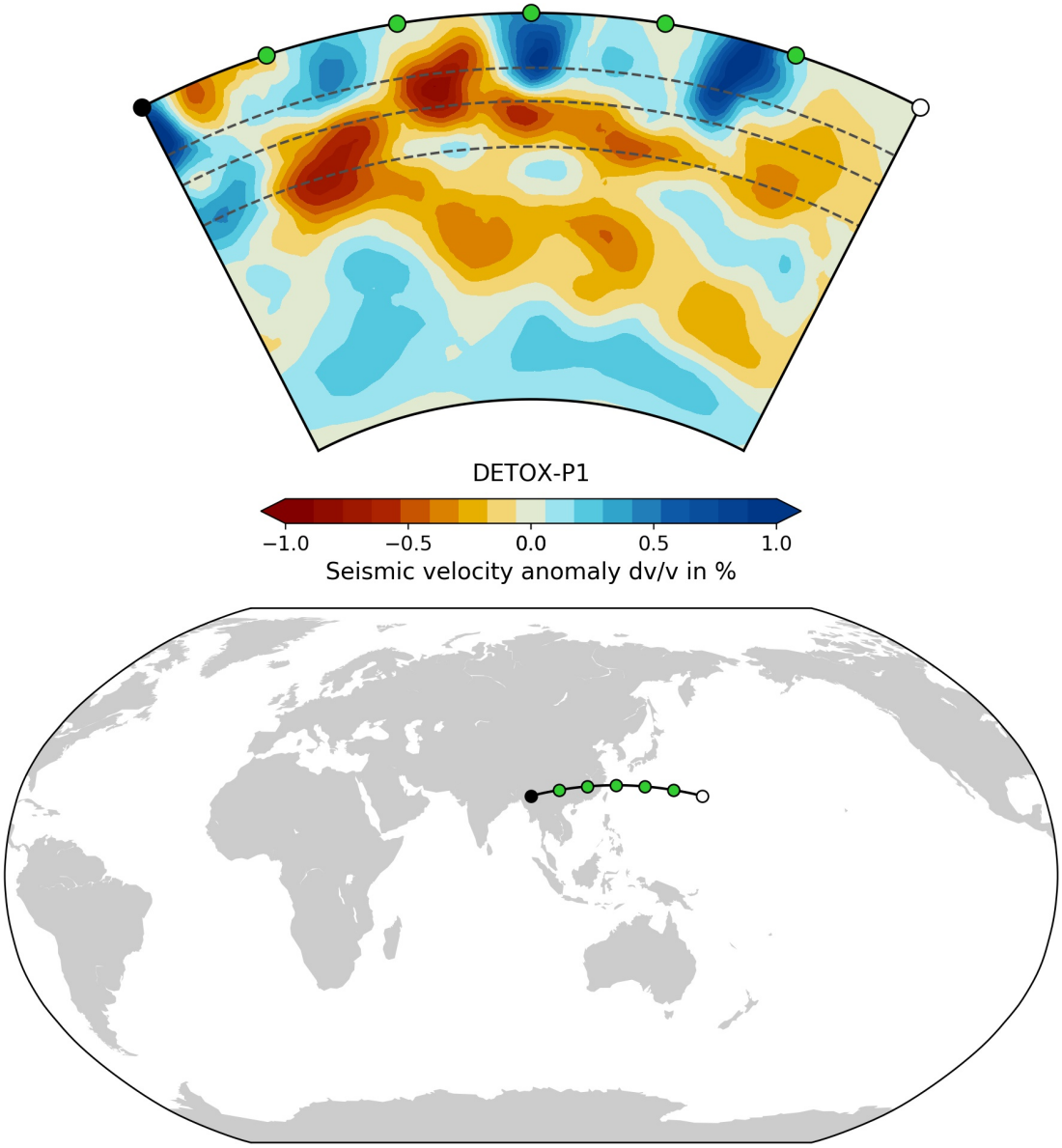

Figure A.92: East-West cross-section through DETOX P1 at 24°N, produced using SubMachine.

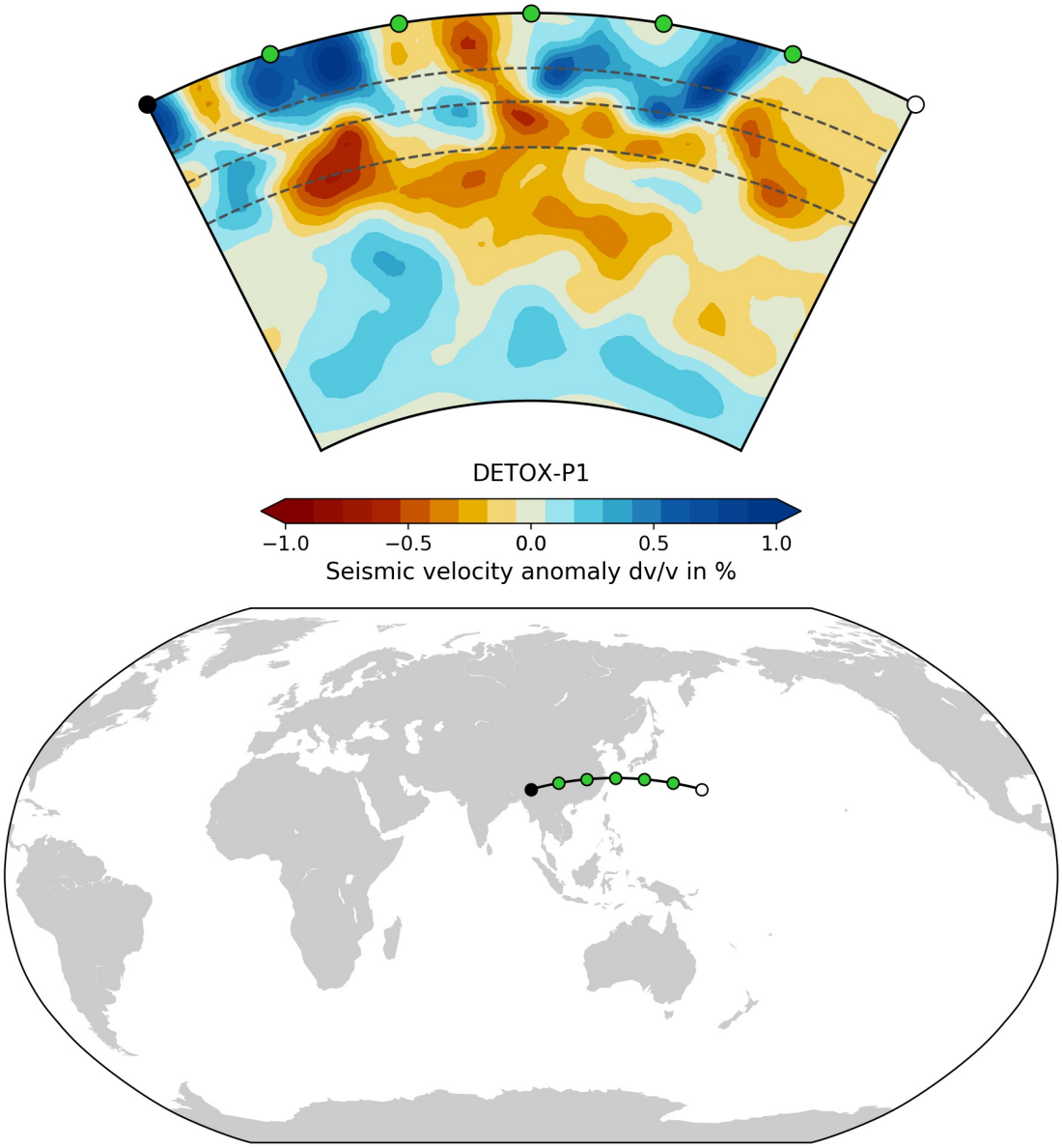

Figure A.93: East-West cross-section through DETOX P1 at 26°N, produced using SubMachine.

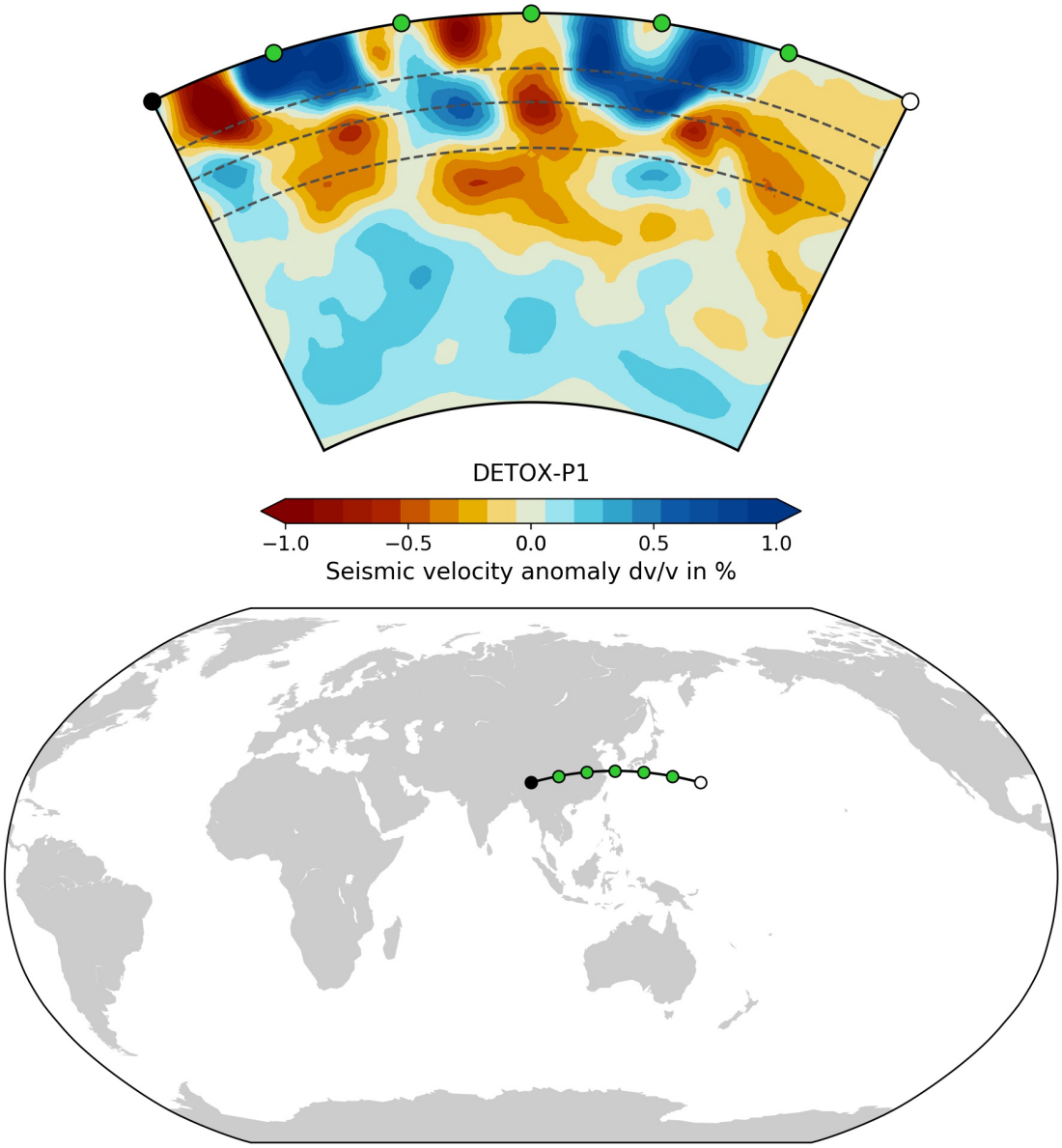

Figure A.94: East-West cross-section through DETOX P1 at 28°N, produced using SubMachine.

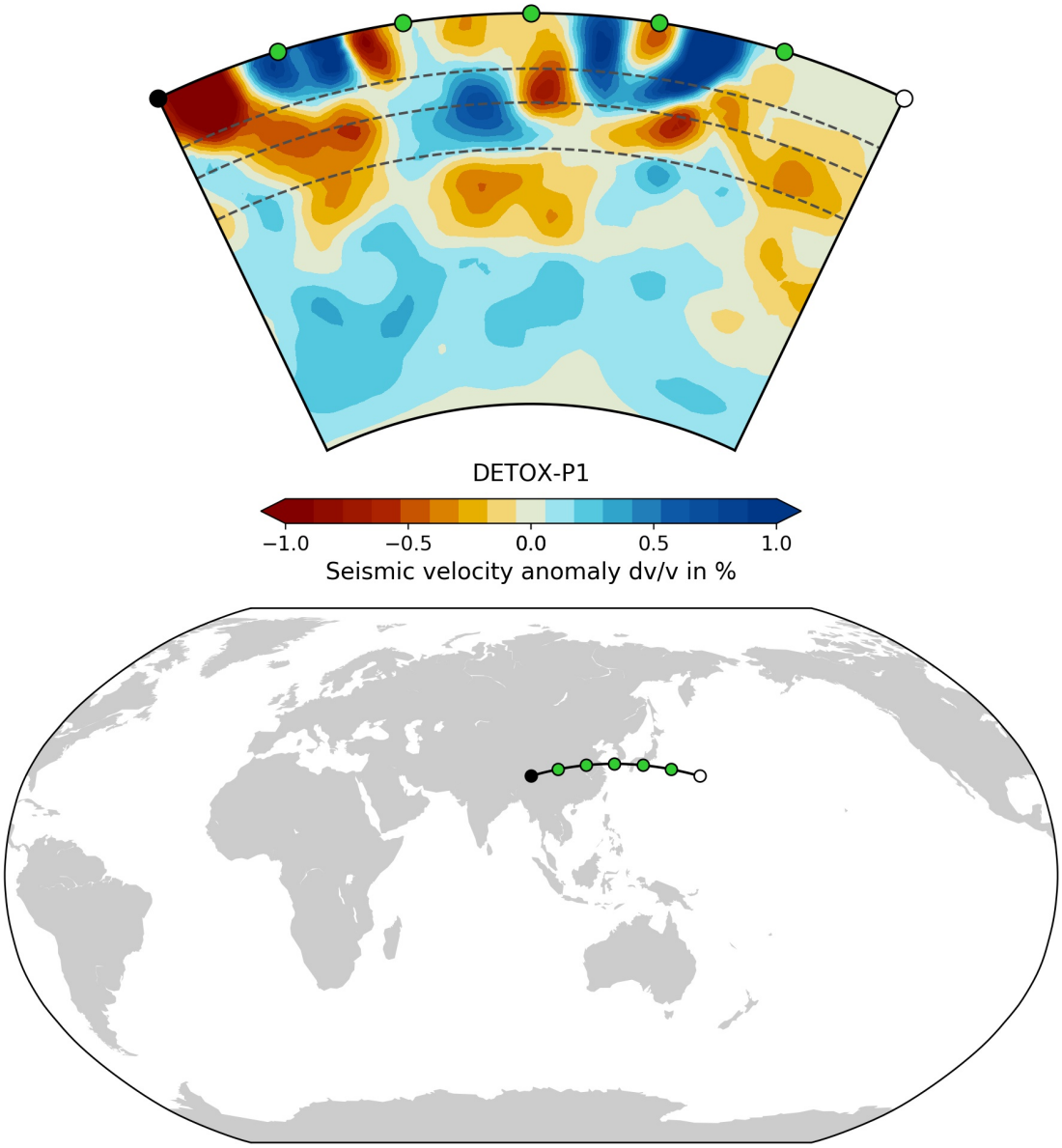

Figure A.95: East-West cross-section through DETOX P1 at 30°N, produced using SubMachine.

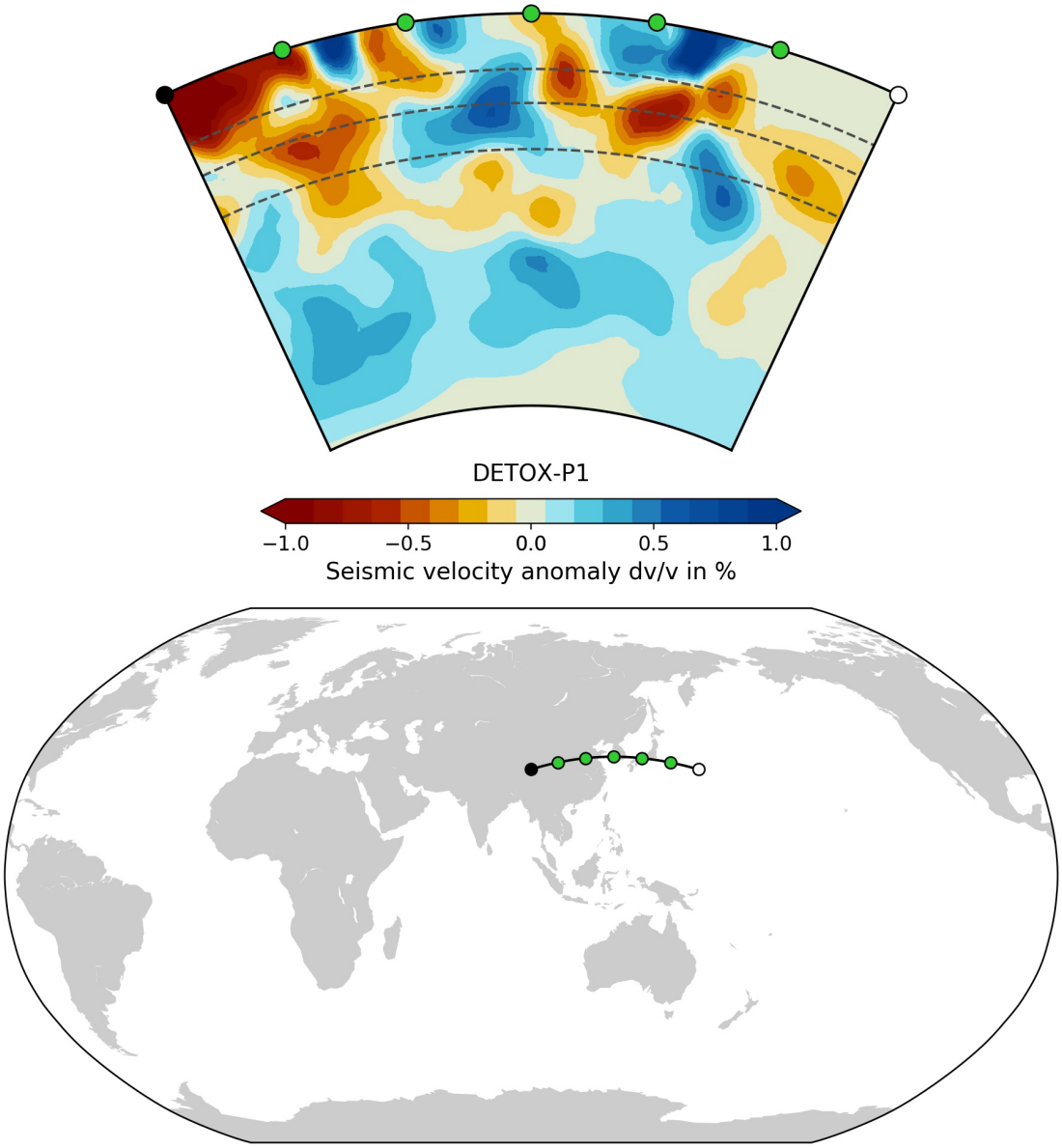

Figure A.96: East-West cross-section through DETOX P1 at 32°N, produced using SubMachine.

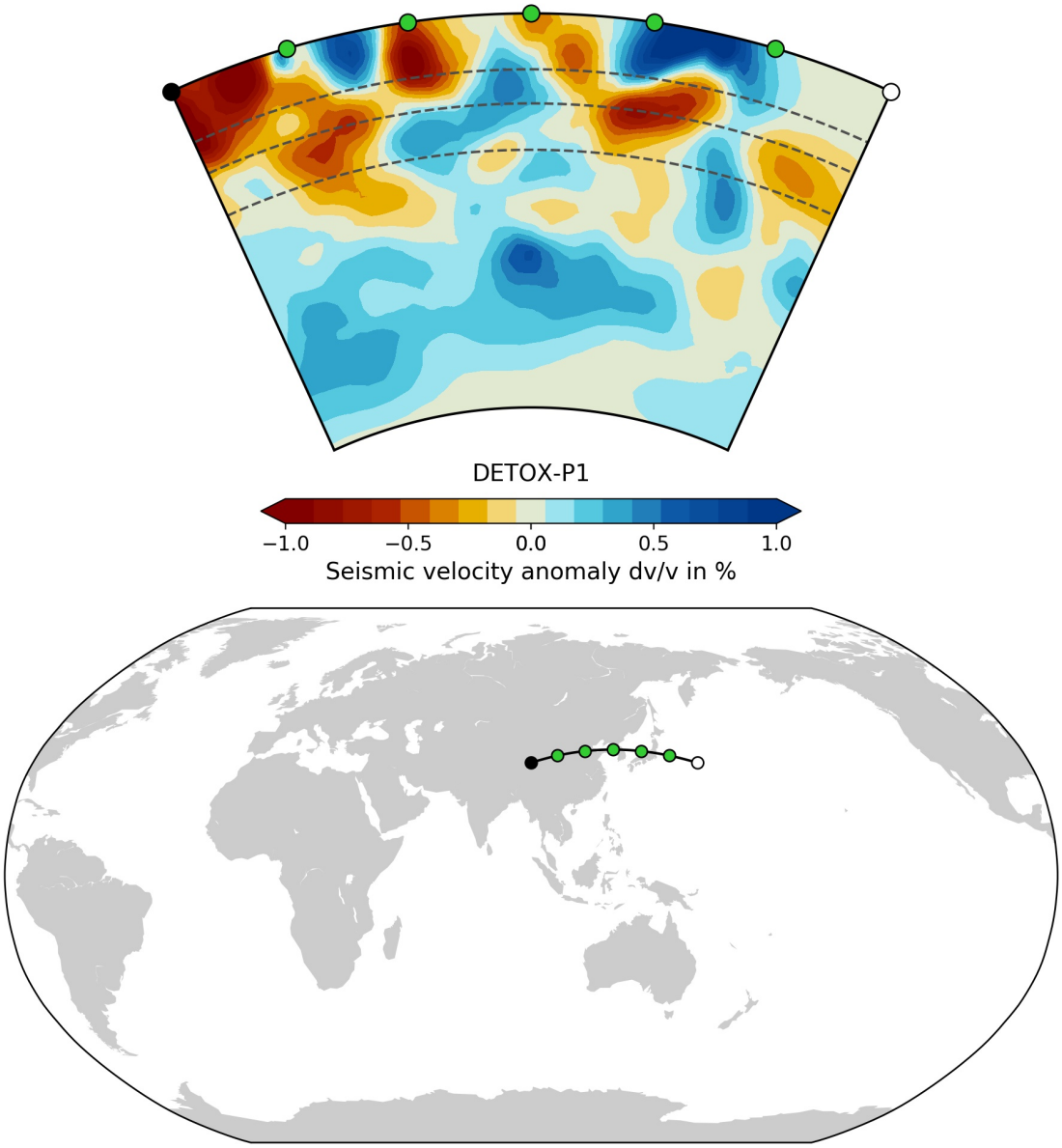

Figure A.97: East-West cross-section through DETOX P1 at 34°N, produced using SubMachine.

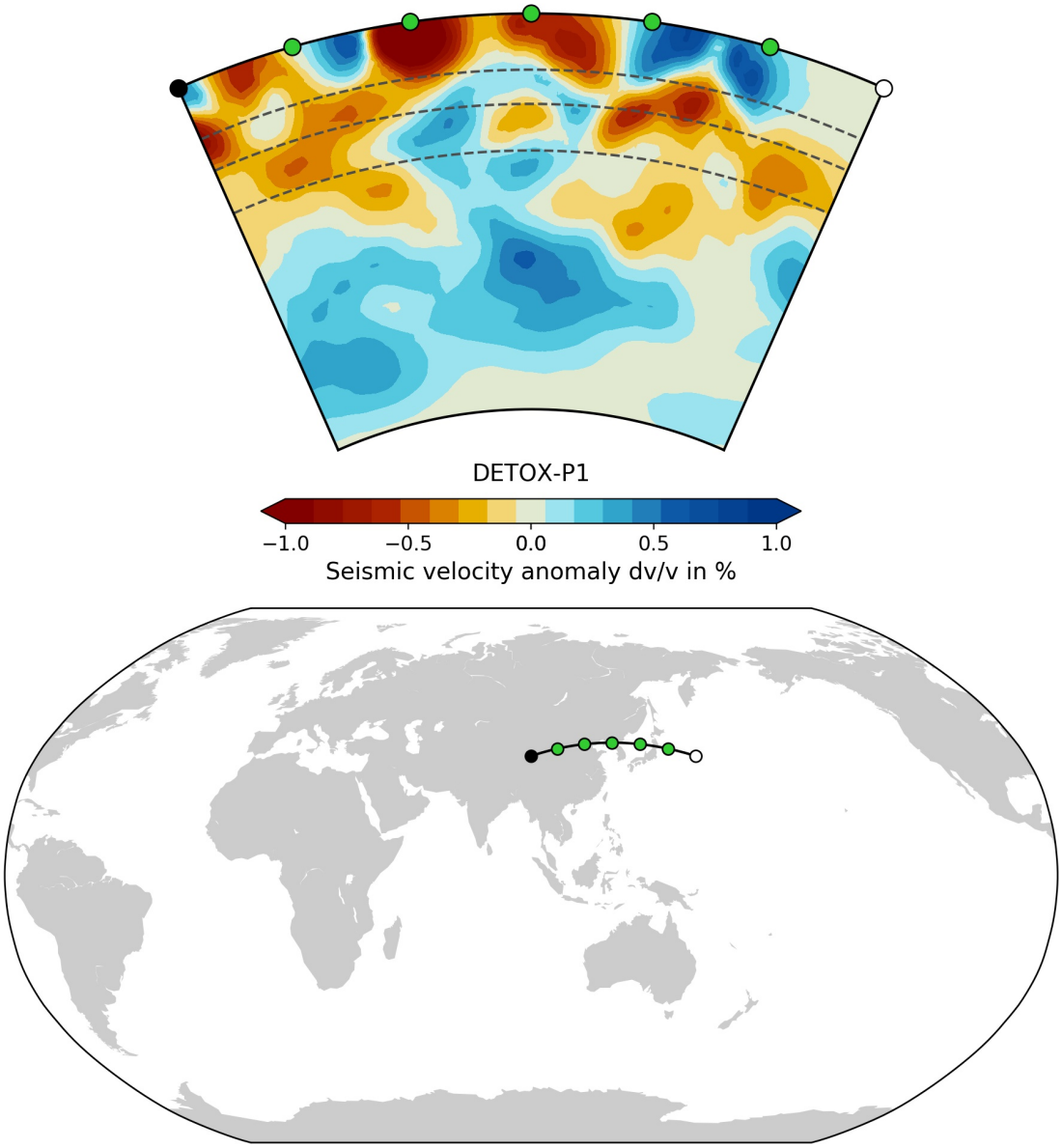

Figure A.98: East-West cross-section through DETOX P1 at 36°N, produced using SubMachine.

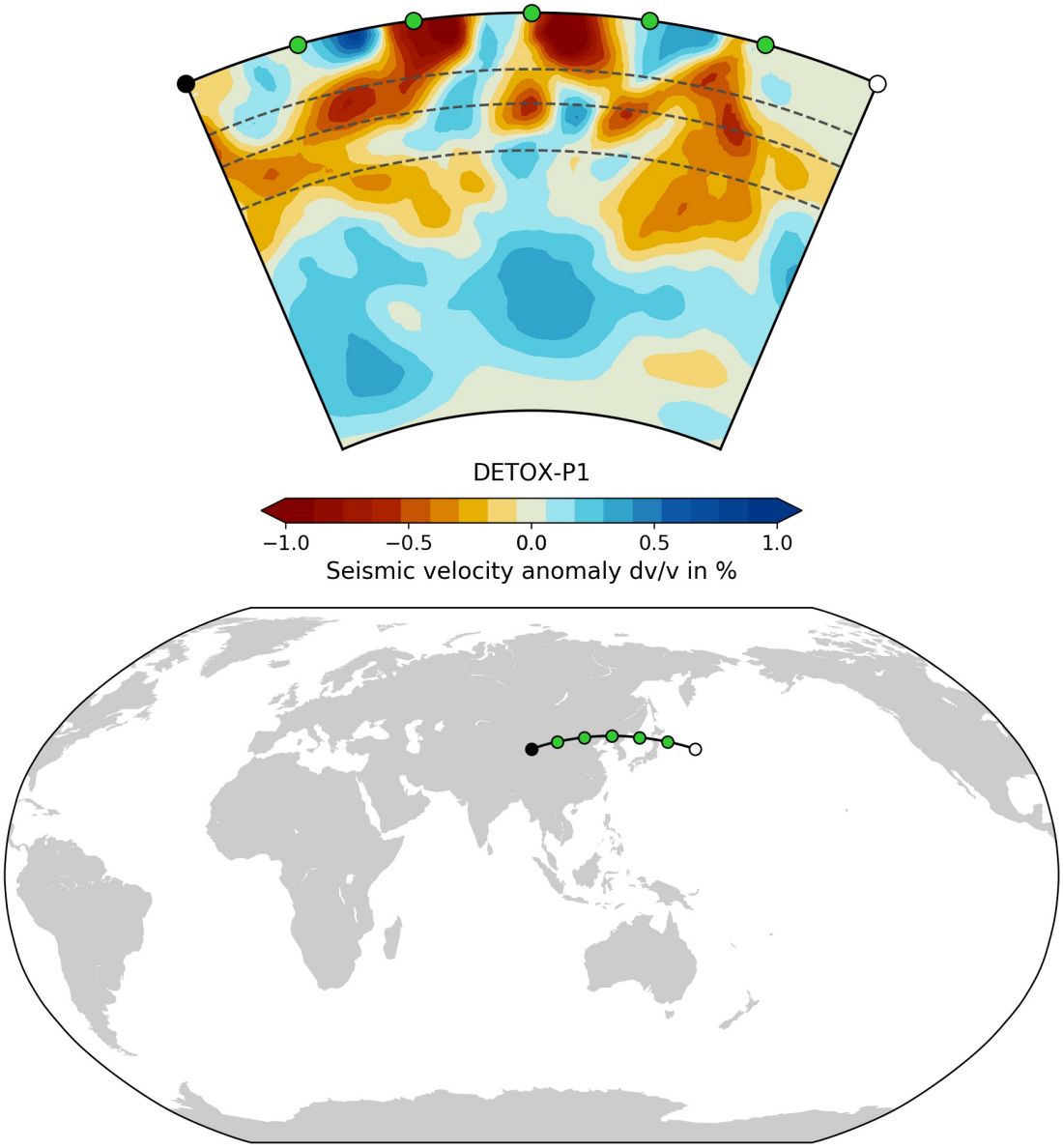

Figure A.99: East-West cross-section through DETOX P1 at 38°N, produced using SubMachine.

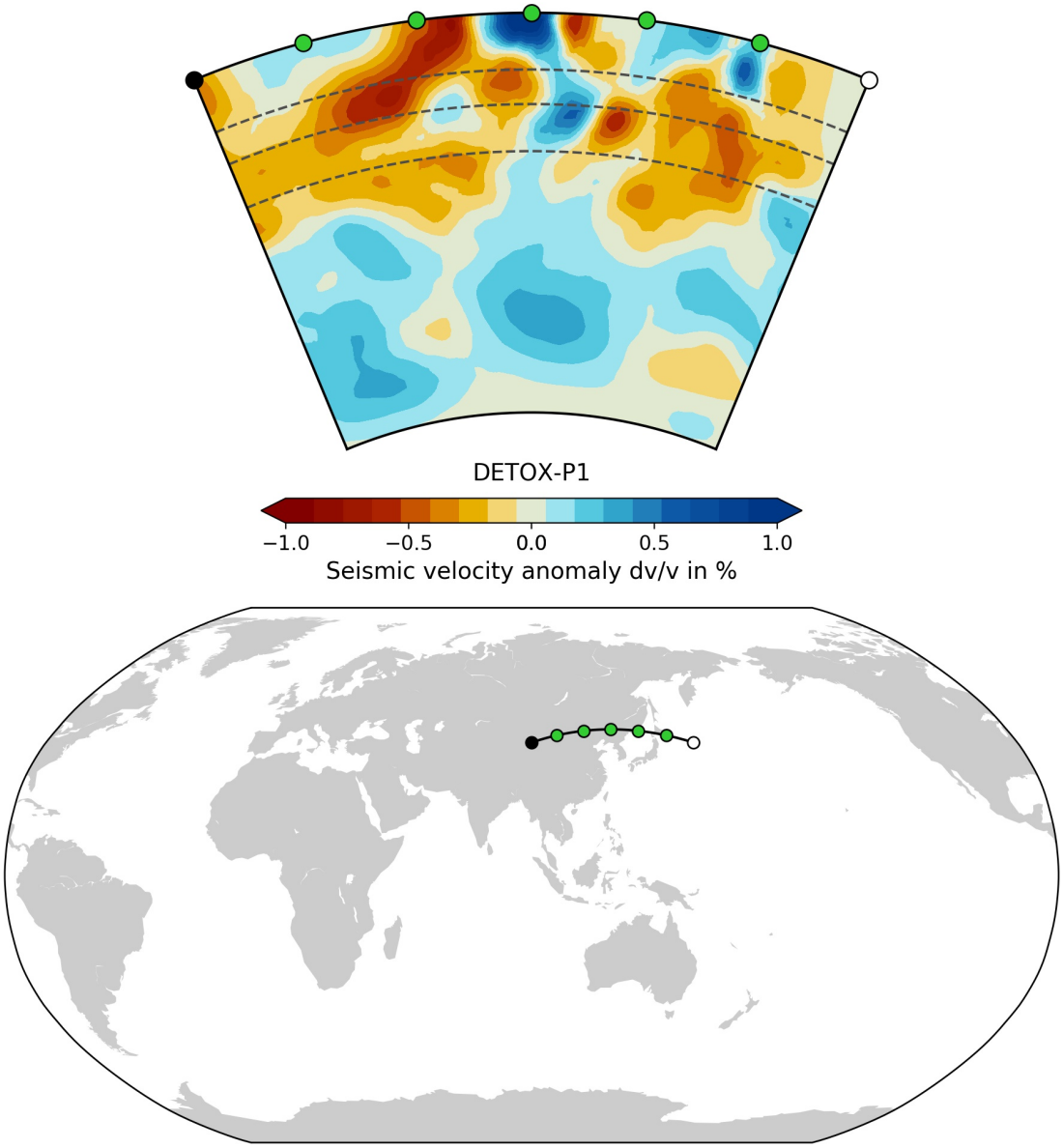

Figure A.100: East-West cross-section through DETOX P1 at 40°N, produced using SubMachine.

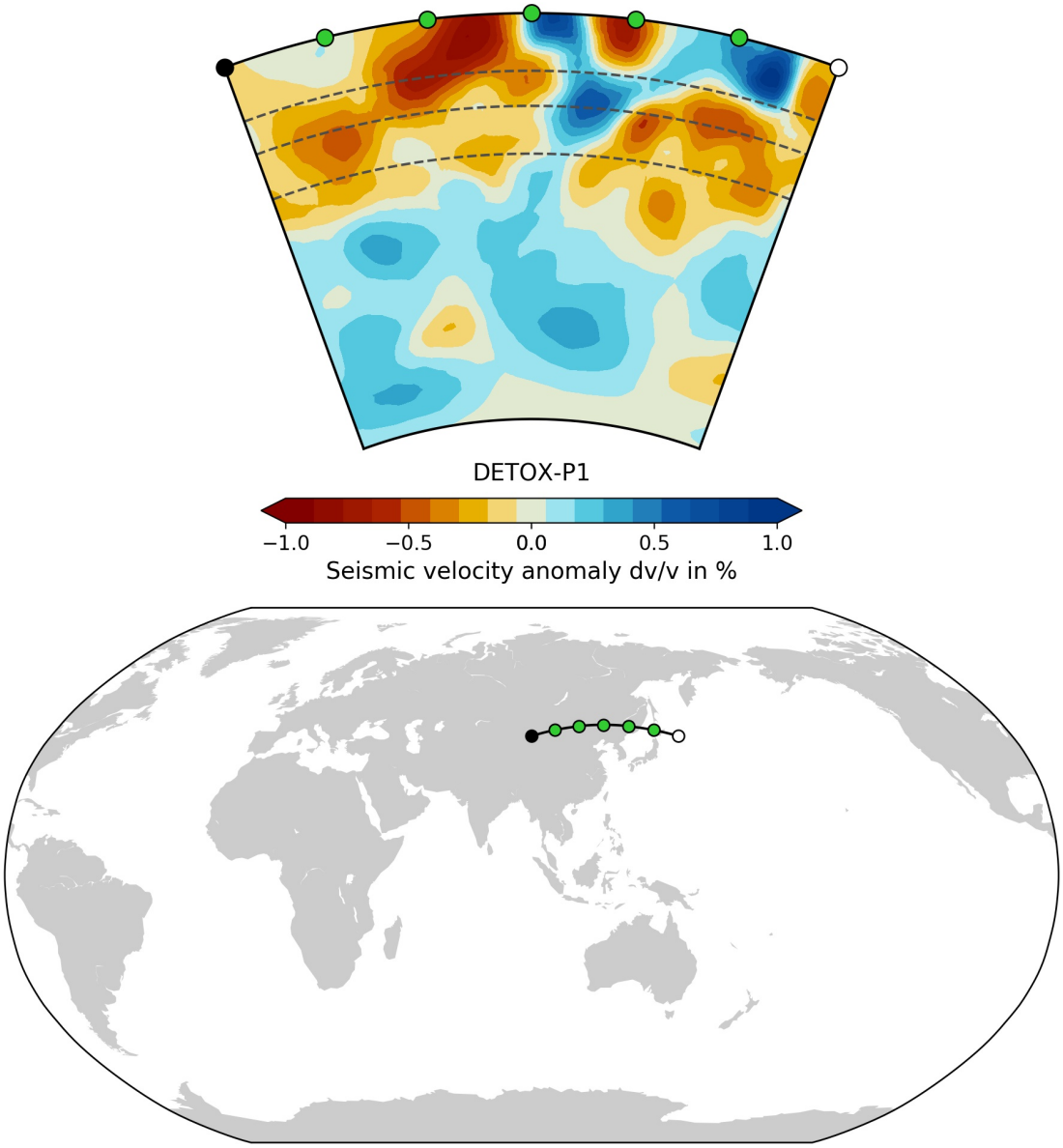

Figure A.101: East-West cross-section through DETOX P1 at 42°N, produced using SubMachine.

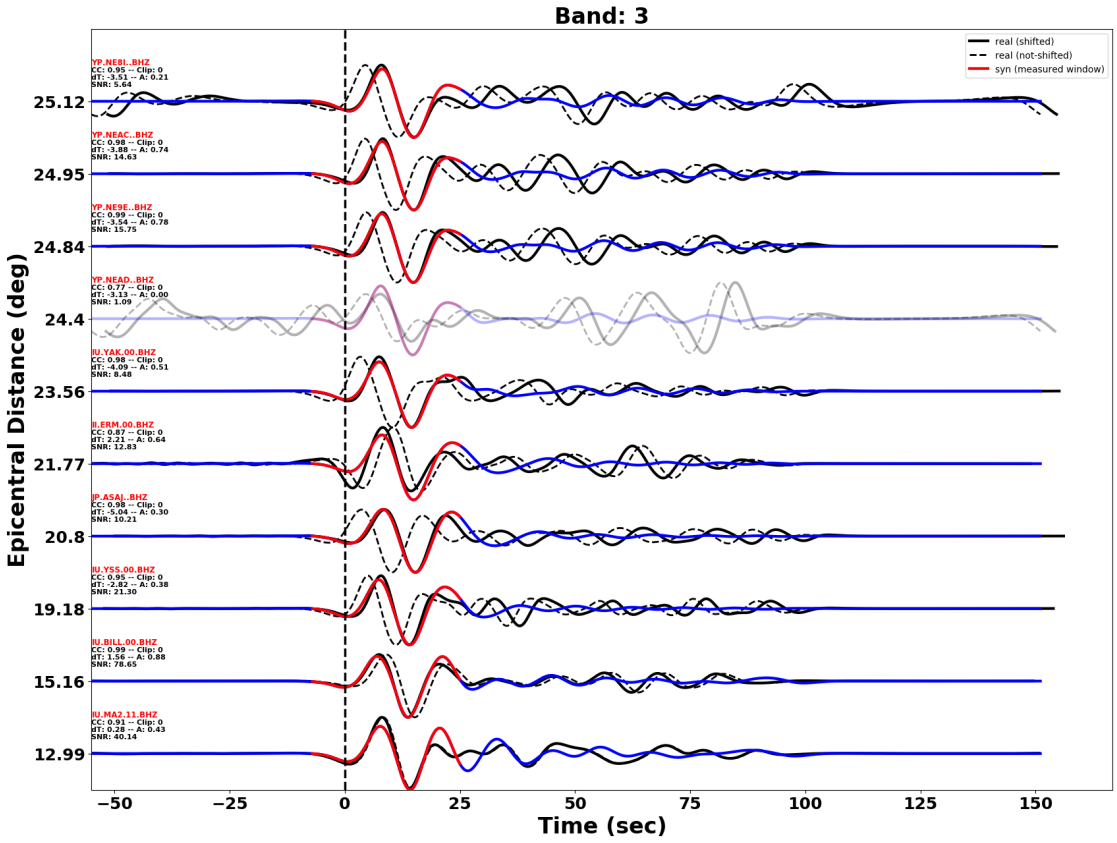

Figure A.102: 15s multifrequency measurements from an earthquake located in the Komandorsky Islands region. Travel-time delays of up to 5s reflect passage through aggregated subducted slab in the mantle transition zone.

References

Amaru, M.L., 2007. Global travel time tomography with 3-D reference models (Doctoral dissertation, University Utrecht).

Barber, C.B., Dobkin, D.P. and Huhdanpaa, H., 1996. The quickhull algorithm for convex hulls.
ACM Transactions on Mathematical Software (TOMS), 22(4), pp.469-483.
DOI: https://doi.org/10.1145/235815.235821

Borgeaud, A.F., Kawai, K. and Geller, R.J., 2019. Three-dimensional S velocity structure of the mantle transition zone beneath Central America and the Gulf of Mexico inferred using waveform inversion. Journal of Geophysical Research: Solid Earth, 124(9), pp.9664-9681. DOI: https://doi.org/10.1029/2018JB016924

Bozdağ, E., Peter, D., Lefebvre, M., Komatitsch, D., Tromp, J., Hill, J., Podhorszki, N. and Pugmire,
D., 2016. Global adjoint tomography: frst-generation model. Geophysical Journal International, 207(3), pp.1739-1766. DOI: https://doi.org/10.1093/gji/ggw356

Chapman, C.H., 1978. A new method for computing synthetic seismograms. Geophysical Journal International, 54(3), pp.481-518. DOI: https://doi.org/10.1111/j.1365-246X.1978.tb05491.x

Chen, M., Niu, F., Liu, Q., Tromp, J. and Zheng, X., 2015. Multiparameter adjoint tomography of the crust and upper mantle beneath East Asia: 1. Model construction and comparisons. Journal of Geophysical Research: Solid Earth, 120(3), pp.1762-1786.
DOI: https://agupubs.onlinelibrary.wiley.com/doi/abs/10.1002/2014JB011638

Čížková, H. and Bina, C.R., 2013. Effects of mantle and subduction-interface rheologies on slab stagnation and trench rollback. Earth and Planetary Science Letters, 379, pp.95-103. DOI: https://doi.org/10.1016/j.epsl.2013.08.011

Colombi, A., Nissen-Meyer, T., Boschi, L. and Giardini, D., 2012. Seismic waveform sensitivity to global boundary topography. Geophysical Journal International, 191(2), pp.832-848. DOI: https://doi.org/10.1111/j.1365-246X.2012.05660.x

Dahlen, F.A., Hung, S.H. and Nolet, G., 2000. Fréchet kernels for fnite-frequency traveltimes—I. Theory. Geophysical Journal International, 141(1), pp.157-174. DOI: https://doi.org/10.1046/j.1365-246X.2000.00070.x

Dziewonski, A.M. and Anderson, D.L., 1981. Preliminary reference Earth model. Physics of the earth and planetary interiors, 25(4), pp.297-356. DOI: https://doi.org/10.1016/0031-9201(81)90046-7

Fichtner, A., 2010. Full seismic waveform modelling and inversion. Springer Science & Business Media.

Fuji, N., Kawai, K. and Geller, R.J., 2010. A methodology for inversion of broadband seismic waveforms for elastic and anelastic structure and its application to the mantle transition zone beneath the Northwestern Pacifc. Physics of the Earth and Planetary Interiors, 180(3-4), pp.118-137. DOI: https://doi.org/10.1016/j.pepi.2009.10.004

Fukao, Y., Obayashi, M., Inoue, H. and Nenbai, M., 1992. Subducting slabs stagnant in the mantle transition zone. Journal of Geophysical Research: Solid Earth, 97(B4), pp.4809-4822. DOI: https://doi.org/10.1029/91JB02749

Fukao, Y. and Obayashi, M., 2013. Subducted slabs stagnant above, penetrating through, and trapped below the 660 km discontinuity. Journal of Geophysical Research: Solid Earth, 118(11), pp.5920-5938. https://doi.org/10.1002/2013JB010466

Garel, F., Goes, S., Davies, D.R., Davies, J.H., Kramer, S.C. and Wilson, C.R., 2014. Interaction of subducted slabs with the mantle transition-zone: A regime diagram from 2-D thermo-mechanical models with a mobile trench and an overriding plate. Geochemistry, Geophysics, Geosystems, 15(5), pp.1739-1765. https://doi.org/10.1002/2014GC005257

Golos, E.M., Fang, H., Yao, H., Zhang, H., Burdick, S., Vernon, F., Schaeffer, A., Lebedev, S. and Van der Hilst, R.D., 2018. Shear wave tomography beneath the United States using a joint inversion of surface and body waves. Journal of Geophysical Research: Solid Earth, 123(6), pp.5169-5189. DOI: https://doi.org/10.1029/2017JB014894

Grand, S.P. and Helmberger, D.V., 1984.
Upper mantle shear structure of North America. Geophysical Journal International, 76(2), pp.399-438. DOI: https://doi.org/10.1111/j.1365-246X.1984.tb05053.x

Godwin, H., 2020. Fast probing of many earth models using full waveforms. PhD thesis, University of Oxford, Oxford.

Hall, R., 2012. Late Jurassic–Cenozoic reconstructions of the Indonesian region and the Indian Ocean. Tectonophysics, 570, pp.1-41. DOI: https://doi.org/10.1016/j.tecto.2012.04.021

Hall, R. and Spakman, W., 2015. Mantle structure and tectonic history of SE Asia. Tectonophysics, 658, pp.14-45. DOI: https://doi.org/10.1016/j.tecto.2015.07.003

Hosseini, K. and Sigloch, K., 2015. Multifrequency measurements of core-diffracted P waves (Pdiff) for global waveform tomography. Geophysical Journal International, 203(1), pp.506-521. DOI: https://doi.org/10.1093/gji/ggv298

Hosseini, K., Matthews, K.J., Sigloch, K., Shephard, G.E., Domeier, M. and Tsekhmistrenko, M., 2018. SubMachine: Web-based tools for exploring seismic tomography and other models of Earth's deep interior. Geochemistry, Geophysics, Geosystems, 19(5), pp.1464-1483. DOI: https://doi.org/10.1029/2018GC007431

Hosseini, K., Sigloch, K., Tsekhmistrenko, M., Zaheri, A., Nissen-Meyer, T. and Igel, H., 2019..
Global mantle structure from multifrequency tomography using P, PP and P-diffracted waves.

Geophysical Journal International, 220(1), pp.96-141.
DOI: https://doi.org/10.1093/gji/ggz394

Kennett, B.L., Engdahl, E.R. and Buland, R., 1995. Constraints on seismic velocities in the Earth from traveltimes. Geophysical Journal International, 122(1), pp.108-124. https://doi.org/10.1111/j.1365-246X.1995.tb03540.x

Komatitsch, D. and Tromp, J., 2002. Spectral-element simulations of global seismic wave propagation—II. Three-dimensional models, oceans, rotation and self-gravitation. Geophysical Journal International, 150(1), pp.303-318.
DOI: https://doi.org/10.1046/j.1365-246X.2002.01716.x

Koroni, M., Bozdağ, E., Paulssen, H. and Trampert, J., 2017.
Sensitivity analysis of seismic waveforms to upper-mantle discontinuities using the adjoint method. Geophysical Journal International, 210(3), pp.1965-1980. DOI: https://doi.org/10.1093/gji/ggx286

Lallemand, S., 2016. Philippine Sea Plate inception, evolution, and consumption with special emphasis on the early stages of Izu-Bonin-Mariana subduction. Progress in Earth and Planetary Science, 3(1), pp.1-27. DOI: https://doi.org/10.1186/s40645-016-0085-6

Li, C., van der Hilst, R.D., Engdahl, E.R. and Burdick, S., 2008. A new global model for P wave speed variations in Earth's mantle. Geochemistry, Geophysics, Geosystems, 9(5). DOI: https://agupubs.onlinelibrary.wiley.com/doi/pdf/10.1029/2007GC001806

Ma, J., Tian, Y., Zhao, D., Liu, C. and Liu, T., 2019. Mantle dynamics of western Pacific and East Asia: New insights from P wave anisotropic tomography. Geochemistry, Geophysics, Geosystems, 20(7), pp.3628-3658. DOI: https://doi.org/10.1029/2019GC008373

Matthews, K.J., Maloney, K.T., Zahirovic, S., Williams, S.E., Seton, M. and Mueller, R.D., 2016. Global plate boundary evolution and kinematics since the late Paleozoic. Global and Planetary Change, 146, pp.226-250. https://doi.org/10.1016/j.gloplacha.2016.10.002

Mercerat, E.D. and Nolet, G., 2013. On the linearity of cross-correlation delay times in fnite-frequency tomography. Geophysical Journal International, 192(2), pp.681-687. DOI: https://doi.org/10.1093/gji/ggs017

Mohammadzaheri, A., Sigloch, K., Hosseini, K. and Mihalynuk, M.G., 2021. Subducted Lithosphere under South America from Multi-frequency P-wave Tomography. Journal of Geophysical Research: Solid Earth, 126, p.e2020JB020704. DOI: https://doi.org/10.1029/2020JB020704

Moreno, T., Wallis, S.R., Kojima, T. and Gibbons, W. eds., 2016, March. The geology of Japan. Geological Society of London.

Morgan, G., 2021. A 3D consideration of the geometry and deformation of slabs in the South-West Pacifc illuminated by seismic tomography and earthquake focal locations. Masters thesis, University of Oxford, Oxford.

Nissen-Meyer, T., van Driel, M., Stähler, S.C., Hosseini, K., Hempel, S., Auer, L., Colombi, A. and Fournier, A., 2014. AxiSEM: broadband 3-D seismic wavefelds in axisymmetric media. Solid Earth, 5(1), pp.425-445. DOI: https://doi.org/10.5194/se-5-425-2014

Nolet, G., 2008. A breviary of seismic tomography. A Breviary of Seismic Tomography.

Obayashi, M., Yoshimitsu, J., Nolet, G., Fukao, Y., Shiobara, H., Sugioka, H., Miyamachi, H. and Gao, Y., 2013. Finite frequency whole mantle P wave tomography: Improvement of subducted slab images. Geophysical Research Letters, 40(21), pp.5652-5657. DOI: https://doi.org/10.1002/2013GL057401

Paige, C.C. and Saunders, M.A., 1982. LSQR: An algorithm for sparse linear equations and sparse least squares. ACM Transactions on Mathematical Software (TOMS), 8(1), pp.43-71.

Percival, D.B. and Walden, A.T., 1993. Spectral analysis for physical applications. Cambridge University press.

Persson, P.O. and Strang, G., 2004. A simple mesh generator in MATLAB. SIAM review, 46(2), pp.329-345. DOI: https://doi.org/10.1137/S0036144503429121

Porritt, R.W. and Yoshioka, S., 2016. Slab pileup in the mantle transition zone and the 30 May 2015 Chichi-jima earthquake. Geophysical Research Letters, 43(10), pp.4905-4912. DOI: https://doi.org/10.1002/2016GL068168

Pownall, J.M., Lister, G.S. and Spakman, W., 2017. Reconstructing subducted oceanic lithosphere by "reverse-engineering" slab geometries: The northern Philippine Sea Plate. Tectonics, 36(9), pp.1814-1834.
DOI: https://doi.org/10.1002/2017TC004686

Ritsema, J. and van Heijst, H.J., 2002. Constraints on the correlation of P-and S-wave velocity heterogeneity in the mantle from P, PP, PPP and PKP ab traveltimes. Geophysical Journal International, 149(2), pp.482-489. DOI: https://doi.org/10.1046/j.1365-246X.2002.01631.x

Schwarz, B. and Gajewski, D., 2017. Accessing the diffracted wavefeld by coherent subtraction. Geophysical Journal International, 211(1), pp.45-49.
DOI: https://doi.org/10.1093/gji/ggx291

Seton, M., Flament, N., Whittaker, J., Müller, R.D., Gurnis, M. and Bower, D.J., 2015. Ridge subduction sparked reorganization of the Pacific plate-mantle system 60–50 million years ago. Geophysical Research Letters, 42(6), pp.1732-1740. https://doi.org/10.1002/2015GL063057

Shearer, P.M., 2009.
Introduction to seismology. Cambridge university press.

Sigloch, K. and Nolet, G., 2006. Measuring fnite-frequency body-wave amplitudes and traveltimes. Geophysical Journal International, 167(1), pp.271-287. DOI: https://doi.org/10.1111/j.1365-246X.2006.03116.x

Sigloch, K., McQuarrie, N. and Nolet, G., 2008. Two-stage subduction history under North America inferred from multiple-frequency tomography. Nature Geoscience, 1(7), pp.458-462. DOI: https://doi.org/10.1038/ngeo231

Sigloch, K. and Mihalynuk, M.G., 2013. Intra-oceanic subduction shaped the assembly of Cordilleran North America. Nature, 496(7443), pp.50-56. Available at: https://www.nature.com/articles/nature12019

Simmons, N.A., Myers, S.C., Johannesson, G. and Matzel, E., 2012. LLNL-G3Dv3: Global P wave tomography model for improved regional and teleseismic travel time prediction. Journal of Geophysical Research: Solid Earth, 117(B10). https://doi.org/10.1029/2012JB009525

Simutė, S., Steptoe, H., Cobden, L., Gokhberg, A. and Fichtner, A., 2016.
Full-waveform inversion of the Japanese Islands region. Journal of Geophysical Research: Solid Earth, 121(5), pp.3722-3741.
DOI: https://agupubs.onlinelibrary.wiley.com/doi/abs/10.1002/2016JB012802

Slepian, D., 1978. Prolate spheroidal wave functions, Fourier analysis, and uncertainty—V: The discrete case. Bell System Technical Journal, 57(5), pp.1371-1430. DOI: https://doi.org/10.1002/j.1538-7305.1978.tb02104.x

Song, T.R.A., Helmberger, D.V. and Grand, S.P., 2004.
Low-velocity zone atop the 410-km seismic discontinuity in the northwestern United States.
Nature, 427(6974), pp.530-533.

Stähler, S.C., Sigloch, K. and Nissen-Meyer, T., 2012. Triplicated P-wave measurements for waveform tomography of the mantle transition zone. Solid Earth, 3(2), pp.339-354. DOI: https://doi.org/10.5194/se-3-339-2012

Stähler, S., vanDriel, M., Godwin, H., Totten, E., Hosseini, K., Auer, L., Sigloch, K. and Nissen-Meyer, T. M.C. Kerner: Global broadband seismic sensitivity kernels on heterogeneous meshes calculated from a wavefeld database (in prep.)

Tajima, F. and Grand, S.P., 1995.
Evidence of high velocity anomalies in the transition zone associated with the southern Kurile subduction zone. Geophysical research letters, 22(23), pp.3139-3142. DOI: https://doi.org/10.1029/95GL03314

Tajima, F. and Grand, S.P., 1998. Variation of transition zone high-velocity anomalies and depression of 660 km discontinuity associated with subduction zones from the southern Kuriles to Izu-Bonin and Ryukyu. Journal of Geophysical Research: Solid Earth, 103(B7), pp.15015-15036. DOI: https://doi.org/10.1029/98JB00752

Tang, Y., Obayashi, M., Niu, F., Grand, S.P., Chen, Y.J., Kawakatsu, H., Tanaka, S., Ning, J. and Ni, J.F., 2014. Changbaishan volcanism in northeast China linked to subduction-induced mantle upwelling. Nature Geoscience, 7(6), pp.470-475. Available at: https://www.nature.com/articles/ngeo2166

Tape, C., Liu, Q. and Tromp, J., 2007.
Finite-frequency tomography using adjoint methods—Methodology and examples using membrane surface waves. Geophysical Journal International, 168(3), pp.1105-1129. DOI: https://doi.org/10.1111/j.1365-246X.2006.03191.x

Tao, K., Grand, S.P. and Niu, F., 2017.
Full-waveform inversion of triplicated data using a normalized-correlation-coeffcient-based
misft function. Geophysical Journal International, 210(3), pp.1517-1524. DOI: https://doi.org/10.1093/gji/ggx249

Tao, K., Grand, S.P. and Niu, F., 2018. Seismic structure of the upper mantle beneath eastern Asia from full waveform seismic tomography. Geochemistry, Geophysics, Geosystems, 19(8), pp.2732-2763. DOI: https://agupubs.onlinelibrary.wiley.com/doi/abs/10.1029/2018GC007460

Tian, Y., Sigloch, K. and Nolet, G., 2009.
Multiple-frequency SH-wave tomography of the western US upper mantle. Geophysical Journal International, 178(3), pp.1384-1402. DOI: https://doi.org/10.1111/j.1365-246X.2009.04225.x

Tsekhmistrenko, M., 2019. Seismic Tomography of the La Reunion Plume.
PhD thesis, University of Oxford, Oxford.

van Driel, M., Krischer, L., Stähler, S.C., Hosseini, K. and Nissen-Meyer, T., 2015. Instaseis: Instant global seismograms based on a broadband waveform database. Solid Earth, 6(2), pp.701-717. DOI: https://se.copernicus.org/articles/6/701/2015/

Weston, J., Engdahl, E.R., Harris, J., Di Giacomo, D. and Storchak, D.A., 2018. ISC-EHB: reconstruction of a robust earthquake data set. Geophysical Journal International, 214(1), pp.474-484. DOI: https://doi.org/10.1093/gji/ggy155

Wu, J., Lin, Y.A., Flament, N., Wu, J.T.J. and Liu, Y., 2022. Northwest Pacific-Izanagi plate tectonics since Cretaceous times from western Pacific mantle structure. Earth and Planetary Science Letters, 583, p.117445. https://doi.org/10.1016/j.epsl.2022.117445

Zaroli, C., 2010 Global multi-frequency S-wave tomography of the Earth's mantle. PhD thesis, University of Strasbourg, Strasbourg.

Zenonos, A., De Siena, L., Widiyantoro, S. and Rawlinson, N., 2019. P and S wave travel time tomography of the SE Asia-Australia collision zone. Physics of the Earth and Planetary Interiors, 293, p.106267. https://doi.org/10.1016/j.pepi.2019.05.010